

MICROSTRUCTURE-BASED MODELING OF DAMAGE AND HEALING IN SALT ROCK WITH APPLICATION TO GEOLOGICAL STORAGE

A Thesis
Presented to
The Academic Faculty

by
Cheng Zhu

In Partial Fulfillment
of the Requirements for the Degree
Doctor of Philosophy in the
School of Civil and Environmental Engineering

Georgia Institute of Technology
August 2016

Copyright © 2016 by Cheng Zhu

MICROSTRUCTURE-BASED MODELING OF DAMAGE AND HEALING IN SALT ROCK WITH APPLICATION TO GEOLOGICAL STORAGE

Approved by:

Dr. Chloé Arson, Advisor
School of Civil and Environmental
Engineering
Georgia Institute of Technology

Dr. David Frost
School of Civil and Environmental
Engineering
Georgia Institute of Technology

Dr. Sheng Dai
School of Civil and Environmental
Engineering
Georgia Institute of Technology

Dr. Christian Huber
School of Earth and Atmospheric
Sciences
Georgia Institute of Technology

Dr. Ahmad Pouya
Laboratory Navier
(ENPC/IFSTTAR/CNRS)
Paris-Est University

Date Approved: May 26th, 2016

To my wife,
Shanshan (Kelly) Han,
for bringing Hannah to my life
and giving me endless support and love.

ACKNOWLEDGEMENTS

First of all, I would like to express my sincere appreciation to my Ph.D. advisor, Dr. Chloé Arson, for her patient guidance, consistent encouragement, and endless support, which gives me such an excellent experience at Georgia Tech. Her professional advice on study and persistent enthusiasm for research turn me into a “young salt” and will continuously lead me in my future endeavors.

I would like to acknowledge my Ph.D. thesis committee members including Dr. Sheng Dai, Dr. David Frost, Dr. Christian Huber, and Dr. Ahmad Pouya, for their insightful comments and suggestions that help me to become a better researcher. I am grateful to Dr. Dai for sharing experience and providing career advice. I want to thank Dr. Frost for always being helpful and supportive. I appreciate Dr. Huber’s suggestions on my research from the earth science aspect of view. Special thanks are given to Dr. Ahmad Pouya for his great guidance and mentorship throughout my Ph.D. study and hosting my visit in France. I am also grateful to Dr. Carlos Santamarina for his discussions and inspirations on my experimental works. I would like to take this opportunity to thank all other geosystems faculty members including Dr. Domniki Asimaki, Dr. Susan Burns, Dr. Leonid Germanovich, Dr. Haiying Huang, Dr. Paul Mayne, and Dr. Glenn Rix, for making such an amazing research and learning atmosphere at Georgia Tech.

I deeply appreciate invaluable supports from my research collaborators: Dr. Fred Chester, Dr. Judith Chester, and Jihui Ding at Texas A&M University; Dr. Van-Linh Nguyen at Paris-Est University; and Dr. Christopher Spiers and Lisanne Douma at Utrecht University. Their rigorous research and insightful suggestions enable me to make progresses and complete my Ph.D. study.

I am thankful to the help and support I received from my past and present lab members: Dr. Hao Xu, Yu-de Chen, Wencheng Jin, Xianda Shen, and Pei Wang. Discussions with visiting students including Erwan Le Bivic, Madeline Fleury, Nicolas Henry, Romain Jeanneret dit Grosjean, and Julien Roze further inspire and motivate my research. I want to express my gratitude to all Geosystems Engineering fellows for bringing joy and happiness to my Ph.D. journey. Sharing experiences, jokes, stories, and progresses with them have always been essential elements of my Ph.D. life. I really enjoy numerous social events organized by our Geosociety. I also want to thank the valuable assistance of undergraduate research assistants involved in the Vertically Integrated Projects Program on Energy Geotechnology at Georgia Tech.

I want to acknowledge the financial support from the School of Civil and Environmental Engineering at Georgia Tech and National Science Foundation, which makes my Ph.D. study at Georgia Tech possible.

Finally, I would like to thank my wife, Shanshan (Kelly) Han, for her everlasting support and love. I am particularly indebted to my parents, Wenbiao Zhu and Zhice Chen, and my parents-in-law, Shanfu Han and Yuqing Zeng, for their continuous encouragement and full support. I would like to express my deepest appreciation to all my relatives and friends near and far for their support and love at all times.

TABLE OF CONTENTS

DEDICATION	iii
ACKNOWLEDGEMENTS	iv
LIST OF TABLES	x
LIST OF FIGURES	xi
SUMMARY	1
I INTRODUCTION	3
1.1 Energy and Storage	3
1.2 Salt Rock Mechanics	4
1.3 Thesis Structure	7
II THEORETICAL BACKGROUND	8
2.1 Introduction	8
2.2 Micromechanical Processes in Salt Rock	9
2.2.1 Crystallographic Structure of Salt	9
2.2.2 Impact of Creep Processes on Microstructure and Deformation	11
2.3 Experimental Assessment of Damage and Healing in Rocks	14
2.4 Multi-scale Aspects of Rock Mechanics	16
2.5 State-of-the-Art of Continuum Damage and Healing Mechanics (CDHM)	19
2.6 Thermodynamic Principles used in Microstructure-enriched CDHM .	22
2.6.1 Inequality of Clausius-Duhem	22
2.6.2 Definition of Internal Variables	23
2.7 Homogenization Method	27
2.8 State-of-the-Art of Finite Element Models of Damage and Healing in Rocks	30
2.9 Research Objectives	32
III FABRIC-BASED DAMAGE AND HEALING MECHANICS . .	34
3.1 Introduction	34

3.2	Thermo-mechanical Model of Crack Opening and Closure	36
3.2.1	Thermo-mechanical Stress Induced Crack Opening and Closure	36
3.2.2	Model Calibration and Verification	39
3.2.3	Simulation of Thermo-mechanical Crack Opening	43
3.2.4	Simulation of Thermo-mechanical Crack Closure	46
3.3	Diffusive Mass Transfer (DMT)-based Healing Model	50
3.3.1	Microstructure Characterization	50
3.3.2	Theoretical Framework	53
3.3.3	Crack Opening, Closure and Rebonding during a Uniaxial Test	61
3.4	Anisotropic Healing Model	66
3.4.1	2D Diffusion Controlled Healing	66
3.4.2	Model Calibration	69
3.4.3	Numerical Analysis at the REV Scale	70
3.5	Fabric-based Permeability Model	77
3.5.1	Fabric Characterization	77
3.5.2	Theoretical Framework	79
3.5.3	Computational Algorithm	84
3.5.4	Numerical Simulation	85
3.6	Conclusions	91
IV	MICRO-MACRO MODEL OF VISCOUS FATIGUE	93
4.1	Introduction	93
4.2	Microscopic Sliding Mechanisms	95
4.3	Macroscopic Fatigue Behavior	97
4.4	Homogenization Scheme	98
4.4.1	Averaging Method	98
4.4.2	Inclusion-Matrix Model	100
4.4.3	Micro-macro Damage Modeling	101
4.5	Micro-Macro Stress Computational Method	105

4.5.1	Stress Redistribution due to Damage	105
4.5.2	Stress Redistribution due to Viscoplasticity	107
4.5.3	Computational method for axial loading	109
4.6	Model Calibration against Creep Tests	111
4.7	Simulation of Salt Fatigue under Creep Loading	113
4.7.1	Microscopic Origin of Creep Recovery	113
4.7.2	Influence of Grain Breakage on Macroscopic Creep Regimes .	117
4.8	Simulation of Salt Fatigue under Cyclic Loading	120
4.8.1	Damage Triggering due to Grain Viscous Deformation	120
4.8.2	Viscous Damage Propagation upon Cyclic Loading	121
4.9	Conclusions	125
V	FINITE ELEMENT ANALYSES APPLIED TO GEOSTORAGE	
	SYSTEMS	128
5.1	Introduction	128
5.2	Inter-granular and Intra-granular Damage in Salt Polycrystal	130
5.2.1	Single-crystal Deformation Mechanisms	130
5.2.2	Hill's Tensor in 2D	131
5.2.3	Joint Element Model	132
5.2.4	Model Configuration	134
5.2.5	Model Calibration	137
5.2.6	Comparison of the Inclusion-matrix Models with Joint-enriched FEM Models	142
5.2.7	Cyclic Loading Tests with the Joint-enriched FEM Model of Inter-granular Crack Propagation	152
5.2.8	Comparison of different damage mechanisms	157
5.3	Viscous Damage in Salt Cavern	169
5.3.1	Phenomenological Modeling Framework	169
5.3.2	Model Calibration	173
5.3.3	Pressurized Salt Cavern under Long-term Creep	177

5.4	Conclusions	185
VI	CONCLUSIONS AND FUTURE STUDY	187
6.1	Summary	187
6.2	Main Findings	190
6.3	Plans for Future Study	193
APPENDIX I	LITERATURE REVIEW	194
A.1	State of the Art: Experimental Assessment of Thermo-mechanical Damage in Rocks	194
A.2	Review of Microstructure-enriched Permeability Model for Rocks . .	196
A.3	Review of Experimental Studies of Salt Fatigue under Cyclic Loading	197
APPENDIX II	RELATION BETWEEN RESIDUAL STRESS AND PROBABILITY DENSITY FUNCTIONS OF FABRIC DESCRIP- TORS	198
APPENDIX III	APPROXIMATED MACROSCOPIC VISCOPLAS- TIC LAW	200
APPENDIX IV	2D PLANE STRAIN HILL'S TENSOR	203
BIBLIOGRAPHY	206
VITA	228

LIST OF TABLES

1	State of the art: phenomenological models of thermo-mechanical rock damage.	26
2	Outline of thermo-mechanical damage model	38
3	Model parameters obtained for sandstone after calibration and verification (with the soil mechanics sign convention).	41
4	Reference set of constitutive parameters used in the sensitivity analysis (after Halm and Dragon (1998)).	42
5	Outline of thermo-mechanical damage and healing model.	56
6	Relations between microscopic and macroscopic variables.	59
7	Model parameters used for the simulation of strain-controlled uniaxial tension loading/unloading/healing.	62
8	Simulation plan for DMT-based healing model.	62
9	Parameters adopted for the diffusion-controlled healing model (Eq. 33 and 34)	69
10	Microscopic stress change due to grain breakage.	106
11	Model parameters calibrated against the creep tests reported in Fuenkajorn and Phueakphum (2010).	111
12	Parameters calibrated for the <i>POROFIS</i> model with inter-granular joints only.	138
13	Cyclic loading tests performed with the joint-enriched FEM model of inter-granular crack propagation (1 - axial direction; 3 - lateral direction).152	

14	Three finite element models based on different damage mechanisms. .	160
15	Model parameters calibrated for damage evolution law 1 based on the experimental data (Fuenkajorn and Phueakphum, 2010).	176
16	Model parameters calibrated for damage evolution law 2 based on the experimental data (Fuenkajorn and Phueakphum, 2010).	177

LIST OF FIGURES

1	The 14 Bravais unit cells (Zumdahl and Zumdahl, 2006).	9
2	General features of the 7 basic unit cell geometry (Silberberg, 2012). .	10
3	Microprocesses leading to plastic deformation in crystalline materials.	11
4	Micro-mechanism map for halite at repository conditions.	12
5	Model of inter-granular pressure solution in a closed thermodynamic system, modified from (Meer and Spiers, 1997). σ_n indicates the mean normal stress and P_f the pore fluid pressure.	13
6	Discontinuities in salt at multiple scales, modified from (Ding et al., 2016; Schleder and Urai, 2007).	16
7	Definition of the Representative Elementary Volume (REV) (Bear, 1972).	18
8	REV window size and statistically homogeneous (SH) response functions (Lacy et al., 1999).	18
9	Microscopic sectional view of synthetic salt rock, prepared by Mr. J. Ding at Texas A&M University. Synthetic salt rock samples were produced through thermo-mechanical coupled consolidation process (Grain size = 0.3 ~ 0.355mm, $T = 150^\circ\text{C}$, $\sigma = 106.7\text{MPa}$, final porosity = 2.93%).	29
10	Multi-scale modeling approaches, modified from (Schleder and Urai, 2007).	33
11	Model development in Chapter 3.	35

12	Strain decomposition (soil mechanics sign convention: compression counted positive).	39
13	Stress-strain curves obtained during drained triaxial compression tests conducted on saturated sandstone. c - model calibration, v - model verification.	40
14	Sensitivity analysis on the mechanical damage parameters used in the model (all expressed in units of pressure). C_0 : initial damage threshold; C_1 : hardening parameter; α & β : parameters controlling the shape of the damaged stress/strain curve (ductile vs. brittle trends).	42
15	Stress paths simulated to study the influence of thermo-mechanical crack opening: comparison of mechanical and thermo-mechanical energy released during the propagation of compression damage.	44
16	Simulation of the two thermo-mechanical stress paths described in Fig. 15 (confining pressure: 20 MPa; maximum axial strain: 0.00226; maximum temperature change: 150K): (a) Deviatoric stress vs. axial and lateral deformation; (b) Damage evolution vs. axial deformation and temperature variation; (c) Damage evolution vs. axial and lateral deformation; (d) Damage evolution vs. temperature variation.	45
17	Stress paths simulated to study the influence of thermo-mechanical crack closure: comparison of mechanical and thermo-mechanical compression loadings.	47

18	Simulation of the thermo-mechanical stress paths described in Fig. 17: (a) total stress vs. axial deformation (crack closure by cooling); (b) thermal stress vs. thermal strain: length of OC equals to length of OD'_1 (crack closure by cooling); (c) evolution of axial damage (direction 1) vs. axial deformation (TM – closure by cooling; M – closure by compression); (d) evolution of stress components with axial deformation (TM – closure by cooling; M – closure by compression).	49
19	Experimental set up for observation of creep in salt.	51
20	Image processing: (a) Stereo-microscopic image; (b) Binary image; (c) Void distribution; (d) Void outline (contours). Salt grains have a transparent cubic structure with flat surfaces. The resulting transmitted and reflected light significantly impair the microscopic image quality (Fig. 20a). Image processing techniques have been proposed in MATLAB and <i>ImageJ</i> to improve the grain boundary detection (Zhu et al., 2015b). We will continue to work on these issues in our future work. Possible approaches include using colored epoxy to enhance the grain-void interfaces and cutting the sample into thin sections.	52
21	Probability density functions obtained for the void area (A) and for the crack length (defined as the major semi-axis of fitting ellipses projected in the three directions of space: R_i , $i=x,y,z$). (a) Power-law distribution of void area $p(A)$; (b) Log-normal distribution of crack length $p(R_i)$. <i>Note that the spikes are due to the presence of small black dots in the binary image obtained after processing.</i>	53

22	Representation of the geometric evolution of micro-cracks in the proposed model (solid line - original shape; dashed line - deformed shape): (a) Elastic tension: $\Delta\lambda_a \neq 0$, $\Delta R = 0$; (b) Non elastic tension: $\Delta\lambda_a \neq 0$, $\Delta R \neq 0$; (c) Elastic unloading (compression): $\Delta\lambda_a \neq 0$, $\Delta R = 0$; (d) Healing (after closure): $\Delta\lambda_a = 0$, $\Delta R \neq 0$	58
23	Schematic representation of a micro-crack subjected to residual stress within the REV	60
24	Computation method to update macroscopic variables through the update of microscopic descriptors.	61
25	Stress path simulated to study thermo-mechanical crack opening, closure, and healing.	63
26	Influence of healing temperature on mechanical recovery (direction 1 is the direction of tensile loading).	65
27	Schematic model of healing propagation front in a crack (crack cusp migration). Damage intensity U varies from 0 (bonded crack faces similar to an intact material with no crack) to 1 (closed but not bonded faces).	67
28	Distribution of damage intensity during the healing process within one planar crack. The evolution of the lag distance is governed by a 2D diffusion model.	68

29	Calibration of the two-dimensional diffusion-controlled healing model against the experimental result. The numerical curve has a step-wise shape because of the technique we used to update the position of the crack circumference: The crack cusp migration distance is the horizontal distance between the bonded crack face ($U = 0$) and the closed but not bonded face ($U = 1$). However, since 1 is the asymptotic value for U as shown in Fig. 28, we consider the crack face as open if $U > 0.95$.	70
30	Stress-strain curve simulated for the compression-tension cycle (The magnified portion shows the details of the unilateral effects).	72
31	Evolution of the damage variable. Cracks perpendicular to the loading axis (left) and parallel to the loading axis (right).	73
32	Evolution of net damage. Cracks perpendicular to the loading axis (left) and parallel to the loading axis (right).	74
33	Evolution of crack length. Cracks parallel to the loading axis (left) and parallel to the loading axis (right).	75
34	Evolution of mean crack area. Cracks parallel to the loading axis (left) and parallel to the loading axis (right).	75
35	Damage intensity after two different healing periods (grain scale). . .	76
36	Image analysis during creep tests realized on table salt: (a) experimental set up; (b) micro-CT image of the solid skeleton; (c) cross-sectional view (original image); (d) cross-sectional view (binary image). Voxel size = $30\mu m$. Sample diameter = $19mm$. Grain size = $300 \sim 400\mu m$.	78
37	Locations of void centroids processed from the binary image in Fig. 36d.	79

38	Normalized probability distribution of the centroid-to-centroid distances for all voids in the binary image (Fig. 36d). The peak appears at about 0.4 mm, which is close to the typical size of a single table salt grain.	79
39	Normalized power law distribution of void area processed from the binary image in Fig. 36d.	80
40	(a) Comparison between a spheroidal crack and a penny-shaped crack (3D view and 2D view). (b) Characterization of the spatial distribution of spheroidal cracks. Each crack is characterized by its radius, aperture, orientation, and the crack spacing.	81
41	The normalized permeability as a function of the probability of intersection between two cracks (p). The percolation threshold for the four-fold coordinated Bethe lattice is $1/3$	84
42	Computational algorithm of the microstructure-enriched model.	86
43	Numerical simulation results from MATLAB at the integration point: (a) stress-strain; (b) damage variable; (c) net damage variable; (d) crack radius; (e) crack aperture; (f) permeability; (g) volume change; (h) connectivity.	89
44	Crystal structure of salt.	95
45	Sliding planes in FCC crystals (Barber et al., 2008).	95
46	Spherical coordinate system adopted to characterize mono crystal orientations.	99
47	Salt rock Representative Elementary Volume (REV). (a) Monocrystal inclusions in the homogeneous matrix. (b) Schematic representation of salt mono-crystals in the inclusion-matrix model.	101

48	Stress computational method: decomposition of the time step into damage and viscous phases, for stress- or strain- controlled tests. . . .	103
49	Calibration of the approximated macroscopic creep law against long-term creep tests reported in Fuenkajorn and Phueakphum (2010). . .	112
50	Simulation of two long-term creep tests (grain breakage was not considered): (a) Stress path. (b) Time evolution of macroscopic strains. .	114
51	Asymptotic creep behavior predicted by the micro- macro- model, in the absence of grain breakage. (a) Stress path. (b) Time evolution of macroscopic strains.	115
52	Graphical representation of the microscopic principal stresses.	115
53	Micro-stress developed in the sample during the two-stage creep test simulated in the absence of grain breakage: loading points C, D, E shown in Fig. 50.	117
54	Comparison of different creep tests, with and without account for grain breakage. (a) Time evolution of total macrostrains. (b) Time evolution of viscoplastic macrostrains. (c) Major microstress component at the end of the creep tests. (d) Minor microstress component at the end of the creep tests.	119

55	Effect of the frequency of loading on macroscopic strains, in the absence of grain breakage. (a) Cyclic loading history. (b) Evolution of macroscopic strains with macroscopic stress. (c) Major principal internal stress distribution at the end of the cyclic loading test. (d) Minor principal internal stress distribution at the end of the cyclic loading test. (e) Major internal stress distribution after 1 cycle (point A) and after 15 cycles (point B). (f) Minor internal stress distribution after 1 cycle (point A) and after 15 cycles (point B).	122
56	Evolution of the damaged Young's modulus with the number of cycles ($f=0.03$ Hz; maximum stress = 14 MPa; stress amplitude = 6 MPa). .	123
57	Simulation of a cyclic loading with a frequency of 0.03 Hz, a maximum loading stress of 20 MPa and an amplitude of 10 MPa (grain breakage considered). 2 grains are broken at A (after 6 cycles). 7 grains are broken at B (after 8 cycles).	124
58	2D salt polycrystal: representative halite crystal orientations are obtained by varying only one degree of freedom, the angle of rotation θ about the axis normal to the plane.	130
59	Representation of the two slips systems that control shear deformation at the grain scale in 2D plane strain (\mathbf{N} and \mathbf{M} are the normal vector and gliding vector, respectively).	131
60	Cross-sectional view of the salt rock REV considered in the homogenization scheme. (a) Salt polycrystal; (b) Inclusion-matrix model; (c) Equivalence of the grain-matrix interaction problem with that of a borehole subject to internal pressure and far-field stresses.	132

61	Evolution of the damage-plasticity criterion used in joint elements, from the intact state to the completely damaged state. The yellow dashed line is parallel to the line that represents the limiting criterion when $D = 1$, and intersects the τ axis at $\sigma_R \tan(\eta)$	134
62	Salt thin sections (adapted from Schleider and Urai (2007)): Microstructure (left) and Automated EBSD map (right).	136
63	<i>POROFIS</i> FEM model with inter-granular joints only (8mm \times 8mm). In the legend, grain numbers refer to grain orientations (12 orientations considered in total), and OG is the color used for joint elements. . . .	136
64	<i>POROFIS</i> FEM model with inter-granular and intra-granular joints (8mm \times 8mm). In the legend, grain numbers refer to grain orientations (12 orientations considered in total), OG is the color used for inter-granular joint elements, and IG is the color used for intra-granular joint elements.	137
65	Evolution of the Young's modulus of the <i>POROFIS</i> model with inter-granular joints only, for different values of joint tangential stiffness, and for three ratios of tangential vs. normal stiffness.	140
66	Evolution of the Young's modulus of the <i>POROFIS</i> model with inter-granular joints only, for different values of joint normal stiffness, and for three ratios of tangential vs. normal stiffness.	140

67	Correlation between macroscopic axial strain rate and macroscopic axial stress, obtained from the simulation of the uniaxial creep tests with <i>POROFIS</i> , in plane strain. The correlation line is obtained from a previous numerical study (Pouya et al., 2016) based on experimental results reported in (Fuenkajorn and Phueakphum, 2010). Red stars: numerical results used for calibration. Black triangles: numerical results used for verification.	141
68	Calibration of the joint element strength parameters of the <i>POROFIS</i> model. For $\sigma_R = 5$ MPa, 6 MPa, and 6.13 MPa, the creep acceleration noted at the end of the simulation corresponds to the initiation of tertiary creep. The vertical dashed line (at $t=0.22$ days) indicates the initiation of tertiary creep noted during a uniaxial creep test performed under 30 MPa (Fuenkajorn and Phueakphum, 2010).	142
69	Stress-time input for the axial creep test simulated with models (1) and (3). P_1 indicates the time needed to apply the total loading stress, which is increased incrementally up to 35 MPa. P_2 (respectively P_3) marks the time just before (respectively after) the transistion between secondary and tertiary creep. P_4 indicates the end of the creep test. .	144
70	Time evolution of the macroscopic axial deformation of the polycrystal during the uniaxial creep test simulated with the joint-enriched FEM model of inter-granular crack propagation (1) and with the inclusion-matrix model of grain breakage (3).	145
71	Macroscopic stress-strain curve of the polycrystal during the uniaxial creep test simulated with the joint-enriched FEM model of inter-granular crack propagation (1) and with the inclusion-matrix model of grain breakage (3).	146

72	Distribution of the major principal micro-stresses of the polycrystal during the creep test simulated with the inclusion-matrix model. . . .	147
73	Distribution of the minor principal micro-stresses of the polycrystal during the creep test simulated with the inclusion-matrix model. . . .	148
74	Results of the creep test obtained with the joint-enriched FEM inter-granular crack propagation model (1) after the initial loading phase (P_1): (a) vertical stress (in MPa); (b) damage in the joint elements - deformed mesh (10 \times).	149
75	Results of the creep tests obtained with the joint-enriched FEM inter-granular crack propagation model (1) at the end of the creep test (P_4): (a) vertical stress (in MPa); (b) damage in the joint elements - deformed mesh (10 \times).	149
76	Vertical stress distribution (S_{yy} , MPa) at the end of the uniaxial creep test simulated with the joint-enriched FEM model that accounts for both intra- and inter-granular crack propagation. The test duration was 0.018 day, i.e. about 26 minutes.	151
77	Distribution of damage in the joints at the end of the uniaxial creep test simulated with the joint-enriched FEM model that accounts for both intra- and inter-granular crack propagation. The test duration was 0.018 day, i.e. about 26 minutes.	151
78	Cyclic loading tests 1-3 (vertical deviatoric stress), simulated with the joint-enriched FEM model of inter-granular crack propagation. . . .	154
79	Variations of the polycrystal Young's modulus with the number of cycles in tests 1-3.	155

80	Cyclic loading tests 4-5 (horizontal deviatoric stress), simulated with the joint-enriched FEM model of inter-granular crack propagation. . .	156
81	Damage in the joint elements at the end of the initial loading cycle in test 4 (mostly horizontal cracks).	157
82	Variations of the polycrystal Young's modulus with the number of cycles in tests 4-5.	157
83	Thin section image of consolidated granular salt saturated with blue epoxy. Left: Grey regions represent granular salt particles while blue areas filled with epoxy indicates inter-granular pores. Right: The FEM mesh was generated with <i>Plot Digitizer</i> and <i>GiD</i>	158
84	Joint-enriched FEM ($12mm \times 12mm$). In the legend, grain numbers refer to grain orientations. Fracture 1 is the inter-granular joint element.	159
85	Stress time history imposed in the creep simulations. Point A marks the transition between the monotonic increasing stress loading and creep loading phases ($t = 0.005d$). Point B is during the creep process ($t = 0.24d$).	161
86	Results at the end of monotonic loading phase at $t = 0.005d$ - Point A (same for the three models): (a) vertical stress (MPa); (b) vertical displacement (mm). Note: compression is negative with <i>POROFIS</i> . .	162
87	Simulation results during the creep process at $t = 0.24d$ - Point B: (a) vertical stress in model 1 (MPa); (b) vertical stress in model 2 (MPa); (c) vertical displacement in model 1 (mm); (d) vertical displacement in model 2 (mm); (e) damage in joint elements in model 1; (f) damage in grain elements in model 2.	164

88	Simulation results during the creep process at $t = 0.24d$ - Point B: (a) vertical stress in model 3 (MPa); (b) vertical displacement in model 3 (mm); (c) inter-granular damage in joint elements in model 3; (d) intra-granular damage in grain elements in model 3.	165
89	Creep curves obtained with the three models. Note that the strains from the initial monotonic loading phase are the same for the three models and not shown in this figure.	167
90	Damage in joints of model 1 at ultimate failure ($t = 6.68d$)	168
91	Damage in grains of model 2 at ultimate failure ($t = 0.25d$).	168
92	Results of model 3 at ultimate failure ($t = 0.276d$): (a) damage in joints; (b) grain damage in the deformed shape.	168
93	Complete creep curve. Tertiary creep phase initiates when first grain breakage occurs.	170
94	Evolution of macroscopic viscoplastic strain during the long-term creep test with 7 MPa creep load.	172
95	Damage criterion determined from micromechanical model (long term and short term).	172
96	Calibration of short-term parameters for the tertiary creep phase. We obtain the experimental data from the short-term creep test with the creep load 30 MPa (Fuenkajorn and Phueakphum, 2010).	174
97	Calibration of long-term parameters for the tertiary creep phase. We obtain the experimental data from the short-term creep test with the creep load 12.6 MPa (Fuenkajorn and Phueakphum, 2010).	175

98	Verification of short-term parameters for the tertiary creep phase. We obtain the experimental data from the short-term creep test with the creep load 21.5 MPa (Yang et al., 1999).	176
99	Geometry and boundary conditions of a typical salt cavern studied in <i>POROFIS</i> . Element W is the tracing element. Maximum width of the cavern is 40m at element W.	178
100	Equivalent stress distribution at the end of stage 2 using a $500m \times 500m$ domain.	179
101	Stress distribution at the end of stage 2: (a) radial stress, (b) vertical stress.	180
102	Damage distribution at the end of stage 3, using damage evolution law 1 (Eq. 98). Only roof elements are damaged in this magnified image.	181
103	Equivalent stress distribution at the end of stage 3, using damage evolution law 2 (Eq. 100). We use the same scale of color bar as in Fig. 100.	181
104	Damage distribution around the cavern wall at the end of stage 3, using damage evolution law 2 (Eq. 100).	182
105	Irreversible equivalent strain at the end of stage 3, using damage evolution law 2 (Eq. 100).	182
106	Radial/vertical stress distributions along path WW' after stages 2 and 3.	183
107	Equivalent stress distributions along path WW' after stages 2 and 3.	183
108	Evolution of equivalent stress of element W.	184
109	Evolution of equivalent viscoplastic strain of element W.	184
110	Evolution of damage variable of element W.	184

SUMMARY

Most mineral and energy resources such as ore, coal, petroleum, natural gas, and geothermal energy are recovered from the Earth. Nuclear waste repositories and CO₂ storage systems are buried underground. Recovery of mineral resources, storage of energy, and disposal of waste involve changes in coupled mechanical and transport rock properties. The evolution of macroscopic poroelastic properties can be explained by variations of microstructure descriptors upon thermo-hydro-chemo-mechanical coupled processes. This research aims to gain fundamental understanding of the damage/healing processes that contribute to the weakening/strengthening of rocks and to the increase/decrease of permeability in porous media. The proposed mechanical models are implemented in Finite Element Methods and applied to the design of geostorage systems. This study focuses on salt rock, which is used as a model material to study rock microstructure evolution under various stress paths, and to understand the microscopic processes that lead to macroscopic mechanical recovery. We investigated two modeling strategies to couple poroelastic properties and microstructure upon damage and healing. First, the framework of Continuum Damage Mechanics was enriched with fabric descriptors used as internal variables in order to predict the changes of stiffness and deformation during crack debonding, opening, closure and rebonding. We carried out creep tests on granular salt to infer the form of fabric tensors from microstructure observation. Net damage evolution is governed by a diffusion equation. Macroscopic and microscopic model predictions highlight the increased efficiency of healing with time and temperature. Secondly, a

self-consistent homogenization scheme was used to upscale the viscoplastic and damage behavior of halite polycrystals from mono-crystal slip mechanisms. The model provided micromechanical interpretations to important aspects of salt rock viscoplastic and fatigue behavior, such as strain hardening, creep recovery, tertiary creep, and plastic adaptation. We implemented the micromechanical model in a finite element program and compared it to the FEM model with joint elements to characterize damage accumulation and crack patterns in salt polycrystals during creep and during cyclic loading paths typical of Compressed Air Energy Storage. We also benchmarked a variety of viscoplastic damage models implemented in FEM to accurately predict the accumulation of damage around salt caverns used for high-pressure gas storage. This study is expected to improve the fundamental understanding of damage and healing in rocks, and the long-term assessment of geological storage facilities.

CHAPTER I

INTRODUCTION

1.1 Energy and Storage

The dominant mineral component of salt rock is halite (NaCl). Some rocks with highly soluble salts, including NaCl, KCl, carnallite, bischofite, tachyhydrite, or anhydrite, generally of evaporitic origin, are also recognized as salt rocks (Liang et al., 2011). Halite polycrystals are typically white or transparent, with other colors possible in the presence of impurities. Due to its favorable properties such as easy solubility in water, low permeability, favorable creep deformation, and fast self-healing abilities, salt rock is viewed as an attractive host medium for underground geological storage, including storage of oil and natural gas (Bérest et al., 2001; Cosenza et al., 1999; Staudtmeister and Rokahr, 1997; Wu et al., 2005), storage of high pressure gas (Ozarslan, 2012), nuclear waste disposals (Chan et al., 1997, 2001; Ghoreychi, 1996; Hunsche and Hampel, 1999; Langer, 1981; Munson and Dawson, 1979; Munson, 1979), and, more recently, Compressed Air Energy Storage (CAES) (Fuenkajorn and Phueakphum, 2010; Kim et al., 2012).

CAES in salt rock is often coupled to windmills: the surplus of energy produced in periods of high wind is used to compress air that is stored to activate turbines at peak hours. Salt rock caverns can also be used to store oil or natural gas for extended periods of time at minimal cost. High in-situ stress closes and rebonds the cracks present in the rock mass, which is said to “self-heal”. The difference of temperature between the top and bottom of salt caverns results in a continuous convective flow of oil, which maintains the quality of the crude oil stored in the caverns. In the U.S., the Strategic Petroleum Reserve (SPR), aimed to store federally-owned emergency

crude oil, is located along the Gulf of Mexico. Moreover, salt rock has been studied extensively in the context of the Waste Isolation Pilot Plant (WIPP) for the disposal of radioactive waste.

In CAES facilities, air injection and withdrawal induce repeated loading phases. By contrast, in nuclear waste disposals, packages release heat with an exponent decay of power, responsible for a long-term increase of temperature in the surrounding rock mass (Liang et al., 2006). Therefore, in the Excavation Damaged Zone (EDZ) of nuclear waste disposals, the rock mass is exposed to non-mechanical damage. These cyclic loading conditions and thermo-mechanical couplings induce complex microstructure changes that result in a variety of deformation regimes operating at very different rates. The goal of this research is to understand the fundamental processes that drive salt rock's long term behavior in stress, temperature, and moisture conditions typical of underground storage, and to formulate continuum damage and healing mechanics models that can be used for engineering design purposes.

1.2 Salt Rock Mechanics

Damage refers to the decrease of bulk stiffness and strength upon the initiation, propagation and even coalescence of microscopic cracks. Healing is defined as the mechanical recovery induced by the rebonding of cracks. Damage and healing mechanics allows predicting variations of stiffness and deformation during thermo-mechanical stress paths, and is grounded on the fundamental understanding of the processes that drive crack opening, propagation, closure and rebonding. That is why we investigate theoretical methods that couple microstructure changes to the evolution of bulk poroelastic properties during damage and healing processes. Salt rock is chosen as a model material to study the mechanics of damage and healing in crystalline and porous media, because the creep processes that drive crack rebonding take place over

short periods of time compared to other rocks. Rapid creep processes make it possible to conduct physical experiments to validate or invalidate the assumptions made on the dominating healing processes that are expected to occur in geological storage conditions, and therefore predict whether crack rebonding will happen at a rate that is fast enough to ensure the safety of repositories in salt formations.

Four creep mechanisms were characterized experimentally in halite (Fam et al., 1998; Senseny et al., 1992). These mechanisms occur over different ranges of temperature T and pressure σ , and include (1) glide ($\sigma/\mu > 5 \cdot 10^{-4}$; $273K < T < 853K$); (2) cross slip (high σ ; $298K < T < 853K$); (3) diffusion ($\sigma/\mu < 5 \cdot 10^{-4}$; $T > 573K$); (4) dynamic recrystallization (low σ ; high T). Note that μ refers to salt rock shear modulus. In typical geological storage conditions, Diffusive Mass Transfer (DMT) is expected to be the dominating mechanism for creep. DMT not only results in creep strain, but also accelerates crack healing through local transfer of mass, and converts cracks into planar arrays of fluid inclusions. Atoms and molecules migrate through the bulk of salt grains (volume diffusion, Nabarro-Herring creep) and along the grain boundaries (boundary diffusion, Coble creep). In salt rock, crack rebonding and consequent mechanical healing induced by DMT occur within a few days at room temperature and low pressure. In addition, DMT is enhanced at higher temperatures. At the microscopic scale, DMT results in the rebonding of crack faces, and at the macroscopic scale, in the total or partial recovery of mechanical properties previously degraded by micro-crack propagation.

However, not all facilities are designed for long-term storage. In CAES systems for instance, the rock mass is subjected to cyclic loading. During these daily cycles, healing processes are expected to occur at a lower rate than fatigue processes. The main challenge is that mechanical properties of salt rocks subjected to cyclic loads differ greatly from those under static loads. The Young's modulus and the compressive strength decrease as the number of loading cycles increase (Dubey and Gairola, 2000;

Fuenkajorn and Phueakphum, 2010; Ma et al., 2013). Fatigue initiates faster for lower loading frequency (Fuenkajorn and Phueakphum, 2010; Liang et al., 2011; Liu et al., 2014a; Ma et al., 2013). The degradation of elastic moduli increases with the maximum stress and with the amplitude of the loading (Guo et al., 2012). Compared to amplitude and frequency, the confining stress does not influence fatigue significantly (Ma et al., 2013). It has to be noted that the range of frequencies investigated in laboratory studies are significantly higher than those in actual CAES conditions. Low frequency experiments are more difficult to conduct in the laboratory, because they require more time: a sufficiently long loading period and a large number of loading cycles. As a result, laboratory tests performed so far were not able to reveal the microscopic origin of fatigue. Furthermore, the long-term behavior of salt rock subjected to thermo-mechanical couplings cannot be elucidated with macroscopic laboratory tests, and requires an investigation of micro-level processes, completed by up-scaling or micro-mechanics approaches.

1.3 Thesis Structure

In the following, we propose continuum mechanics models of damage and healing. The structure of this thesis is organized as follows.

Chapter 2 "Theoretical Background" presents the thermodynamic principles at the foundation of the Continuum Damage and Healing Mechanics models formulated and tested in this study.

Chapter 3 "Fabric-based Damage and Healing Mechanics" explains a "top-to-bottom" microstructure-enrichment method, in which moments of probability of microstructure descriptors are used as fabric tensors in a Continuum Damage and Healing Mechanics closed formulation. The micro-macro model is used to predict the effects of damage and healing on salt stiffness, deformation, and permeability, and to interpret these effects from the evolution of microstructure descriptors.

Chapter 4 "Micro-macro Model of Viscous Fatigue" explains a "bottom-up" up-scaling method, in which a self-consistent homogenization scheme is used to predict the viscous damage and fatigue behavior of halite polycrystals from mono-crystal slip mechanisms.

Chapter 5 "Finite Element Analyses Applied to Geostorage Systems" describes the Finite Element Method (FEM) implementation, calibration and validation of micro-macro models of salt damage. Finite Element continuum-based damage models are benchmarked against joint element models to explain the formation of intra- and inter-granular crack patterns in halite polycrystals. FEM models of viscoplastic damage are also used to predict the long-term damage accumulation around salt caverns used for geological storage.

Chapter 6 "Conclusions and Future Study" summarizes the major results obtained in this doctoral thesis and proposes a few directions for future research.

CHAPTER II

THEORETICAL BACKGROUND

2.1 Introduction

This chapter aims to provide a comprehensive review of the theoretical backgrounds of salt damage and healing mechanics. We review crack evolution processes, experimental assessments of damage and healing, theoretical salt mechanics models, and numerical studies of rock damage and healing. The structure of this chapter is organized as follows: Section 2.2 describes the crystallographic structure of salt and explains how macroscopic phenomena are related to microscopic processes; Section 2.3 summarizes published experimental studies conducted on rocks for damage and healing analyses; Section 2.4 explains why rock mechanics requires multi-scale models and discusses the applicability of different modeling approach at different scales; Section 2.5 provides a summary of the state-of-the-art models based on Continuum Damage and Healing Mechanics; Section 2.6 presents the thermodynamic foundation of the models formulated in this thesis, in particular the derivation of the Inequality of Clausius-Duhem and the definition of internal variables; Section 2.7 explains the principle of self-consistent method and introduces the Hill's tensor; Section 2.8 compares state-of-the-art numerical models of damage and healing in rocks; Section 2.9 lists the main objectives of this research work.

2.2 *Micromechanical Processes in Salt Rock*

2.2.1 Crystallographic Structure of Salt

The crystallographic structure of a mineral describes the form in which atoms, ions, or molecules are spatially arranged. In 1850, Auguste Bravais found that crystals could be described by means of 14 unit cells (Fig. 1), defined according to the following criteria: (1) The unit cell is the simplest repeating unit; (2) Opposite faces of a unit cell are parallel; (3) The edge of the unit cell connects equivalent points.

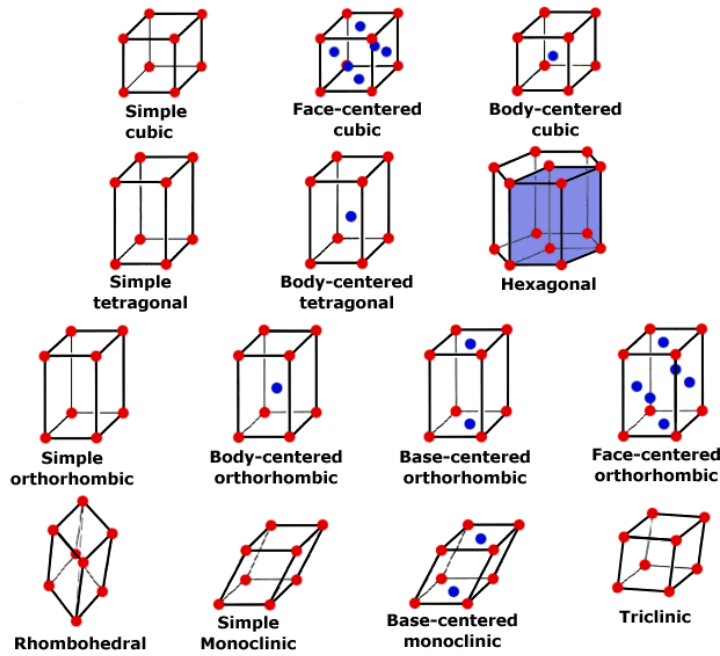


Figure 1 The 14 Bravais unit cells (Zumdahl and Zumdahl, 2006).

Each of the 14 unit cells characterizes a lattice. The 7 possible lattices, from most to least symmetric, are: cubic, tetragonal, orthorhombic, rhombohedral, hexagonal, monoclinic, and triclinic (Fig. 2).

Directional vectors (to describe a slip mechanism for example) are defined by the intersections of grain boundaries with the axes and are indicated with square brackets “[]”. Parallel directions are indicated with the same values into square brackets. In addition, Miller indices, indicated with parenthesis “()”, define crystal planes. Miller indices are based on the reciprocal of the intersection of the plane with the cell axes.

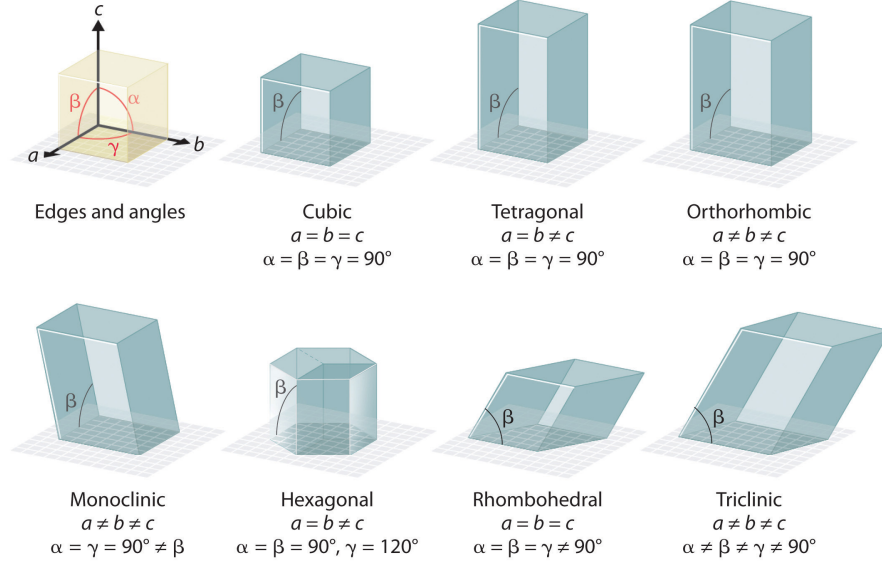


Figure 2 General features of the 7 basic unit cell geometry (Silberberg, 2012).

Fractions are converted to integers. Negative directions are denoted by a top bar on the coordinate value. Coordinates in angle brackets such as $\langle 100 \rangle$ denote a family of directions which are equivalent due to symmetry operations, such as $[100]$, $[010]$, $[001]$ or the negative of any of those directions. In the cubic system, planes having the same indices regardless of order and sign are equivalent. Coordinates in curly brackets or braces such as $\{100\}$ denote a family of crystallographic planes, such as (hkl) , (lhk) and (hkl) , which are equivalent due to symmetry operations, similar to the way that angle brackets denote a family of directions. The mechanisms that originate plastic deformation in crystalline materials are very different from those that occur in amorphous materials (e.g., glasses). Although plasticity induced by slip mechanism is the most common mechanism of plastic deformation, there are other mechanisms as well (Fig. 3).

Slip usually occurs on planes of highest packing density (atom/area) or in directions of highest linear density (atom/length). Slip preferentially occurs along those directions because the distance of the distortion is minimum there. In general, metals with Face-Centered Cubic (FCC) and Body-Centered Cubic (BCC) crystal structures

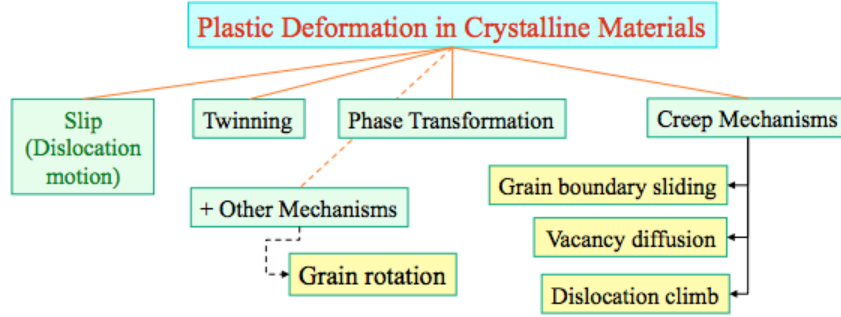


Figure 3 Microprocesses leading to plastic deformation in crystalline materials.

have a relatively large number of slip systems (at least 12). Extensive plastic deformation can be observed in those metals, which translates into a ductile behavior. In contrast, metals with hexagonal close-packed (HCP) crystal structure have only a few active slip systems. So they are usually brittle and can sustain less plastic deformation. According to experimental studies (Carter and Heard, 1970; Munson, 1979; Stokes, 1966), at room temperature, halite plastic deformation is mainly due to the glide of dislocations. The stress-strain response of FCC salt crystals under a compression in the $[001]$ direction presents distinct hardening stages similar to those of FCC metals. In FCC metals (Pouya, 2000), glide along the $\{101\}$ planes is easier than glide along the $\{111\}$ planes. By contrast in halite, the preferential slip systems belong to the $\{101\} \langle 101 \rangle$ family at room temperature. Under larger stresses, $\{111\} \langle 110 \rangle$ and also $\{001\} \langle 110 \rangle$ slip systems can be activated and contribute to the plastic deformation.

2.2.2 Impact of Creep Processes on Microstructure and Deformation

Halite is considered herein as a model material to characterize rock microstructure organization during brittle, ductile and viscoplastic deformation, and to study the microscopic processes leading to macroscopic mechanical recovery. Although polycrystalline halite (salt rock) is known for deformation by isochoric dislocation and diffusion processes, cracking is also an important grain-scale process at lower mean

stress (Fig. 4). The relationship between these micro-mechanisms and macroscopic strain evolution is still not well understood, especially in transient states. The relation between complex macroscopic phenomena (e.g., creep, damage, healing) with elementary microscopic processes is still an open issue.

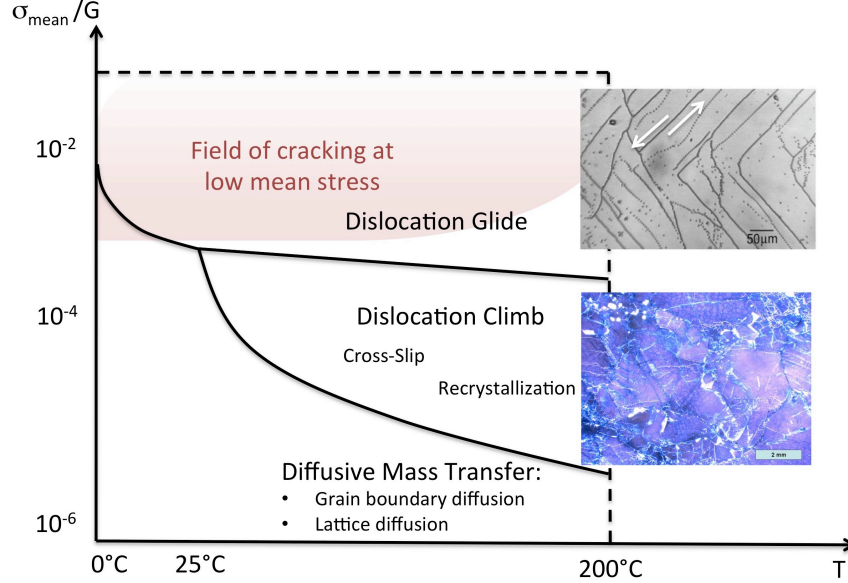


Figure 4 Micro-mechanism map for halite at repository conditions.

Microscopic dislocation processes are known to originate isochoric viscoplastic deformation during transient creep. At the transition to secondary creep, dislocation generation is balanced by cross-slip, diffusion and recrystallization processes (Senseney et al., 1992). Recent studies based on electron-backscattered-diffraction (EBSD) indicate that under given conditions of temperature and water saturation, sub-grain recrystallization depends on grain orientation relative to the compression axis, and on rock texture (Pennock and Drury, 2005). At low pressure, dislocation pile-ups and strain incompatibilities between grains induce stress concentrations resulting in dilatant micro-cracking. The presence of brine can enhance diffusion processes, by allowing mass transfer at lower temperature. The solution-precipitation mechanism explained by Raj (1982) can only occur when the liquid phase is continuous: dissolved crystal is transported at another location of the lattice, where it precipitates.

The pressure-solution mechanism presented by De Boer (1977) can take place in a crack network partially saturated with brine - according to the island-channel flow model proposed by Rutter (1976) and Spiers et al. (1990). The inter-granular pressure solution will result in compaction of the bulk rock and decrease of porosity and permeability (Meer and Spiers, 1997). As illustrated in Fig. 5, the chemical potential difference between the solid at the grain-to-grain contact and the pore wall drives the dissolution of materials at the grain contacts ($\Delta\mu_s$), transport through the fluid films at the grain boundaries ($\Delta\mu_d$) and the precipitation at the free pore walls ($\Delta\mu_p$).

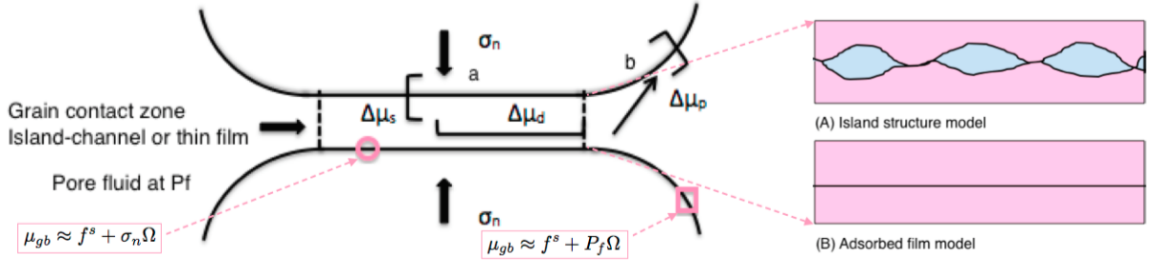


Figure 5 Model of inter-granular pressure solution in a closed thermodynamic system, modified from (Meer and Spiers, 1997). σ_n indicates the mean normal stress and P_f the pore fluid pressure.

Under favorable temperature and pressure conditions, solution-precipitation creep can produce similar strain rates to those solid-state creep processes (Carter and Heard, 1970). Fluid-assisted DMT not only can result in creep strain, but also can accelerate healing of cracks through local transfer of mass and convert cracks into planar arrays of fluid inclusions (Smith and Evans, 1984).

2.3 Experimental Assessment of Damage and Healing in Rocks

Rock thermo-mechanical behavior was investigated with a variety of stress paths, both at laboratory scale and field scale. Different types of mechanical loading conditions were considered, including monotonic/cyclic, uniaxial/triaxial, short term/long term, and drained/undrained. Table A.1 in Appendix I provides the strength and Young's modulus of rocks of interest for geological storage purposes. Rock samples were tested in the laboratory under different thermo-mechanical stress paths, mainly: (1) a temperature-controlled mechanical loading, or (2) a heating phase followed by a mechanical loading, or (3) a heating phase followed by a relaxation period (until the temperature of the sample reached room temperature) followed by a mechanical loading. Most of the experimental results reported in the literature focus on rock compressive strength. Temperature changes were limited to less than 1000 °C to prevent any chemical change in rock minerals. Most often, rocks were subjected to a heating phase. To the authors' best knowledge, only granite and tuff were studied upon cooling. Rock stiffness tends to increase (respectively decrease) upon cooling (respectively heating). Granite has the highest compressive strength among all the rocks tested. In gabbro, there exists a critical temperature above which drastic change in mechanical properties occur (Keshavarz et al., 2010). Confined salt rock is subject to complex time-dependent microscopic processes, such as dislocation, glide, and cross-slip. At the bulk scale, coupled processes make it challenging to discriminate viscoplastic (dislocation-induced) deformation and damage (crack-induced) deformation. Overall, creep processes in salt rock result in much larger deformation at failure compared to other types of rock (Wawersik and Hannum, 1980).

Mechanical properties of rocks subjected to cyclic loads differ greatly from those under static loads. Rock fatigue is largely affected by the boundary and loading conditions, such as the confining stress (Ma et al., 2013; Zhu and Arson, 2014a), the stress/strain rate (Lajtai et al., 1991; Ray et al., 1999; Taylor et al., 1986), the loading

amplitude and the maximum stress (Fuenkajorn and Phueakphum, 2010; Prost, 1988; Tao and Mo, 1990; Xiao et al., 2010), as well as the type and frequency of the signal (Attewell and Farmer, 1973), and the number of cycles (Singh, 1989). A review of the fatigue behavior of different types of rocks is provided in (Bagde and Petroš, 2005). The presence of joints (Jafari et al., 2004; Li et al., 2003), the size of grains (Burdine, 1963), humidity conditions (Ishizuka et al., 1990; Lajtai et al., 1991) and fluid migration (Mahnken and Kohlmeier, 2001) play a critical role in the triggering and evolution of fatigue in rocks. Experimental studies of rock fatigue under cyclic loading remain scarce, and mostly focus on salt rock. Therefore, salt rock is an adequate model material to study the microscopic origin of fatigue in crystalline materials. Recently, a model of salt rock fatigue under cyclic loading was proposed in (Ladani and Dasgupta, 2009). However, due to the numerous variables influencing salt damage under cyclic loading (e.g., stress amplitude, loading frequency), and due to the high number of cycles necessary to assess fatigue effects in the laboratory, experimental characterization of fatigue in salt rock remains a challenge.

Much less has been done on crack healing effects in rocks although numerous experiments have been executed upon other geological materials. Only a few laboratory tests were conducted on salt rock under various temperatures for different durations to study the role of crack rebonding on strength (Fuenkajorn and Phueakphum, 2011; Miao et al., 1995), permeability (Chan et al., 2001; Schulze, 2007) and inelastic strains (Hou, 2003; Lux et al., 2000). Houben et al. (2013) recently studied diffusion in adsorbed aqueous films in salt and identified three physical mechanisms govern crack healing and permeability reduction in halite: (1) purely mechanical closure of cracks induced by an increase of the mean normal stress; (2) diffusive or "chemical" crack healing driven by surface energy reduction; (3) recrystallization-induced crack healing.

2.4 Multi-scale Aspects of Rock Mechanics

Discontinuities in rocks exist at multiple scales. The propagation of isolated cracks that do not interact with other cracks is well captured by fracture mechanics models. However, computations becomes complicated and challenging when crack coalescence or interactions are accounted for. That is why in Continuum Damage Mechanics (CDM), subsets of cracks, defined as “damage”, are considered in the evolution laws. Fig. 6 provides an overview of the types of heterogeneities found in salt rock. In the following, we use the following definitions to designate the subjects of interest: (1) The microscopic scale (e.g., salt grain scale) ranges from 10^{-6}m to 10^{-3}m in size; (2) The mesoscopic/laboratory/Representative Elementary Volume (REV) scale (e.g., coalesced crack, specimen scale) ranges between 10^{-3}m to 10^{-1}m in size; (3) The macroscopic/reservoir/field scale (e.g., fault, cavity) ranges from 10^{-1}m to 10^3m in size.

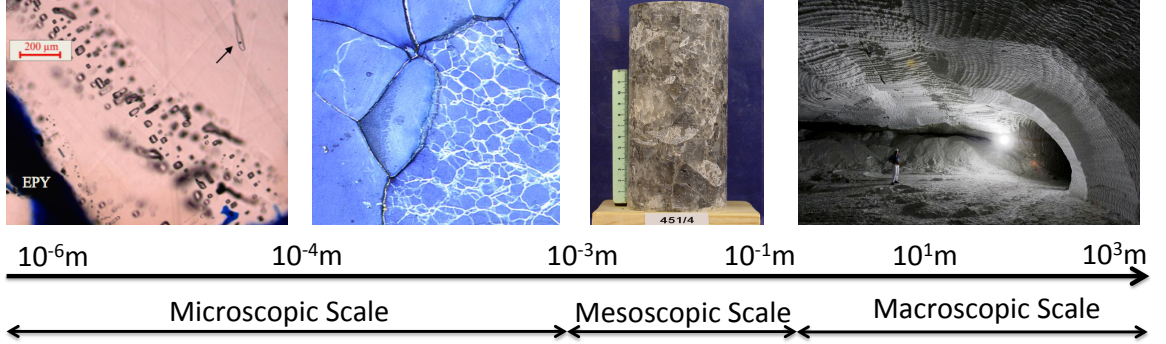


Figure 6 Discontinuities in salt at multiple scales, modified from (Ding et al., 2016; Schleder and Urai, 2007).

At the microscopic scale, we are interested in modeling the topological evolution of micropores and microcracks. Diffusion, slip, dislocation, and recrystallization are all microscopic processes occurring along the grain boundaries, which should be modeled at the grain scale. The non-uniform distribution of micro-cracks and minerals with various properties are the main contributing factor to the rock heterogeneity. Mechanical anisotropy is usually modeled through the density, size, and geometry of

cracks (Oda, 1984).

Engineering properties such as stiffness and porosity are defined over a “mesoscopic” domain that contains heterogeneities; such properties are averaged over a subdomain; the average typically oscillates around an asymptotic value as the subdomain size is increased; the REV is the minimum subdomain size that needs to be considered to ensure that the average reaches this asymptotic value. Note that the REV is specific to the property or field variable considered. For instance, in fractured rocks, the permeability REV is typically larger than the stiffness REV because crack coalescence implies fluid flow but not necessarily mechanical interaction or failure. Note also that the REV is not necessarily defined in terms of space variables. For instance, if an average is performed over a set of possible crystal orientations, the REV size is the number of crystal orientations considered. Fig. 7 illustrates the definition of the REV for one specific property. In general, individual response functions should be averaged over different REV window sizes to ensure statistical homogeneity (Lacy et al., 1999). In Fig. 8, the observation window B may be sufficient for stiffness characterization. However, it may be insufficient to characterize statistically homogeneous (SH) response functions pertaining to damage evolution, such as thermodynamic conjugate forces, damage evolution, and dissipation potential.

Basic assumptions made at the REV scale do not hold when studying a field problem in which damage zone is much larger than the REV size. At the macroscopic scale, numerical methods are required to solve complex coupled problems or analyze the critical state of damaged materials. Typical numerical approaches include: (1) Continuum methods, such as the Finite Difference Method (FDM), Finite Element Method (FEM), Finite Volume Method (FVM), Extended Finite Element Method (XFEM), Cohesive Zone Models (CZM), and Boundary Element Methods (BEM); (2) Discontinuum methods, such as Discrete Element Method (DEM) and Discrete Fracture Network Method (DFN); (3) Hybrid methods, such as the Combined

Finite-Discrete Element Method (FEMDEM). The choice of the numerical modeling approach depends, among other factors, on the heterogeneous rock properties of interest, the type of fracture processes at stakes, the thermo-hydro-chemo-mechanical couplings involved in the problem, and the time dependency of the rock properties. More details are provided in Section 2.8.

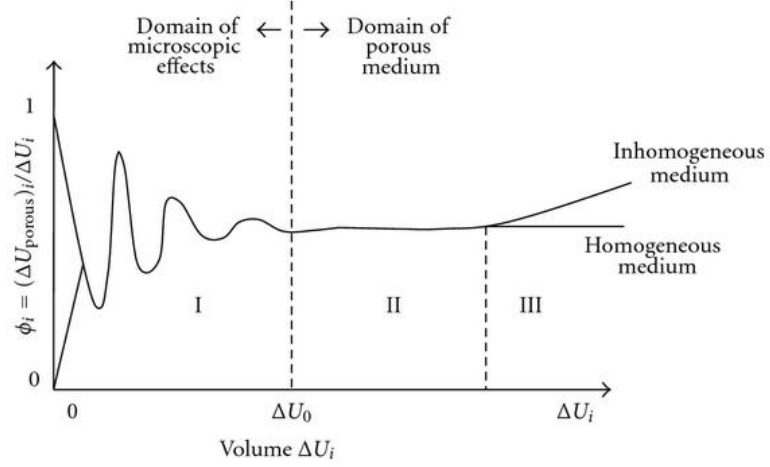


Figure 7 Definition of the Representative Elementary Volume (REV) (Bear, 1972).

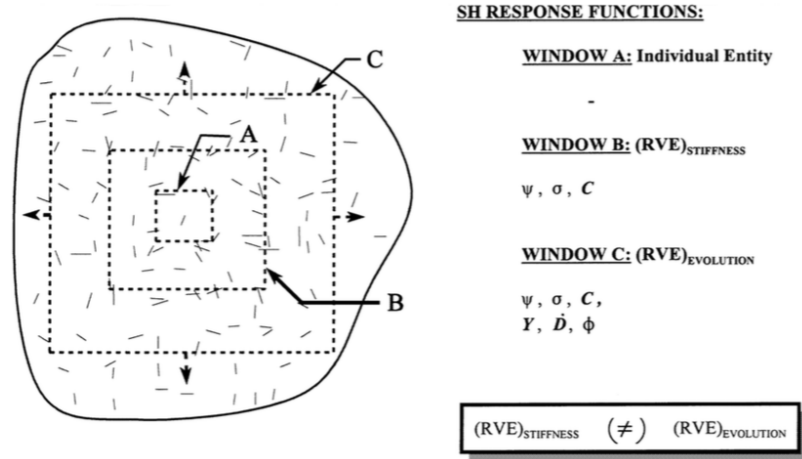


Figure 8 REV window size and statistically homogeneous (SH) response functions (Lacy et al., 1999).

2.5 *State-of-the-Art of Continuum Damage and Healing Mechanics (CDHM)*

Due to the multi-scale nature of damage in rocks, several approaches were proposed to predict the evolution of stiffness degradation and recovery during damage and healing processes. Micromechanical damage models (Dormieux et al., 2006; Levasseur et al., 2011) assume that the rock REV is populated with a given distribution of cracks characterized by a specific shape (usually, spherical, penny-shaped or ellipsoidal cracks). Assumptions on the shape and density of cracks allow expressing explicitly the strain concentration tensor, which is used to derive the theoretical expression of the Helmholtz free energy of the rock solid skeleton. For dilute distributions of cracks, the self-consistent method proved to provide an efficient scheme to model the loss of stored elastic deformation energy induced by cracking. If microscopic cracks open in pure mode I (crack displacement vector is normal to the crack planes), the only damage variable needed to express the dissipation of energy associated to the degradation of elastic moduli is the second-order crack density tensor, defined by Kachanov (1992) as:

$$\boldsymbol{\Omega} = \sum_{k=1}^N d_k \mathbf{n}_k \otimes \mathbf{n}_k \quad (1)$$

in which the REV is assumed to contain N planar cracks with a normal direction \mathbf{n}_k and a volumetric fraction d_k . For mixed crack propagation modes (inducing a non-zero tangential displacement at crack faces), a higher damage tensor is required - at least of order four (Cauvin and Testa, 1999; Chaboche, 1992a; Halm and Dragon, 1998). Increasing the order of the damage tensor generally improves the compliance of the model to symmetry properties required for the elasticity tensor (Lubarda and Krajcinovic, 1993).

Phenomenological damage models are based on energy postulates (i.e. assumptions made on the expression of the free energy and dissipation of the REV) rather than hypotheses on micro-structure geometry. Such formulations often resort to the

concept of effective stress, which stands for the stress developed in the fictive undamaged counterpart of the system (de Borst et al., 1999). The principle of equivalent elastic energy or the principle of equivalent elastic deformation (Lemaitre and Desmorat, 2005) then makes it possible to compute the damaged stiffness tensor, provided that the expression of the free energy of the solid skeleton of the rock is given. The key point consists in defining a damage operator to express the effective stress as a function of damage and of the stress applied at the boundaries (far-field stress), so as to satisfy the symmetry and positivity requirements for the elasticity tensor (Cordebois and Sidoroff, 1982).

In salt, creep damage has often been associated with inelastic dilatant deformation because deformation induced by dislocation creep is isochoric (Chan et al., 2001). Damage grows in stress states above the “dilatancy boundary”, whereas below this boundary, the decrease of inelastic strains compensates damage deformation (Hou, 2003; Lux and Eberth, 2007). Damage cannot grow or decrease within the dilatancy boundary (Hunsche and Hampel, 1999). The model proposed by Chan et al. (1998) can predict the influence of creep and micro-crack propagation on deformation, but cannot account for the anisotropy induced by damage on strains and stiffness. A scalar damage variable is introduced (Hou, 2003; Hunsche and Hampel, 1999) in order to describe material softening and define long-term creep failure. This class of models (see also Chan et al. (2001)) do not capture stiffness changes and could not predict damage-induced anisotropy in a sedimentary rock. In the modeling approach by Miao et al. (1995), stiffness reduction is modeled within the framework of CDM, whereas inelastic deformation is considered to obey a plastic flow rule. Two dissipation potentials are necessary to close the formulation (one for CDM, one for plasticity).

In most constitutive models that account for creep, damage and healing, water content and brine saturation are not part of the thermodynamic variables. The dependence on temperature is based on experimental observations made in isothermal

conditions. By contrast, a coupled thermo-mechanical thermodynamic framework was proposed by Zhou et al. (2011) to model creep and damage in geomaterials, and a thermo-mechanical model of crack opening and closure was proposed by Zhu and Arson (2014b). However, these models did not account for healing (defined herein as mechanical recovery resulting from crack rebonding). Two groups of self-healing systems have been recognized so far (Voyiadjis et al., 2011), including active systems triggered by damage mechanisms (Kessler and White, 2001), and passive systems requiring external stimulation. The damage and healing models proposed in this thesis belong to the category of uncoupled passive systems, analogous to the close-then-heal scheme proposed by Li and Uppu (2010).

2.6 *Thermodynamic Principles used in Microstructure-enriched CDHM*

2.6.1 Inequality of Clausius-Duhem

In the following, we explain the energy conservation and dissipation principles that need to be enforced in order to satisfy “thermodynamic consistency” in our CDHM models. The first law of thermodynamics is an energy balance equation. It states that the change in the internal energy (U) of a closed system is equal to the energy brought by external actions to the system (P) minus the amount of heat that the system gives to the environment (Q).

$$\dot{P} - \dot{Q} = \dot{U} \quad (2)$$

Entropy provides a measure of the amount of energy that cannot be used to produce mechanical work. The time-dependent entropy change (\dot{S}) can be divided into external entropy change (\dot{S}_e) and internal entropy change (\dot{S}_i):

$$\dot{S} = \dot{S}_e + \dot{S}_i = -\frac{\dot{Q}}{\tau} + \dot{S}_i \quad (3)$$

in which τ is the temperature change relative to a reference temperature. The second law of thermodynamics states that the energy that cannot be used to produce mechanical work is dissipated because of irreversible microstructure changes:

$$\dot{S}_i \geq 0 \quad \implies \quad \dot{S} \geq \frac{-\dot{Q}}{\tau} \quad (4)$$

Locally, the rate of heat brought to the system from the surroundings is related to entropy by:

$$\dot{S} \geq \frac{-\dot{Q}}{\tau} = -\nabla \cdot \frac{q}{\tau} \quad (5)$$

in which q is the outgoing heat flow vector. The Helmholtz free energy (Ψ) is a thermodynamic potential that measures the maximum amount of work that can be done by a system.

$$\Psi = U - \tau S \quad (6)$$

Combining the two first laws of thermodynamics, we have

$$\dot{P} - \dot{\tau}S - \dot{\Psi} - \frac{q}{\tau} \cdot \nabla \tau \geq 0 \quad (7)$$

Using the Principle of Virtual Work, the Inequality of Clausius-Duhem can be obtained:

$$\sigma : \dot{\varepsilon} - \dot{\tau}S - \dot{\Psi} - \frac{q}{\tau} \cdot \nabla \tau \geq 0 \quad (8)$$

For reversible mechanical processes, in the absence of heat transfer, the inequality changes to:

$$\sigma : \dot{\varepsilon}^e - \dot{\tau}S_e \cdot \nabla \tau - \dot{\Psi} = 0 \quad (9)$$

in which $\dot{\varepsilon}^e$ is the elastic deformation (reversible). Helmholtz free energy is sought in the form $\Psi = \Psi(\varepsilon^e, \tau)$:

$$\left(\sigma - \frac{\partial \Psi}{\partial \varepsilon^e}\right) : \dot{\varepsilon}^e - \left(S + \frac{\partial \Psi}{\partial \tau}\right) \dot{\tau} = 0 \quad (10)$$

The thermodynamic conjugation relationships are:

$$\sigma = \frac{\partial \Psi}{\partial \varepsilon^e}, \quad S_e = -\frac{\partial \Psi}{\partial \tau} \quad (11)$$

For irreversible process, the reduced Inequality of Clausius-Duhem is:

$$\Phi_M + \Phi_T \geq 0, \quad \Phi_M = \sigma : (\dot{\varepsilon} - \dot{\varepsilon}^e) + \chi : \dot{\xi} \geq 0, \quad \Phi_T = -\frac{q}{\tau} \cdot \nabla \tau \quad (12)$$

in which $\dot{\varepsilon} - \dot{\varepsilon}^e$ represents the irreversible deformation (such as plastic deformation, viscoplastic deformation, or residual crack opening), χ and ξ denote internal variables (such as damage variable or hardening variables).

2.6.2 Definition of Internal Variables

Three kinds of postulates are needed to close the CDHM model formulation: the expression of the free energy Ψ (dependent on the expression of the damage and healing variables), the expression of rate-independent dissipation criteria (e.g., time-independent damage propagation) and the expression of evolution laws for the dissipation variables (typically a damage potential and a time-dependent law for healing).

Table 1 summarizes the postulates made in phenomenological thermo-mechanical damage models proposed for rock. In most models, the damage flow rule was assumed to be associate, i.e. the damage criterion (f_d) was used as a damage potential (g_d) (Arson and Gatmiri, 2010, 2012; Shao et al., 2005). Damage models proposed for rock could predict the occurrence of residual strains without resorting to any additional plastic potential (Abu Al-Rub and Voyiadjis, 2003; Halm and Dragon, 1998). Even so, two flow rules are needed to close the model formulation (Xu et al., 2013): the rate of inelastic deformation and the rate of damage. Models reviewed in Table 1 are based on a purely mechanical damage evolution law, which implies that temperature can only affect damage if the tensile stress induced by heating exceeds the threshold of mechanical tensile strain necessary to open cracks. In practice, this means that most models are based on the expression of a damaged stiffness tensor, introduced in a thermo-elastic stress-strain relationship. The damaged stiffness tensor itself is a function of a mechanical damage variable.

In fact, the second-order crack density tensor emerging from micromechanical analyses is a particular form of Oda’s fabric tensor, commonly used in structural geology (Oda, 1984):

$$\mathbf{F} = \frac{\pi}{4} \frac{N}{V_{REV}} \int_0^\infty \int_\Omega r^3 E(r, \mathbf{n}) \mathbf{n} \otimes \mathbf{n} d\mathbf{n} dr \quad (13)$$

in which $E(r, \mathbf{n})$ is the mathematical expectancy of the presence of a crack of radius r and normal direction \mathbf{n} in a REV of size V_{REV} . For a given crack density and for given probability density functions of crack shapes and orientations, a direct relationship can be established between fabric tensors and the elasticity tensor of the rock (Cowin, 1985; Lubarda and Krajcinovic, 1993). The key issue is to choose relevant microstructure descriptors (Lecampion, 2010; Lu and Torquato, 1992) and associated probability density functions to capture the overall mechanical degradation process. Typical microstructure descriptors include local properties of grains, cracks, or pores (e.g., size, shape, area, sphericity, aspect ratio for 2D; volume, specific surface for 3D)

and their global properties (e.g., relative distance, coordination number, connectivity, tortuosity).

Table 1 State of the art: phenomenological models of thermo-mechanical rock damage.

Main governing equations	“Stress” paths simulated	Phenomena observed	References
$\Psi = \Psi^e(\varepsilon_e, T, \Omega) + \Psi^p(\gamma^p, T, \Omega) + \Psi^{vp}(\gamma^{vp}, T, \Omega),$ $f^p(\sigma, \eta) = q - g(\theta)\eta^p(T, \gamma^p, \Omega)R_c(C_s + \frac{p}{R_c})^m,$ $g^p = q - (\eta^p - \beta^p)(p + C_s R_c),$ $f^\omega(Y^\omega, \Omega) = Y^\omega - r(\Omega) \leq 0$	(1) triaxial compression tests (different confining stress, different T); (2) creep tests (different stresses, different T)	temperature variable is introduced in hardening function; capture both long-term and short-term deformation behavior under thermal effect	Zhou et al. (2011)
$\Psi = \Psi_e - g_M \Omega : \varepsilon_M - \frac{g_s}{3} \Omega : \delta \varepsilon_{sv} - \frac{g_T}{3} \Omega : \delta \varepsilon_T, \Psi_e =$ $\frac{1}{2} \varepsilon_M : D_e(\Omega) : \varepsilon_M + \frac{1}{2} \varepsilon_{sv} \beta_s(\Omega) \varepsilon_{sv} + \frac{1}{2} \varepsilon_T \beta_T(\Omega) \varepsilon_T,$ $f_d(Y_{d1}^+, \Omega) = \sqrt{\frac{1}{2} Y_{d1}^+ : Y_{d1}^+} - (C_0 + C_1 \Omega)$	(1) isothermal drained and undrained triaxial compression tests; (2) study the behavior of an unsaturated massif hosting a heating source	damage influences heat transfer isotropically; damage increases with higher damage rigidities; water permeability grows with damage and with the internal length parameter	Arson and Gatmiri (2010)
$\Psi = \frac{1}{2} \varepsilon : E(d, g) : \varepsilon - T n(d, g) : \varepsilon - \frac{1}{2} c \frac{T^2}{T_0},$ $f_d = \bar{\varepsilon} - k(d, T),$ $f_g = T - \bar{k}(g, T)$	heating without loading, and then the temperature is kept constant while load is applied	specific heat depends on damage; positive dissipation when thermal energy is in logarithmic form	Stabler and Baker (2000)
$\Psi = W(\varepsilon_e^i, \kappa, d^+, d^-) + V(T) + L(T, \xi) + H(\xi),$ $W = (1 - d^+) W_e^+(\varepsilon_e^i, \kappa) + (1 - d^-) W_e^-(\varepsilon_e^i, \kappa),$ $\hat{f}^\pm = \sqrt{\bar{\sigma}^\pm} : C^\pm : \bar{\sigma} - f_e^\pm r^\pm,$ $\varepsilon_T = \alpha_T (T - T_0)$	(1) short term test with isothermal or adiabatic conditions considered; (2) long term test with monotonic or cyclic loadings	both the elastic moduli and the strength depend on the hardening; strain-driven model allows its possibility for large-scale computation	Cervera et al. (1999)
$\Psi = \varepsilon_c(J_s) + \Psi_T(J_s, T) + \frac{G(J_s, T)(\alpha_1 - 3)}{2\rho_{s0}},$ $Y_f = Y_c(c_m + \frac{c_n p}{Y_c} - \frac{c_n Y_f}{3Y_c})z,$ $Y(\phi, p, \theta, \Omega, \delta_h, T) = Y_{TXC}(p) F_{Lode}(\theta) F_{therm}(J_s, T),$ $F_{therm}(J_s, T) = G(J_s, T) / G(J_s, T=0)$	(1) uniaxial/triaxial compression to a single joint set and randomly jointed volumes; (2) wave propagation induced by spherical explosions	use a 3D contact algorithm to model block interaction; account for rocks with various rock quality and porosity; effective properties of jointed rocks is available numerically in explicit calculations	Vorobiev (2008)
$\Psi = \Psi(\varepsilon - \varepsilon^p, T) = e - sT,$ $f^p = \sqrt{J_2} + \alpha I_1 - k_m,$ $g^p = \sqrt{J_2} + \beta I_1,$ $\rho c \dot{T} = -\nabla q_h + (\sigma : \dot{\varepsilon}^p - \alpha_T T \delta : C : \dot{\varepsilon}^e)$	(1) excavation of test tunnel and deposition holes under isothermal condition; (2) heating of rock pillar for one hundred days in total	elastic and elastoplastic models cannot accurately describe the failure process; heating increases the tangential stress on the pillar wall	Chen et al. (2010)
Ψ = Helmholtz’s free energy Ψ^e = degraded elastic free energy Ψ^p, Ψ^{vp} = plastic, viscoplastic strain energy e = specific internal energy V, Ψ_T = thermal part of free energy W = mechanical free energy L = thermo-mechanical part of free energy H = chemical part of free energy ε_c = volume-dependent potential Y^ω, Y_d = damage conjugate force R_c, Y_c = unconfined compressive strength Y_f = failure strength Ω = damage variable d = mechanical damage parameter g = thermal damage parameter p = mean stress q = deviatoric stress θ = Lode angle m = curvature of yield surface n = thermo-elastic coupling tensor K_w = permeability d^+, d^- = damage indices	g_M, g_S, g_T = crack-related rigidity D_e, β_s, β_T = damaged stiffness r = damage energy release threshold β^p = transition point η^p = instantaneous plastic hardening $\bar{\sigma}, \sigma$ = stress tensor ε_e = elastic strain ε_M = mechanical strain ε_{sv} = capillary volumetric strain ε_T = thermal volumetric strain $\bar{\varepsilon}$ = non-local equivalent strain α_T = thermal expansion coefficient f^\pm, f^p, f^{vp} = yield criterion γ^p, γ^{vp} = hardening variable g^p, g^{vp} = plastic potential c = specific heat capacity C = tangential modulus tensor C_0 = initial damage-stress rate C_1 = damage increase rate C^\pm = tensile/compressive metric tensor c_m, c_n, z = material parameter C_s = coefficient of material cohesion	k_m = material property q_h = heat conduction J_2 = deviatoric stress invariant I_1 = principal stress invariant α, β = experimental coefficient ρ = density ϕ = porosity Y_{TXC} = triaxial compression yield strength α_1 = invariant of symmetric unimodular tensor k, \bar{k} = hardening-softening parameter κ = aging degree r^\pm = damage threshold f_e^\pm = elastic limit in uniaxial test G = shear modulus ξ = hydration degree T = absolute temperature T_0 = reference temperature s = entropy F_{therm} = thermal softening term F_{lode} = Lode angle function ε^{id} = irreversible strain J_s = average dilatation of the solid	

2.7 Homogenization Method

When the evolution laws that represent the damage and healing dissipation processes are better understood at the microscopic level, it is advisable to adopt a bottom-up approach, e.g. a self-consistent homogenization scheme, instead of a top-to-bottom approach such as microstructure-enriched CDHM. In homogenization theories, threshold damage functions and flow rules are formulated at the microscopic scale. The balance of microscopic stresses at the interface between two constituents (e.g. two grains) is ensured by correcting the macroscopic stress (respectively strain) by a so-called *eigenstress* (respectively *eigenstrain*). REV properties (such as the REV stiffness matrix) is deduced from the knowledge of stress (respectively strain) concentration tensors, which depend on the geometry of the heterogeneity present in the REV (Berryman, 1995; Nemat-Nasser and Hori, 1993).

Salt is a polycrystalline aggregate, which can be macroscopically homogeneous and infinite. The stress and strain tensors in the mesoscopic polycrystal and in a single grain are denoted by $\bar{\sigma}$, $\bar{\epsilon}$ and σ , ϵ , respectively. The local tensors σ and ϵ vary from one grain to another because grains differ in size, shape, and crystallographic orientations. The average value of a local quantity is used to represent the macroscopic value:

$$\bar{\sigma} = \langle \sigma \rangle, \quad \bar{\epsilon} = \langle \epsilon \rangle \quad (14)$$

in which $\langle \quad \rangle$ represents the average value. In general, the single crystal behavior is known, which will be used to determine the macroscopic response of stress and strain. In the following, we upscale the stress state in salt grains subject to active slip systems in order to predict salt viscous damage and fatigue. We use the self-consistent method initially proposed by Kröner (1961). Hill (1965) applied the self-consistent method to elastic composites for spherical inclusions. In Hill's model, small variations of the local stress in the inclusions and the small variations of the far-field stress in the matrix are coupled to those of the microscopic strain and those of the macroscopic

strain. The tensor that links the properties of the crystal at different scales is known as the Hill's tensor (denoted by \mathbf{L}^*):

$$L_{ijkl}^* = \frac{\mu}{4 - 5\nu} [(3 - 5\nu)\delta_{ij}\delta_{kl} + \frac{7 - 5\nu}{2}(\delta_{ik}\delta_{jl} + \delta_{il}\delta_{jk})] \quad (15)$$

When all grains have identical linear and isotropic elastic characteristics, we have:

$$\overline{\boldsymbol{\epsilon}^e} = \langle \boldsymbol{\epsilon}^e \rangle, \quad \overline{\boldsymbol{\epsilon}^p} = \langle \boldsymbol{\epsilon}^p \rangle \quad (16)$$

in which $\overline{\boldsymbol{\epsilon}^e}$, $\boldsymbol{\epsilon}^e$, $\overline{\boldsymbol{\epsilon}^p}$, and $\boldsymbol{\epsilon}^p$ represent respectively the macroscopic and local elastic and plastic strain tensors.

In salt polycrystals, plastic and viscous deformation result from several fundamental mechanisms, e.g., dislocation glide, dislocation climb, polygonalization, intergranular slip, dissolution-precipitation. Under stress and temperature typical of storage conditions, dislocation glide is the predominant mechanism that contributes to macroscopic salt rock deformation (Arson et al., 2012; Munson, 1979; Senseny et al., 1992). Dislocation glide can only occur on specific crystallographic planes, and in a limited number of directions. The non-elastic deformation of mono crystals can result in geometric incompatibilities between adjacent grains. Restricted movements within monocrystals originate internal stresses within the polycrystal. Therefore, it is natural to employ a bottom-up approach with threshold damage functions that represent glide or crack propagation mechanisms to explain salt viscous damage. Plastic deformation of crystals generally occurs in some preferential directions with respect to the crystallographic axes. For salt polycrystal, since the grain properties are relatively homogeneous (Fig. 9), the orientation of the crystal lattice with respect to the macroscopic stress or strain orientation is the most critical parameter affecting the plastic strain of the grain (Pouya, 2000). Therefore, in this thesis, the orientation is considered as the only heterogeneity of the polycrystal, i.e., the constituent grains will be considered to differ only by their crystallographic orientation with respect to the polycrystal axes.

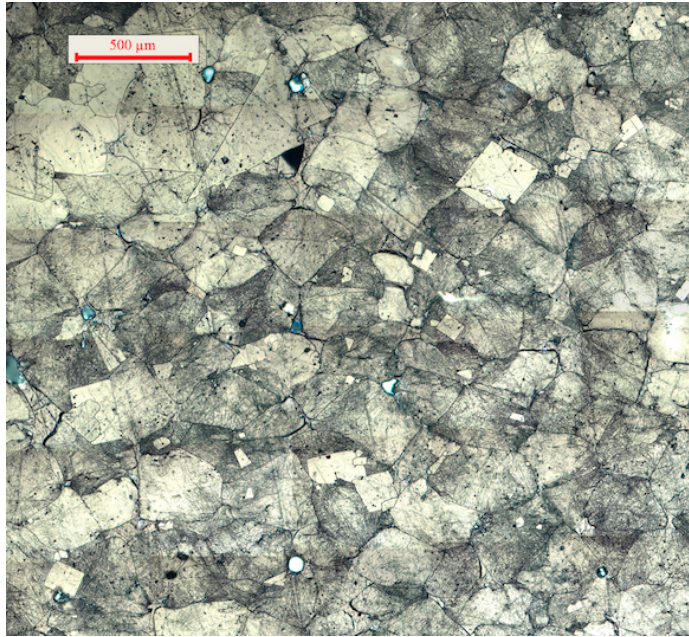


Figure 9 Microscopic sectional view of synthetic salt rock, prepared by Mr. J. Ding at Texas A&M University. Synthetic salt rock samples were produced through thermo-mechanical coupled consolidation process (Grain size = $0.3 \sim 0.355\text{mm}$, $T = 150^\circ\text{C}$, $\sigma = 106.7\text{MPa}$, final porosity = 2.93%).

2.8 State-of-the-Art of Finite Element Models of Damage and Healing in Rocks

Microstructure has a strong impact on damage evolution and strength recovery in rocks. Microstructure-enriched models have been developed to understand the influence of grain size, orientation, shape, and boundary topology in polycrystalline materials (e.g., Barbe et al. (2001)). Simplified grain shapes (e.g., squared or a cubic) were assumed to implement these models in Finite Element Methods, in which each element corresponds to a specific grain orientation (Beaudoin et al., 1995; Havlicek et al., 1990; Takahashi et al., 1998). Such methods are not based on a realistic representation of microstructure and cannot explain the fundamental processes that drive the macroscopic behavior of a polycrystal. By contrast, the influence of microstructure on crack propagation in a stress-induced heterogeneous medium was investigated using Voronoi cell FEM (Li and Ghosh, 2004). Microstructure-based FEM simulations were used to study metallic materials such as aluminum (Becker and Panchanadeeswaran, 1995), copper (Delaire et al., 2000; Musienko et al., 2007), interstitial-free (IF) steel (Erieau and Rey, 2004), and a variety of alloys (Eberl et al., 2002; Musienko and Cailletaud, 2009). To date however, FEM models cannot explain the time-dependent viscous damage and fatigue behavior of polycrystals subject to long-term creep or cyclic loading. Only a few studies are based on real grain structure and account for various damage mechanisms including inter- and intra- granular crack propagation (Musienko and Cailletaud, 2009).

Finite Element Methods (FEM) with discontinuities were proposed to predict the deformation and strength of polycrystals at various scales in 2D, extended 2D, or 3D (e.g., Musienko et al. (2007)). For instance, crack propagation within polycrystals was simulated with Cohesive Zone Models (CZM) (Clayton and McDowell, 2004; Espinosa and Zavattieri, 2003; Gui et al., 2015; Needleman, 1987) and XFEM (Sukumar et al.,

2003) enriched with jump interpolation functions. Fracture propagation in homogeneous and layered media such as composites with delamination was also simulated with extended Finite Element Methods (XFEM) (Nagashima and Suemasu, 2006). To model the damaged zone ahead of the fracture tip, several numerical methods were developed, including multi-scale frameworks (Sethuraman and Reddy, 2008), or methods based on average damage variables (defined at the mesoscopic scale) (Suzuki, 2012; Valko and Economides, 1994). But such methods do not track damage variables explicitly and justify the links between length scales for stress intensity factors.

CDM models were initially formulated to predict the degradation of stiffness and strength properties of metals. With the increasing energy demand and the important environmental issues that arose from waste management, rocks became an interesting object of study for fracture mechanicians and material scientists - and not only geologists. Fracture Mechanics models allows predicting the state of stress around crack tips, as well as the change of crack dimensions. Formulations get very complex when several cracks propagate simultaneously. By contrast, CDM avoids modeling each crack individually and was seen as a computationally efficient framework to predict the changes of stress and deformation at the mesoscopic (REV) scale, which was well suited for engineering design. The CDM thermodynamic framework is also well-suited for numerical implementation in FEM because discontinuities are modeled as energy losses at the REV scale.

2.9 Research Objectives

Crack closure is the result of the normal displacement of open cracks faces under compression, which is assumed to produce an elastic deformation at the REV scale. Crack healing does not occur during crack closure, i.e. unilateral effects are not synonymous of mechanical recovery. Healing requires an energy input to trigger the migration of ions within the lattice, and is therefore a dissipative process independent from damage (Arson et al., 2012). As a result, the free energy of the REV shall depend on two state variables (purely elastic deformation ϵ^{el} , temperature change τ) and two dissipation variables (damage Ω , healing \mathbf{H}). At low moisture content, crack rebonding in salt is mainly driven by DMT. Healing during DMT is usually described as the time-dependent counter effect of dilatant cracking, which can be modeled by viscoplastic deformation laws (Hou, 2003; Senseny et al., 1992). During DMT processes, wave velocities increase exponentially with time (Brodsky and Munson, 1994) and elastic moduli also increase exponentially over time (Chan et al., 1998). Damaged elastic moduli can be related to wave velocities by means of O’Connell and Budiansky’s (1974) micro-mechanical relationships, but these equations do not allow predicting the evolution of microstructure over time or during changes of stress conditions. The goal of this research work is to understand and predict the damage and healing processes in salt rock at various scales subjected to complex geomechanical couplings or extreme loading conditions, by correlating fabric descriptors with phenomenological variables. We propose three complementary multi-scale analyses (Fig. 10):

- *From REV-scale to grain-scale, “top-to-bottom approach” (Chapter 3):* CDM is enriched with fabric tensors in order to couple damage and healing variables to microstructure evolution during crack debonding, opening, closure, and rebonding.

- *From grain-scale to REV-scale, “bottom-up approach” (Chapter 4):* A self-consistent homogenization scheme is employed to analyze the origin of salt fatigue from the mechanisms of deformation of halite crystals forming the polycrystalline aggregates.
- *From REV-scale to reservoir-scale (Chapter 5):* Micro-macro models are implemented in the Finite Element Method in order to investigate fracture propagation in salt polycrystals and assess the long-term performance of salt caverns.

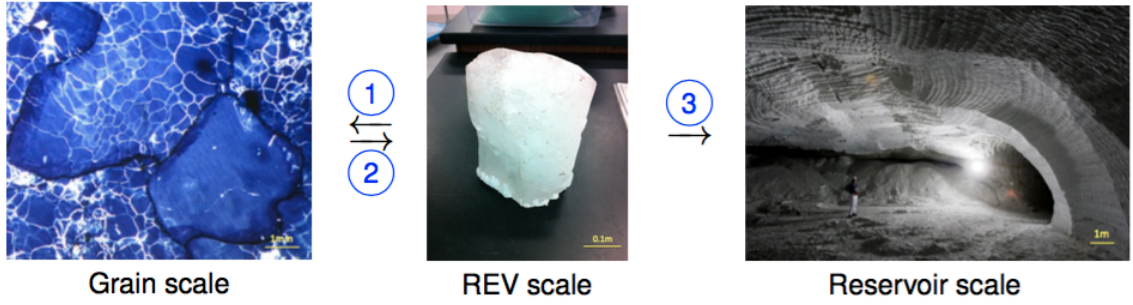


Figure 10 Multi-scale modeling approaches, modified from (Schleder and Urai, 2007).

CHAPTER III

FABRIC-BASED DAMAGE AND HEALING MECHANICS

3.1 Introduction

This chapter presents the progressive development of our “top-to-bottom” microstructure-enriched CDHM modeling approach, which is illustrated by Fig. 11. We use the anisotropic Continuum Damage Mechanics (CDM) model of crack opening and closure formulated by Dragon et al. (2000) as a basis. This CDM framework is coupled with a thermo-elastic model to study crack opening and closure in rocks subjected to thermo-mechanical couplings (Section 3.2). The model is then extended to couple halite thermo-mechanical behavior to micro-structure evolution during crack debonding, opening, closure and rebonding (Section 3.3). In order to infer the form of fabric tensors from microstructure observation, creep tests are carried out on granular salt under constant stress and humidity conditions. With a microphysical model, we calculate the crack cusp migration distance for three families of cracks represented by the damage eigenvalues, which allows us to distinguish the cracks that heal from those that do not heal under a given state of stress and temperature (Section 3.4). Using microscope imaging and micro-CT scanning, we finally analyze the probability distributions of crack radius, void areas and crack spacing and use them as a basis to derive macroscopic evolution laws. Using the percolation theory, we enhance the fabric-enriched CDM model to investigate the coupled influence of damage and healing on the mechanical and transport properties of salt rock (Section 3.5).

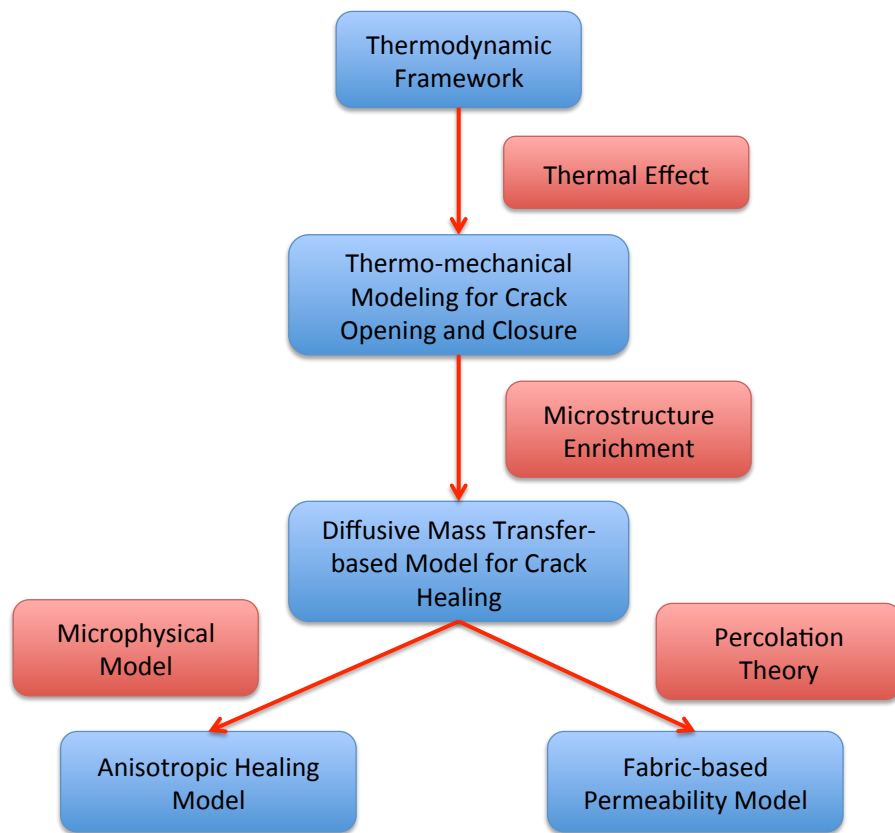


Figure 11 Model development in Chapter 3.

3.2 Thermo-mechanical Model of Crack Opening and Closure

3.2.1 Thermo-mechanical Stress Induced Crack Opening and Closure

The proposed constitutive model is formulated to couple crack opening and closure within the framework of CDM. The strain energy loss due to crack propagation is used to compute damaged stiffness and deformation. The second order crack density tensor defined by Kachanov (1992) is adopted in the expression of energy dissipation. State equations must be combined with the laws governing the evolution of internal variables and the associated dissipative mechanisms. In the present work, the anisotropic CDM model of crack opening and closure formulated by Dragon et al. (2000) is used as a basis to predict thermo-mechanical anisotropic damage induced by crack debonding, opening and closure. An associate flow rule is assumed for damage, which represents crack debonding. Inelastic strains coupled to damage are introduced in order to account for the geometric incompatibilities that remain at crack faces even after tensile stress relaxation (irreversible crack opening). Crack closure is accounted for by means of a unilateral effect in the expression of the stiffness tensor: crack closure induces mechanical recovery of the damaged stiffness only in the directions in which the strain field is compressive. This framework relies on very few equations, which makes it a good exploratory tool before going further in the modeling of multiple damage and healing processes. Table 2 summarizes the constitutive equations proposed in the model.

Assuming that undamaged rock has a linear thermo-elastic behavior, the free energy of the damaged rock solid skeleton is expressed as a polynomial of order 2 in elastic deformation $\boldsymbol{\varepsilon}^E$ and order 1 in temperature change τ . The damage criterion is expressed as the difference between the norm of the energy release rate and an energy threshold. As shown in Fig. 12, the total deformation tensor is split into three components: purely elastic deformation ($\boldsymbol{\varepsilon}^e$) that may occur in the absence of damage, damage induced elastic deformation ($\boldsymbol{\varepsilon}^{ed}$) that is due to the degradation of stiffness,

and damage induced irreversible deformation (ϵ^{id}) which is due to the residual effect. Conjugation relationships derived from thermodynamic principles provide the expression of stress and of the energy release rate. The latter can be further decomposed into two parts: \mathbf{Y}_1 accounts for crack propagation; \mathbf{Y}_2 describes rock property changes due to temperature variation. It is assumed that only certain components of the thermodynamic variable conjugate to damage (\mathbf{Y}) have an influence on the damage growth: the thermo-mechanical tensile damage-driving force ($\mathbf{Y}_{1a}^+ = -g\epsilon^+$) and the thermal damage-driving force (\mathbf{Y}_2^d). A dimensional analysis indicates that the term $\frac{1}{2\tau_0} \frac{\partial C(\Omega)}{\partial \Omega} \tau^2$ is negligible compared to $\tau \frac{\partial \mathbf{K}(\Omega)}{\partial \Omega} : \epsilon^E$. Note that the distance between rock crystals increases with temperature. At higher temperatures, more energy is required to separate rock crystals, which are already more distant than at lower temperature. To capture this temperature-induced reduction of rock strength, which counter-acts the tensile damage-driving force \mathbf{Y}_{1a}^+ , the thermal damage driving force is defined as:

$$\mathbf{Y}_2^d = A \cdot \tau \cdot \alpha_T (\alpha + 2\beta) tr(\epsilon^{E+}) \quad (17)$$

Where ϵ^{E+} is the tensile elastic deformation, which indicates the increase of inter-particle distance at high temperature. A is a proportionality constant.

The concept of unilateral effect is adopted in order to account for crack closure. Following Chaboche's (1992b) approach, the Heaviside function (H) is used in the expression of the stiffness tensor, in order to distinguish material response in tension and compression (Table 2). The damage criterion is modified in order to capture the recovery of stiffness induced by crack closure under compression: in these conditions, the rock REV behaves like the undamaged REV. In this study, it is assumed that full compressive strength recovery is achieved ($\eta = 1$) if all cracks are closed under compression. Crack closure increases the number of inter-granular contacts in the REV, which leads to a recovery in both stiffness (Fig. 12) and heat capacity.

Table 2 Outline of thermo-mechanical damage model

Postulates	
Free Energy for Crack Opening (Ψ_S)	$\Psi_S(\boldsymbol{\varepsilon}^E, \tau, \boldsymbol{\Omega}) = \frac{1}{2}\boldsymbol{\varepsilon}^E : \mathbf{D}(\boldsymbol{\Omega}) : \boldsymbol{\varepsilon}^E + g\boldsymbol{\Omega} : \boldsymbol{\varepsilon} - \frac{1}{2\tau_0}C(\boldsymbol{\Omega})\tau^2 - \tau\mathbf{K}(\boldsymbol{\Omega}) : \boldsymbol{\varepsilon}^E$ $\frac{1}{2}\boldsymbol{\varepsilon}^E : \mathbf{D}(\boldsymbol{\Omega}) : \boldsymbol{\varepsilon}^E = \frac{1}{2}\lambda(tr\boldsymbol{\varepsilon}^E)^2 + \mu tr(\boldsymbol{\varepsilon}^E \cdot \boldsymbol{\varepsilon}^E) + \alpha tr\boldsymbol{\varepsilon}^E tr(\boldsymbol{\varepsilon}^E \cdot \boldsymbol{\Omega}) + 2\beta tr(\boldsymbol{\varepsilon}^E \cdot \boldsymbol{\varepsilon}^E \cdot \boldsymbol{\Omega})$
Free Energy for Crack Closure (Ψ_S)	$\Psi_S(\boldsymbol{\varepsilon}^E, \tau, \boldsymbol{\Omega}) = \frac{1}{2}\boldsymbol{\varepsilon}^E : \mathbf{D}_{\text{eff}}(\boldsymbol{\Omega}) : \boldsymbol{\varepsilon}^E + g\boldsymbol{\Omega} : \boldsymbol{\varepsilon} - \frac{1}{2\tau_0}C_{\text{eff}}(\boldsymbol{\Omega})\tau^2 - \tau\mathbf{K}_{\text{eff}}(\boldsymbol{\Omega}) : \boldsymbol{\varepsilon}^E$ $\mathbf{D}_{\text{eff}}(\boldsymbol{\Omega}) = \mathbf{D}(\boldsymbol{\Omega}) + \eta \sum_{i=1}^3 H(-tr(\mathbf{P}_i : \boldsymbol{\varepsilon}))\mathbf{P}_i : (\mathbf{D}_0 - \mathbf{D}(\boldsymbol{\Omega})) : \mathbf{P}_i, \quad 0 < \eta \leq 1$ $\mathbf{K}_{\text{eff}}(\boldsymbol{\Omega}) = \mathbf{K}(\boldsymbol{\Omega}) + \eta \sum_{i=1}^3 H(-tr(\mathbf{P}_i : \boldsymbol{\varepsilon}))\mathbf{P}_i : (\mathbf{K}_0 - \mathbf{K}(\boldsymbol{\Omega})) : \mathbf{P}_i, \quad 0 < \eta \leq 1$ $C_{\text{eff}}(\boldsymbol{\Omega}) = C(\boldsymbol{\Omega}) + \eta \sum_{i=1}^3 H(-tr(\mathbf{P}_i : \boldsymbol{\varepsilon}))\mathbf{P}_i : [(C_0 - C(\boldsymbol{\Omega}))\boldsymbol{\delta} \otimes \boldsymbol{\delta}] : \mathbf{P}_i, \quad 0 < \eta \leq 1$
Damage Criterion for Crack Opening (f_d)	$f_d(\mathbf{Y}_d^+, \boldsymbol{\Omega}) = \sqrt{\frac{1}{2}\mathbf{Y}_d^+ : \mathbf{Y}_d^+} - (C_0 + C_1\boldsymbol{\Omega})$
Damage Criterion for Crack Closure (f_d)	$f_d(\mathbf{Y}_d^+, \boldsymbol{\Omega}) = \sqrt{\frac{1}{2}\mathbf{Y}_d^+ : \mathbf{Y}_d^+} - [C_0 + C_1 \sum_{i=1}^3 H(-\varepsilon_i)\Omega_i]$
Strain Decomposition	$\boldsymbol{\varepsilon} = \boldsymbol{\varepsilon}^{el} + \boldsymbol{\varepsilon}^{ed} + \boldsymbol{\varepsilon}^{id} = \boldsymbol{\varepsilon}^{EM} + \boldsymbol{\varepsilon}^{ET} + \boldsymbol{\varepsilon}^{id}$
Conjugation Relationships	
Stress ($\boldsymbol{\sigma}$)	$\boldsymbol{\sigma} = \mathbf{D}(\boldsymbol{\Omega}) : \boldsymbol{\varepsilon}^E + g\boldsymbol{\Omega} - \mathbf{K}(\boldsymbol{\Omega})\tau$ $\mathbf{Y} = -\frac{\partial \Psi_S(\boldsymbol{\varepsilon}, \tau, \boldsymbol{\Omega})}{\partial \boldsymbol{\Omega}} = \mathbf{Y}_1 + \mathbf{Y}_2$
Damage Driving Force (\mathbf{Y}_d^+)	$\mathbf{Y}_1 = -g\boldsymbol{\varepsilon} - \alpha(tr\boldsymbol{\varepsilon}^E)\boldsymbol{\varepsilon}^E - 2\beta(\boldsymbol{\varepsilon}^E \cdot \boldsymbol{\varepsilon}^E)$ $\mathbf{Y}_2 = \frac{1}{2\tau_0}\frac{\partial C(\boldsymbol{\Omega})}{\partial \boldsymbol{\Omega}}\tau^2 + \tau\frac{\partial \mathbf{K}(\boldsymbol{\Omega})}{\partial \boldsymbol{\Omega}} : \boldsymbol{\varepsilon}^E$ $\mathbf{Y}_d^+ = -g\boldsymbol{\varepsilon}^+ + A \cdot \tau \cdot \alpha_T(\alpha + 2\beta)tr(\boldsymbol{\varepsilon}^E)$
$\boldsymbol{\varepsilon}^{EM}$	= mechanical deformation component
$\boldsymbol{\varepsilon}^{ET}$	= thermal deformation component
α, β	= mechanical damage parameters
C_0	= initial damage threshold
λ, μ	= Lamé coefficients
C_1	= damage hardening parameter
τ_0	= initial temperature
g	= toughness parameter
\mathbf{D}	= damaged stiffness tensor
k	= bulk modulus
α_T	= thermal expansion coefficient
\mathbf{K}	= $k\alpha_T$ “diagonal tensor”
\mathbf{D}_{eff}	= effective stiffness tensor after “partial recovery”
C	= damaged heat capacity
\mathbf{K}_{eff}	= effective diagonal tensor after “partial recovery”
A	= thermo-mechanical damage paramter
C_{eff}	= effective heat capacity after “partial recovery”
η	= degree of maximum stiffness recovery
\mathbf{P}_i	= 4 th order project tensor for the projection in crack planes normal to direction i
$\boldsymbol{\delta}$	= second order identity tensor

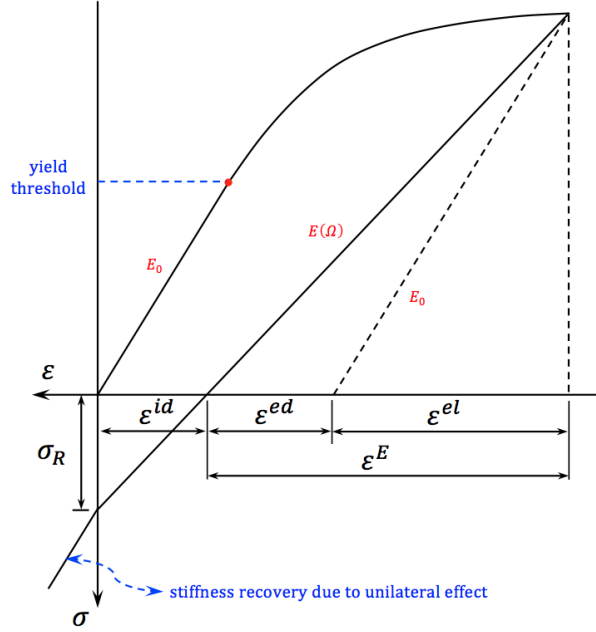


Figure 12 Strain decomposition (soil mechanics sign convention: compression counted positive).

3.2.2 Model Calibration and Verification

The advantage of the model proposed above is that the number of parameters required is minimal (seven mechanical parameters: λ , μ , α , β , g , C_0 , C_1 ; and one thermal parameter: α_T). Published datasets on thermo-mechanical behavior of sandstone and granite are available in the literature (Homand-Etienne and Houpert, 1989; Li et al., 2013; Tian et al., 2012; Wong, 1982). Table A.1 in Appendix I provides an overview of experimental data available on the assessment of thermo-mechanical damage in a variety of rocks. Most of the data is analyzed within the framework of thermo-elasticity, and there is not enough evidence on stiffness weakening and irreversible deformation induced by temperature gradients to really verify the proposed model against experimental data. According to Halm and Dragon (1998, 2002), the proposed thermo-mechanical damage model is expected to provide good predictions of tight rock macroscopic failure induced by crack opening and closure. Many authors used a similar mechanical damage model for sandstone, even though other mechanisms

such as grain crushing and pore collapse are expected to drive macroscopic failure in porous rock. The proposed model is seen as a versatile framework, that can be used to capture the loss of energy induced by damage in any rock material, provided that model parameters are well calibrated. In order to assess the performance of the model in doing so, calibration and verification simulations were performed on sandstone, for which experimental data was found in Sulem and Ouffroukh (2006) (drained triaxial compression tests on saturated sandstone). Reference stress-strain curves for this calibration were obtained for a confining pressure of 40 MPa. The triaxial tests used for model verification purposes were performed for confining pressures amounting to 28 MPa and 50 MPa. The corresponding stress-strain curves are shown in Fig. 13. Note that the soil mechanics sign convention is adopted (with compression counted positive). Dots are reported experimental data found in Sulem and Ouffroukh (2006). Solid and dashed lines represent the results of simulations performed in MATLAB with the proposed damage model.

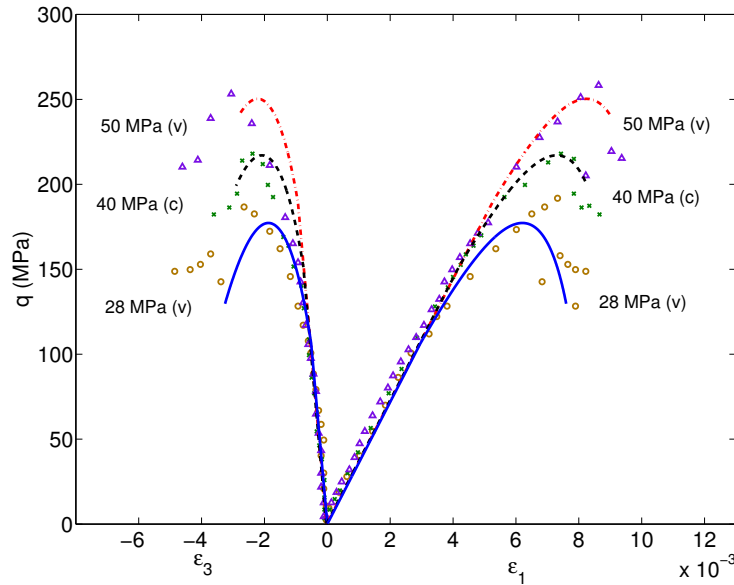


Figure 13 Stress-strain curves obtained during drained triaxial compression tests conducted on saturated sandstone. c - model calibration, v - model verification.

The plots obtained for the verification tests (at 28 MPa and 50 MPa) show that the model predictions match experimental data with an error less than 5% before the

peak of stress. This is considered as a satisfactory result, since the purpose of this study is to predict the effect of thermo-mechanical crack opening and closure before softening. Due to the thermo-elastic framework adopted in the proposed model, the expression of the damaged thermo-mechanical stiffness $\mathbf{K}(\boldsymbol{\Omega})$ results from the expression of the damaged stiffness tensor, so that the thermal expansion coefficient α_T can be considered as a purely thermo-elastic parameter. That is the reason why in the present study, α_T is assigned a value known to be a standard for rock materials (negative with the soil mechanics sign convention). Table 3 summarizes the parameters obtained for sandstone after calibration and verification.

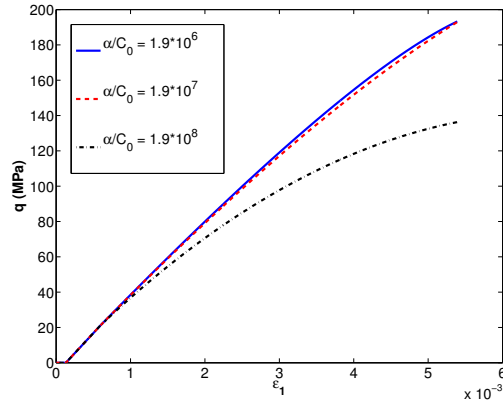
Table 3 Model parameters obtained for sandstone after calibration and verification (with the soil mechanics sign convention).

λ (Pa)	μ (Pa)	α (Pa)	β (Pa)	g (Pa)	C_0 (Pa)	C_1 (Pa)	α_T (K^{-1})
8.13×10^9	1.53×10^{10}	1.2×10^{10}	-4×10^{10}	1.17×10^8	700	3.8×10^5	-1×10^{-5}

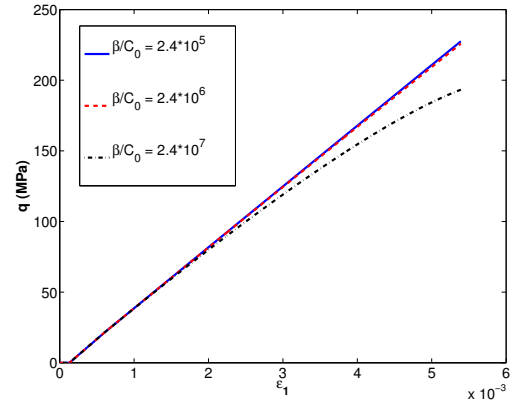
A sensitivity analysis was carried out in order to explain the physical meaning of the five mechanical damage parameters (α , β , g , C_0 , C_1). Strain controlled triaxial compression tests were simulated (for a confining pressure of 15 MPa). The initial damage threshold C_0 was used as a scaling factor. The values of the normalized damage parameters (α/C_0 , β/C_0 , g/C_0 , C_1/C_0) were first assigned a value according to the calibration study published in Halm and Dragon (1998) for sandstone (for reference, the set of constitutive parameter is reported in Table 4). Each normalized parameter was then varied one by one, keeping all the other parameters constant (Fig. 14). Larger α and β values imply a more ductile behavior, as can be seen from the portion of the stress-strain curve corresponding to higher deformation (Fig. 14a&b). As g increases, the irreversible deformation and corresponding residual stress increase. So the peak of the stress-strain curve tends to shift downward (Fig. 14c). C_1 has an influence on the strain hardening portion as damage starts to accumulate (Fig. 14d).

Table 4 Reference set of constitutive parameters used in the sensitivity analysis (after Halm and Dragon (1998)).

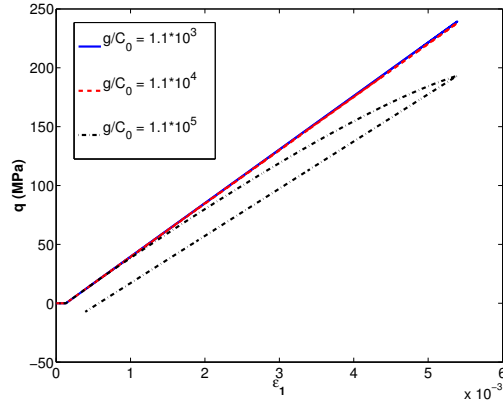
λ (Pa)	μ (Pa)	α (Pa)	β (Pa)	g (Pa)	C_0 (Pa)	C_1 (Pa)	α_T (K^{-1})
2.63×10^{10}	1.75×10^{10}	1.9×10^9	-2.04×10^{10}	1.1×10^8	1000	5.5×10^5	-1×10^{-5}



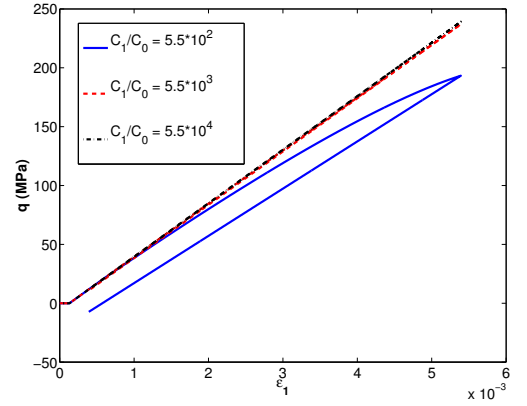
(a) Effect of α



(b) Effect of β



(c) Effect of g



(d) Effect of C_1

Figure 14 Sensitivity analysis on the mechanical damage parameters used in the model (all expressed in units of pressure). C_0 : initial damage threshold; C_1 : hardening parameter; α & β : parameters controlling the shape of the damaged stress/strain curve (ductile vs. brittle trends).

3.2.3 Simulation of Thermo-mechanical Crack Opening

The thermo-mechanical damage model presented in Section 3.2.1 is used to simulate crack-induced damage during a triaxial compression test comprising a thermo-mechanical loading phase, for the sandstone studied in Section 3.2.2. The energy released to propagate damage in a sample under mechanical compression is compared to the energy released to propagate damage in a sample subject to heating under zero axial strain. Such an analysis could be used, for instance, to study underground rock pillars subjected to a rapid temperature increase caused by a fire or an explosion. Three loading phases are considered:

(M1) *Isotropic compression*. An isotropic confining pressure (20 MPa) is applied under stress-controlled conditions. The confining pressure is chosen so as to ensure that the damage criterion is not reached: during this phase, the material remains elastic.

(M2) *Triaxial compression*. The sample is loaded by increasing the axial strain (direction 1) at a constant strain rate (so as to reach a maximal axial strain of 0.00226). The lateral stresses do not change throughout this phase.

(TM) *Confined heating*. Axial deformation is fixed while the temperature is increased by 150K from the initial room temperature (assumed 293K). Lateral stresses are fixed, which means that lateral expansion can occur.

Two sequences are simulated (Fig. 15):

(1) $M1 \rightarrow M2 \rightarrow TM$; (2) $M1 \rightarrow TM \rightarrow M2$.

During the triaxial compression phase (M2), deviatoric stress q generates lateral tensile strain, causing lateral damage ($\Omega_1 = 0$, $\Omega_2 = \Omega_3 \neq 0$). Correspondingly, a degradation of rock stiffness is observed, in both stress-strain curves (AB_1 & B_2C_2 in Fig. 16a). For both sequences, q increases with temperature (AB_2 & B_1C_1 in Fig. 16a). This is due to the mechanical boundary conditions: axial thermal expansion is constrained, which generates compressive internal stress - in virtue of the action/reaction principle. Temperature-induced compression adds to mechanical

compression. Damage induced during the mechanical phase AB_1 (axial compression) lowers stiffness, which explains why the thermal compressive stress developed in reaction to thermal expansion during the heating phase B_1C_1 (sequence 1) is smaller than during the heating phase AB_2 (sequence 2) (Fig. 16a).

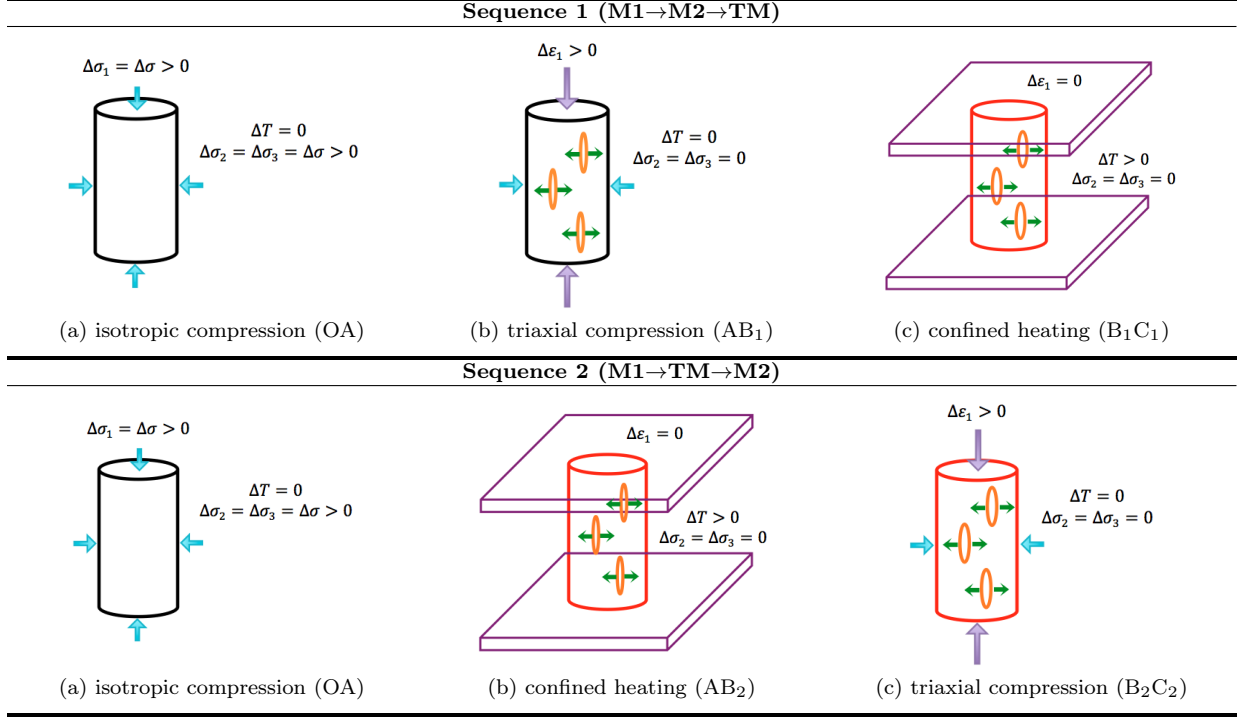


Figure 15 Stress paths simulated to study the influence of thermo-mechanical crack opening: comparison of mechanical and thermo-mechanical energy released during the propagation of compression damage.

The 3D plot in Fig. 16b shows the evolution of damage for the stress paths simulated in the two sequences described above. Fig. 16c and 16d are projections in the strain-damage and temperature-damage spaces, respectively. Overall, less damage occurs in sequence 2. This could be expected from the model formulation: in sequence 2, a mechanical loading is applied to a heated material, in which the “counter-acting” damage driving force \mathbf{Y}_2^d , accounting for the decrease of rock strength with temperature increase (Eq. 17), is larger than in sequence 1. As a result, the cumulated damage driving force \mathbf{Y}_d^+ in sequence 2 is smaller than in sequence 1 - in other words,

less energy is released to open cracks in sequence 2. Moreover, Fig. 16c indicates that lateral damage progresses faster in a cooler sample (slope $A'B_1 > \text{slope } B_2C_2$; segment AA' represents the purely elastic range).

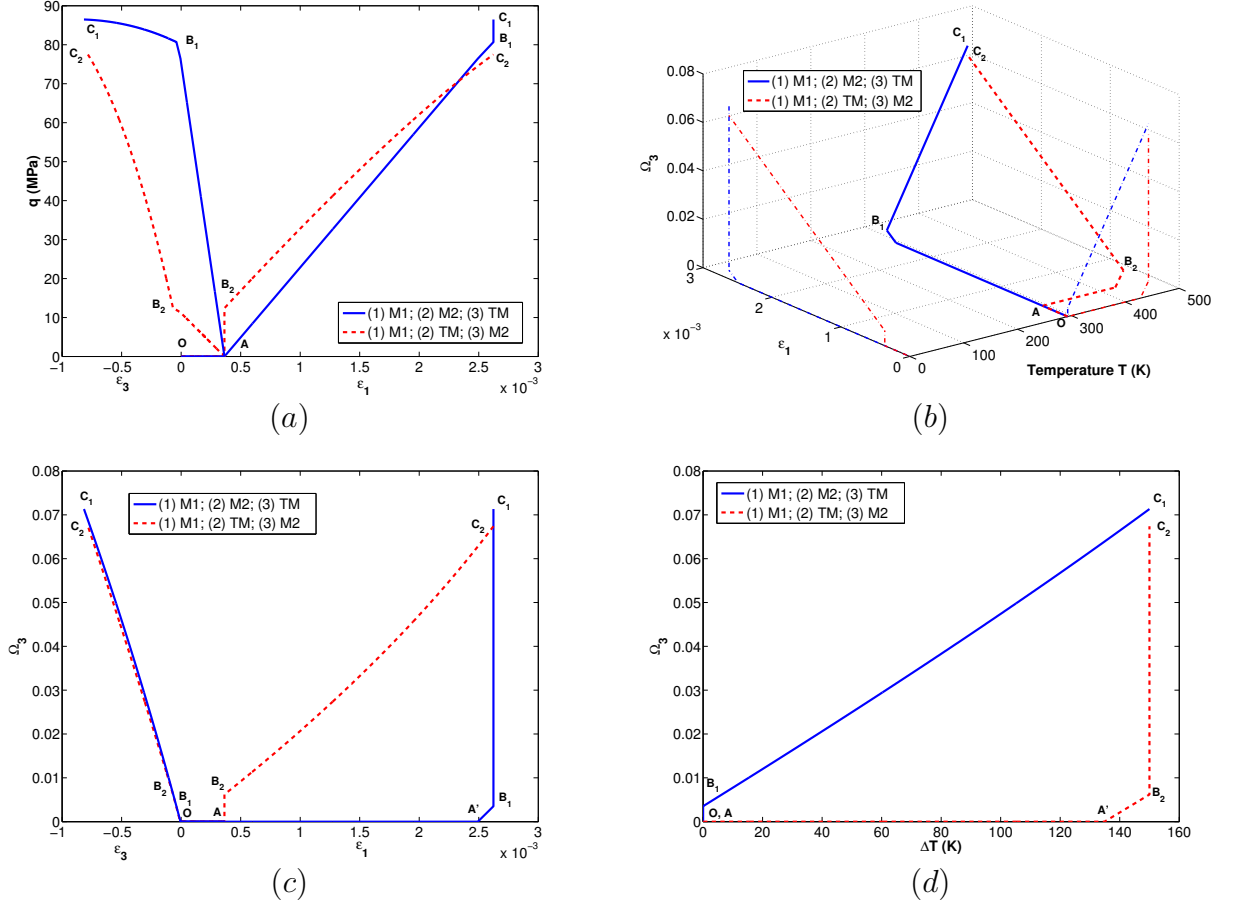


Figure 16 Simulation of the two thermo-mechanical stress paths described in Fig. 15 (confining pressure: 20 MPa; maximum axial strain: 0.00226; maximum temperature change: 150K): (a) Deviatoric stress vs. axial and lateral deformation; (b) Damage evolution vs. axial deformation and temperature variation; (c) Damage evolution vs. axial and lateral deformation; (d) Damage evolution vs. temperature variation.

In both sequences, the sample expands laterally (due to mechanical or thermo-mechanical compression). As expected, larger damage results in larger deformation, and lateral strains (ϵ_3) obtained at the end of sequence 1 are larger than at the end of sequence 2 (Fig. 16c). In sequence 1, damage induced by mechanical compression increases the minimum energy release rate required to further propagate cracks in the

heating phase (slope of $B_1C_1 < \text{slope of } OB_1$ in Fig. 16c for ε_3). On the other hand, for sequence 2, the damage threshold (i.e. the energy required to propagate cracks) increases with both thermo-mechanical stress and higher ambient temperature. As a result, slope of B_2C_2 is smaller than OB_2 (Fig. 16c). In the undamaged material, there is a damaged temperature threshold, below which thermo-mechanical cracks will not develop - the temperature threshold is about $427K$ for the sandstone studied (OAA', Fig. 16d). However, if mechanical cracks have been produced before heating the sample, any increase in temperature will immediately cause damage to propagate in the sample (B_1C_1 , Fig. 16d).

3.2.4 Simulation of Thermo-mechanical Crack Closure

The thermo-mechanical damage model presented in Section 3.2.1 is used to simulate the evolution of damage in the same sandstone, during a uniaxial tension test followed by a compression induced by either mechanical or thermo-mechanical stresses. This stress path could be encountered in the context of tunneling. Indeed, galleries need to be cooled before being exploited for mining, which raises some interest in studying potential crack closure due to cooling in rock subject to displacement boundary conditions. The stress path (Fig. 17) is as follows:

- (1) *Uniaxial tension*: crack opening (OA-AB). The sample is loaded by increasing the axial tensile strain (direction 1) at a constant strain rate ($\Delta\varepsilon_1$), up to $\varepsilon_1 = -0.00016$. Temperature and lateral stresses are kept constant ($\Delta\sigma_2 = \Delta\sigma_3 = 0$, $\Delta T = 0$). Crack planes perpendicular to the axis are produced due to the tensile stress.
- (2) *Mechanical "relaxation"*: release of tensile stress (BC). The sample is unloaded in order to release the tensile stresses completely. The unloading process is elastic (linear stress / strain plot), and only the elastic part of crack-induced deformation is compensated (at the end of this loading phase: $\varepsilon^{ed} = 0$, but $\varepsilon^{id} \neq 0$).
- (3) *Compression* (CD-DE). Two stress paths are considered to study unilateral effects

induced by crack closure: a) decrease of temperature ($\Delta T = -60K$) with zero axial deformation; b) purely mechanical axial compression at constant temperature.

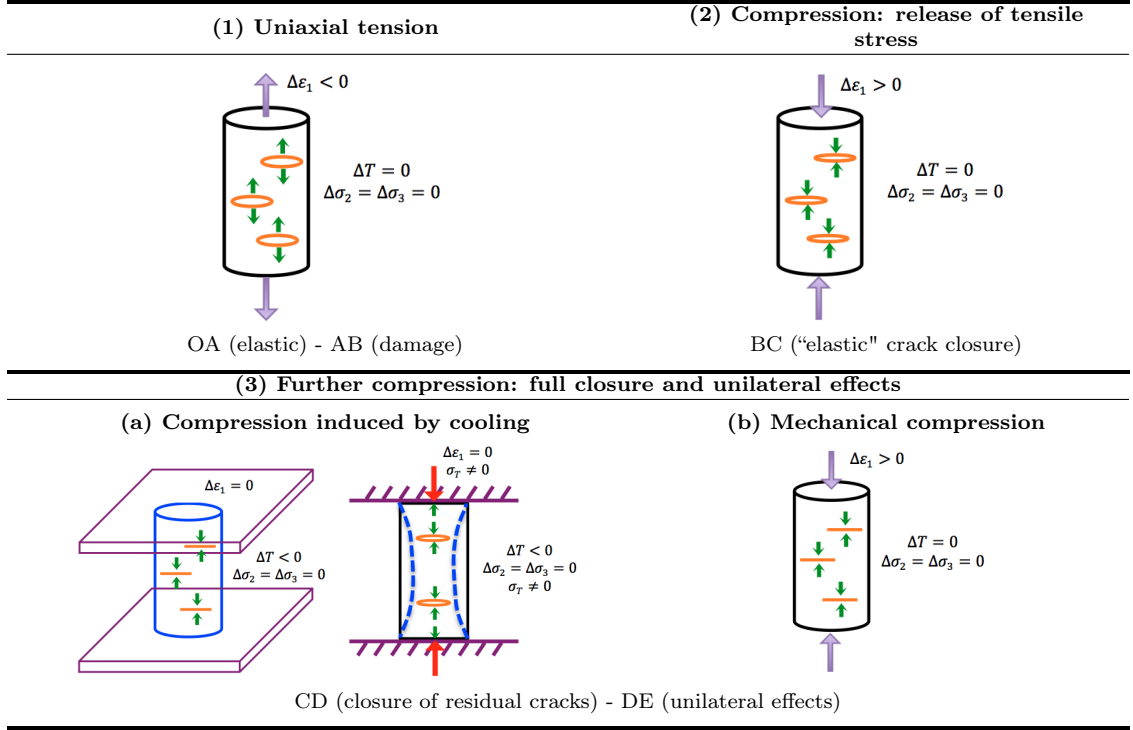


Figure 17 Stress paths simulated to study the influence of thermo-mechanical crack closure: comparison of mechanical and thermo-mechanical compression loadings.

The present analysis focuses on opening and closure of one family of cracks perpendicular to the axis of loading. To avoid the formation of axial cracks, compression in the third loading phase was kept below the compressive strength of the material considered (Fig. 17). During cooling (3a, Fig. 17), the sample was free to contract laterally, but not axially. Consequently, internal tensile forces developed in the undamaged part of the sample (i.e., outside the cracks). In virtue of the principle of action and reaction, cracks closed due to the internal compression forces acting at crack faces. In the mechanical compression phase (3b, Fig. 17), further compressive strain was applied at a constant rate ($\Delta \epsilon_1$) under constant lateral stress ($\Delta \sigma_2 = \Delta \sigma_3 = 0$).

Rock tensile strength is relatively low, so that damage starts to develop quickly after the tensile load is applied. Correspondingly, the stress-strain curve is linear

on a very short interval (OA, Fig. 18a), which is followed by a non-linear response (AB, Fig. 18a) associated to the development of damage (AB, Fig. 18c). The stress-strain curve compares satisfactorily with the experimental results obtained for a direct tension test, reported in Luong (1990). During the stress release phase, the sample is unloaded elastically. Pure elastic deformation (ε^{el}) and damage-induced elastic deformation (ε^{ed}) are recovered (BC, Fig. 18a). During this phase, damage does not evolve (BC, Fig. 18c).

When cracks are completely closed, unilateral effects induce an increase of stiffness, thus, an increase of the bulk modulus (slope D_1E_1 , Fig. 18b). If cracks are closed by cooling, lateral deformation is a contraction, and the sum of thermal and mechanical axial deformation is zero (so that $OC = OD'_1$ in Fig. 18a & 18b). Consequently, the damage-driving force remains constant. As a result, damage does not increase (C- D_1 - E_1 , Fig. 18c). If cracks are closed by mechanical compression, unilateral effects are observed once cracks are completely closed (i.e. $\varepsilon = 0$). The slope (CD_2) of the stress-strain diagram in stage 3 is the same as in stage 2 (BC) (Fig. 18d) because tensile deformation still exists. The slope of the stress-strain diagram becomes steeper when deformation is negative (D_2E_2 , Fig. 18d) and is actually equal to the slope of OA (characteristic of the undamaged material).

The combined plots shown in Fig. 18d reveal that both thermo-mechanical and purely mechanical processes can completely close the residual cracks. For the elastic moduli and thermal expansion parameters of this sandstone, mechanical axial compression produces more axial deformation (ε_1) than cooling. The stress-strain diagrams also show that the strain energy needed to close residual cracks by mechanical compression is slightly larger than the energy needed to close residual cracks by cooling. In other words, mechanical compression is less work-efficient than cooling to close the cracks.

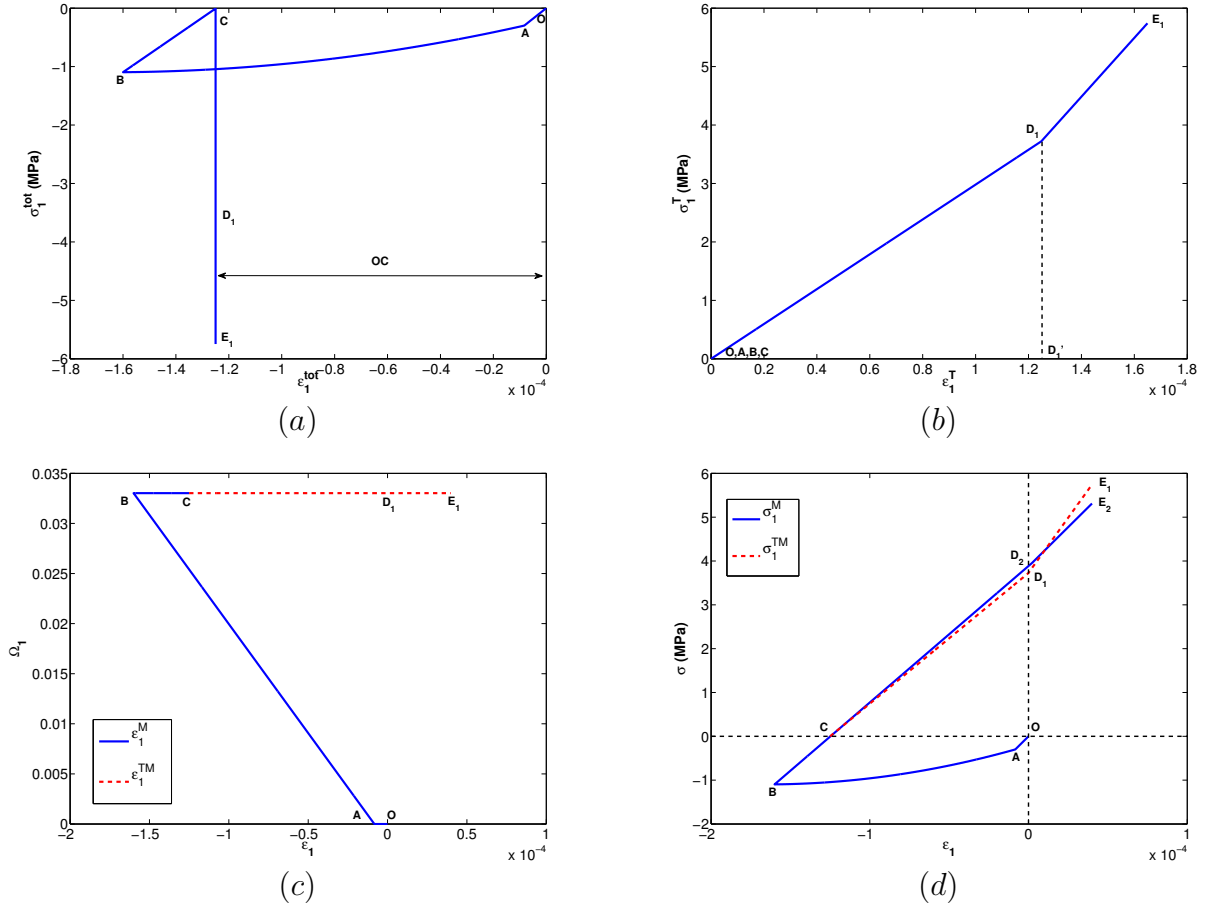


Figure 18 Simulation of the thermo-mechanical stress paths described in Fig. 17: (a) total stress vs. axial deformation (crack closure by cooling); (b) thermal stress vs. thermal strain: length of OC equals to length of OD₁'(crack closure by cooling); (c) evolution of axial damage (direction 1) vs. axial deformation (TM – closure by cooling; M – closure by compression); (d) evolution of stress components with axial deformation (TM – closure by cooling; M – closure by compression).

3.3 Diffusive Mass Transfer (DMT)-based Healing Model

3.3.1 Microstructure Characterization

The thermo-mechanical model presented above allows predicting the mechanical effects of crack debonding, opening and closure with a minimum set of parameters. However, crack rebonding and subsequent stiffness recovery was not represented, and the damage variable was purely phenomenological. In the following, we aim to overcome these two shortcomings by introducing a healing variable that represents mechanical recovery induced by solid diffusion. Solid diffusion in the salt crystal is expected to result in the rebonding of inter-crystalline cracks. Ideally, micrographs acquired at successive stages of the healing process could inform and constrain our mechanical model. Unfortunately, such data is not available in the literature for salt rock. Therefore, we propose to generate our own dataset from an analog material, table salt, which has the same crystallographic structure and halite content as salt rock. In the proposed model, we represent inter-granular space as cracks.

Observations are made in table salt in order to find mathematical descriptors that can be used as parameters to model microstructure changes that occur during creep processes. In the experiment described below, salt grains were confined in tubes with both ends fixed by nails. The tubes were placed in a chamber with controlled moisture conditions, at room temperature (Fig. 19). Constant humidity was ensured by adding saturated salt water to the bottom of the container, as explained in Wexler and Hasegawa (1954). Three constant loads (0.1MPa, 0.15MPa, and 0.2MPa) were applied through the compression of springs of same rigidity. Constant stress could be maintained since the deformed spring length was almost unchanged throughout the test.

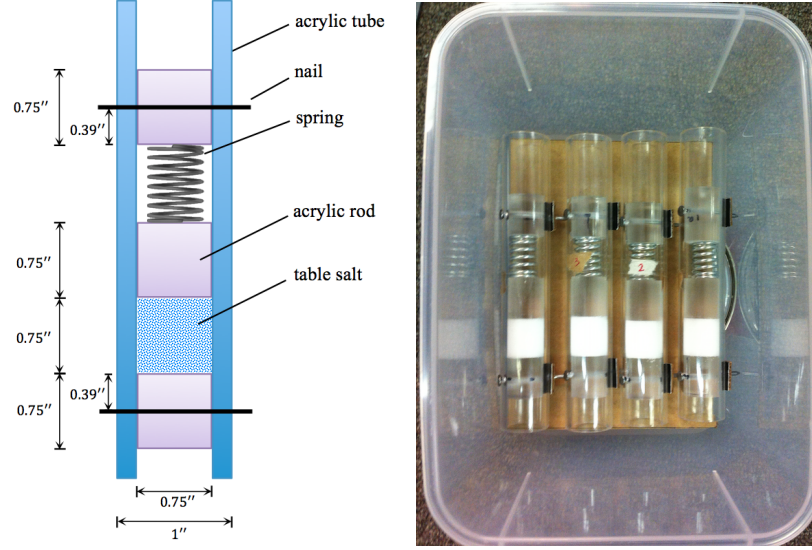


Figure 19 Experimental set up for observation of creep in salt.

Microscopic images of salt were recorded at regular time intervals. *ImageJ* application (Abràmoff et al., 2004) was used for image processing. Fig. 20 presents the principle of the image analysis. Transparent salt particles reflect light at their planar surfaces during the stereoscopic observation, which impaired the quality of the images. After enhancing the contrast and removing the background, a binary image was obtained. Removing outliers and filtering steps helped achieving an image of better quality. The black regions indicate the presence of void space between salt grains. Quantitative geometrical analysis was then carried out to determine appropriate fabric descriptors.

Through testing of several shapes, fitting ellipses presented the best match with void contours. Statistical results indicated that the probability density function of ellipses' area ("Void area", A_v) follows a power law distribution (Fig. 21a):

$$p_A(A_v) = a \cdot A_v^t \quad (18)$$

For high values of A_v , it was found that the power law did not fit the experimental data as well as for smaller values of A_v , but the error was found acceptable. Fitting

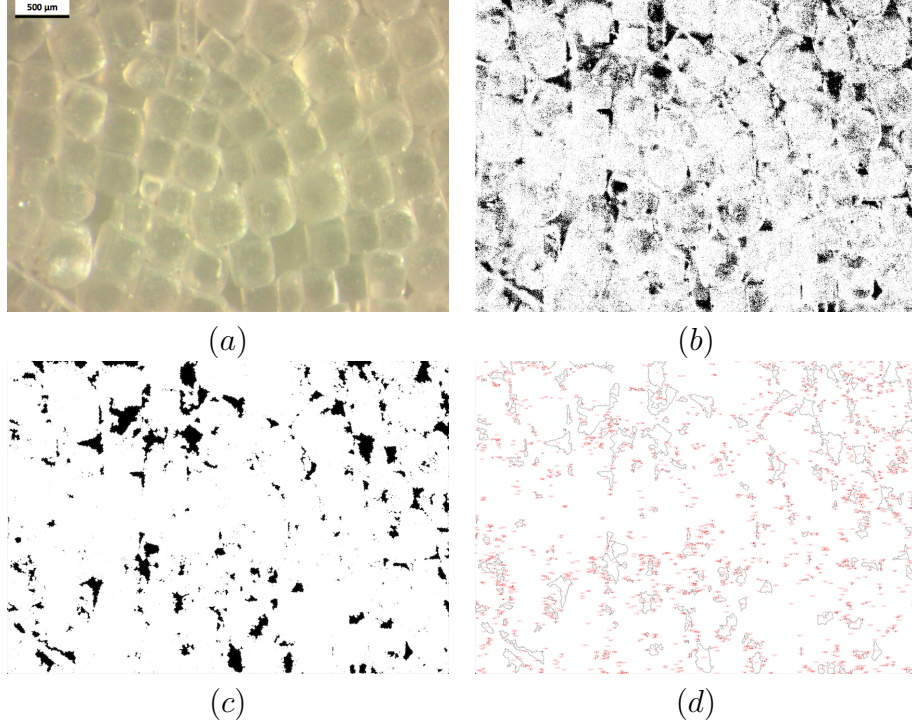


Figure 20 Image processing: (a) Stereo-microscopic image; (b) Binary image; (c) Void distribution; (d) Void outline (contours). Salt grains have a transparent cubic structure with flat surfaces. The resulting transmitted and reflected light significantly impair the microscopic image quality (Fig. 20a). Image processing techniques have been proposed in MATLAB and *ImageJ* to improve the grain boundary detection (Zhu et al., 2015b). We will continue to work on these issues in our future work. Possible approaches include using colored epoxy to enhance the grain-void interfaces and cutting the sample into thin sections.

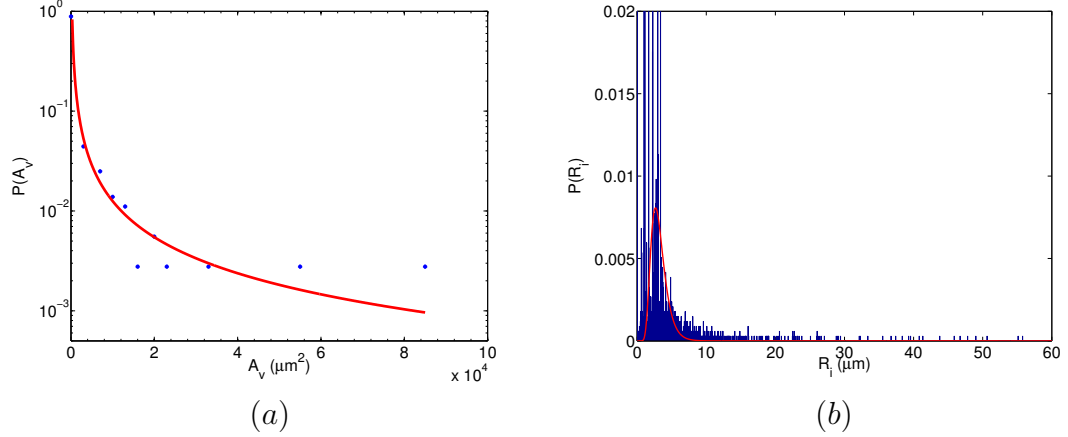


Figure 21 Probability density functions obtained for the void area (A) and for the crack length (defined as the major semi-axis of fitting ellipses projected in the three directions of space: R_i , $i=x,y,z$). (a) Power-law distribution of void area $p(A)$; (b) Log-normal distribution of crack length $p(R_i)$. *Note that the spikes are due to the presence of small black dots in the binary image obtained after processing.*

of microscopic data provided: $a = 5 \times 10^{-5}$ and $t = -1.2$. Despite the existence of several spikes, the projections of the major semi-axes in three principal directions of space (referred to as “crack length” in the following: R_i , $i = x, y, z$) were found to follow a lognormal distribution (Fig. 21b):

$$p_i(R_i) = \frac{1}{\sqrt{2\pi}R_i s_i} e^{-\frac{(\ln R_i - m_i)^2}{2s_i^2}} \quad (19)$$

in which s_i is the standard deviation and m_i is the mean value.

The main purpose of our experiment work is to infer the appropriate microstructure descriptors and bridge the gap between microscopic phenomenon and macroscopic response. We study the effects of different governing factors such as loading, temperature, and humidity conditions. It should be noted that further testing is required to test the reproducibility of these experiments.

3.3.2 Theoretical Framework

A model is proposed to couple microscopic and macroscopic thermo-mechanical evolution laws, in order to capture the effects of grain interface debonding, opening,

closure and rebonding, on deformation and stiffness. Table 5 summarizes the outline of the CDM model used as a basis to study healing driven by Diffusion Mass Transfer (DMT).

3.3.2.1 Continuum Damage Model

The free energy of the solid skeleton is written as the the sum of the purely thermo-elastic deformation energy (ψ_s^{ET}) and the potential energy of crack faces ($\psi_s^{\Omega T}$). The latter depends on a second-order tensor of damage (Ω), and on a damage-induced deformation (ϵ^d). Thermodynamic conjugation relationships give the stress and the damage driving force. Like in the thermo-mechanical damage model presented above, a dimensional analysis shows that the quadratic term in temperature $\frac{\tau^2}{2\tau_0} \frac{\partial C(\Omega)}{\partial \Omega}$ is negligible. For simplicity, it is assumed that the damage criterion is independent of temperature variation. The active damage driving force (\mathbf{Y}_d) is further simplified as a function of total strain only. To capture the hardening phenomenon, which accounts for the release of energy needed for growth of microcracks, the damage criterion is expressed in the form of a norm minus the damage threshold (Table 5). Following the classical CDM assumption recalled in the previous sections (Arson and Gatmiri, 2009, 2012; Dragon et al., 2000; Shao and Rudnicki, 2000), the damage flow rule is assumed to be associative, i.e. f_d is used as the damage potential:

$$d\Omega = d\lambda_d \frac{\partial f_d(\mathbf{Y}_d, \Omega)}{\partial \mathbf{Y}_d} = \frac{\left[\frac{\mathbf{Y}_d}{\sqrt{2\mathbf{Y}_d : \mathbf{Y}_d}} \right] : d\mathbf{Y}_d}{a_1 \delta : \left[\frac{\mathbf{Y}_d}{\sqrt{2\mathbf{Y}_d : \mathbf{Y}_d}} \right]} : \left[\frac{\mathbf{Y}_d}{\sqrt{2\mathbf{Y}_d : \mathbf{Y}_d}} \right] \quad (20)$$

Like in the thermo-mechanical damage model described previously, Chaboche's (1992a) approach is used to account for the unilateral effects induced by crack closure.

3.3.2.2 DMT-induced Healing

Healing by crack rebonding does not occur upon mechanical closure. An energy input is required to trigger the migration of ions within the lattice, and is therefore a dissipative process independent from damage. DMT is the main driving factor

for crack rebonding at low temperature. Cracks tend to be sealed by different ionic species at the crack faces. Intra-granular diffusion is assumed to be an isotropic phenomenon because of the uniform distribution of grain orientations. The healing tensor \mathbf{H} reduces to a scalar h : $\mathbf{H} = h\boldsymbol{\delta}$. Healing is time-dependent, whereas damage is a rate-independent dissipation variable which accounts for instantaneous grain interface debonding and opening. Kuhn-Tucker consistency conditions impose that damage cannot decrease. In order to represent the difference between damage and healing, a mixed damage variable \mathbf{A} is introduced as (Table 5)

$$\mathbf{A} = \boldsymbol{\Omega} - \boldsymbol{\delta}h \quad (21)$$

The expressions of the recovered stiffness and heat capacity now depend on \mathbf{A} instead of $\boldsymbol{\Omega}$. The kinetics of healing are assumed to be governed by a general diffusion equation:

$$\frac{\partial u}{\partial t} = D_c \nabla^2 u \quad (22)$$

in which D_c is the diffusion coefficient, which is considered constant in our model, u represents the “intensity of net damage”, defined as

$$u = U_0 - h \quad (23)$$

in which U_0 is the intensity of damage in the REV before healing occurs: $U_0 = \text{tr}(\boldsymbol{\Omega})_{t=0}$. In our model, we constrain the healing variable h to be smaller than the initial damage intensity U_0 . However, in reality, the material can achieve a larger strength through the healing process, i.e., $h > U_0$.

Crack healing is considered as complete when an ion reaches a crack face and electronic forces bonds this ion to the lattice of the opposite crack face. Therefore, the maximum diffusion distance within a salt grain is equal to half of the edge length of the grain. At the boundaries, the net damage is taken as zero. The initial conditions for healing in the REV are:

$$h(x, t = 0) = 0, \quad u(x, t = 0) = U_0 \quad (24)$$

Table 5 Outline of thermo-mechanical damage and healing model.

Postulates	
Free Energy for Crack Opening (Ψ_S)	$\psi_s = \psi_s^{ET} + \psi_s^{\Omega T}$ $\psi_s^{ET} = \frac{1}{2} \boldsymbol{\varepsilon}^{el} : \mathbb{C}_0 : \boldsymbol{\varepsilon}^{el} - \frac{C_0 \tau^2}{2\tau_0} - \tau \mathbf{K}_0 : \boldsymbol{\varepsilon}^{el}$ $\psi_s^{\Omega T} = \frac{1}{2} \boldsymbol{\varepsilon}^d : \mathbb{C}(\boldsymbol{\Omega}) : \boldsymbol{\varepsilon}^d - \frac{C(\boldsymbol{\Omega}) \tau^2}{2\tau_0} - \tau \mathbf{K}(\boldsymbol{\Omega}) : \boldsymbol{\varepsilon}^d$ $\frac{1}{2} \boldsymbol{\varepsilon}^d : \mathbf{D}(\boldsymbol{\Omega}) : \boldsymbol{\varepsilon}^d = \frac{1}{2} \lambda (tr \boldsymbol{\varepsilon}^d)^2 + \mu tr(\boldsymbol{\varepsilon}^d \cdot \boldsymbol{\varepsilon}^d) + \alpha tr \boldsymbol{\varepsilon}^d tr(\boldsymbol{\varepsilon}^d \cdot \boldsymbol{\Omega}) + 2\beta tr(\boldsymbol{\varepsilon}^d \cdot \boldsymbol{\varepsilon}^d \cdot \boldsymbol{\Omega})$
Free Energy for Crack Closure (Ψ_S)	$\psi_s = [\frac{1}{2} \boldsymbol{\varepsilon}^{el} : \mathbb{C}_0 : \boldsymbol{\varepsilon}^{el} - \frac{C_0 \tau^2}{2\tau_0} - \tau \mathbf{K}_0 : \boldsymbol{\varepsilon}^{el}] + [\frac{1}{2} \boldsymbol{\varepsilon}^d : \mathbb{C}^*(\boldsymbol{\Omega}) : \boldsymbol{\varepsilon}^d - \frac{C^*(\boldsymbol{\Omega}) \tau^2}{2\tau_0} - \tau \mathbf{K}^*(\boldsymbol{\Omega}) : \boldsymbol{\varepsilon}^d]$ $\mathbb{C}^*(\boldsymbol{\Omega}) = \mathbb{C}(\boldsymbol{\Omega}) + \sum_{i=1}^3 H(-tr(\mathbf{P}_i : \boldsymbol{\varepsilon})) \mathbf{P}_i : (\mathbb{C}_0 - \mathbb{C}(\boldsymbol{\Omega})) : \mathbf{P}_i, \quad 0 < \eta \leq 1$ $\mathbf{K}^*(\boldsymbol{\Omega}) = \mathbf{K}(\boldsymbol{\Omega}) + \sum_{i=1}^3 H(-tr(\mathbf{P}_i : \boldsymbol{\varepsilon})) \mathbf{P}_i : (\mathbf{K}_0 - \mathbf{K}(\boldsymbol{\Omega})) : \mathbf{P}_i, \quad 0 < \eta \leq 1$ $C^*(\boldsymbol{\Omega}) = C(\boldsymbol{\Omega}) + \sum_{i=1}^3 H(-tr(\mathbf{P}_i : \boldsymbol{\varepsilon})) \mathbf{P}_i : [(C_0 - C(\boldsymbol{\Omega})) \boldsymbol{\delta} \otimes \boldsymbol{\delta}] : \mathbf{P}_i, \quad 0 < \eta \leq 1$
Free Energy for Crack Rebonding (Ψ_S)	<p>Replace $\boldsymbol{\Omega}$ by \mathbf{A} in the free energy for crack closure</p> $\mathbf{A} = \boldsymbol{\Omega} - \boldsymbol{\delta} h$
Damage Criterion (f_d)	$f_d(\mathbf{Y}_d^+, \boldsymbol{\Omega}) = \sqrt{\frac{1}{2} \mathbf{Y}_d^+ : \mathbf{Y}_d^+} - (a_0 + a_1 \boldsymbol{\Omega})$
Strain Decomposition	$\boldsymbol{\varepsilon} = \boldsymbol{\varepsilon}^E + \boldsymbol{\varepsilon}^{id} = \boldsymbol{\varepsilon}^{el} + \boldsymbol{\varepsilon}^d = \boldsymbol{\varepsilon}^{el} + \boldsymbol{\varepsilon}^{ed} + \boldsymbol{\varepsilon}^{id}$
Diffusion Equation	$\bar{u}(t) = \langle u(x, t) \rangle = \frac{1}{l} \int_0^l u(x, t) dx = \frac{8U_0}{\pi l} \sum_{n=1,3,5,\dots}^{\infty} \frac{e^{-\lambda_n^2 D_c t}}{n \lambda_n}$ $D_c = D_{c0} e^{-\frac{Q}{RT}}$ $h(t) = 1 - \bar{u}(t)$
Conjugation Relationships	
Stress ($\boldsymbol{\sigma}$)	$\boldsymbol{\sigma} = \frac{\partial \psi_s}{\partial \boldsymbol{\varepsilon}^{el}} = \frac{\partial \psi_s^{ET}}{\partial \boldsymbol{\varepsilon}^{el}} = \mathbb{C}_0 : \boldsymbol{\varepsilon}^{el} - \tau \mathbf{K}_0$
Damage Driving Force (\mathbf{Y}_d)	$\mathbf{Y} = -\frac{\partial \psi_s}{\partial \boldsymbol{\Omega}} = -[\mathbb{C}(\boldsymbol{\Omega}) : \boldsymbol{\varepsilon}^d] : \frac{\partial \boldsymbol{\varepsilon}^d}{\partial \boldsymbol{\Omega}} - \frac{1}{2} \boldsymbol{\varepsilon}^d : \frac{\partial \mathbb{C}(\boldsymbol{\Omega})}{\partial \boldsymbol{\Omega}} : \boldsymbol{\varepsilon}^d + \frac{\tau^2}{2\tau_0} \frac{\partial C(\boldsymbol{\Omega})}{\partial \boldsymbol{\Omega}}$ $+ \tau \mathbf{K}(\boldsymbol{\Omega}) : \frac{\partial \boldsymbol{\varepsilon}^d}{\partial \boldsymbol{\Omega}} + \tau \frac{\partial \mathbf{K}(\boldsymbol{\Omega})}{\partial \boldsymbol{\Omega}} : \boldsymbol{\varepsilon}^d$ $\mathbf{Y}_d = -(\alpha + 2\beta) \boldsymbol{\varepsilon} \cdot \boldsymbol{\varepsilon}$
\mathbb{C} = damaged stiffness tensor	a_0 = initial damage threshold
\mathbb{C}^* = effective stiffness tensor after “partial recovery”	a_1 = damage hardening parameter
\mathbf{K}^* = effective diagonal tensor after “partial recovery”	C^* = effective heat capacity after “partial recovery”

Therefore, the solution can be written as follows:

$$u(x, t) = \frac{4U_0}{\pi} \sum_{i=1,3,5,\dots}^{\infty} \frac{e^{-\lambda_n^2 D_c t} \sin(\lambda_n x)}{n} \quad (25)$$

in which $\lambda_n = \frac{n\pi}{l}$. The space average of the density of net damage $\bar{u}(t)$ is given in Table 5. The diffusion coefficient D_c depends on both pressure and temperature, following the constitutive model proposed in Weertman (1955). It requires more activation energy for a chloride ion to jump into a chloride vacancy than for a sodium ion to jump into a sodium ion vacancy (Mapother et al., 1950). So it can be reasonably assumed that migration of sodium ions dominates the diffusion of sodium chloride. Based on Mapother's study on the temperature dependence of the self-diffusion coefficient D_c of sodium (for a temperature range of $573K \sim 973K$), the following logarithmic relationship is adopted:

$$D_c = -\frac{1.67 \times 10^{-12}}{T} + 2.99 \times 10^{-15} \quad (26)$$

in which T is expressed in Kelvin, and D_c is expressed in m^2/s .

3.3.2.3 Upscaling Method

Grain cementation is considered as the analog of crack rebonding. In the upscaling method proposed in the following, damage and healing fabric tensors are defined as moments of probability of microstructure descriptors determined above by image analysis. Microscopic cracks are thus modeled as oblate spheroids, oriented perpendicular to the loading axis (Fig. 22). The analogy to link microstructure changes and phenomenological variables is established as follows:

- (1) During elastic loading or unloading, only crack aperture varies.
- (2) When damage occurs, the crack length increases. Note that we assumed that the number of cracks was kept constant.
- (3) Healing only occurs when the deformation in the loading direction is compressive. During healing, the crack length decreases whereas the aperture remains constant.

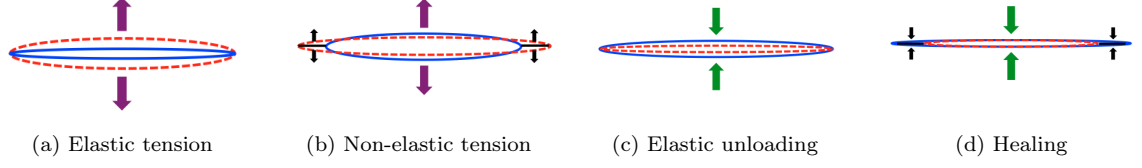


Figure 22 Representation of the geometric evolution of micro-cracks in the proposed model (solid line - original shape; dashed line - deformed shape): (a) Elastic tension: $\Delta\lambda_a \neq 0$, $\Delta R = 0$; (b) Non elastic tension: $\Delta\lambda_a \neq 0$, $\Delta R \neq 0$; (c) Elastic unloading (compression): $\Delta\lambda_a \neq 0$, $\Delta R = 0$; (d) Healing (after closure): $\Delta\lambda_a = 0$, $\Delta R \neq 0$.

The concept of crack density tensor is adopted to account for the difference of crack length in the three directions of space. Assuming that the principal directions of stress and net damage are parallel, net damage eigenvalues (\mathbf{A}) are related to the means of the crack length components (R_j) as presented in Table 6. Standard deviations are considered constant, because sensitivity analyses showed that it does not vary significantly under the pressure and temperature conditions of the creep tests presented. In the adopted micro-macro computational method (Zhu and Arson, 2014a), only the means m_i are updated, according to the relationships established in Arson and Pereira (2013). After some computations, it was shown that the probability density function of R_j can be updated from the macroscopic strain as follows:

$$\Delta\epsilon \xrightarrow{\text{Table 5}} \Delta\mathbf{A} \xrightarrow{\text{Table 6}} \overline{R}_1, \overline{R}_2, \overline{R}_3 \xrightarrow{\text{Table 6}} p_j(R_j) \quad (27)$$

Grains are considered incompressible, so that the volume change of the REV is equal to the porosity change. The variation of three-dimensional void volume cannot be captured by microscopic observation. A linear interpolation is used to correlate 3D porosity with 2D porosity. Based on the expressions of the lower and upper bounds of 2D and 3D porosities (Zhu and Arson, 2014a), the probability density function of void areas are updated as follows:

$$\Delta\epsilon \rightarrow \Delta n_{3D} \xrightarrow{\text{Table 6}} \Delta n_{2D} \xrightarrow{\text{Table 6}} p_A(A_v) \quad (28)$$

The lower bound of porosity is obtained at maximum packing. Salt grains tend to rearrange and form an ordered pattern. However, voids exist even at the maximum

packing state since particles do not have a perfect cubic shape. In this ordered configuration, the lower bound of porosity is obtained by assuming that inter-granular voids are spheres. The upper bound of porosity is reached at the initial stage, when salt particles are assembled in a loose packing before the creep test starts. The 2D porosity was obtained through microscopic observation. The 3D porosity was approximated from experimental measures of sample deformation. Using the strain decomposition, the stress tensor is expressed as:

$$\boldsymbol{\sigma} = \mathbb{C}_0 : \boldsymbol{\varepsilon}^{el} - \tau \mathbf{K}_0 = \mathbb{C}(\boldsymbol{\Omega}) : \underbrace{(\boldsymbol{\varepsilon}^{el} + \boldsymbol{\varepsilon}^{ed})}_{\boldsymbol{\varepsilon}^E} - \tau \mathbf{K}(\boldsymbol{\Omega}) \quad (29)$$

The stress rate under isothermal conditions is obtained as follows:

$$d\boldsymbol{\sigma} = \mathbb{C}(\boldsymbol{\Omega}) : d\boldsymbol{\varepsilon} + \frac{\partial \mathbb{C}(\boldsymbol{\Omega})}{\partial \boldsymbol{\Omega}} : \boldsymbol{\varepsilon} : d\boldsymbol{\Omega} - d(\mathbb{C}(\boldsymbol{\Omega}) : \boldsymbol{\varepsilon}^{id}) = \mathbb{C}(\boldsymbol{\Omega}) : d\boldsymbol{\varepsilon} + \frac{\partial \mathbb{C}(\boldsymbol{\Omega})}{\partial \boldsymbol{\Omega}} : \boldsymbol{\varepsilon} : d\boldsymbol{\Omega} + d\boldsymbol{\sigma}_R \quad (30)$$

Table 6 Relations between microscopic and macroscopic variables.

Relation between Fabric Descriptors and Phenomenological Variables	
\mathbf{R} and \mathbf{A}	$\mathbf{A} = \sum_{j=1}^3 A_j \mathbf{e}_j \otimes \mathbf{e}_j$, $A_1 = N_v \frac{(\bar{R}_2 \bar{R}_3)^{\frac{3}{2}}}{V_{REV}}$, $A_2 = N_v \frac{(\bar{R}_1 \bar{R}_3)^{\frac{3}{2}}}{V_{REV}}$, $A_3 = N_v \frac{(\bar{R}_1 \bar{R}_2)^{\frac{3}{2}}}{V_{REV}}$ $\bar{R}_j = \int R_j p_j(R_j) dR_j$
n_{3D} and A_v	$\frac{n_{3D} - n_{3D,lower}}{n_{3D,upper} - n_{3D,lower}} = \frac{n_{2D} - n_{2D,lower}}{n_{2D,upper} - n_{2D,lower}}$ $n_{2D,lower} = \frac{A_{v,lower}}{A_{REV}} = \frac{\pi r^2}{l^2}$, $n_{3D,lower} = \frac{V_{v,lower}}{V_{REV}} = \frac{\frac{4}{3}\pi r^3}{l^3}$ $n_{2D,upper} = \frac{A_{v,upper}}{A_T}$, $n_{3D,upper} = \frac{V_{v,upper}}{V_T}$, $V_{v,upper} = V_T - V_s = A_{tube} \cdot L_{upper} - \frac{m_s}{\rho_s}$ $\bar{n}_{2D} = \int \frac{A_v}{A_{REV}} p_A(A_v) dA$
Relation between Fabric Descriptor and Residual Stress	
$\boldsymbol{\sigma}_R$ and R , A_v	$\boldsymbol{\sigma}_R = N_v \boldsymbol{\sigma}_r = N_v \frac{2\sqrt{2}}{\pi} \frac{\mu}{\kappa+1} \frac{A_v}{R^2}$
\bar{R}_j	= mean value of crack length
$n_{2D,lower}$	= lower bound of 2D porosity
$n_{3D,lower}$	= lower bound of 3D porosity
$n_{2D,upper}$	= upper bound of 2D porosity
$n_{3D,upper}$	= upper bound of 3D porosity
V_s	= volume of the salt solid
ρ_s	= density of the salt solid
m_s	= mass of the salt solid
A_j	= net damage in principal direction j
V_{REV}	= volume of REV
$\boldsymbol{\sigma}_R$	= macroscopic residual stress for N_v cracks
$\boldsymbol{\sigma}_r$	= macroscopic residual stress for single crack
A_T	= longitudinal cross-sectional area of sample cylinder
V_T	= total volume of the sample cylinder
A_v	= void area
A_{tube}	= inner cross-sectional area of tube

Micro-cracks are assumed to be non-interacting, so that the zone of influence of each crack (in the surrounding solid matrix) is considered to be constituted of an isotropic linear elastic material. Thus we ignore microscopic crack coalescence and the resulting macroscopic fracture propagation. Note that our goal is to capture the

macroscopic damage behavior of the material and to correlate it with microcrack descriptors. The theory of fracture mechanics (Anderson, 2005) is used to compute the micro-crack opening vector of an ellipsoidal micro-crack propagating in mode I (Fig. 23). The micro-crack displacement in the direction perpendicular to the micro-crack axis is expressed as:

$$u_y(r, \theta) = \frac{K_I}{2\mu} \sqrt{\frac{r}{2\pi}} \sin\left(\frac{\theta}{2}\right) [\kappa + 1 - 2\cos^2\left(\frac{\theta}{2}\right)] \quad (31)$$

in which u_y is half of the crack aperture at location (r, θ) , K_I is the stress intensity factor in mode I at the crack tip ($r = 0$), and μ is the shear modulus of the linear elastic bulk material. κ depends on the bulk Poisson's ratio ν . K_I depends on the microscopic residual stress that applied to the micro-crack faces: $K_I = \sigma_r \sqrt{\pi R}$. The half aperture $0.5\lambda_a$ defined above is equal to the displacement u_y when $\theta = \pi$ and $r = R$, in which R is half of the crack length:

$$\frac{1}{2}\lambda_a = \frac{\kappa + 1}{2\sqrt{2\mu}} R \sigma_r \quad (32)$$

With the void area $A_v = 0.5\pi\lambda_a R$, the macroscopic residual stress for N_v micro-cracks can be obtained (Table 6).

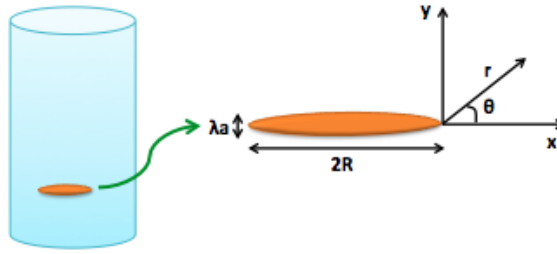


Figure 23 Schematic representation of a micro-crack subjected to residual stress within the REV

The probability density functions of fabric descriptors are updated with deformation and damage (Eq. 27 and 28). Then the residual stress is updated based on those descriptors. The determination of the residual stress requires the computation of the mean of the probability $p(A_v/R_j R_k)$. Details are provided in Appendix II.

The relations between fabric descriptors and macroscopic variables are summarized in Table 6. Fig. 24 describes the computational method used to update macroscopic variables from the knowledge of microscopic descriptors.

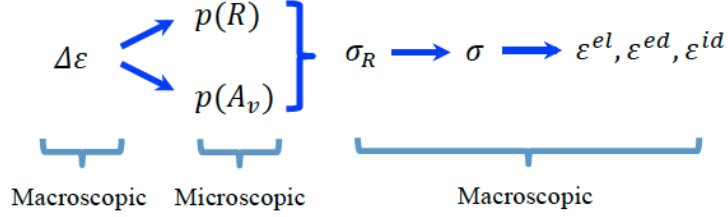


Figure 24 Computation method to update macroscopic variables through the update of microscopic descriptors.

3.3.3 Crack Opening, Closure and Rebonding during a Uniaxial Test

The macroscopic damage and healing model depends on seven mechanical parameters $\lambda, \mu, \alpha, \beta, g, C_0, C_1$ and one thermal parameter α_T . In the absence of relevant quantitative experimental datasets, macroscopic parameters could not be calibrated for salt rock. For illustrative purposes, a set of parameters fitted for sandstone (Zhu and Arson, 2014b) is employed in the following simulations. The microscopic parameters are determined as follows:

- (1) The solution of the diffusion equation (Table 5) is normalized ($U_0 = 1$), and D_c is computed according to Eq. 26.
- (2) $n_{2D,lower}, n_{2D,upper}, n_{3D,lower}, n_{3D,upper}, l$ are computed by using data obtained from microscopic observation.
- (3) The bounds of the fabric descriptors ($A_{min}, A_{max}, R_{min}, R_{max}$) are estimated, by referring to the actual grain size and initial simulation results.
- (4) The exponent of the power-law distribution of the void area (Eq. 18) is determined from microscopic observation: $t = -1.2$.
- (5) The number of voids N_v and the standard deviations of the distributions of crack

length components (s_1, s_2, s_3) are computed in the initialization phase of the algorithm, and then kept constant.

(6) The means of void area and crack length components (a, m_1, m_2, m_3) are updated with the macroscopic phenomenological variables.

Table 7 summarizes the model parameters used in the simulations. Note that the soil mechanics sign convention is adopted, with tension counted negative.

Numerical simulations are performed to study the influence of temperature on the healing process leading to mechanical recovery during the stress path shown in Fig. 25. Mechanical loading and unloading before and after the healing process are simulated for a room temperature $T_{room} = 293K$, whereas the healing process is taking place at a higher temperature T_{heal} . In the simulations, healing is occurring at constant axial strain, under zero lateral stress, and under constant temperature. Table 8 summarizes the simulation plan for this sensitivity analysis. Scenario 1 is taken as the reference case with a 10,000 second-healing period (about 3 hours) at temperature $T_{heal} = 593K$. The influence of temperature is studied with scenarios 2 and 3. The diffusion coefficient is updated with temperature according to Eq. 26.

Table 7 Model parameters used for the simulation of strain-controlled uniaxial tension loading/unloading/healing.

λ (Pa)	μ (Pa)	α (Pa)	β (Pa)	g (Pa)	C_0 (Pa)	C_1 (Pa)	$\alpha_T(K^{-1})$	$U_0(-)$	l (m)
2.63×10^{10}	1.75×10^{10}	1.9×10^9	-2.04×10^{10}	1.1×10^8	1000	2.5×10^5	-1×10^{-5}	1	1×10^{-4}
$n_{2D,lower}(-)$	$n_{2D,upper}(-)$	$n_{3D,lower}(-)$	$n_{3D,upper}(-)$	$t(-)$	$R_{min}(m)$	$R_{max}(m)$	$A_{min}(m^2)$	$A_{max}(m^2)$	$e_0(-)$
0.03	0.165	0.004	0.321	-1.2	1×10^{-5}	1×10^{-4}	1×10^{-14}	1×10^{-12}	0.008

Table 8 Simulation plan for DMT-based healing model.

Scenario	Duration (s)	T_{heal} (K)	D_c (m^2/s)
1 (ref)	10,000	593	1.74×10^{-16}
2	10,000	643	3.93×10^{-16}
3	10,000	693	5.80×10^{-16}

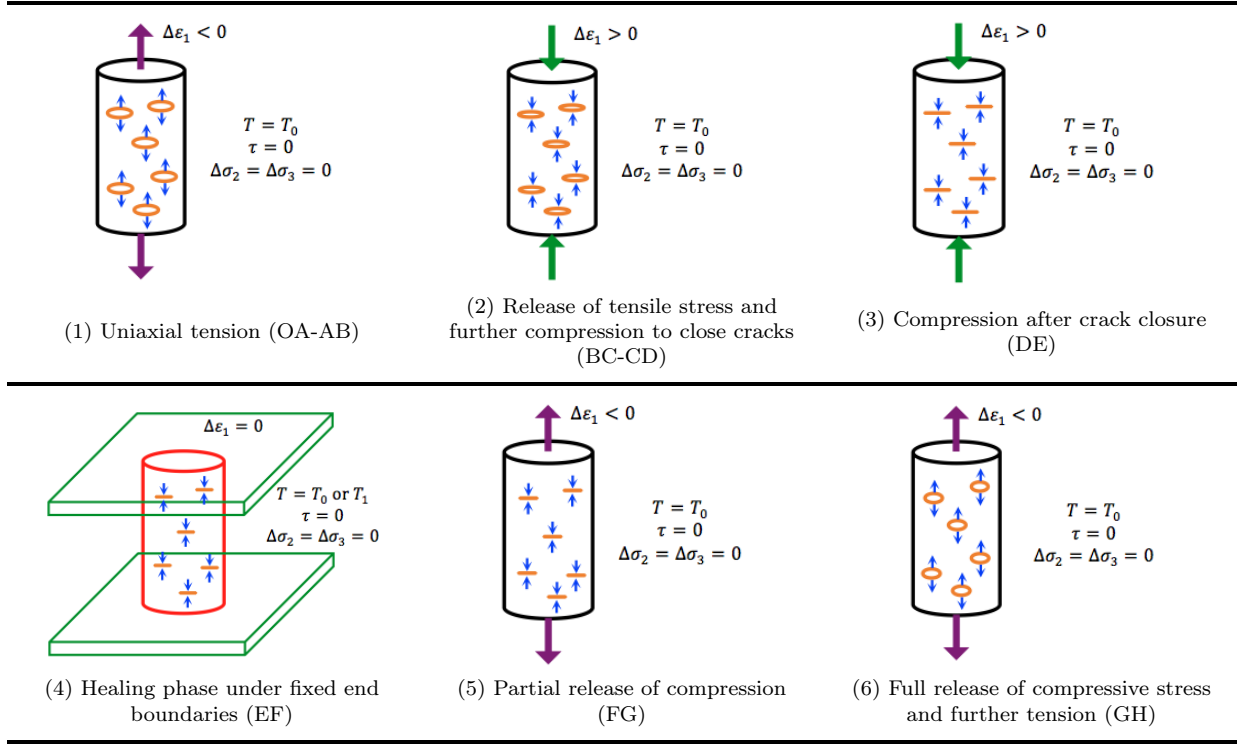


Figure 25 Stress path simulated to study thermo-mechanical crack opening, closure, and healing.

Parametric studies on the effect of temperature on healing are presented in Fig. 26. The evolution of macroscopic variables is presented, followed by the evolution of microscopic variables. The stress-strain plots obtained numerically (Fig. 26a) follow the expected trends: the slope first decreases due to damage propagation (AB); unilateral effects are noted during the compression phase (DE); internal compressive stress develops due to the restrained thermal expansion of the sample during the creep phase at high temperature (EF), and partial mechanical recovery is achieved after the healing phase (FG₁). Additional damage is produced after recovery (G₁H) when the new damage threshold is reached (larger than the initial threshold but smaller than the threshold obtained after the tension phase). The net damage variable (**A**) increases when damage increases, and decreases when healing increases (Fig. 26b). The model captures time-independent damage induced by thermo-mechanical tension or compression, and time-dependent healing under compression. Stiffness recovery is more important for higher healing temperatures.

Figures 26c & d show the evolution of the fabric descriptors for the stress paths simulated. Due to the axis-symmetry of the problem and by construction of the model, microscopic cracks propagate only in planes orthogonal to direction 1 (loading axis), therefore crack lengths are non-zero only in directions 2 and 3 ($\overline{R}_2 = \overline{R}_3 \neq 0$, $\overline{R}_1 = 0$). According to the definition of net damage, the evolution of crack lengths follows the evolution of net damage. The difference of convexity in Fig. 26c is due to the cubic relationship between the eigenvalues of net damage and crack length. The mean of void areas is proportional to the porosity of the sample, which is assumed to vary like the volumetric deformation. In the tests simulated, axial deformation is about three times larger than lateral deformation, therefore volumetric deformation mostly varies with axial deformation. As a result, the mean of the void area evolves quasi-linearly with axial deformation during the mechanical loading and unloading phases (Fig. 26d). During the healing phase, crack lengths shorten while crack apertures

remain constant (according to the modeling assumptions summarized in Fig. 22), therefore, overall the mean void area decreases. Note that the drop observed for the void area during the healing phase is equal to the drop of crack length times 10^{-9}m , which is the order of magnitude of the crack aperture. The link between microstructure changes and macroscopic variables is complex and will require further analyses with different stress paths and different fabric descriptors.

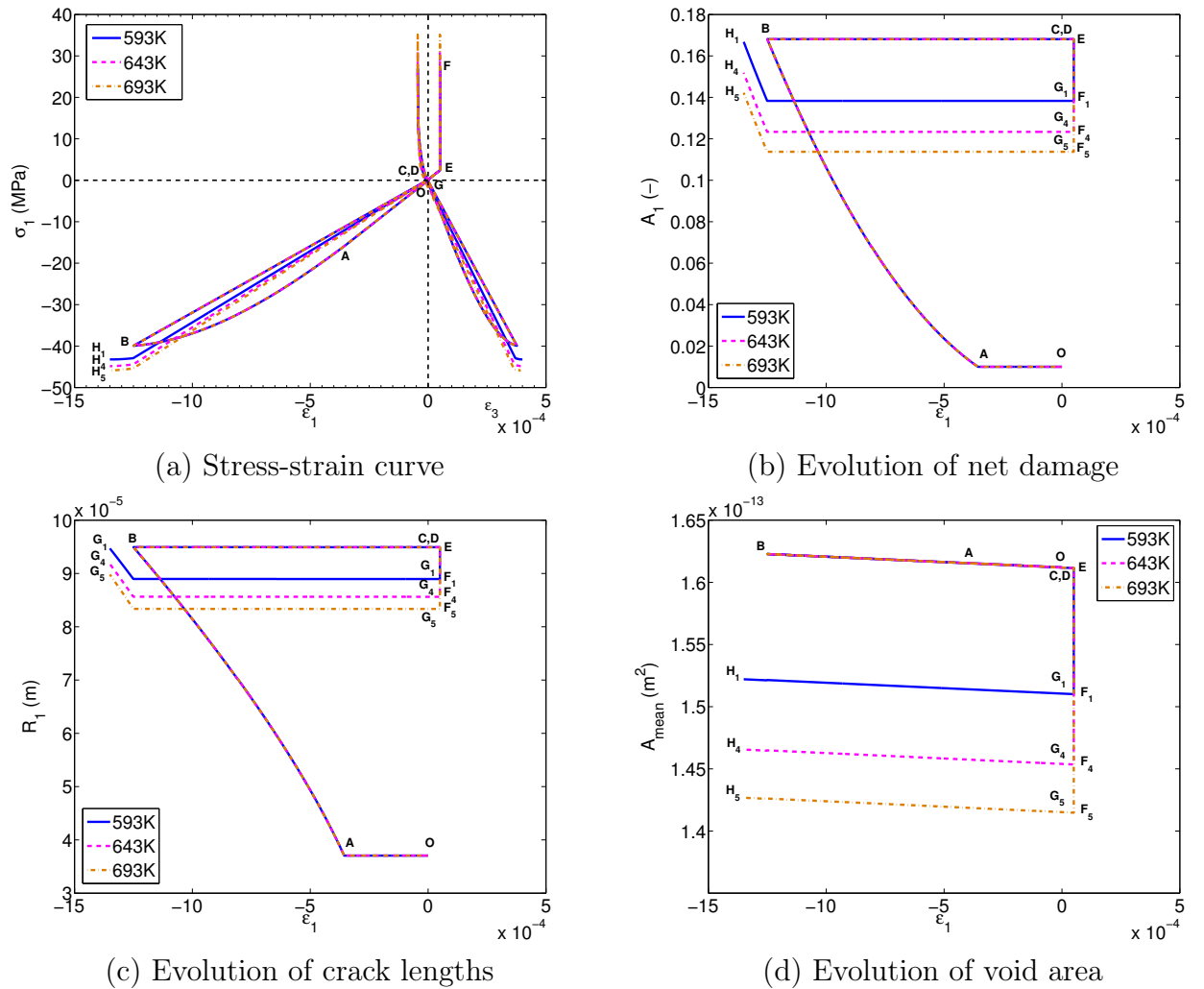


Figure 26 Influence of healing temperature on mechanical recovery (direction 1 is the direction of tensile loading).

3.4 *Anisotropic Healing Model*

3.4.1 2D Diffusion Controlled Healing

We now improve the model presented in Section 3.3 to account for the anisotropy caused by healing - and not only for the anisotropy caused by damage. Healing-induced anisotropy is expected to occur if the medium contains various population of cracks with different orientations and/or different normal displacement vectors (i.e., open vs. closed). In order to distinguish the cracks that heal from those that do not heal under a given state of stress and temperature, we calculate the crack cusp migration distance for three families of cracks represented by the damage eigenvalues. The microphysical model of crack cusp migration proposed by Houben et al. (2013), based on single crack healing experiments, is used for that purpose:

$$x = \left[\frac{DCV_{\Omega}(\gamma_{SL} + \gamma_{LV})}{\pi RT} \frac{\delta}{a} \frac{4\cos\frac{\theta}{2}}{\alpha^3} t \right]^{0.25} \quad (33)$$

in which D is the diffusion coefficient, C is the solubility, δ is the fluid film thickness, a is a characteristic length scale, $\alpha = \tan(\frac{\theta}{2})$ is the orientation of the crack face (in reference to the loading axis), V_{Ω} is the molecular volume of the solid, γ_{SL} is the solid-liquid interfacial energy, γ_{LV} is the liquid-vapor interfacial energy, R is the gas constant, T is the absolute temperature.

The intensity of damage U varies over the distance x ("lag") that separates the crack cusp and the point at which the crack is fully rebonded (Fig. 27). During the healing process, tubular and porous structures emerging in that lag area induce a partial mechanical recovery. These structures will gradually disappear over time (Houben et al., 2013).

We assume that healing starts at the circumference of crack planes. The crack cusp migrates towards the center of the crack region, according to a two-dimension diffusion process, which is expressed as

$$D_x \frac{\partial^2 U}{\partial^2 x} + D_y \frac{\partial^2 U}{\partial^2 y} = \frac{\partial U}{\partial t} \quad (34)$$

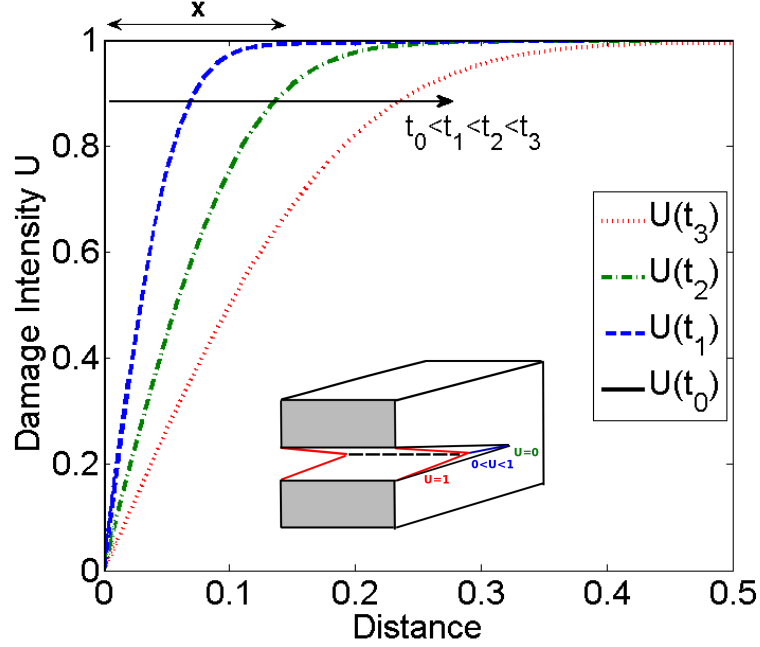


Figure 27 Schematic model of healing propagation front in a crack (crack cusp migration). Damage intensity U varies from 0 (bonded crack faces similar to an intact material with no crack) to 1 (closed but not bonded faces).

in which $U(x, y, t)$ is the damage intensity depending on position and time. D_x and D_y are the diffusion coefficients along x and y directions, respectively.

Diffusion in x and y directions affects crack planes perpendicular to the z direction, and therefore, the z component of the damage tensor. Fig. 28 shows the variations of damage intensity $U = \Omega z$ within a (x, y) crack plane. The lag distance is indicated by a solid line, over which the damage intensity varies from 0 (at the circumference) to 1 (towards to the center of the grain). The mean value of the damage intensity $\bar{U}(t)$ is

$$\int_0^{l_y} \int_0^{l_x} U(x, y, t) dx dy = \bar{U}(t) \cdot A \quad (35)$$

in which $A = l_x l_y$ is the crack face area ($A = 1$ for the normalized crack area).

We define the net damage tensor (\mathbf{A}) as the difference between the damage tensor ($\mathbf{\Omega}$) and the healing tensor (\mathbf{H}) as

$$A_i = \Omega_i - H_i = \Omega_i - H(\sigma_i)(1 - \bar{U}) \quad (36)$$

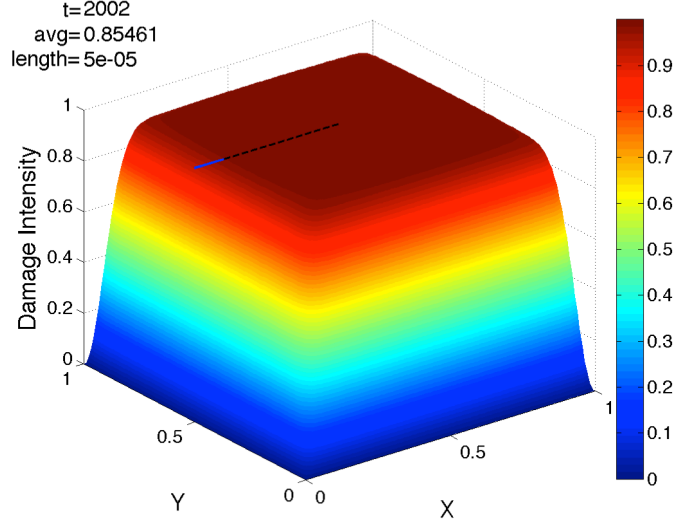


Figure 28 Distribution of damage intensity during the healing process within one planar crack. The evolution of the lag distance is governed by a 2D diffusion model.

in which $H(\sigma_i)$ is the Heaviside function depending on the stress sign. In our model, we assume that healing takes place in damage directions in which cracks faces are closed and subjected to local compressive stresses (which are known to enhance healing). Note that the Heaviside function is a function of the current stress state rather than the current stress rate. If a crack is subjected to tension unloading, the stress is negative whereas the stress rate is positive. Under such circumstance using stress rate may be inappropriate because crack faces are not closed and healing process has not started yet.

High temperature is not a necessary condition for healing to occur. In the presence of brine, thin adsorbed water films between crack faces will assist in accelerating the diffusion process. But higher temperature will provide more efficient healing (Zhu and Arson, 2014a).

Grain size is not directly accounted for in this framework. Alternatively, we use a characteristic length scale to indicate the effect of crack size on the healing process. Here, healing is assumed to be governed by diffusive mass transfer. Accounting for grain size is essential if we take into account other healing processes such as dissolution

and precipitation controlled pressure solution at the interfaces.

3.4.2 Model Calibration

We calibrated the diffusion-controlled healing model against the experimental data provided in Table 9. The first eight values are taken from (Houben et al., 2013; de Meer et al., 2005). α is the slope of the crack wall, which has the same order of magnitude as those values adopted in Houben et al. (2013). d is the diffusion distance, which is equal to the half of a typical crack size. D_x and D_y are parameters to be calibrated for the healing model. Since the structure of salt crystals is symmetric, we assume: $D_x = D_y$, which implies that healing occurs at the same rate along the x - and y -directions of each face. The lag $x(t)$ in Eq. 33 is the distance between a point at the circumference of the initial crack plane and a point at the circumference of the current crack plane, after healing has started. We considered that the position of the current crack circumference was at the point at which $U = 1 \pm 5\%$ (Fig. 27). We calibrated the diffusion coefficient in order to minimize the difference between the numerical and experimental values after 20,000 seconds of healing (i.e., about 5.6 hours). Despite some deviations induced by the technique we used to update the position of the crack circumference, the time evolution of the lag predicted with the calibrated model follows the trends observed experimentally (Fig. 29).

Table 9 Parameters adopted for the diffusion-controlled healing model (Eq. 33 and 34)

R ($JK^{-1}\text{mol}^{-1}$)	T (K)	D (m^2s^{-1})	C (-)
8.314	296	1.3e-9	0.1675
γ_{SL} (Jm^{-2})	γ_{LV} (Jm^{-2})	Ω ($m^3\text{mol}^{-1}$)	δ/a (-)
0.129	0.064	2.7e-5	9e-13
α	d (m)	D_x (m^2s^{-1})	D_y (m^2s^{-1})
2.5e-3	1e-4	9e-7	9e-7

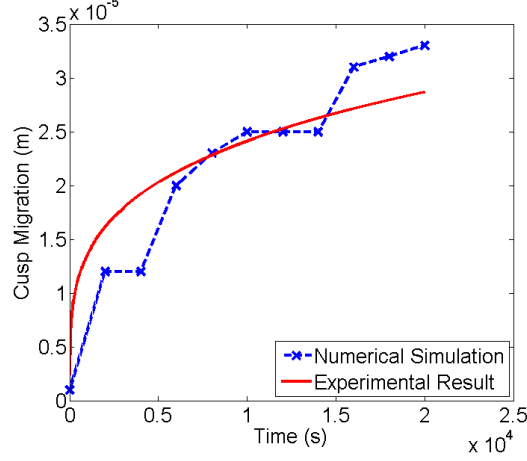


Figure 29 Calibration of the two-dimensional diffusion-controlled healing model against the experimental result. The numerical curve has a step-wise shape because of the technique we used to update the position of the crack circumference: The crack cusp migration distance is the horizontal distance between the bonded crack face ($U = 0$) and the closed but not bonded face ($U = 1$). However, since 1 is the asymptotic value for U as shown in Fig. 28, we consider the crack face as open if $U > 0.95$.

3.4.3 Numerical Analysis at the REV Scale

We simulated a strain-controlled one-dimensional loading test in MATLAB. In order to generate anisotropic damage in the specimen, we simulated a compression-tension loading cycle, in stress conditions similar to those encountered in CAES or gas storage sites (Ibrahim et al., 2008). The loading cycle consisted of uniaxial compression, followed by compression unloading, uniaxial tension, tension unloading, time-dependent healing, and reloading in tension. We assumed that the tension and compression loads were applied instantaneously, and that the healing phase was the only time-dependent load step. We assumed that the initial porosity of the sample was due to pre-existing micro-cracks with various orientations (i.e. damage was non-zero in the initial state before loading: $\Omega_1 = 0.01$, $\Omega_2 = \Omega_3 = 0.02$). We assumed that these micro-cracks

were filled with saturated brine, which triggered DMT and consequent healing. Table 7 in Subsection 3.3.3 provides the model parameters used in the simulations, after (Maleki, 2004; Zhu and Arson, 2014a).

To facilitate the calculation of micro-macro relationships, we made a few simplifying assumptions:

- During elastic compression, cracks perpendicular to the loading axis close, whereas cracks parallel to the axis keep the same shape.
- The mass balance of the fluid inside cracks was not accounted for, since our focus is the effect of DMT on the recovery of mechanical properties. The fluid amount is relatively small and the resulting poroelastic effect is ignored.
- When the strain increment is tensile, only the cracks perpendicular to the loading axis change shape.

We performed numerical simulations at room temperature (296K) for two different diffusion periods: 10,000s and 20,000s. Contrary to the previous study in Section 3.3, healing is fast even at room temperature because we assumed here that the intergranular space was filled with aqueous films. Fig. 30 presents the overall stress-strain response of the sample. Under compression (in direction 1), the sample behaves elastically before reaching the damage threshold (OA). Damage starts to accumulate afterwards, causing significant stiffness degradation (AB). Compression unloading is elastic (i.e. cracks parallel to direction 1 do not propagate), therefore the response of the material on portion BC is linear elastic, with a stress-strain slope that is smaller than during the loading phase OA, because of the accumulation of damage on portion AB.

Point C lies slightly below the origin, which indicates the presence of residual stress after unloading. At C, the axial deformation is zero: we assume that cracks are closed at that point. Portion CD (in tension) illustrates the recovery of compression strength

after crack closure (i.e., the slope of the stress-strain curve is the same as portion OA). In this particular simulation, a smaller value was assumed for tensile strength than for compressive strength as expected for rocks. At D, damage starts to propagate in tension, up to point E. EF shows the elastic tension unloading that follows. At F, tension cracks (perpendicular to direction 1) are closed, and compression cracks (parallel to direction 1) start to re- open. The stress-strain plot of compression reloading (FG) is parallel to that of compression unloading (BC). We simulated the healing phase (constant stress, varying time) under the compression stress at point G. Portions GH_1 and GH_2 show the response of the material when the material is reloaded in tension (for two different healing periods). The slopes of GH_1 and GH_2 are steeper than that of DE and less steep than that of OA, which indicates partial mechanical recovery. As expected, higher recovery is achieved for longer healing periods.

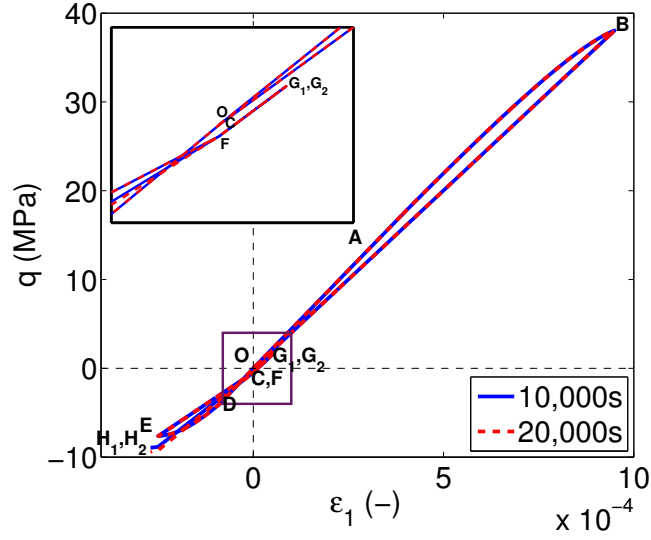


Figure 30 Stress-strain curve simulated for the compression-tension cycle (The magnified portion shows the details of the unilateral effects).

Fig. 31 illustrates the evolution of the damage variable. As expected, micro-cracks perpendicular to direction 1 (loading axis) do not propagate during the compression

phase (OC) nor during the elastic phase under tension (CD). Damage in direction 1 propagates during the non-elastic tension phases (DE, GH) and remains constant during the unloading and healing phases (EFG). Damage in directions 2 and 3 (micro-cracks parallel to the axis of the loading) increase during non-elastic compression (AB) and remain constant during compression unloading and tension loading (BH). The evolution of net damage in Fig. 32 is the same as that of damage except for portion GH, after healing has occurred. Cracks parallel to the loading axis do not heal under compression, therefore damage and net damage in directions 2 and 3 are equal. Cracks perpendicular to the loading axis heal at constant controlled deformation, which explains the drop of net damage after point G. On portion GH, net damage in direction 1 remains constant until the recovered tensile strength is exceeded. Longer healing periods lead to a larger decrease of net damage.

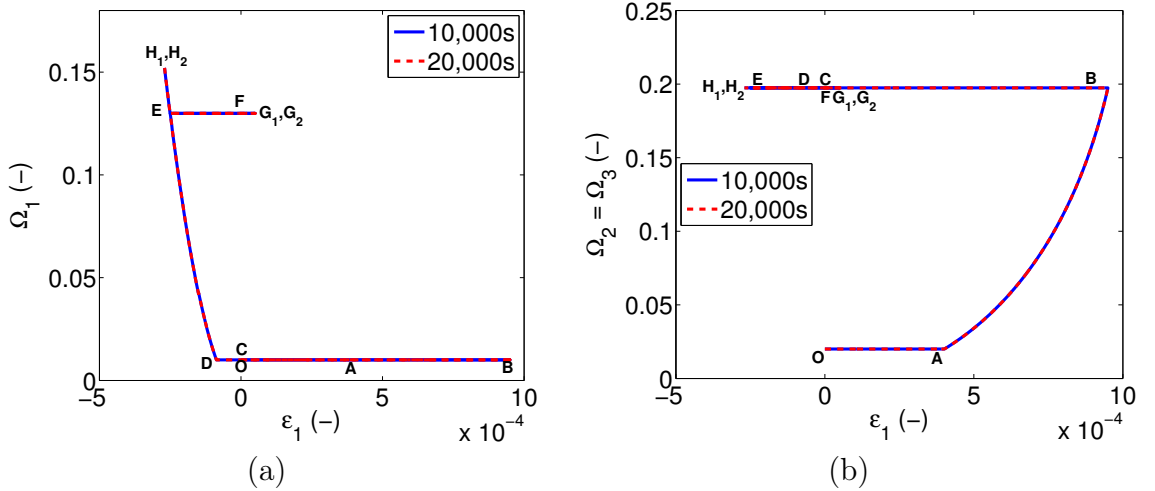


Figure 31 Evolution of the damage variable. Cracks perpendicular to the loading axis (left) and parallel to the loading axis (right).

Figures 33 and 34 show the evolutions of the fabric descriptors introduced in the model. By construction of the model, the evolution of crack length mirrors that of net damage. The mean of void areas is proportional to the porosity of the sample, which varies like the volumetric deformation in our model. The mean void area of micro-cracks perpendicular to direction 1 decreases first because of the compression of cracks

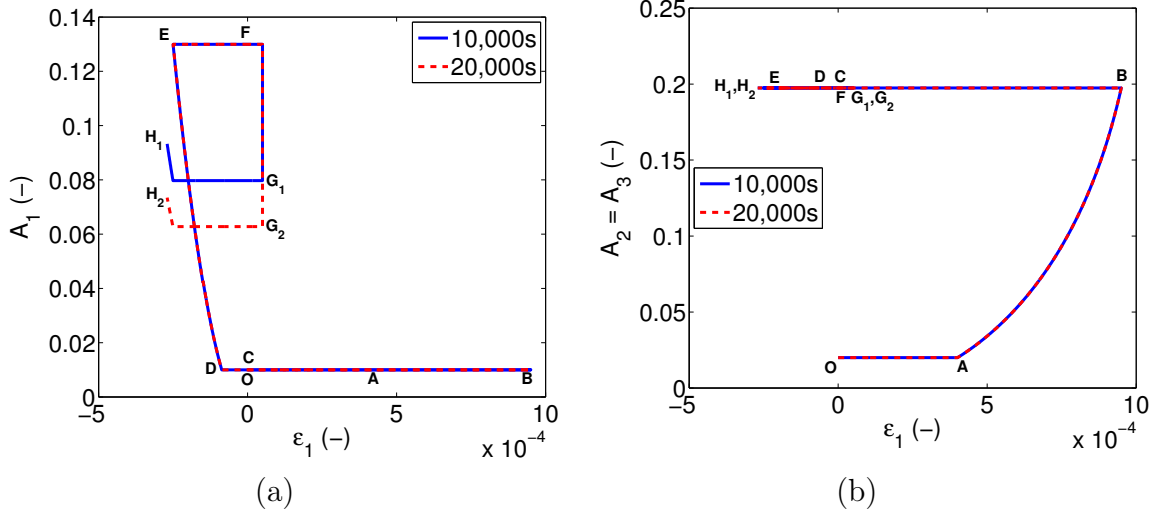


Figure 32 Evolution of net damage. Cracks perpendicular to the loading axis (left) and parallel to the loading axis (right).

during the elastic state, remains constant after damage occurs (because we assume that cracks parallel to the loading axis dominate deformation during compression), and increases again when tension is applied. On the other hand, the surface area of compression cracks varies only during compression phases. Healing under compression leads to a drop in the mean void area of cracks perpendicular to the loading axis. Since cracks parallel to the loading axis do not rebond, their mean area does not change during the healing phase GH.

Fig. 35 illustrates the distribution of the damage intensity within a crack face of normalized area. We verify that longer healing periods provide longer lags and therefore lower damage intensity along the grain radial direction. We also check that the lags shown in Fig. 35 are in agreement with the drop in crack lengths calculated during the healing phase (Fig. 33). The average damage intensity value (shown in Fig. 35) also matches the decrease in net damage variable (shown in Fig. 32).

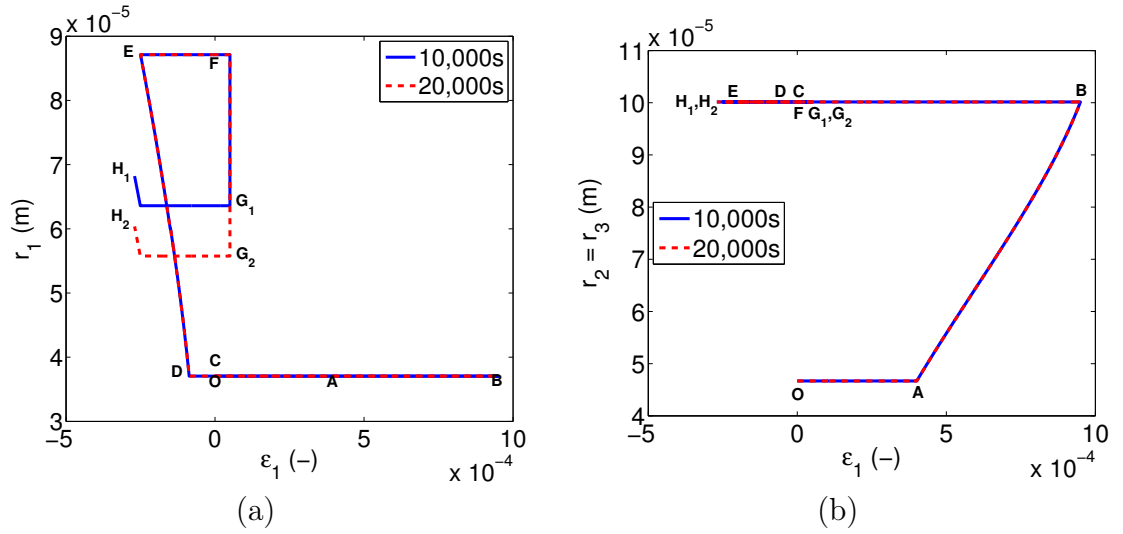


Figure 33 Evolution of crack length. Cracks parallel to the loading axis (left) and parallel to the loading axis (right).

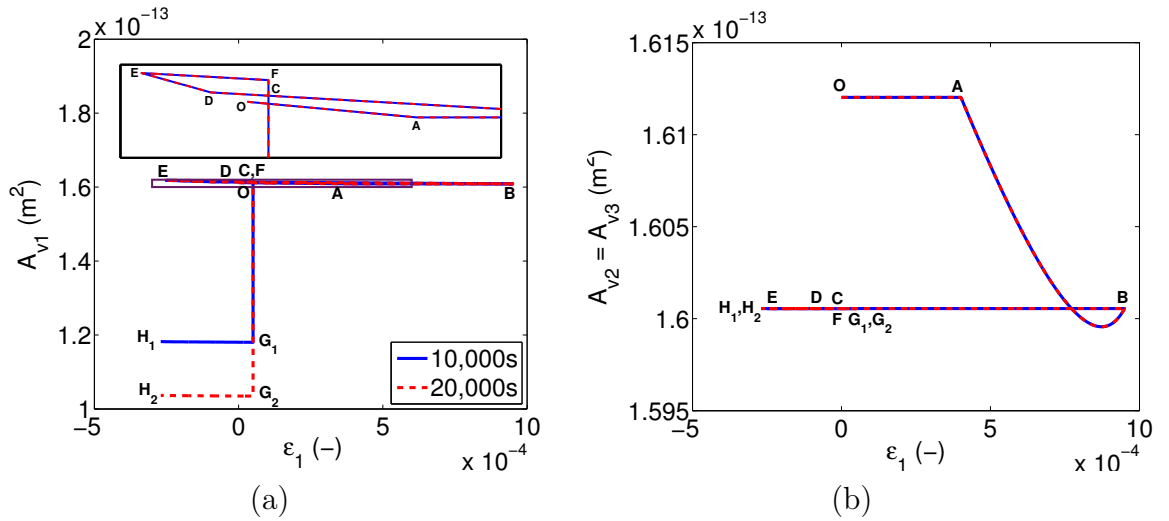


Figure 34 Evolution of mean crack area. Cracks parallel to the loading axis (left) and parallel to the loading axis (right).

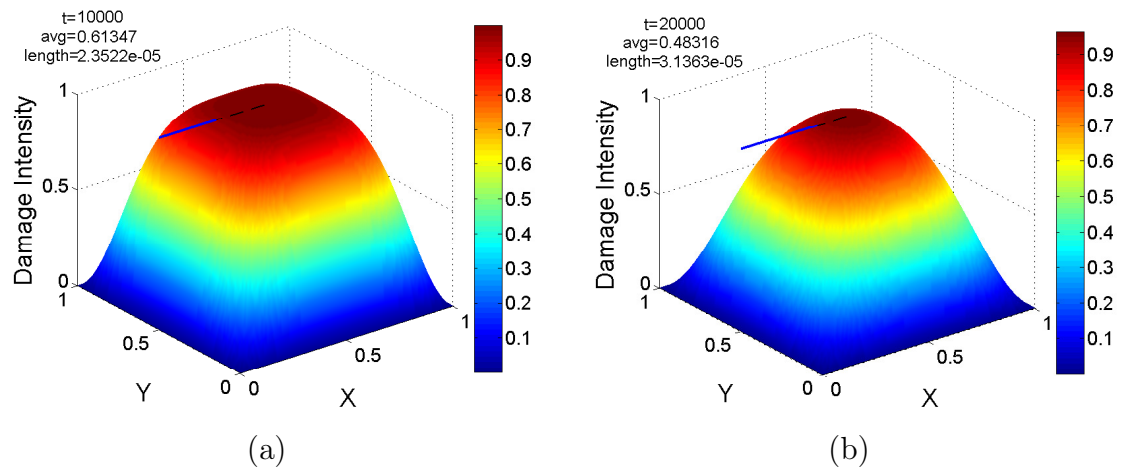


Figure 35 Damage intensity after two different healing periods (grain scale).

3.5 *Fabric-based Permeability Model*

3.5.1 Fabric Characterization

In Subsection 3.3.1, we did microscope observations of the salt granular assembly through the tube walls at regular time intervals in order ensure continuous microstructure characterization without taking out the sample. However, light reflection and transmission induced by transparent and cubic-shaped grains significantly impaired the image quality, which increased the difficulty to detect grain boundaries (Zhu et al., 2015b). To overcome this problem, we used micro-computed tomography (micro-CT), which allows observing and re-generating the 3D porous structure of the salt granular assembly. This technique can easily distinguish the solid $NaCl$ from voids because the salt grains and the porous fluid present a high density contrast. Micro-CT observations of the granular salt assembly confined in the tube (Fig. 36a) were conducted at the Guldberg Laboratory at Georgia Tech. The voxel size was $30\ \mu m$ while the size of a single particle is $300 \sim 400\mu m$. We used *ImageJ* (Abràmoff et al., 2004) for 3D porous structure reconstruction (Fig. 36b). Cross-sectional views were produced throughout the sample (Fig. 36c), from which we extracted binary images for further image processing (Fig. 36d).

We performed statistical image analyses of the binary images to extract information on the fabric. In particular, we characterized pore connectivity by studying the distribution of void centroid-to-centroid distances. Using the location of the void centroids (Fig. 37), we calculated the distance between each void centroid and its nearest neighboring void centroid. We found that these centroid-to-centroid distances follow a lognormal distribution (Fig. 38):

$$p_i(l_i) = \frac{1}{\sqrt{2\pi}l_i s_i} e^{-\frac{(\ln l_i - m_i)^2}{2s_i^2}} \quad (37)$$

This lognormal distribution reaches its peak value at a distance of about 0.4mm, which corresponds to the typical size of a table salt grain.

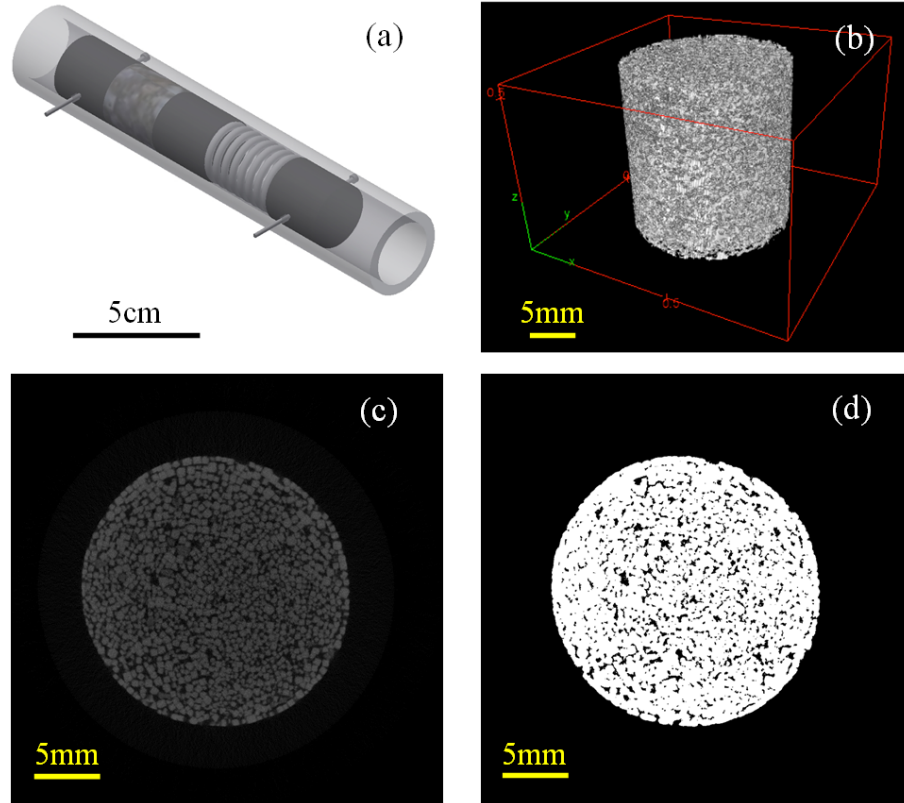


Figure 36 Image analysis during creep tests realized on table salt: (a) experimental set up; (b) micro-CT image of the solid skeleton; (c) cross-sectional view (original image); (d) cross-sectional view (binary image). Voxel size = $30\mu m$. Sample diameter = $19mm$. Grain size = $300 \sim 400\mu m$.

We also analyzed the distribution of void surface areas, which was found to follow a power law distribution (Fig. 39), which is conform to our previous observations:

$$p_A(A_v) = a \cdot A_v^t \quad (38)$$

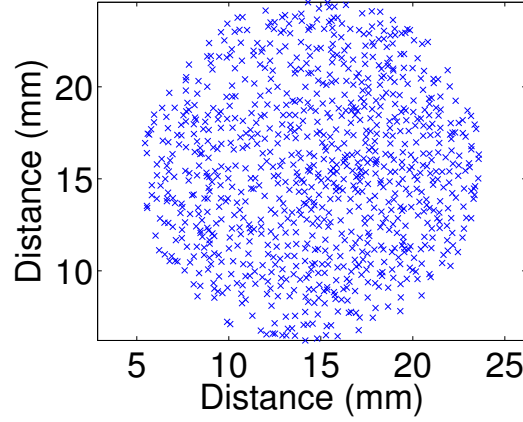


Figure 37 Locations of void centroids processed from the binary image in Fig. 36d.

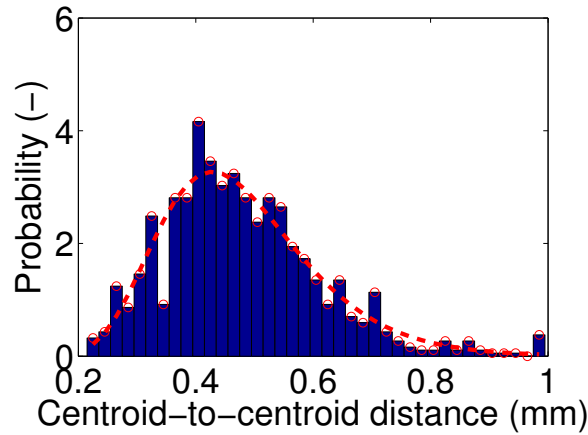


Figure 38 Normalized probability distribution of the centroid-to-centroid distances for all voids in the binary image (Fig. 36d). The peak appears at about 0.4 mm, which is close to the typical size of a single table salt grain.

3.5.2 Theoretical Framework

Fabric evolution impacts both the mechanical stiffness and the hydraulic properties of rocks. Table A.2 in Appendix I provides a summary of classical models that couple rock microstructure to permeability.

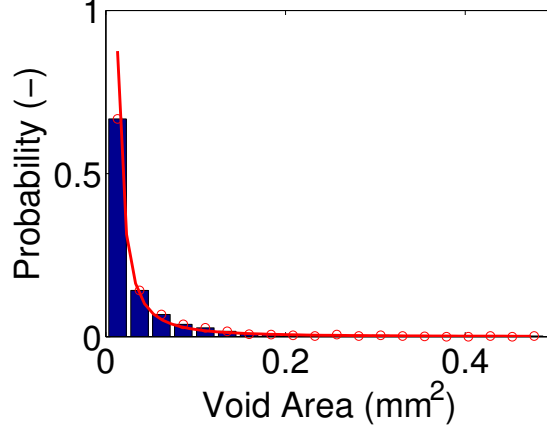


Figure 39 Normalized power law distribution of void area processed from the binary image in Fig. 36d.

In the following, we improve the mechanical damage and healing model with isotropic healing and anisotropic net damage, proposed in Section 3.3, in order to account for the impact of damage and healing on permeability. We use the intergranular space as an analog of salt rock crack space, and we consider that cracks are 3D spheroids. Spheroidal cracks are more realistic than the penny-shaped cracks considered in Section 3.3, and can be described by geometric parameters similar to the ones identified above: radius R , aperture $2 * \lambda$, and orientation \mathbf{n} . L is the crack spacing, i.e., the centroid-to-centroid distance between adjacent cracks (Fig. 40b).

We use the crack model proposed by Dienes (1982) and further modified by Guéguen and Dienes (1989) as a basis to calculate permeability. This crack model is chosen since it is established based on crack geometry, crack spacing, and the pore network connectivity. For an isotropic distribution of cracks with narrowly distributed width, radius, and spacing, the permeability can be computed as

$$k = \frac{4\pi}{15} f \frac{\bar{\lambda}^3 \bar{R}^2}{\bar{l}^3} \quad (39)$$

in which $\bar{\lambda}$ is the average half-crack aperture, \bar{R} is the average crack radius, \bar{l} is the average crack spacing, and the connectivity factor f accounts for the fraction of cracks that belong to an infinite network (i.e., the fraction of cracks that passed

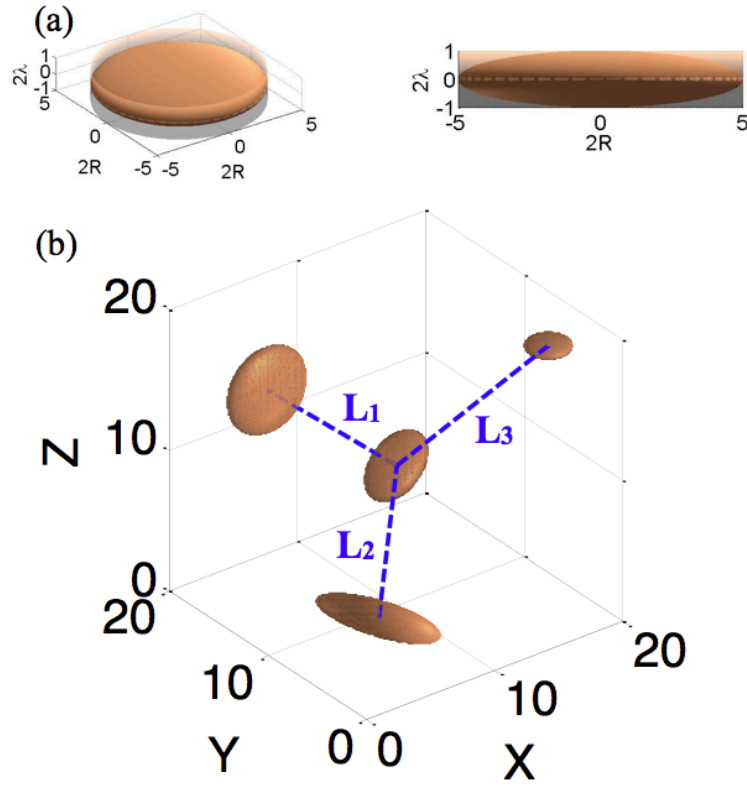


Figure 40 (a) Comparison between a spheroidal crack and a penny-shaped crack (3D view and 2D view). (b) Characterization of the spatial distribution of spheroidal cracks. Each crack is characterized by its radius, aperture, orientation, and the crack spacing.

the percolation threshold). These three microstructural parameters are independent from each other. From the CT-scan image analysis presented and from our previous microscope observations (Zhu and Arson, 2014a), we know the probability density functions of these fabric descriptors: the crack radius follows a lognormal distribution (Subsection 3.3.1); the crack area follows a power law distribution (Fig. 39); the crack spacing follows a lognormal distribution (Fig. 38). f is determined by the percolation theory.

In this model, spheroidal cracks are allowed to grow, intersect, and form connected porous pathways. Such pathways are limited to local regions at low crack number densities, but percolation can occur after a critical density is reached, which originates macroscopic permeability. After the percolation threshold is reached, permeability rapidly increases with crack density. Crack spacing is set as a constant in this model, i.e. crack centroids are assumed to remain the same upon crack growth (this means that cracks grow symmetrically about their centroid). In the absence of further experimental evidence, this assumption was considered acceptable for the proposed model of permeability.

The projection of orderly-packed granular salt assembly in 2D shows that each void has a maximum number of four neighboring voids. Therefore, we used the four-fold coordinated Bethe lattice (Dienes, 1982; Stauffer, 1985) to calculate the connectivity factor f . This lattice is based on an idealized geometric representation, and becomes inappropriate in 3D. Therefore, in future studies, we will resort to a pore network model to predict the value of f . For the chosen Bethe lattice, the percolation factor, which is used to determine whether a crack is connected to at least two infinite paths for throughout flow, is given by:

$$f = 1 - 4\left[\sqrt{\frac{1}{p} - \frac{3}{4}} - \frac{1}{2}\right]^3 + 3\left[\sqrt{\frac{1}{p} - \frac{3}{4}} - \frac{1}{2}\right]^4 \quad (40)$$

in which p is the probability of existence of a connection between cracks, which is equivalent to the probability of intersection between two cracks. We adopt the concept

of excluded volume (De Gennes, 1976) to calculate p . The excluded volume is the average volume around one crack within which a second crack must have its center in order for the cracks to intersect. For two discs, the excluded volume is found as:

$$V_e = \pi^2 \bar{R}^3 \quad (41)$$

Given that $1/\bar{l}^3$ is the crack density, the probability of crack intersection is given as (Guéguen and Dienes, 1989):

$$p \approx \frac{\pi^2 \bar{R}^3}{4\bar{l}^3} \quad (42)$$

in which it is assumed that each crack has 4 neighbors.

Combining Eq. 39, 40, 42, the expression of permeability in terms of crack geometry and percolation parameters becomes:

$$f = \frac{4\pi \bar{\lambda}^3 \bar{R}^2}{15 \bar{l}^3} \left\{ 1 - 4 \left[\sqrt{\frac{4\bar{l}^3}{\pi^2 \bar{R}^3} - \frac{3}{4} - \frac{1}{2}} \right]^3 + 3 \left[\sqrt{\frac{4\bar{l}^3}{\pi^2 \bar{R}^3} - \frac{3}{4} - \frac{1}{2}} \right]^4 \right\} \quad (43)$$

The value of k_{max} is given by Eq. 39 for $f = 1$. Nonzero permeability is observed for $p > \frac{1}{3}$: After this threshold is reached, the resulting crack intersection network will percolate and carry flows through the cluster of intersecting cracks (Fig. 41).

Two possibilities exist for the development of permeability from critical region ($f < 1$) to post-critical region ($f = 1$): (1) the crack number density increases and the crack geometry does not change after $f = 1$; (2) a constant number of cracks widen after $f = 1$. In this study, we fixed the total number of cracks and the crack spacing parameter, but crack geometry evolves during the damage and healing processes. For consistency, we thus used the 2nd scenario (crack widening) to model the increase of crack- permeability after percolation. Beyond the critical region, permeability is maximum:

$$k = \frac{4\pi \bar{\lambda}^3 \bar{R}^2}{15 \bar{l}^3} \quad (44)$$

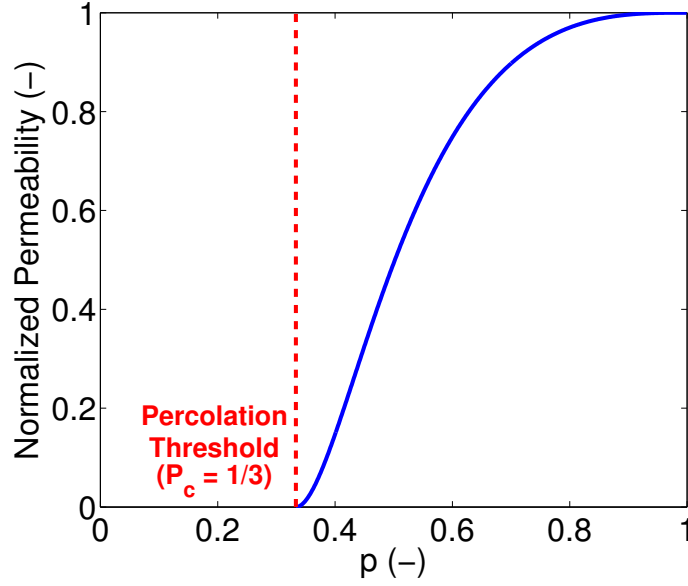


Figure 41 The normalized permeability as a function of the probability of intersection between two cracks (p). The percolation threshold for the four-fold coordinated Bethe lattice is $1/3$.

3.5.3 Computational Algorithm

The full resolution algorithm is summarized in Fig. 42. In the simulations presented in the following, the computation is strain-controlled with a strain increment given at the beginning of each step.

First, the crack closure condition is checked. Crack healing may occur only if crack closure is satisfied. Crack closure influences the stiffness, heat capacity, and bulk modulus, but does not change the microstructure descriptors and damage variable. By contrast, crack geometry evolves during the healing process, which results in a change in mixed damage variable and stress state.

If crack closure does not occur, we use the damage criterion to determine whether the material reaches its damage state or remains elastic during the current increment. In the elastic domain (elastic loading or unloading), the damage in the material does not change and only the microstructure changes, which induces a change in stress. If damage occurs, iterations are required to update the new damage variable. The

microstructure and stress variables are updated accordingly.

Based on the calculation at the current step, strain, stress, damage, and microstructure variables are updated and stored for the next computational step.

3.5.4 Numerical Simulation

We simulate a strain-controlled uniaxial loading test in MATLAB. The stress path consists of uniaxial tension, tension unloading, healing, and reloading in tension. We assume that only the healing phase is time-dependent. Mechanical loads are applied instantaneously. Model parameters used in the simulations are summarized in Table 7. Mechanical loading and unloading phases were assumed to take place at room temperature ($22^{\circ}C = 295K$), whereas the healing process was simulated at elevated temperature ($595K, 695K$). The healing period was $10000s$ (about 3 hours).

The stress-strain response follows the expected trends (Fig. 43a). The linear segment (OA) represents the initial elastic response - until damage initiates at point A. The accumulation of damage degrades the stiffness (AB) before the unloading phase. After releasing all tensile stress (BC) and applying additional compression to close all cracks (CD), unilateral effects result in some unilateral recovery of the stiffness in compression (DE). Healing occurs at elevated temperature (EF). Temperature was set back to room temperature before initiating tensile deformation for the reloading phase (FG). Additional damage is produced after recovery (GH) when the new damage threshold is reached. The change in slope after reloading illustrates the effect of temperature on healing: higher temperature over the same period of time leads to a more mechanical recovery (i.e., stiffness recovery).

The evolution of damage is the same for both healing temperatures investigated (Fig. 43b). Micro-cracks do not propagate during the elastic phase (OA) or the unloading phase (BCDE). Damage increases during the non-elastic tension phase (AB), remains constant during healing phase (EF), and increases again during reloading

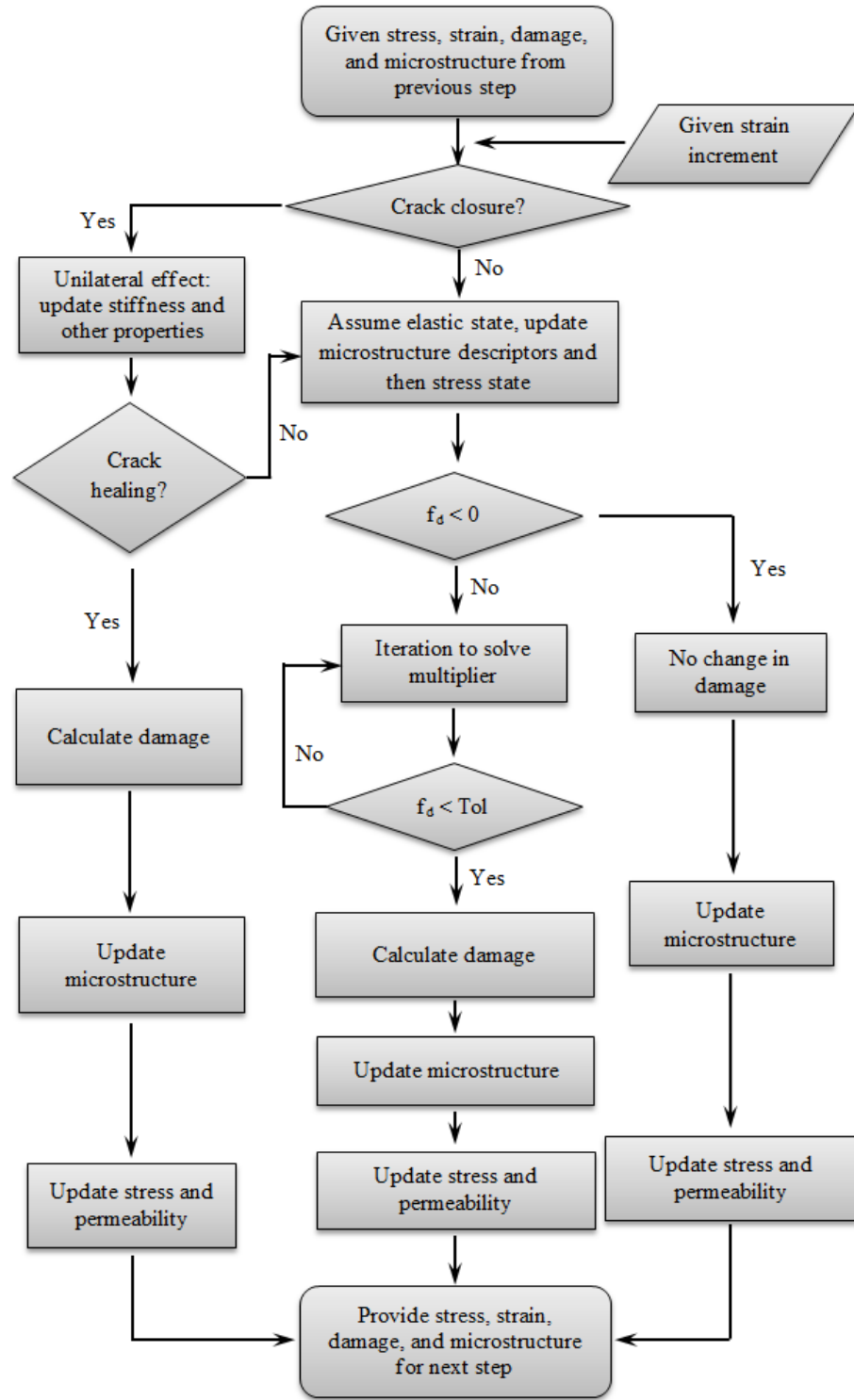
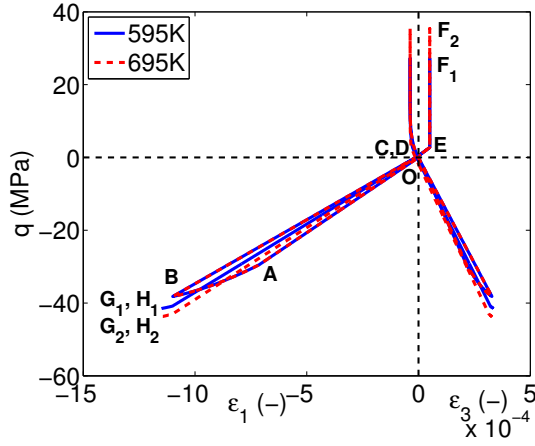


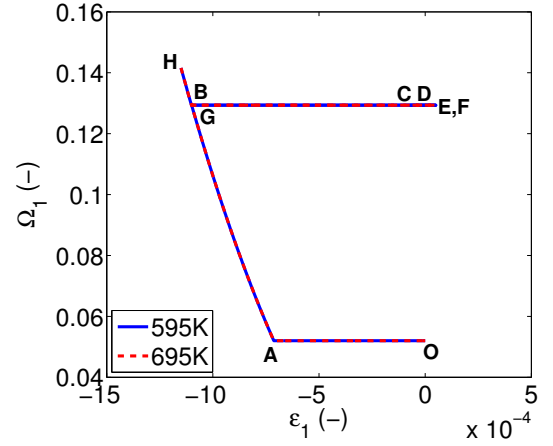
Figure 42 Computational algorithm of the microstructure-enriched model.

(GH). The mixed damage variable evolution follows a similar trend except during the healing phase (Fig. 43c). When healing occurs at constant axial deformation, h increases due to crack rebonding, which results in a decrease in net damage. After 10,000s healing at 595K and 695K, the healed stiffness increases from 81% of the initial stiffness (after damage and before healing, point E) to 86% and 89% of the initial stiffness (after healing, point F), respectively. Compared to healing processes that occur in the presence of brine (Zhu and Arson, 2015), healing in dry conditions is slower and requires higher temperature or longer healing time to produce the same effect.

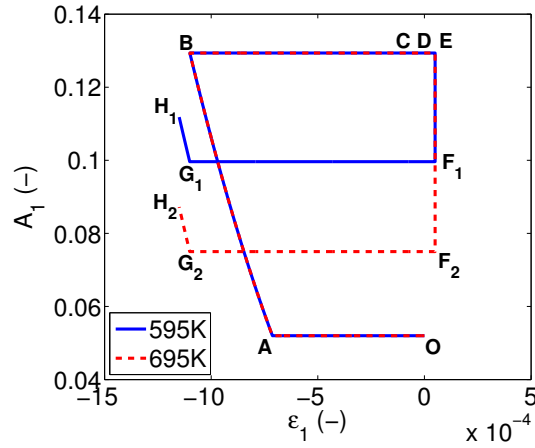
Evolutions of fabric descriptors are presented in Fig. 43d and Fig. 43e. Because of the axis-symmetry of the problem and by construction of the model, micro-cracks only propagate in planes orthogonal to the loading direction ($R_2 = R_3 \neq 0$, $R_1 = 0$). Since crack length is updated with net damage, evolution of crack length is similar to that of net damage (Fig. 43d). Crack aperture increases during elastic phase and decreases when damage propagates (Fig. 43e), which means that microcracks become longer but thinner during crack propagation.



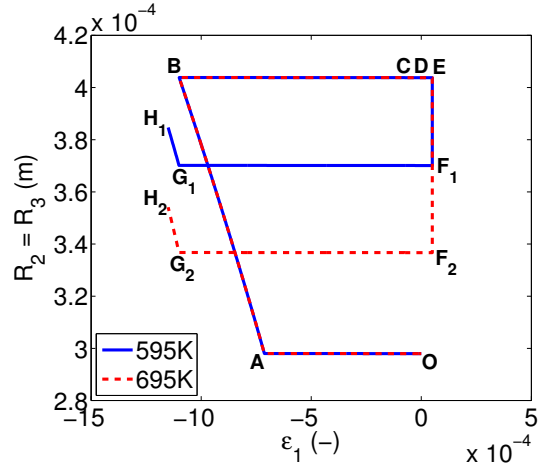
(a)



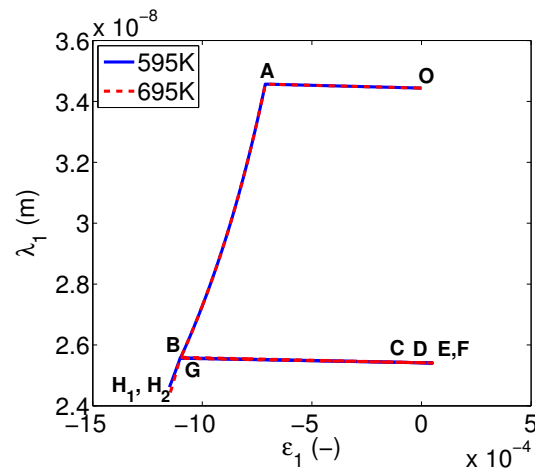
(b)



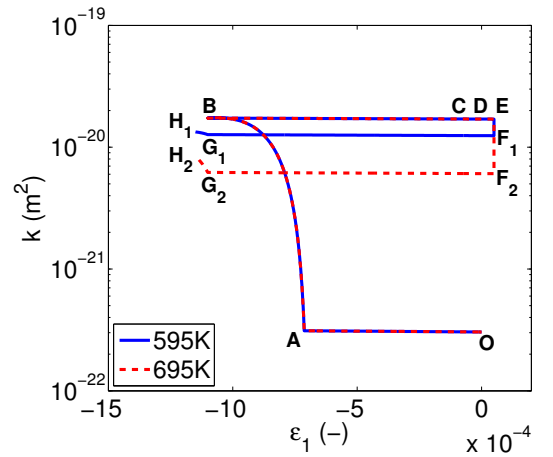
(c)



(d)



(e)



(f)

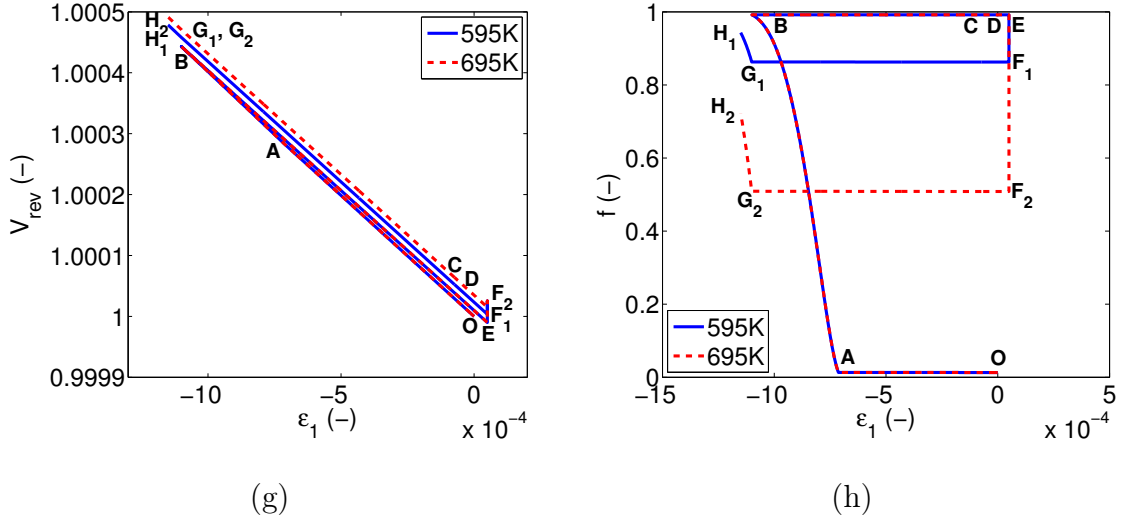


Figure 43 Numerical simulation results from MATLAB at the integration point: (a) stress-strain; (b) damage variable; (c) net damage variable; (d) crack radius; (e) crack aperture; (f) permeability; (g) volume change; (h) connectivity.

The material permeability depends on the evolution of microstructure descriptors (Eq. 43 and 44). The overall trend of permeability evolution is similar to the evolution of the crack radius (Fig. 43f). Permeability increases slightly during the elastic phase since the crack aperture increases (OA). Note that we assumed that salt had a non-zero initial permeability. Therefore, the variations of permeability due to damage shown in Fig. 41 occur in addition to that initial permeability in our simulation results. When damage starts to accumulate after point A, the radius of cracks increases, which rapidly leads to the percolation threshold (Fig. 41). That is why permeability increases dramatically after the initiation of damage (AB). Once the crack network stabilizes and forms a fully connected flow path, the permeability will gradually reach its maximum value. Similar trends were observed in many experimental studies (e.g., (Alkan, 2009)). During unloading, crack aperture decreases, however, crack faces are not fully closed. As a result, permeability decreases but does not go back to its initial value (BCDE). The change of crack radius also contributes to the decrease of

permeability during healing (EF). Crack radius and permeability increase again when the new damage criterion is satisfied during reloading (GH).

Permeability evolution is governed by changes of porosity (or equivalently REV volume since grains are incompressible, Fig. 43h) and pore connectivity (Fig. 43g). It is obvious that connectivity varies significantly when damage or healing occurs, whereas the REV volume change is negligible. We conclude that for the case simulated, permeability evolution is controlled by crack connectivity. Therefore, in-situ measurement of volume or deformation change may not be sufficient to infer the permeability change of the rock. It would be necessary to obtain the microstructure evolution through techniques such as in-situ X-ray microtomography.

3.6 Conclusions

The fabric-enriched Continuum Damage and Healing Mechanics (CDHM) framework is a top-to-bottom modeling approach that allows predicting damage and healing anisotropy induced by thermo-mechanical crack opening, closure and healing in rocks. In the work presented above on salt, the rearrangement of salt particles and the rebonding of grain boundaries during creep are described by the probability density functions of two geometric descriptors: the void area and the crack lengths. Crack closure is considered by adopting the concept of unilateral effect on rock stiffness. Crack rebonding is assumed to result from Diffusive Mass Transfer (DMT) processes. Net damage evolution obeys a diffusion equation in which the characteristic time scales with the typical size of a grain of salt. The thermo-mechanical damage model is calibrated and verified against experimental stress-strain curves during drained tri-axial compression tests conducted on saturated sandstone. Healing parameters are calibrated by comparing crack cusp migration distance with published experimental results. Constitutive models are programmed at the integration point in MATLAB to simulate thermo-mechanical loading and unloading cycles in axis-symmetric conditions. Macroscopic and microscopic model predictions are in agreement with the assumptions made in the constitutive framework. Under anisotropic mechanical boundary conditions, cracks can be produced during heating. Higher ambient temperature increases the lateral expansion and produces more damage. The efficiency of healing increases with temperature, time, and the presence of moisture. Permeability changes are predominantly controlled by changes in crack connectivity rather than the porosity change.

These numerical observations are expected to bring new thoughts to engineers and guide the choice of rock material in the design of geological storage facilities. For a nuclear waste disposal site, a proper control of the site temperature is advantageous for damage recovery and long-term maintenance. Humidity control plays a key role

in accelerating the rock healing process. Thermo-hydro-chemo-mechanical couplings should be accounted for in the most general case where all factors such as temperature, humidity and various healing mechanisms play a part.

CHAPTER IV

MICRO-MACRO MODEL OF VISCOUS FATIGUE

4.1 Introduction

In this chapter, we present a “bottom-up” modeling approach, in which a self-consistent homogenization scheme is used to predict the viscous damage and fatigue behavior of halite polycrystals from mono-crystal slip mechanisms. Following the micromechanical approach adopted by Pouya to study salt rock plastic behavior (Pouya, 1991a, 2000), our goal is to model the viscous behavior of polycrystalline salt by upscaling viscous gliding mechanisms formulated at the crystal scale. Our study focuses on the combination of time-dependent gliding and breakage mechanisms that occur at the grain scale under cyclic loading. In this chapter, we propose a homogenization scheme based on Hill’s incremental interaction model (Hill, 1965), in which we account for the heterogeneity of the elastic stiffness tensor that results from different damage mechanisms occurring at the grain scale. In order to focus on the effects of grain breakage on macroscopic viscoplastic strains, we disregard the viscous accommodation of the matrix in the inclusion-matrix interaction model (evidenced in (Mercier and Molinari, 2009; Rougier et al., 1994) for instance). Note that in the absence of damage, this simplifying assumption yields the Kröner - Weng interaction model (Kröner, 1961; Weng, 1982). For future work, a review of incremental, secant, tangent, affine and variational formulations may be found in (Bornert et al., 2001; Masson and Zaoui, 1999; Masson et al., 2000; Nebozhyn et al., 2001).

We first explain the microscopic origin of fatigue (Section 4.2) and the corresponding macroscopic fatigue behavior (Section 4.3) in salt rock. Then we present the homogenization scheme in Section 4.4. In Section 4.5, we explain a method to

calculate the internal stress and damage in the polycrystal during cyclic loading. We calibrate our micro-macro model of salt viscous fatigue against creep tests reported in the literature: results are reported in Section 4.6. We simulate creep tests (Section 4.7) and cyclic loading tests (Section 4.8), and conduct several parametric studies in order to examine the micromechanical origin of fatigue.

4.2 Microscopic Sliding Mechanisms

Halite is a Face-Centered Cubic crystal (FCC, Fig. 44). If all constituents of the crystal were atoms, intra-granular dislocations would occur on planes separating the two densest grain fractions, i.e. on planes normal to the $\langle 111 \rangle$ direction of the grain coordinate system (Fig. 45). However, halite crystals comprise two FCC ionic sub-networks (sodium Na^+ and chloride Cl^-). Due to electronic interaction forces between ions, the planes along which sliding requires the minimum energy input are the $\{101\}$ planes.

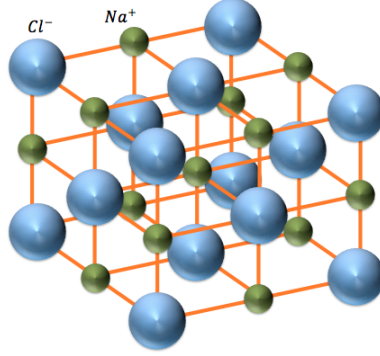


Figure 44 Crystal structure of salt.

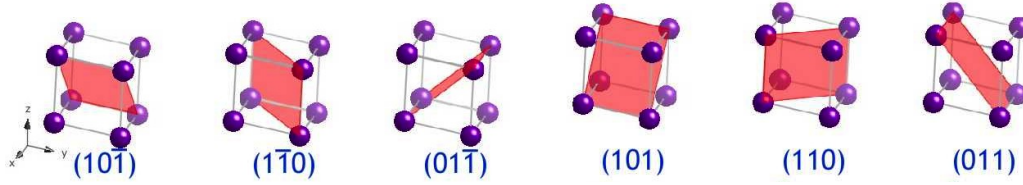


Figure 45 Sliding planes in FCC crystals (Barber et al., 2008).

In the local coordinate system of the mono-crystal, sliding systems (\mathbf{A}^l) are written:

$$\mathbf{A}^l = \mathbf{N}^l \otimes \mathbf{M}^l \quad (45)$$

in which \mathbf{N}^l and \mathbf{M}^l are respectively the vector normal to the l^{th} sliding plane and the l^{th} unit sliding vector. The vectors normal to the preferential sliding planes are

the following:

$$\begin{aligned}\mathbf{N}^1 &= \frac{1}{\sqrt{2}}(0, 1, 1) & \mathbf{N}^2 &= \frac{1}{\sqrt{2}}(1, 0, 1) & \mathbf{N}^3 &= \frac{1}{\sqrt{2}}(-1, -1, 0) \\ \mathbf{N}^4 &= \frac{1}{\sqrt{2}}(0, -1, 1) & \mathbf{N}^5 &= \frac{1}{\sqrt{2}}(-1, 0, 1) & \mathbf{N}^6 &= \frac{1}{\sqrt{2}}(-1, 1, 0)\end{aligned}\quad (46)$$

The sliding directions are given by:

$$\begin{aligned}\mathbf{M}^1 &= -\mathbf{N}^4 & \mathbf{M}^2 &= -\mathbf{N}^5 & \mathbf{M}^3 &= -\mathbf{N}^6 \\ \mathbf{M}^4 &= -\mathbf{N}^1 & \mathbf{M}^5 &= -\mathbf{N}^2 & \mathbf{M}^6 &= -\mathbf{N}^3\end{aligned}\quad (47)$$

Sliding system $\mathbf{N}^4 \otimes \mathbf{M}^4$ (respectively $\mathbf{N}^5 \otimes \mathbf{M}^5$ and $\mathbf{N}^6 \otimes \mathbf{M}^6$) is normal to sliding system $\mathbf{N}^1 \otimes \mathbf{M}^1$ (respectively $\mathbf{N}^2 \otimes \mathbf{M}^2$ and $\mathbf{N}^3 \otimes \mathbf{M}^3$). Moreover, we have:

$$\mathbf{N}^1 \otimes \mathbf{M}^1 = \mathbf{N}^2 \otimes \mathbf{M}^2 + \mathbf{N}^3 \otimes \mathbf{M}^3 \quad (48)$$

So that there are only two independent sliding mechanisms for each grain. Note that in *global matrix coordinates*, the l^{th} sliding system of the mono-crystal is noted:

$$a_{ij}^l = \frac{n_i^l m_j^l + n_j^l m_i^l}{2} \quad (49)$$

In which \mathbf{n}^l and \mathbf{m}^l are respectively the vector normal to the l^{th} sliding plane and the l^{th} unit sliding vector. Moreover, the viscoplastic deformation of the grain is written:

$$\epsilon_{ij}^{vp} = \sum_{l=1}^L \dot{\gamma}^l a_{ij}^l \quad (50)$$

In which $\dot{\gamma}^l$ is the viscoplastic (shear) deformation of grains subjected to the l^{th} sliding mechanism in the grain. For halite mono-crystals, $L = 6$ (with only 2 independent sliding mechanisms). The local shear stress is related to the micro-stress by:

$$\tau^l = \boldsymbol{\sigma} : \mathbf{a}^l \quad (51)$$

Based on experimental correlations (Pouya, 1991b; Wanten et al., 1996), the irreversible shear deformation is assumed to obey a power law:

$$\dot{\gamma}^l = \gamma_0 h^l \left| \frac{\tau^l}{\tau_0} \right|^n \quad (52)$$

in which n is a material parameter, γ_0 is a reference deformation rate, and τ_0 is a reference shear stress, arbitrarily set equal to 1MPa in the following (the model is calibrated with γ_0). h^l depends on the sign of τ^l : if τ^l is positive, $h^l = 1$; if τ^l is negative, $h^l = -1$.

4.3 *Macroscopic Fatigue Behavior*

Table A.3 in Appendix I gives an overview of the main experimental results obtained for salt rock under cyclic loading. Observations made in a variety of salt rocks are very similar. The Young's modulus and the compressive strength decrease as the number of loading cycles increase (Dubey and Gairola, 2000; Fuenkajorn and Phueakphum, 2010; Ma et al., 2013). Fatigue initiates faster for lower loading frequency (Fuenkajorn and Phueakphum, 2010; Liang et al., 2011; Liu et al., 2014a; Ma et al., 2013). The degradation of elastic moduli increases with the maximum stress and with the amplitude of the loading (Guo et al., 2012). Compared to amplitude and frequency, the confining stress does not influence fatigue significantly (Ma et al., 2013). The influence of the orientation of the bedding planes was investigated in Dubey and Gairola (2000). Memory effects in salt subject to triaxial stress states were analyzed in Filimonov et al. (2001). It has to be noted that the range of frequencies investigated in laboratory studies are significantly higher than those in actual CAES conditions. Low frequency experiments are more difficult to conduct in the laboratory, because they require more time: a sufficiently long loading period and a large number of loading cycles. Laboratory tests, performed at the macroscopic scale, were not able to reveal the microscopic origin of fatigue. The micro-macro modeling approach presented in the following addresses this shortcoming: numerical simulations were conducted to relate the development of salt fatigue under cyclic loading to the evolution of micro-stresses in halite grains.

4.4 Homogenization Scheme

4.4.1 Averaging Method

The Representative Elementary Volume (REV) considered is an aggregate of halite mono-crystals of different orientations. The upscaling scheme is based on averages computed in the space of crystal orientations. To determine a system of coordinates in this space, let (X, Y, Z) denote a system of crystallographic axes attached to the inclusion (Fig. 46). The orientation of the Z -axis is determined by two spherical coordinates (angles Ψ and θ), defined in the Cartesian coordinate system (x, y, z) . Let (u, v, z) be the system obtained from (x, y, z) through a rotation around the z -axis by an angle Ψ . Let (U, v, Z) be the system obtained from (u, v, z) through a rotation around the v -axis by an angle θ . The system (X, Y, Z) is obtained from (U, v, Z) by an additional “spinal” rotation around the Z -axis by an angle Φ , which varies between 0 and 2π .

The probability of having a Z -axis of orientation (Ψ, θ, Φ) is the product of the probability of occurrence of the solid angle Ω (measured by $d\Omega = \sin\theta d\theta d\Psi$) by that of the spinal rotation Φ (measured by $d\Phi$). Therefore, the density of the probability of occurrence of a grain orientation ω_1 is measured by:

$$dp = p(\omega_1)d\omega_1 = p(\Psi, \theta, \Phi) \sin\theta d\theta d\Psi d\Phi \quad (53)$$

Moreover, the average of a function $f(\omega_1)$ is defined as:

$$\bar{f} = \frac{1}{\Omega_1} \int_{\Omega_1} f(\omega_1)d\omega_1 = \frac{1}{8\pi^2} \int_{\theta=0}^{\pi} \int_{\Psi=0}^{2\pi} \int_{\Phi=0}^{2\pi} f(\Psi, \theta, \Phi) \sin\theta d\theta d\Psi d\Phi \quad (54)$$

Salt rock is made of halite (NaCl) mono-crystals, which all have the same FCC structure. Since the inclusion (or “grain”) considered represents a single crystal, crystalline symmetries allow reducing the variation of Φ to the interval $[0, \pi/2]$. Finally, changing θ to $\pi - \theta$, Ψ to $2\pi - \Psi$ and Φ to $2\pi - \Phi$ leads to the same crystallographic orientation (in which Y is changed into $-Y$). This allows reducing the domain of

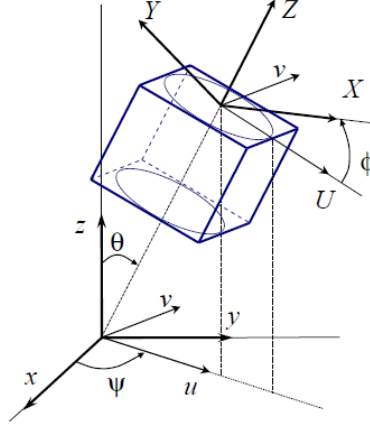


Figure 46 Spherical coordinate system adopted to characterize mono crystal orientations.

variation of θ to the interval $[0, \pi/2]$. Moreover, the following simulations focus on a uniaxial macroscopic loading, in which the REV presents a symmetry about the z -axis. Therefore, Ψ can be set equal to a constant. Without reducing the generality of the model, $\Psi = 0$ is adopted in the following. As a result, in the proposed approach, the average is defined as:

$$\bar{f} = \frac{2}{\pi} \int_{\theta=0}^{\pi/2} \int_{\Phi=0}^{\pi/2} f(\theta, \Phi) \sin\theta \, d\theta d\Phi \quad (55)$$

Using the variable change $u = \cos\theta$, Eq. 55 can be rewritten as:

$$\bar{f} = \frac{2}{\pi} \int_{u=0}^1 \int_{\Phi=0}^{\pi/2} f(u, \Phi) \, du d\Phi \quad (56)$$

All grain orientations are assumed to have the same probability of occurrence, i.e., the orientation of the mono-crystals is assumed to follow a uniform probability density function. To obtain equipotent points in a discrete integration scheme, it is sufficient to divide the domain of variation of u ($[0, 1]$) into n_u intervals of central value u_i , and the domain of variation of Φ ($[0, \pi/2]$) into n_Φ intervals of central value Φ_j . The average is finally computed as:

$$\bar{f} = \frac{1}{N} \sum_{i,j} f(\theta_i, \Phi_j) \quad (57)$$

in which $N = n_u n_\Phi$, and $\theta_i = \text{Arcos}(u_i)$. In the simulations presented in the following, 200 orientations are considered (i.e., $N = 200$).

4.4.2 Inclusion-Matrix Model

The stresses and strains in mono-crystals depend on the macroscopic load imposed to the aggregate, and on the interactions between these mono-crystals. A simplified “inclusion-matrix model” is used to account for the interaction between grains. Following a self-consistent upscaling scheme, each mono-crystal is viewed as an inclusion embedded in an infinite homogeneous matrix, which represents the macroscopic aggregate. The behavior of the matrix is *a priori* unknown. Therefore, the upscaling method is based on an implicit system of equations: the unknown matrix model has to be determined iteratively. In the model proposed below, mono-crystals are viewed as spherical inclusions (Fig. 47).

For a homogeneous and isotropic elastic matrix, the model of Kröner, proposed initially for elasto-plastic materials, was extended by Weng (1982) for viscoplastic materials, in the following form:

$$\dot{\boldsymbol{\sigma}} - \dot{\bar{\boldsymbol{\sigma}}} = 2\mu(1 - \beta)(\dot{\bar{\boldsymbol{\epsilon}}}^{vp} - \dot{\boldsymbol{\epsilon}}^{vp}) \quad (58)$$

in which $\dot{\boldsymbol{\sigma}}$ is the rate of microscopic stress, and $\dot{\bar{\boldsymbol{\sigma}}}$ is the rate of macroscopic stress. $\dot{\bar{\boldsymbol{\epsilon}}}^{vp}$ and $\dot{\boldsymbol{\epsilon}}^{vp}$ denote the macroscopic and microscopic viscoplastic strain rates. β is given by:

$$\beta = \frac{2(4 - 5\nu)}{15(1 - \nu)} \quad (59)$$

in which ν is the Poisson’s ratio of the homogenized REV (*a priori* unknown).

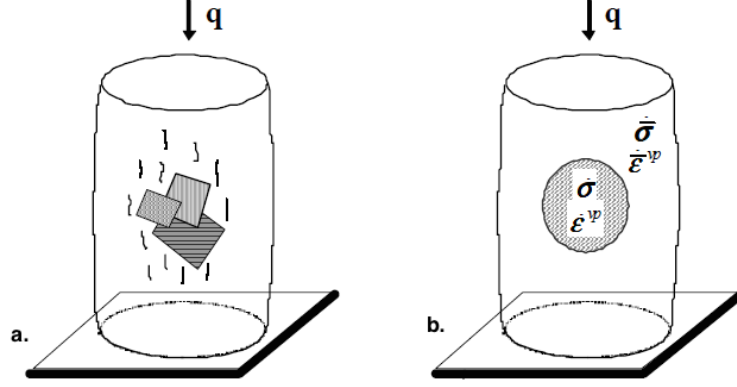


Figure 47 Salt rock Representative Elementary Volume (REV). (a) Monocrystal inclusions in the homogeneous matrix. (b) Schematic representation of salt monocrystals in the inclusion-matrix model.

Both the mono-crystal inclusions and the matrix are considered to be viscoplastic. The viscoelastic self-consistent model of Weng is adopted, which is based on Eshelby's inclusion model. But the matrix-inclusion interaction is assumed to be purely elastic, which implies that macroscopic viscoplasticity only stems from grain-scale viscoplastic deformation, and not from grain/matrix incompatibilities. The local stress in the inclusions (σ) and the far-field stress in the matrix ($\bar{\sigma}$) are coupled to the microscopic strain (ϵ) and the macroscopic strain ($\bar{\epsilon}$) by the following relationship:

$$\sigma - \bar{\sigma} = -\mathbf{L}^* : (\epsilon - \bar{\epsilon}) \quad (60)$$

in which \mathbf{L}^* is Hill's tensor for a spherical inclusion in an isotropic matrix (Hill, 1965).

4.4.3 Micro-macro Damage Modeling

At the REV scale, damage is defined as the reduction of elastic moduli and rock strength. Macroscopically, crack propagation in a rock REV can be driven by tension, compression or shear (Bobet and Einstein, 1998; Ortiz, 1985). In the model proposed here, macroscopic damage triggers when one mono-crystal fails. Microscopically, the initiation of damage at the grain scale is restricted to mode I failure, which occurs

when the microscopic stress exceeds the tensile strength of salt mono-crystals (equal to 2MPa): if the major principal local stress of a grain exceeds 2 MPa, the grain is breaking. Damage propagates when subsequent stress redistribution and further loading bring micro-stress in other grains to the tensile limit. The number of unbroken grains is noted N_g , the number of broken grains is noted N_b , and the total number of grains in the REV is noted N (with $N = n_u n_\Phi$, the number of mono-crystal orientations considered in the REV). The dilute scheme estimate for the elastic matrix yields the following effective bulk modulus ($\tilde{\kappa}$) and shear modulus ($\tilde{\mu}$):

$$\tilde{\kappa} = \frac{N_g}{N} \kappa = \frac{N - N_b}{N} \kappa = (1 - D) \kappa, \quad \tilde{\mu} = \frac{N_g}{N} \mu = \frac{N - N_b}{N} \mu = (1 - D) \mu \quad (61)$$

In which the damage variable is defined as $D = N_b/N = 1 - N_g/N$. From the expressions of the damaged bulk and shear moduli in Eq. 61, it can be shown that Poisson's ratio does not change upon grain breakage: $\tilde{\nu} = \nu$. The micro-macro modeling approach proposed combines Hill's scheme (Hill, 1965) for the rate-independent non linear elastic matrix behavior (to represent the inclusion-matrix interaction), and a brittle constitutive law for the grains subject to breakage (to represent damage). Hill's tensor is calculated for the damaged matrix. So, in the present work, the inclusion-matrix interaction model accounts for brittle grain breakage, but does not capture the “viscous accommodation” due to the viscous deformation of the matrix. This simplification is considered acceptable for the sake of this study, which focuses on macroscopic fatigue behavior induced by cyclic loading.

For each macroscopic stress loading increment $\delta q(t)$ applied between times t_n and t_{n+1} , the macroscopic and microscopic variables are updated in two steps, as illustrated in Fig. 48:

1. The “damage phase” ($t_n \sim t_n^+$) accounts for instantaneous variations due to grain breakage at time t_n : these variations are noted $\delta \boldsymbol{\sigma}$, $\delta \boldsymbol{\varepsilon}$, $\delta \overline{\boldsymbol{\sigma}}$, $\delta \overline{\boldsymbol{\varepsilon}}$.
2. The “viscous phase” ($t_n^+ \sim t_{n+1}$): accounts for time-dependent variations due to

viscous deformation on the time interval $\Delta_n t = t_{n+1} - t_n$: these variations are noted $\dot{\sigma}\Delta_n t$, $\dot{\varepsilon}\Delta_n t$, $\dot{\bar{\sigma}}\Delta_n t$, $\dot{\bar{\varepsilon}}\Delta_n t$.

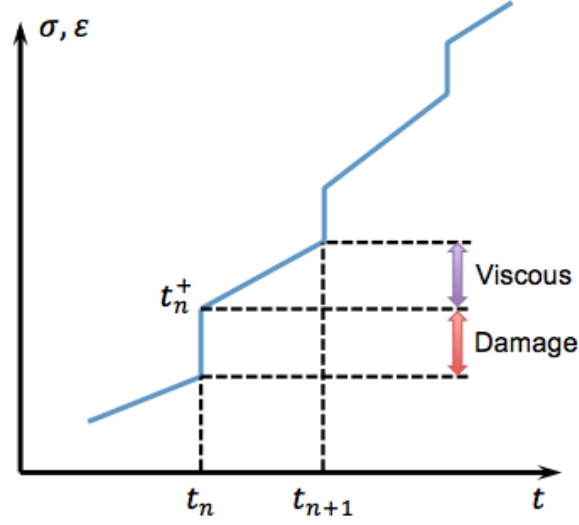


Figure 48 Stress computational method: decomposition of the time step into damage and viscous phases, for stress- or strain- controlled tests.

At each stress increment (i.e., time step), the grain breakage criterion is checked at the beginning of the damage phase ($t = t_n$). Grains are sorted into three categories, depending on their stress state:

- The grain is non-broken if the maximum principal microscopic stress is less than the mono-crystal tensile strength of 2 MPa;
- The grain is breaking if the maximum principal microscopic stress exceeds the mono-crystal tensile strength of 2 MPa during the current loading increment;
- The grain is broken if the mono-crystal had already broken in a previous loading increment.

Initially at $t = t_n$, the damaged elastic moduli are calculated from Eq. 61, in which N_b accounts for both breaking and broken grains. For all types of grains, the inclusion-matrix interaction is governed by Kröner formula in Eq. 60. Grain breakage results

in a redistribution of micro-stresses: when breaking grains actually fail, non-broken grains become subjected to microscopic stresses of higher magnitude. At the beginning of the viscous phase (at $t = t_n^+$), resulting micro-stresses are updated by using the equations governing the sliding mechanisms. Note that in some of the grains, the redistribution of micro-stresses due to grain breakage (at $t = t_n^+$) can result in tensile stresses that exceed the tensile strength. Grains that are subjected to higher stresses than the tensile strength are considered as non-broken during the viscous phase of the loading (between $t = t_n^+$ and $t = t_{n+1}$), and the status of the grains is checked and updated at the beginning of the damage phase of the following loading increment (at $t = t_{n+1}$).

4.5 *Micro-Macro Stress Computational Method*

4.5.1 Stress Redistribution due to Damage

By definition, the macroscopic stress (respectively strain) is the average of microscopic stresses (respectively strains). Other averaged local quantities are not necessarily equal to the corresponding macroscopic quantities. For instance, the macroscopic viscoplastic strain is the average of the microscopic viscoplastic strains, only if the elastic tensor is uniform or homogeneous. In the present modeling approach, macroscopic damage is caused by the breakage of the grains where microscopic tensile stress is the highest. In general, the spatial distribution of broken grains is not uniform. Therefore the macroscopic viscous strain is not the average of the local viscous strain: $\langle \epsilon^{vp} \rangle \neq \bar{\epsilon}^{vp}$. This difference can be shown by using different stiffness tensors for different grains in Eq. 60.

We assumed that the microscopic stress in a broken grain vanishes, which corresponds to a perfectly brittle failure. The elastic moduli of broken grains are assigned a zero value, and broken grains are modeled as void inclusions in the matrix. When the REV is subjected to a macroscopic stress at its boundary, the whole matrix deforms, and these void inclusions deform as well. By definition, $\delta \bar{\sigma} = \mathbf{C} : \delta \bar{\epsilon}$, where the damaged elasticity tensor of the matrix (\mathbf{C}) is related to the elasticity tensor of non-broken grains (\mathbf{C}_0) as

$$\mathbf{C} = (1 - D) \mathbf{C}_0. \quad (62)$$

The breaking and broken grains have no stiffness, and are both subjected to zero microstress, therefore $D(t_n) = N_b(t_n)/N$ in which $N_b(t_n) = N - N_g(t_n)$. The damaged elastic properties are updated as

$$\begin{aligned} \mu(t_n) &= (1 - D(t_n)) \mu(t_0) = \frac{N_g(t_n)}{N} \mu(t_0), \\ \kappa(t_n) &= (1 - D(t_n)) \kappa(t_0) = \frac{N_g(t_n)}{N_T} \kappa(t_0), \quad \nu(t_n) = \nu(t_0), \end{aligned} \quad (63)$$

in which $\mu(t_0)$, $\kappa(t_0)$, $\nu(t_0)$ are the elastic properties of the undamaged matrix. The change of microscopic deformation ($\delta\boldsymbol{\varepsilon}$) is obtained by combining Eq. 60 with the expression of the change of microscopic stress ($\delta\boldsymbol{\sigma}$). Each type of grain undergoes a different change of microscopic stress during the damage phase of the loading increment: $\delta\boldsymbol{\sigma} = \mathbf{C}_0 : \delta\boldsymbol{\varepsilon}$ for non-broken grains, $\delta\boldsymbol{\sigma} = -\boldsymbol{\sigma}$ for breaking grains and $\delta\boldsymbol{\sigma} = 0$ for broken grains. The resulting expressions of the change of microstress is given in Table 10 for each type of grain.

Table 10 Microscopic stress change due to grain breakage.

	Microscopic stress	Microscopic deformation
Non-broken grains	$\delta\boldsymbol{\sigma} = \mathbf{C}_0 : \delta\boldsymbol{\varepsilon}$	$\delta\boldsymbol{\varepsilon} = [\mathbf{I} + \mathbf{M}^* : \mathbf{C}_0]^{-1} : (\delta\bar{\boldsymbol{\varepsilon}} + \mathbf{M}^* : \delta\bar{\boldsymbol{\sigma}})$
Breaking grains	$\delta\boldsymbol{\sigma} = -\boldsymbol{\sigma}$	$\delta\boldsymbol{\varepsilon} = \mathbf{M}^* : \boldsymbol{\sigma} + \delta\bar{\boldsymbol{\varepsilon}} + \mathbf{M}^* : \delta\bar{\boldsymbol{\sigma}}$
Broken grains	$\delta\boldsymbol{\sigma} = 0$	$\delta\boldsymbol{\varepsilon} = \delta\bar{\boldsymbol{\varepsilon}} + \mathbf{M}^* : \delta\bar{\boldsymbol{\sigma}}$
Notation:	$\mathbf{M}^* = \mathbf{L}^{*-1} \quad I_{ijkl} = \frac{1}{2}(\delta_{ik}\delta_{jl} + \delta_{il}\delta_{jk})$	

For the special case of stress-controlled loading paths studied here, the variation of macroscopic stress is applied during the viscous phase of the loading ($t_n^+ \sim t_{n+1}$). Therefore, during the damage phase: $\delta\bar{\boldsymbol{\sigma}} = 0$. Therefore, the variations of microscopic deformation during the damage phase of the time step are given by

$$\text{Non-broken grain: } \delta\boldsymbol{\varepsilon} = [\mathbf{I} + \mathbf{M}^* : \mathbf{C}_0]^{-1} : \delta\bar{\boldsymbol{\varepsilon}},$$

$$\text{Breaking grain: } \delta\boldsymbol{\varepsilon} = \mathbf{M}^* : \boldsymbol{\sigma} + \delta\bar{\boldsymbol{\varepsilon}},$$

$$\text{Broken grain: } \delta\boldsymbol{\varepsilon} = \delta\bar{\boldsymbol{\varepsilon}}.$$

(64)

Recalling that $\delta\bar{\epsilon} = \langle \delta\epsilon \rangle$, at time t_n^+ , Eq. 64 can be rewritten as

$$\begin{aligned}
N\delta\bar{\epsilon} &= \sum_{\text{non-broken}} [\mathbf{I} + \mathbf{M}^* : \mathbf{C}_0]^{-1} : \delta\bar{\epsilon} \\
&+ \sum_{\text{breaking}} \mathbf{M}^* : \boldsymbol{\sigma} + \sum_{\text{breaking}} \mathbf{I} : \delta\bar{\epsilon} \\
&+ \sum_{\text{broken}} \mathbf{I} : \delta\bar{\epsilon}.
\end{aligned} \tag{65}$$

The variation of macroscopic strain $\delta\bar{\epsilon}$ is obtained from Eq. 65 as

$$\delta\bar{\epsilon} = \frac{1}{N_g(t_n)} [\mathbf{I} - (\mathbf{I} + \mathbf{M}^* : \mathbf{C}_0)^{-1}]^{-1} : [\mathbf{M}^* : (\sum_{\text{breaking}} \boldsymbol{\sigma})]. \tag{66}$$

Then $\delta\epsilon$ and $\delta\sigma$ can be updated for each type of grain (according to the equations listed in Table 10). It should be noted that at the end of the damage phase (at $t = t_n^+$), there are only two types of grains: non-broken and broken (the breaking grains get counted as part of the broken grains). Broken grains are considered as voids, with: $\sigma(t_n^+) = 0$, $\dot{\sigma}(t_n^+) = 0$, $\dot{\epsilon}^{vp}(t_n^+) = 0$.

In summary, in the damage phase of each loading increment, calculations are performed in the following order:

$$\sigma(t_n) \rightarrow \left\{ \begin{array}{l} < 2 \text{ MPa} : \text{grain is non-broken} \\ \geq 2 \text{ MPa} : \text{grain is breaking} \\ \text{broken grains remain broken} \end{array} \right\} \rightarrow \begin{array}{l} N_g(t_n) \\ N_b(t_n) \end{array} \rightarrow \tilde{\mu}(t_n) \xrightarrow{\sigma(t_n)} \delta\bar{\epsilon}(t_n) \rightarrow \delta\epsilon(t_n) \rightarrow \delta\sigma(t_n) \rightarrow \sigma(t_n^+)$$

4.5.2 Stress Redistribution due to Viscoplasticity

At the beginning of the viscous phase (at $t = t_n^+$ in Fig. 48), the following variables are known:

- At the macroscopic scale: $p(t_n^+)$, $q(t_n^+)$, $\bar{\sigma}(t_n^+)$, $\bar{\epsilon}^{vp}(t_n^+)$, $\bar{\epsilon}(t_n^+)$, $\mu(t_n^+)$, $\nu(t_n^+) = \nu(t_0)$, $\mathbf{C}(t_n^+)$, $\mathbf{L}^*(t_n^+)$, $N_g(t_n^+) = N_g(t_n)$, $N_b(t_n^+) = N_b(t_n)$
- At the microscopic scale: $\sigma(t_n^+)$, $\epsilon^{vp}(t_n^+)$, $\epsilon(t_n^+)$

Viscous loading phase for the grains that are non-broken at time $t = t_n^+$

The microscopic stress $\boldsymbol{\sigma}(t_n^+)$ is used to calculate the viscoplastic strain rate at the grain scale:

$$\dot{\gamma}^l(t_n^+) = \gamma_0 h^l \left| \frac{\tau^l(t_n^+)}{\tau_0} \right|^n = \gamma_0 h^l \left| \frac{\boldsymbol{\sigma}(t_n^+) : \mathbf{a}^l}{\tau_0} \right|^n \Rightarrow \dot{\boldsymbol{\epsilon}}^{vp}(t_n^+) = \sum_{l=1}^6 \dot{\gamma}^l(t_n^+) \mathbf{a}^l. \quad (67)$$

The macroscopic loading rate $\dot{\bar{\boldsymbol{\sigma}}}(t_n^+)$ is assumed to be given; it depends on the type of loading considered, creep or sinusoidal cyclic loading. After replacing small variations by rates in Eq. 60, and after some computations, the microscopic stress rate $\dot{\boldsymbol{\sigma}}(t_n^+)$ can be expressed as

$$\begin{aligned} (\mathbf{I} + \mathbf{L}^*(t_n^+) : \mathbf{C}_0^{-1}) : \dot{\boldsymbol{\sigma}}(t_n^+) &= (\mathbf{I} + \mathbf{L}^*(t_n^+) : \mathbf{C}^{-1}(t_n^+)) : \dot{\bar{\boldsymbol{\sigma}}}(t_n^+) \\ &\quad + \mathbf{L}^*(t_n^+) : (\dot{\bar{\boldsymbol{\epsilon}}}^{vp}(t_n^+) - \dot{\boldsymbol{\epsilon}}^{vp}(t_n^+)). \end{aligned} \quad (68)$$

The cumulated macroscopic stress at $t = t_{n+1}$ is calculated as

$$\boldsymbol{\sigma}(t_{n+1}) = \boldsymbol{\sigma}(t_n^+) + \dot{\boldsymbol{\sigma}}(t_n^+) \times \Delta_n t. \quad (69)$$

For non-broken grains, variables $\bar{\boldsymbol{\sigma}}(t_{n+1})$, $\bar{\boldsymbol{\epsilon}}^{vp}(t_{n+1})$, $\bar{\boldsymbol{\epsilon}}(t_{n+1})$, $\boldsymbol{\epsilon}^{vp}(t_{n+1})$ are obtained by time integration (similar to Eq. 69). The microstress in non-broken grains is compared to the tensile strength of the mono-crystal at the following loading increment.

Viscous loading phase for the grains that are broken at time $t = t_n^+$

Grains that are already broken at time $t = t_n^+$ are replaced by voids, i.e. by stress-free cavities with zero stiffness. Gliding mechanisms are no longer active in broken grains, so that: $\boldsymbol{\sigma}(t_{n+1}) = \boldsymbol{\sigma}(t_n^+) = 0$, $\dot{\boldsymbol{\sigma}}(t_{n+1}) = \dot{\boldsymbol{\sigma}}(t_n^+) = 0$, $\dot{\boldsymbol{\epsilon}}^{vp}(t_{n+1}) = \dot{\boldsymbol{\epsilon}}^{vp}(t_n^+) = 0$. Then the total strain rate of the broken grain (i.e. the deformation rate of the hole) is computed as

$$\dot{\boldsymbol{\epsilon}}(t_n^+) = \mathbf{S}_D(t_n^+) : \dot{\bar{\boldsymbol{\sigma}}}(t_n^+), \quad (70)$$

in which $\dot{\bar{\boldsymbol{\sigma}}}(t_n^+)$ is given by the type of macroscopic loading considered. Moreover, $\mathbf{S}_D(t_n^+) = \mathbf{L}^{*-1}(t_n^+) + \mathbf{C}^{-1}(t_n^+)$.

In summary, in the viscous phase of each loading increment, calculations are performed in the following order:

$$\begin{array}{l} \dot{\bar{\boldsymbol{\sigma}}}(t_n^+) \\ \tilde{\mu}(t_n^+) = \tilde{\mu}(t_n) \end{array} \rightarrow \left\{ \begin{array}{l} \dot{\bar{\boldsymbol{\varepsilon}}}^{vp}(t_n^+) \\ \dot{\gamma}^l(t_n^+) \rightarrow \dot{\bar{\boldsymbol{\varepsilon}}}^{vp}(t_n^+) \end{array} \right\} \rightarrow \dot{\boldsymbol{\sigma}}(t_n^+) \xrightarrow{\boldsymbol{\sigma}(t_n^+)} \boldsymbol{\sigma}(t_{n+1})$$

4.5.3 Computational method for axial loading

The computational method can be used to determine micro-stresses in an aggregate subjected to axial macroscopic loading. We note, for a macroscopic axial loading along the \mathbf{e}_3 axis:

$$\bar{\boldsymbol{\sigma}} = q(t)\mathbf{r}, \quad \bar{\mathbf{s}} = \bar{\boldsymbol{\sigma}} - \frac{Tr(\bar{\boldsymbol{\sigma}})}{3}\boldsymbol{\delta} = q(t)\boldsymbol{\Psi}, \quad \dot{\bar{\boldsymbol{\varepsilon}}}^{vp} = \frac{3}{2}\dot{p}(t)\boldsymbol{\Psi}, \quad (71)$$

in which:

$$\mathbf{r} = -\mathbf{e}_3 \otimes \mathbf{e}_3, \quad \boldsymbol{\Psi} = \mathbf{r} - \frac{1}{3}Tr(\mathbf{r})\boldsymbol{\delta}. \quad (72)$$

The loading rate \dot{q} at time t_n^+ is calculated according to the type of loading considered:

- For a creep loading test:

$$\dot{q}(t_0) = \infty, \quad \dot{q}(t_n^+, t_n \neq t_0) = 0 \quad (73)$$

- For a sinusoidal cyclic loading test:

$$\dot{q}(t_n^+) = q_0\omega\cos(\omega t_n) \quad (74)$$

We introduce the following notation:

$$\dot{\rho}(t) = \dot{q}(t) + 3\mu(1 - \beta)\dot{p}(t), \quad (75)$$

in which β is given by:

$$\beta = \frac{2(4 - 5\nu)}{15(1 - \nu)} \quad (76)$$

The value of $\dot{\rho}$ is obtained from $N_g(t_n^+)$ (calculated during the damage phase), and from Eq. 73-74:

$$\dot{\rho}(t_n^+) = \dot{q}(t_n^+) + 3\mu(t_n^+)(1 - \beta(t_n^+)) < \dot{\epsilon}^{vp}(t_n^+) >: \Psi, \quad (77)$$

from which, the rate of macroscopic viscoplastic strain can be obtained as

$$\dot{\rho}(t_n^+) = \frac{\dot{\rho}(t_n^+) - \dot{q}(t_n^+)}{3\mu(t_n^+)[1 - \beta(t_n^+)]} = < \dot{\epsilon}^{vp}(t_n^+) >: \Psi \quad \Rightarrow \quad \dot{\epsilon}^{vp}(t_n^+) = \frac{3}{2}\dot{\rho}(t_n^+)\Psi. \quad (78)$$

The simulations presented in the following are based on Eq. 71-78 for a stress-controlled axial loading.

4.6 Model Calibration against Creep Tests

The following macroscopic relationship can be obtained from the micro-macro model proposed above:

$$\dot{p}(t) = \frac{M}{3\mu(1-\beta)} \frac{q^n(t)}{(\tau_0)^n} \quad (79)$$

in which:

$$M = 3\mu(1-\beta) \left\langle \sum_{l=1}^L \gamma_0 |\mathbf{r} : \mathbf{a}^l|^{n+1} \right\rangle \quad (80)$$

The details of the derivations are provided in Appendix III. Note that an approximation was made: in Eq. 50 and 52, the microscopic stress $\boldsymbol{\sigma}$ was replaced by the macroscopic stress $\bar{\boldsymbol{\sigma}} = q(t)\mathbf{r}$. The advantage of the form of relationship given by Eq. 79 is that it directly relates the macroscopic viscoplastic strain rate to the macroscopic stress imposed in the simulations. Therefore, it is convenient to use it for calibration purposes. Note that an approximation is made: in the homogenized Eq. 51, the microscopic stress $\boldsymbol{\sigma}$ is replaced by the macroscopic stress $\bar{\boldsymbol{\sigma}} = q(t)\mathbf{r}$. After calibration, we verified that the variations of the macroscopic viscoplastic strains predicted by the approximate law in Eq. 79 followed those predicted by the non-approximated micro-macro model with less than 5% error.

Table 11 Model parameters calibrated against the creep tests reported in Fuenkajorn and Phueakphum (2010).

Creep Test	γ_0 (day^{-1})	n (-)
Short Term (7 hours)	5.17×10^{-4}	3.58
Long Term (30 days)	2.93×10^{-5}	4.04

The microscopic constitutive law in Eq. 52 depends on two parameters: γ_0 and n . In addition, the parameter β depends on the macroscopic elastic properties of the polycrystal in the reference state. The Poisson's ratio is not affected by damage in the proposed model: a standard value of $\nu_0 = 0.3$ is adopted. The polycrystal Young's modulus is also given a value typical of rock salt (Fuenkajorn and Phueakphum, 2010): $E_0 = 23GPa$. The calibration procedure is based on a genetic algorithm that selects

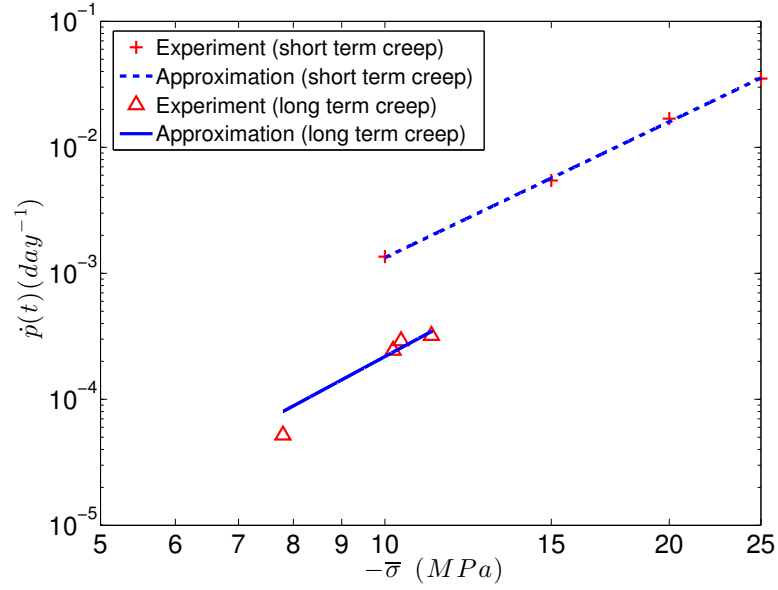


Figure 49 Calibration of the approximated macroscopic creep law against long-term creep tests reported in Fuenkajorn and Phueakphum (2010).

the optimal set of parameters, i.e. the set of parameters that minimizes the difference between the experimental and simulated creep curves. The distance between the two curves is computed with a Least Square Method. The asymptotic strain rates at the end of the 7-hour and 30-day creep tests reported in Fuenkajorn and Phueakphum (2010) are computed for each loading condition considered, and are used as reference data (Fig. 49). The best fit for the two creep tests provide the optimal values of γ_0 and n , which are reported in Table 11 for both short-term and long-term creep. In the following simulations, the long-term creep test parameters are used.

4.7 *Simulation of Salt Fatigue under Creep Loading*

4.7.1 Microscopic Origin of Creep Recovery

In the following simulations, grain breakage is not accounted for, which implies that macroscopic viscoplastic deformation is solely due to microscopic viscoplastic strains. Two long-term creep tests are simulated, with the parameters calibrated against the long-term creep test. The stress paths for both tests are illustrated in Fig. 50a. In the first test, a constant macroscopic stress of 7 MPa is maintained for three days. The second test includes the four following phases: (1) an instantaneous axial stress loading from 0 MPa to 7 MPa, (2) a creep phase under a constant stress of 7 MPa, maintained for about half a day, (3) an instantaneous stress unloading, from 7 MPa to 1 MPa, (4) creep phase under a constant stress of 1 MPa, maintained for about two and half days. The evolution of total macroscopic strains is shown in Fig. 50b.

As expected, macroscopic viscoplastic strains do not vary during the instantaneous loading and unloading phases (Fig. 50b). In the first creep test, the macroscopic strain increases (from B to C, and from C to E), which illustrates the macroscopic strain hardening noted in most experiments. For extended periods of time, the strain rate tends asymptotically to zero: Fig. 51, from E to F, illustrates the asymptotic creep behavior over 180 days. After the unloading phase simulated in the second creep test (i.e., after point D in Fig. 50b), the macroscopic strain rate is positive, which indicates that the specimen is in extension, although the macroscopic load imposed during phase 4 of test 2 is a compression. This phenomenon, named “creep recovery”, was observed experimentally, and modeled phenomenologically. For instance, Munson and Dawson (1979) introduced *ad hoc* parameters explicitly in their formulation to match model predictions with experimental data. Qualitative explanations based on internal stresses were sometimes invoked by researchers, but the cause of creep recovery was not well understood. In the proposed micro-macro approach, creep recovery is automatically captured, as a model output. The method is powerful, because results

confirm that the origin of recovery actually stems from grain viscoplastic deformation and grain interactions within the polycrystal.

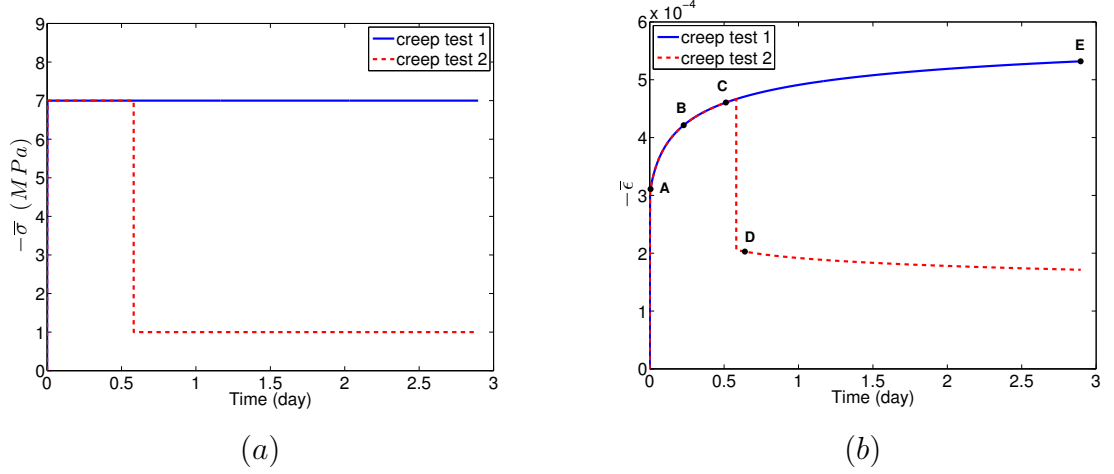


Figure 50 Simulation of two long-term creep tests (grain breakage was not considered): (a) Stress path. (b) Time evolution of macroscopic strains.

For each grain, the principal values of the micro-stress can be represented by a vector $\sigma_i \vec{v}_i$, where the unit vector \vec{v}_i is the i^{th} microstress eigenvector and σ_i is the i^{th} microstress eigenvalue. In the plane (r, z) , a tensile principal stress is represented by a vector \overrightarrow{OM} (in the upper right quadrant, $z > 0, r > 0$), and a compressive principal stress is represented by a vector \overrightarrow{ON} (in the lower left quadrant, $z < 0, r < 0$). The convention adopted to plot microscopic stresses is illustrated in Fig. 52, in which α measures the angle between the direction of the principal microstress considered and the compression axis z . Stress maps drawn according to the convention explained in Fig. 52 show the sign and amplitude of the principal microstresses, as well as the angle made by the principal microstresses with the compression axis, for each grain orientation considered in the REV.

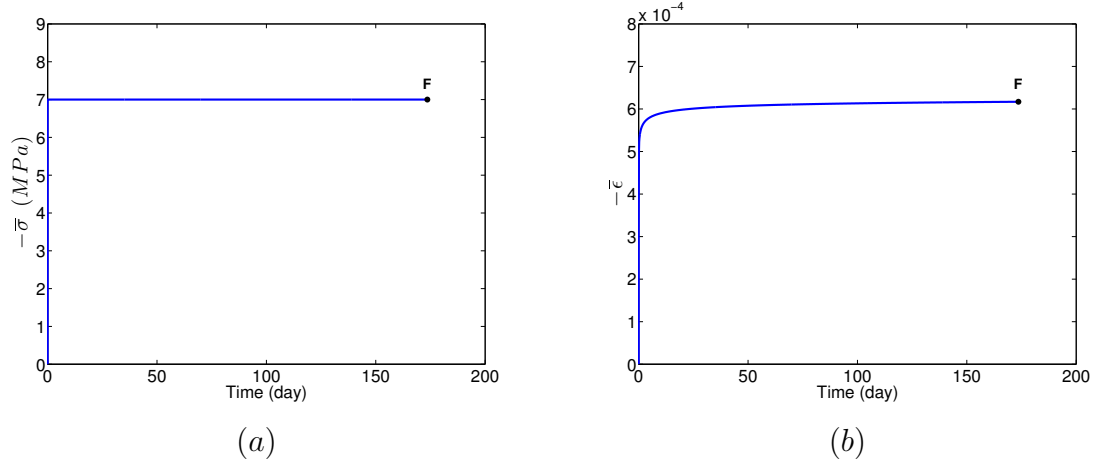


Figure 51 Asymptotic creep behavior predicted by the micro- macro- model, in the absence of grain breakage. (a) Stress path. (b) Time evolution of macroscopic strains.

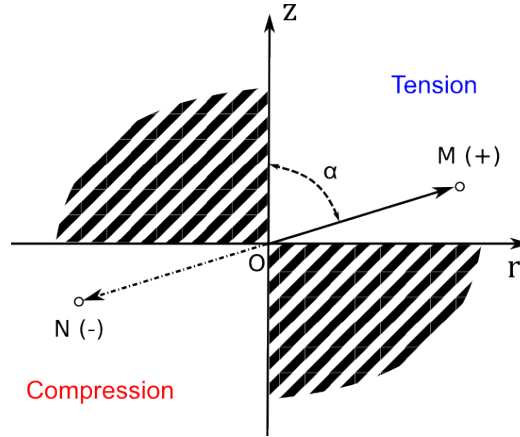


Figure 52 Graphical representation of the microscopic principal stresses.

The comparison of the distribution of microscopic stresses at points C and D (Fig. 53) provides a micromechanical explanation to the phenomenon of creep recovery. If the sample are instantaneously subjected to axial stress increase from 0 MPa to 1 MPa, lateral tensile microstresses would increase over time, starting from a state of microstress equal to that of macrostress (the explanation is the same as for the first loading stage of 7 MPa in Fig. 53). The response predicted when a creep load of 1 MPa is applied after a creep load at 7 MPa is very different from the one

that would be expected without pre-loading phase: the distribution of microstresses tends to an isotropic distribution. A vertical tensile microstress of up to 1.3 MPa is noted in some of the grains, despite the applied macroscopic compressive stress, which amounts to 1MPa. The presence of vertical tensile microstresses within the aggregate explains why the specimen is in extension during this creep recovery stage (Fig. 50). By contrast, if the first creep load of 7 MPa is maintained for extended periods of time, tensile lateral microstresses will continue to increase at a slower rate (point E). It is worth noticing that in in this simulation, the value of the tensile microstresses exceeds the tensile strength (2MPa) in some of the grains, because grain breakage is not accounted for in the simulations.

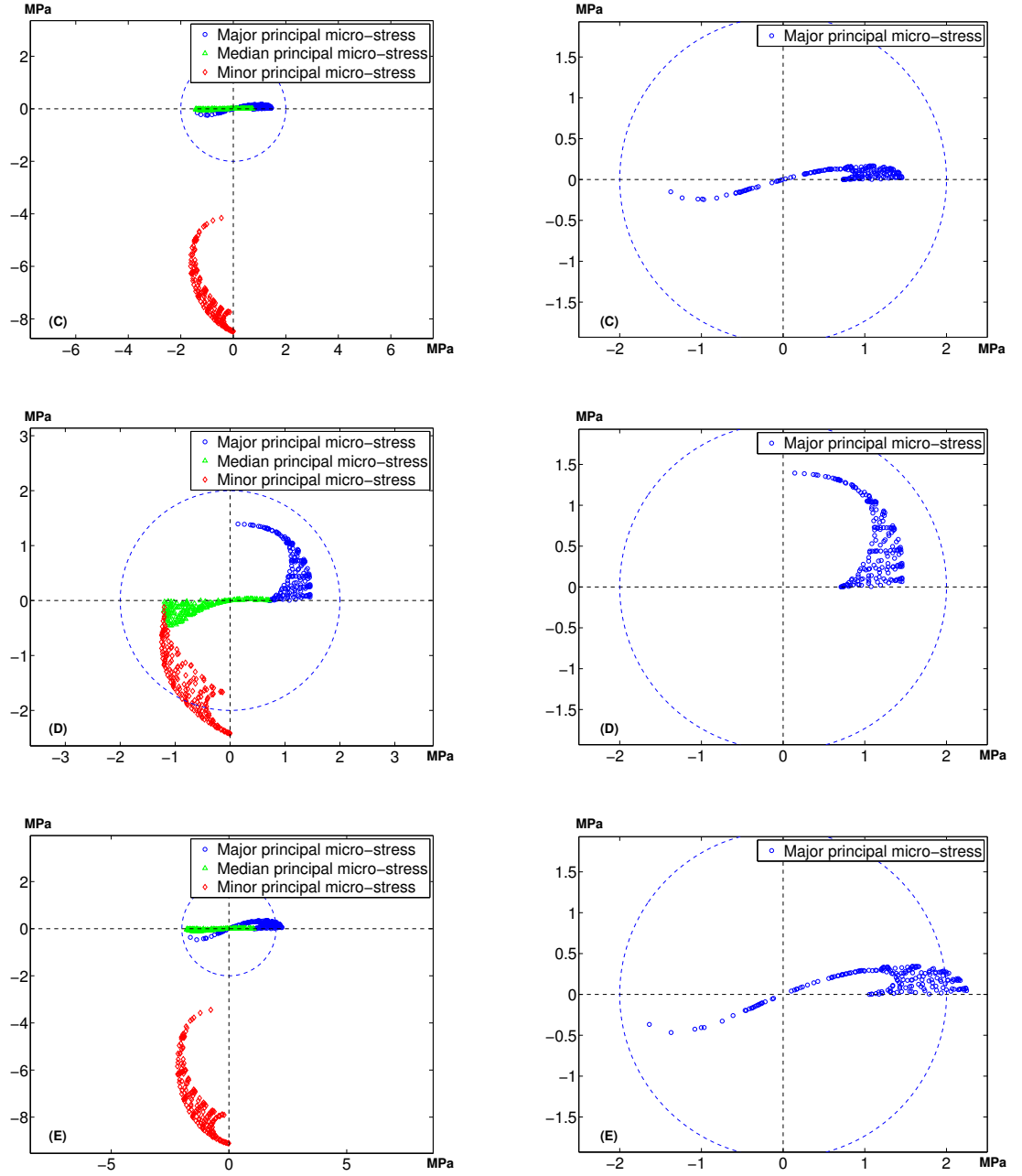


Figure 53 Micro-stress developed in the sample during the two-stage creep test simulated in the absence of grain breakage: loading points C, D, E shown in Fig. 50.

4.7.2 Influence of Grain Breakage on Macroscopic Creep Regimes

Now, we investigate the impact of grain breakage on the creep deformation regime of the salt polycrystal. The three following long-term creep tests are simulated:

- In the first test (“no damage” case), a low creep stress (5 MPa) is applied, and grain breakage is accounted for.
- In the second test (“non-damage model” case), a higher creep stress (7 MPa) is applied, and grain breakage is not accounted for.
- In the third test (“damage model” case), a high creep stress (7 MPa) is applied, and grain breakage is accounted for.

Results are presented in Fig. 54:

- First test: the macroscopic strain rate reaches a steady state in the secondary creep phase, which indicates an absence of accelerated creep. Microscopic tensile stresses remain below 2 MPa, which implies that none of the mono crystals break, even though grain breakage is taken into account in the model.
- Second test: the macroscopic strain rate remains almost constant, and microscopic stresses exceed the tensile strength limit, which indicates that grains would have broken if damage had been accounted for.
- Third test: the microstress goes to zero in some of the grains, and the macroscopic strain rate increases abruptly at the end of the creep test.

These results indicate that the model can capture the accelerated creep regime (tertiary creep) caused by grain breakage. The simulations reproduce well the trends observed in the experiments reported in Fuenkajorn and Phueakphum (2010) (Fig. 4 and 5 in particular). Based on the results, we understand that it is critical to capture the transition between steady state creep and tertiary creep for geostorage in salt caverns. Continuous monitoring of the deformation, especially the deformation rate, at the cavern wall is essential. Once the hosting rock reaches tertiary state, its deformation increases rapidly, which could induce significant problems to geological storage facilities.

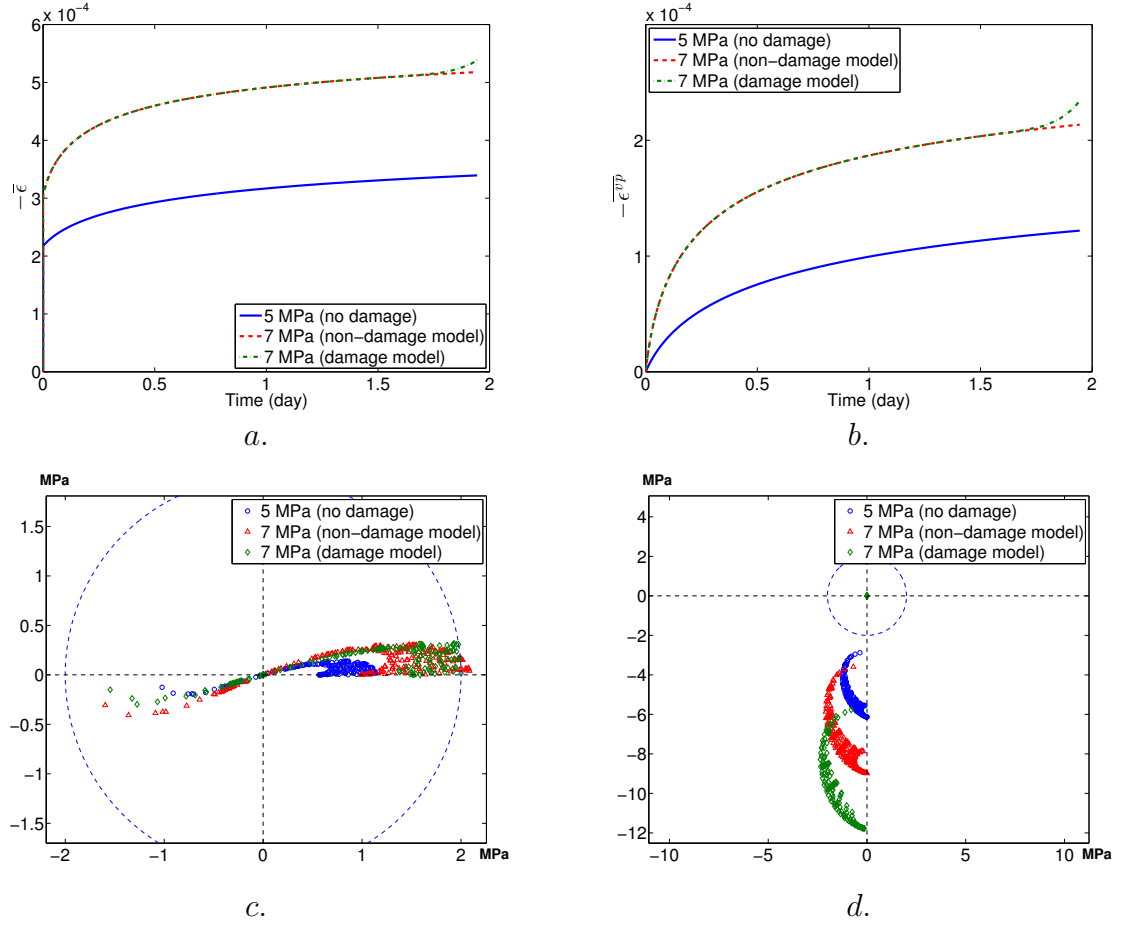


Figure 54 Comparison of different creep tests, with and without account for grain breakage. (a) Time evolution of total macrostrains. (b) Time evolution of viscoplastic macrostrains. (c) Major microstress component at the end of the creep tests. (d) Minor microstress component at the end of the creep tests.

4.8 *Simulation of Salt Fatigue under Cyclic Loading*

4.8.1 **Damage Triggering due to Grain Viscous Deformation**

The simulations presented in this subsection are performed with no account for grain breakage, in order to focus the discussion on the increase of microscopic stress leading to the initiation of damage due to grain breakage. The parameters calibrated for the long-term creep behavior are adopted: $\gamma_0 = 2.93 \times 10^{-5} \text{day}^{-1}$, $n = 4.04$.

4.8.1.1 *Effect of the Loading Frequency*

Stress-controlled cyclic loading tests are simulated, for the sinusoidal loading, with a maximum stress of 8 MPa and a loading amplitude of 2 MPa. Results after 15 cycles are compared for two frequencies typical of CAES conditions: 2 day^{-1} and 1 day^{-1} (Fig. 55a). The imposed stress rate depends on the frequency. Fig. 55b shows the resulting stress-strain curve, which is similar to the experimental curves reported in Fuenkajorn and Phueakphum (2010) (Fig. 7 in particular). The stress-strain cycles tend to a limit behavior, with a constant shifting at each cycle. This limit behavior has some analogy with the “accommodation” or “shakedown” effect in elastoplastic media. The determination of the limit cycle could enable the prediction of the response expected after a high number of cycles, without modeling the transient effects of intermediate cycles. Fig. 55c & d shows the distribution of internal stresses at the end of the loading tests, at the maximum stress. The results confirm that at higher frequency, less microscopic viscoplastic strains develop, which leads to smaller microscopic stresses.

4.8.1.2 *Effect of the Number of Cycles*

For the cyclic loading test simulated at a frequency of 2 day^{-1} , the distribution of internal stresses at maximum stress after 15 cycles (point B in Fig. 55a) is compared to that after the first loading cycle (point A in Fig. 55a). As expected, microscopic stresses increase with the number of cycles: the tensile microstresses in the grains

remain below the mono-crystal tensile strength after one cycle, and exceed the tensile limit after 15 cycles. Higher the number of cycles under the same loading frequency, longer the loading time, larger the microscopic viscoplastic strains, and higher the microstresses. In fact, the effect of the number of cycles is essentially an effect of time.

4.8.2 Viscous Damage Propagation upon Cyclic Loading

In the simulations presented in this subsection, grain breakage is accounted for. The parameters calibrated for the long-term creep behavior are adopted: $\gamma_0 = 2.93 \times 10^{-5} \text{day}^{-1}$, $n = 4.04$. The response of the polycrystal to a sinusoidal cyclic loading of frequency 0.03 Hz ($= 2592 \text{ day}^{-1}$) is studied for several maximum loading stresses and loading amplitudes. Two types of behaviors are observed:

(1) For small maximum stress and small loading amplitude, a limit cycle is reached. The number of broken grains (N_b) remains low, and Young's modulus decreases to finite limit value. An example is shown in Fig. 56, in which the maximum loading stress is 14 MPa and the amplitude is 6 MPa. Grain breakage first occurred at the 164th cycle. The whole polycrystal fails after the 191th cycle.

(2) For larger maximum stress or larger loading amplitude, failure occurs after a limited number of cycles. Fig. 57 shows the results obtained for a cyclic loading with a maximum loading stress of 20 MPa and an amplitude of 10 MPa. For minor principal microstresses, some grains experience zero stress, which indicates that they are broken. Grain breakage first occurred at the 6th cycle, and the whole polycrystal failed after the 8th cycle. The increasing number of broken grains is visible in the progressive reduction of the Young's modulus in the plot shown the macroscopic stress-strain curve. These results are in agreement with the experimental results reported in Fig. 7 of Fuenkajorn and Phueakphum (2010). Damage initiates after a low number of cycles, and the behavior becomes extremely brittle thereafter: total failure usually occurs less than five cycles after the initiation of damage.

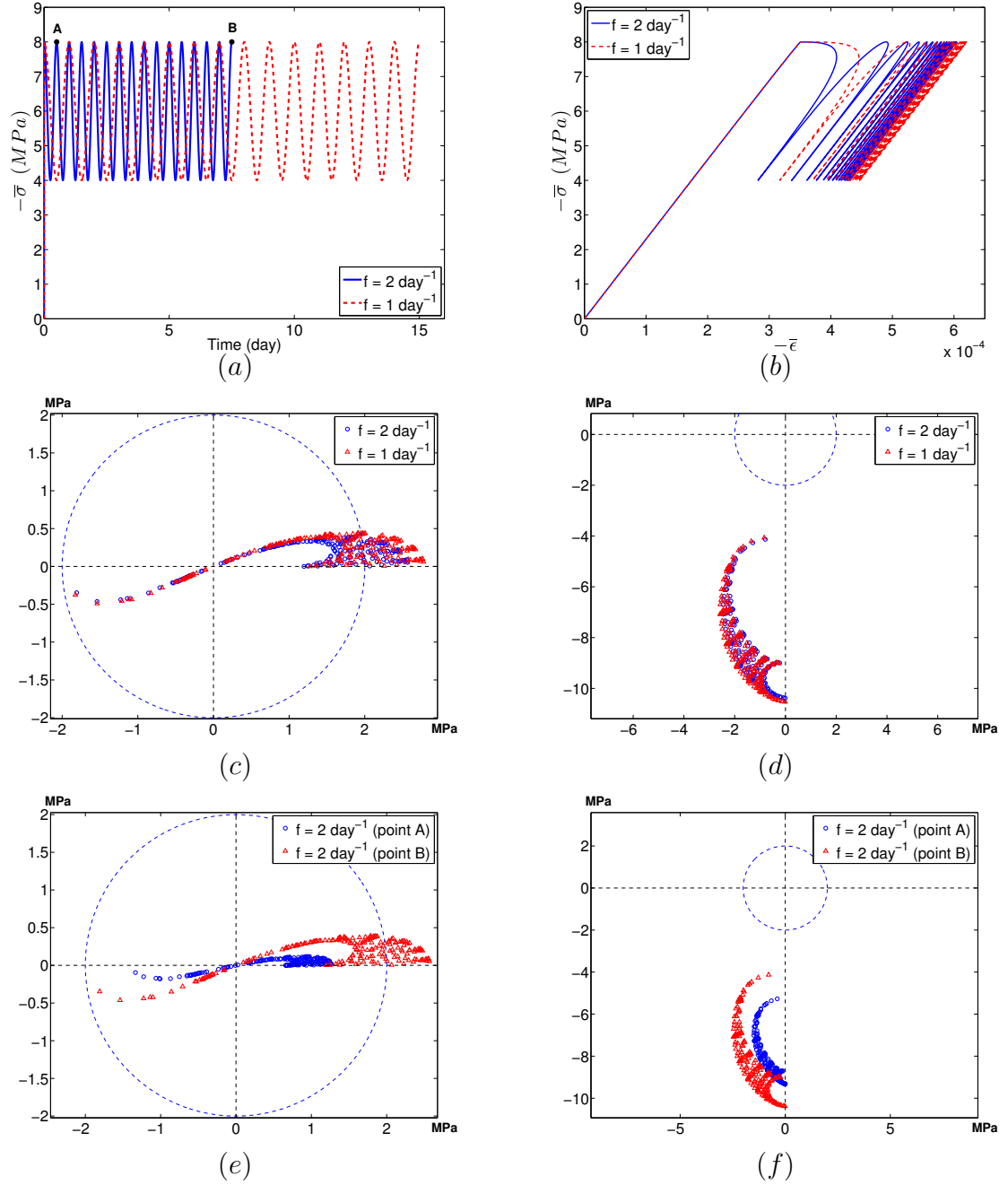


Figure 55 Effect of the frequency of loading on macroscopic strains, in the absence of grain breakage. (a) Cyclic loading history. (b) Evolution of macroscopic strains with macroscopic stress. (c) Major principal internal stress distribution at the end of the cyclic loading test. (d) Minor principal internal stress distribution at the end of the cyclic loading test. (e) Major internal stress distribution after 1 cycle (point A) and after 15 cycles (point B). (f) Minor internal stress distribution after 1 cycle (point A) and after 15 cycles (point B).

Under typical operational conditions, the CAES site is usually subjected to low frequency cyclic loadings. Simulation results indicates that it becomes more critical to check for early stage damage when the cavern pressure increases. Once damage is detected, the operation of the CAES site should be suspended until the damage issue can be solved. Otherwise, such damage may accumulate rapidly in the following loading cycles, with the possibility of leading to a detrimental failure. A typical CAES site is expected to sustain more than 700 loading cycles every year according to the daily cavern pressure change at the Huntorf CAES plant in Germany (Crotagino et al., 2001). The Huntorf power station is known as the first CAES plant in the world and has been successfully operated for 38 years since 1978.

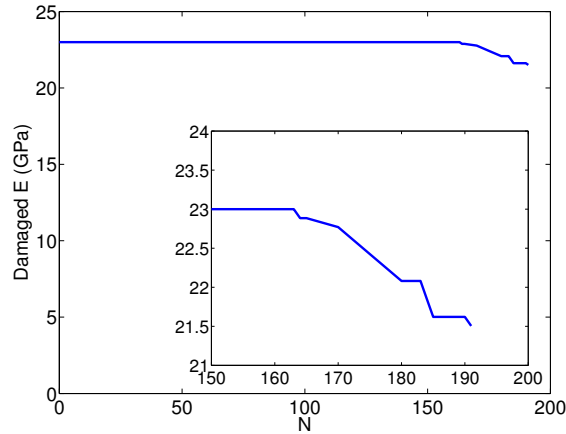


Figure 56 Evolution of the damaged Young's modulus with the number of cycles (f=0.03 Hz; maximum stress = 14 MPa; stress amplitude = 6 MPa).

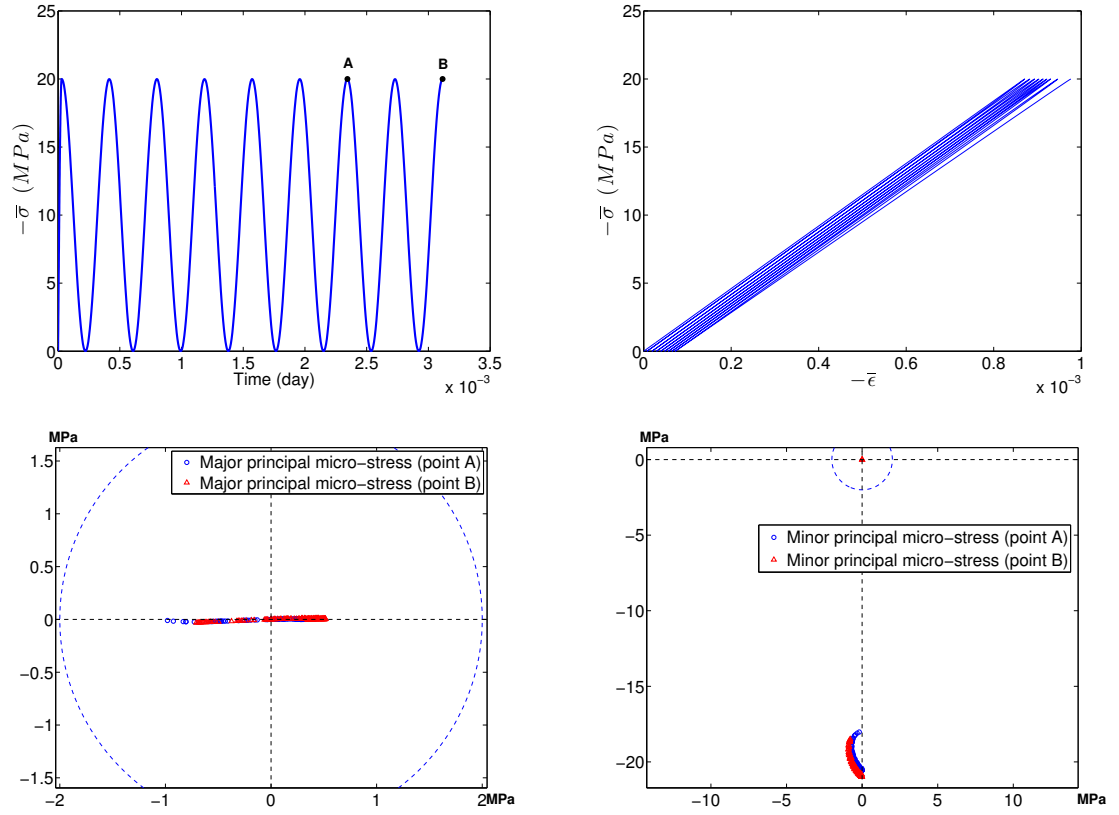


Figure 57 Simulation of a cyclic loading with a frequency of 0.03 Hz, a maximum loading stress of 20 MPa and an amplitude of 10 MPa (grain breakage considered). 2 grains are broken at A (after 6 cycles). 7 grains are broken at B (after 8 cycles).

4.9 Conclusions

In this chapter, we formulated a micromechanical model of viscous fatigue for salt rock, which was considered as an aggregate of halite mono-crystals. The REV contains mono-crystals that have a uniform distribution of orientations. Viscoplastic strains at the grain scale are triggered by the activation of preferential gliding mechanisms, which are governed by a power law. We related microscopic stresses to macroscopic stress, macroscopic viscoplastic strains and microscopic viscoplastic strains, by means of an inclusion-matrix model. We extended a self-consistent homogenization scheme, initially proposed for elasto-plasticity, to viscoplasticity. We introduced a grain breakage condition, which allowed predicting the progressive loss of stiffness and strength of the aggregate upon cyclic loading. Damage was defined as the ratio of the number of broken grains by the total number of grain orientations considered in the REV.

The micromechanical modeling approach enabled predicting important aspects of salt rock viscoplastic and damage behavior. Strain hardening during creep was evidenced by the increase of macroscopic viscoplastic strains at a decreasing rate, and by the progressive increase of microscopic stresses over time, until an asymptotic value. In creep tests in which a high compressive stress was applied before a lower compressive stress, tensile macroscopic strains were accompanied by a re-orientation of microscopic stresses towards an isotropic distribution: simulations provided a microscopic interpretation to the phenomenon known as “creep recovery”, which is a memory effect. Grain breakage occurred for creep tests under high stress, and for cyclic loading tests simulated at lower frequencies, higher maximum stress, and/or higher loading amplitude. As expected, the Young’s modulus decreases with the increase of damage. Grain breakage provides a micro mechanical explanation to the phenomenon known as “accelerated creep” (also called “tertiary creep”). The dependence of viscoplastic strains to cyclic loading frequency is well captured by the model:

higher the frequency, smaller the macroscopic viscoplastic strain, and smaller the microscopic stresses. The increment of macroscopic viscoplastic deformation decreased over the cycles, which is in agreement with the phenomenon of plastic adaptation or “shakedown” observed in elasto-plastic media. Such findings are critical in optimizing the usage of salt for geological storage purpose. For example, a comprehensive investigation of mechanical properties of salt will assist engineers in determining the feasible operational pressure and period for a CAES site.

The study of this “adaptation” effect was beyond the scope of this thesis. However, the determination of limit cycles would open interesting perspectives for the modeling the long term behavior of, for instance, salt caverns under cyclic loading. More work is needed to account for non-elastic inclusion/matrix interactions known as “viscous accommodation”, which results from geometric incompatibilities between grains. The micro-macro model is currently being improved in order to account for the progressive breakage of the grains in preferential directions, which is more representative than replacing broken grains by voids. Elastic anisotropy is introduced both at the grain and at the matrix scales:

$$\boldsymbol{\sigma} = \tilde{\mathbf{C}}(\mathbf{d}^{(n)}) : \boldsymbol{\varepsilon}, \quad \bar{\boldsymbol{\sigma}} = \mathbf{C}(\mathbf{D}) : \bar{\boldsymbol{\varepsilon}} \quad (81)$$

in which $\tilde{\mathbf{C}}(\mathbf{d}^{(n)})$ is the damage stiffness tensor of the n^{th} grain, \mathbf{d} represents the microscopic damage tensor, $\mathbf{C}(\mathbf{D})$ is the damage stiffness tensor of the matrix, and \mathbf{D} represents the macroscopic phenomenological damage tensor. The resulting matrix-inclusion interaction model is expressed as:

$$\boldsymbol{\sigma} - \bar{\boldsymbol{\sigma}} = -\mathbf{L}^*(\mathbf{D}) : (\boldsymbol{\varepsilon} - \bar{\boldsymbol{\varepsilon}}) \quad (82)$$

The main theoretical challenges are: (1) The linkage between grain unidirectional anisotropy and REV anisotropy, (2) The derivation of Hill’s tensor for an anisotropic elastic matrix (we are assuming ellipsoidal anisotropy in our current developments);

(3) The calculation of the macroscopic and microscopic responses through an iterative process.

CHAPTER V

FINITE ELEMENT ANALYSES APPLIED TO GEOSTORAGE SYSTEMS

5.1 *Introduction*

Finite Element Method (FEM) is a powerful numerical tool for modeling transient and coupled thermo-hydro-mechanical phenomena in engineering or physics problems. FEM allows accounting for heterogeneities and nonlinearities and is generally more time-efficient than other (discrete) methods. Nevertheless, the FEM has not been used extensively for fractured porous media, for two different reasons (Pouya, 2015). The first one is related to automatic mesh generation method for domains containing a great number of fractures. The second one is related to the difficult modeling of fracture-matrix interactions in various stress conditions. Dr. A. Pouya at Paris-Est University developed 2D numerical codes to address these issues. In this thesis, we use *POROFIS* (for *POROUS FISsured* media). Other tools are available, such as *DIS-ROC*, which permits the creation of FEM meshes for domains containing thousands of fractures in a few minutes. In *POROFIS*, transient problems are treated with the Euler explicit method for time integration, with very small time increments (Pouya, 2015). The geometry can be meshed by linear triangular or quadrilateral elements. *POROFIS* is written in Fortran and requires using the FEM pre- and post-processor *GiD* (GiD, 2002) for mesh generation and results visualization.

In Section 5.2, we compared a *POROFIS* model that contains Finite Elements and joint elements with micro-macro model presented above in Chapter 4. We simulated intra- and inter-granular damage in salt polycrystal subjected to creep and cyclic loadings. In Section 5.3, we used phenomenological models of secondary and tertiary

creep in order to simulate the accumulation of viscous damage around a salt cavern subject to depressurization with the FEM.

5.2 *Inter-granular and Intra-granular Damage in Salt Polycrystal*

5.2.1 Single-crystal Deformation Mechanisms

In Chapter 4, we presented an inclusion-matrix model of grain breakage, based on a 3D self-consistent method. In the following, we compare our homogenized model to a 2D Finite-Element based model that distinguishes intra- and inter- granular damage. In order to make this comparison and see the benefits of both modeling approaches, we start by adapting our homogenization scheme to 2D plane strain conditions. In plane strain, all representative salt crystal orientations are contained in the plane, i.e. representative grain orientations are obtained by rotation about the axis normal to the plane under study, as shown in Fig. 58.

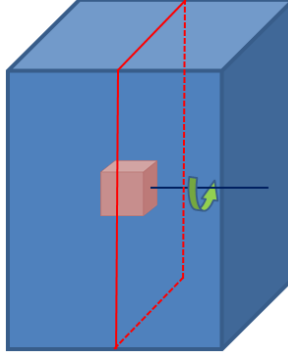


Figure 58 2D salt polycrystal: representative halite crystal orientations are obtained by varying only one degree of freedom, the angle of rotation θ about the axis normal to the plane.

In a two-dimensional plane strain case, two of the six salt slip systems control shear deformation (Fig. 59). The two slip systems are oriented by an angle of 90 degrees. We note \mathbf{N} and \mathbf{M} the normal vector and the gliding vector in the local coordinate system of the grain, respectively.

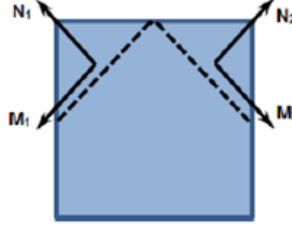


Figure 59 Representation of the two slips systems that control shear deformation at the grain scale in 2D plane strain (\mathbf{N} and \mathbf{M} are the normal vector and gliding vector, respectively).

Given a specific angle θ , the two possible slip systems in the global coordinate system $(\mathbf{n}^1, \mathbf{m}^1)$ and $(\mathbf{n}^2, \mathbf{m}^2)$ are:

$$\mathbf{n}^1 = \begin{pmatrix} \cos(\theta + \frac{\pi}{4}) \\ \sin(\theta + \frac{\pi}{4}) \end{pmatrix}, \quad \mathbf{m}^1 = \begin{pmatrix} \cos(\theta + \frac{3\pi}{4}) \\ \sin(\theta + \frac{3\pi}{4}) \end{pmatrix} \quad (83)$$

$$\mathbf{n}^2 = \begin{pmatrix} \cos(\theta + \frac{3\pi}{4}) \\ \sin(\theta + \frac{3\pi}{4}) \end{pmatrix}, \quad \mathbf{m}^2 = \begin{pmatrix} \cos(\theta + \frac{\pi}{4}) \\ \sin(\theta + \frac{\pi}{4}) \end{pmatrix} \quad (84)$$

5.2.2 Hill's Tensor in 2D

The Hill's tensor for a spherical inclusion embedded in a 3D isotropic elastic matrix is available in the literature (e.g., (Hill, 1965)). To express Hill's tensor for a 2D plane strain case, we consider the spherical inclusion as a cylinder of circular section ("borehole") subject to internal pressure and far-field stresses (Fig. 60). The solution is obtained by superimposing three independent displacement fields that correspond to three independent stress fields in plane strain conditions: (1) Displacements induced by an isotropic pressure field applied at the borehole wall; (2) Pure shear displacements; (3) Homogeneous displacements. The detailed derivations are provided in Appendix IV. The Hill's tensor \mathbf{L}^* for 2D plane strain conditions is finally expressed as:

$$L_{ijkl}^* = \frac{E}{2(1+\nu)(3-4\nu)} \left[\frac{1-2\nu}{\nu} \delta_{ij} \delta_{kl} + (\delta_{ik} \delta_{jl} + \delta_{il} \delta_{jk}) \right], \quad (85)$$

in which E and ν are the Young's modulus and Poisson's ratio of the matrix, and δ is the 2D identity tensor. We verified the solution for the asymptotic case in which an internal pressure σ_p is applied on the inner wall of a borehole that has an outer radius that tends to infinity.

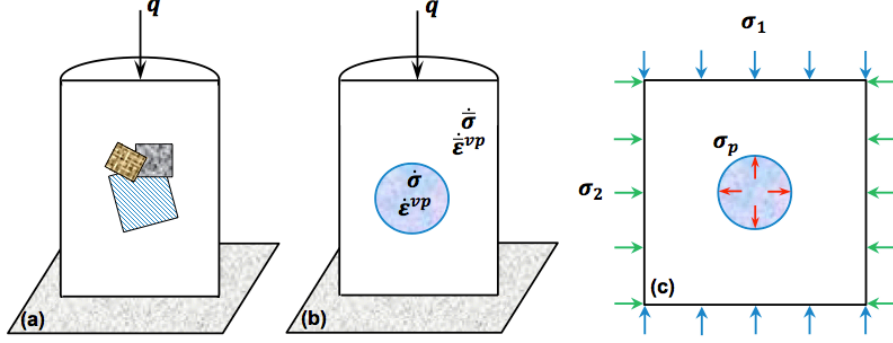


Figure 60 Cross-sectional view of the salt rock REV considered in the homogenization scheme. (a) Salt polycrystal; (b) Inclusion-matrix model; (c) Equivalence of the grain-matrix interaction problem with that of a borehole subject to internal pressure and far-field stresses.

5.2.3 Joint Element Model

To design a numerical model in which salt grains are modeled with Finite Elements (FE), and cracks are modeled with joint elements, we use *POROFIS* as introduced in Section 5.1. Grain FEs are assigned the single-crystal viscoplastic behavior described in Subsection 5.2.1, and different crystal orientations are accounted for by using FEs with different slip mechanisms (see Subsection 5.2.4). For the joint elements, we adopt the strength model presented in Pouya and Yazdi (2015). Strength evolves with damage (D) as follows:

$$F(\sigma, D) = \tau^2 - \sigma_n^2 \tan^2 \eta + 2g(D)\sigma_c \sigma_n - g^2(D)C^2 \quad (86)$$

in which C and η are respectively the cohesion and the friction angle of intact rock joints. Stresses at joint faces (σ) are related to the joint stiffness (k) and to the joint

relative displacement (\mathbf{u}) by the following elastic damage law:

$$\boldsymbol{\sigma} = (1 - D)\mathbf{k} : \mathbf{u} \quad (87)$$

The expression of $g(D)$ is (Pouya and Yazdi, 2015):

$$g(D) = (1 - D)(1 - \beta \ln(1 - D)) \quad (88)$$

in which $g(D = 0) = 1$ represents the initial intact state and $g(D = 1) = 0$ represents the completely damaged state (i.e. ultimate failure). σ_c is a constant related to C , η , and to the tensile strength σ_R of the intact rock joint by the following relation:

$$\sigma_c = \frac{C^2 + \sigma_R^2 \tan^2 \eta}{2\sigma_R} \quad (89)$$

in which σ_c is an auxiliary stress value related to the shape of the yield surface (Fig. 61). When $g = 1$, we obtain the outer hyperbolic surface. The asymptotic behavior under high compressive stresses corresponds to a conical surface that forms an angle η with the σ_n axis. When damage increases, the yield surface moves towards the interior while the friction angle η remains the same. For the limiting case of a completely damaged joint with $g = 0$, the frictional fracture has zero cohesion and the friction angle η satisfies the following criterion:

$$F(\tau, \sigma_n) = \tau^2 - \sigma_n^2 \tan^2 \eta \quad (90)$$

As can be seen in Fig. 61, the tensile strength σ_R and the cohesion parameter C have to satisfy the following inequality:

$$\sigma_R \tan(\eta) < C \quad (91)$$

Under a normal tensile stress, the cohesive joint remains undamaged until a critical displacement value u_0 is reached. The corresponding damage D is assumed to depend exponentially on the relative displacement:

$$D = 1 - e^{-(u-u_0)/\beta u_0} \quad (92)$$

in which the constant parameter β characterizes the material ductility (the smaller β , the more brittle the material behavior). Note that damage models similar to that presented in Eq. 92 are often used for interfaces in cementitious materials (Jefferson, 1998).

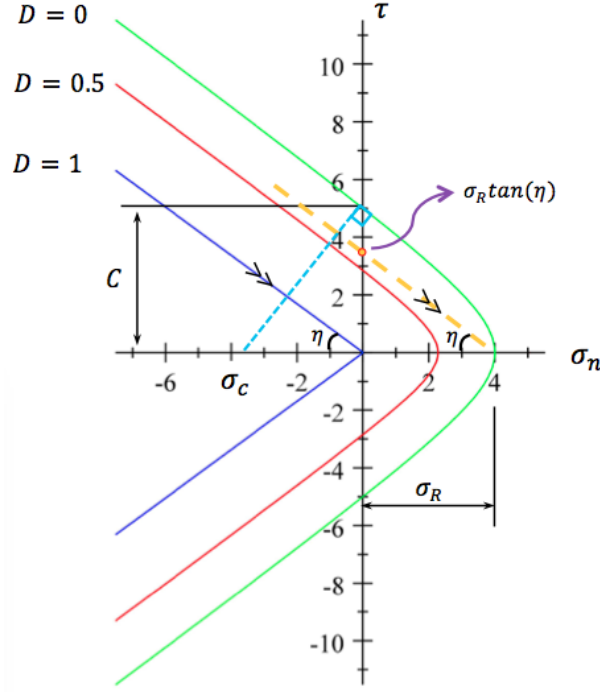


Figure 61 Evolution of the damage-plasticity criterion used in joint elements, from the intact state to the completely damaged state. The yellow dashed line is parallel to the line that represents the limiting criterion when $D = 1$, and intersects the τ axis at $\sigma_R \tan(\eta)$.

5.2.4 Model Configuration

We used *POROFIS* to model a single inclusion embedded in a homogeneous medium (Zhu et al., 2015a). The match between this FEM model and the 3D inclusion-matrix model was satisfactory. The next step, presented in detail in the following, is to model a polycrystal made of a representative number of inclusions (i.e., grains). However, 3D images of halite microstructure are scarce in the literature. Several methods can

be used to represent crystal orientations in 2D micrographs, including optical and electron microscopy, automated Electron BackScatter Diffraction (EBSD) and serial sectioning techniques (Lewis and Geltmacher, 2006). In the following, we construct a 2D FEM polycrystal model based on the EBSD map of the salt specimen studied by Schleder and Urai (2007). Crystal orientations are represented by different colors in the EBSD map (Fig. 62).

We use the software *Plot Digitizer* to extract grain boundaries from the EBSD map, and we export them in *GiD* in order to construct the mesh. For the sake of simplicity, we select only 12 crystal orientations for this 2D model (in which θ is the only orientation angle that varies). These 12 grain FE orientations are uniformly distributed in the interval $[\cos(\theta = 0) = 0, \cos(\theta = \frac{\pi}{2}) = 1]$, in order to follow the same microstructure assumptions as in the inclusion-matrix model, and to approximately match the orientations represented in the EBSD map. Our mesh contains a relatively isotropic and uniform distribution of grains with various orientations, which is a realistic representation of a salt polycrystal. We construct two FEM models with: (1) Joint elements that are only located along the grain boundaries (inter-granular cracks); and (2) Joint elements that are located both between and inside the grains (inter- and intra- granular cracks). In total, model (1) comprises 3,368 surface elements, which are all 0.2 mm in size (Fig. 63). In model (2), inter-granular and intra-granular joint elements follow the same behavior (Subsection 5.2.3), but have different constitutive parameters (Fig. 64).

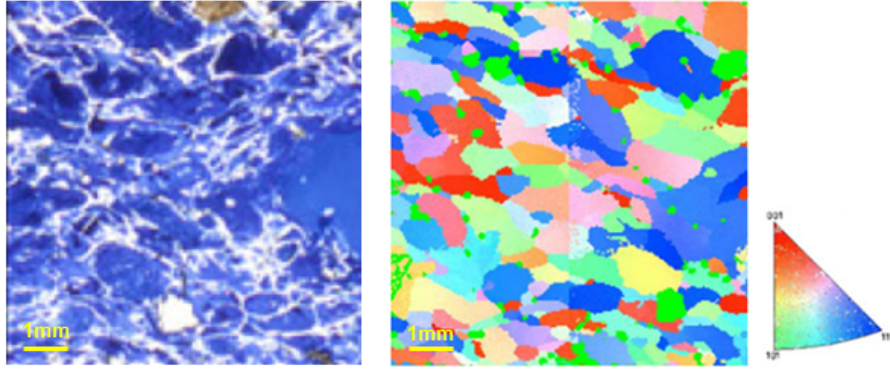


Figure 62 Salt thin sections (adapted from Schleder and Urai (2007)): Microstructure (left) and Automated EBSD map (right).

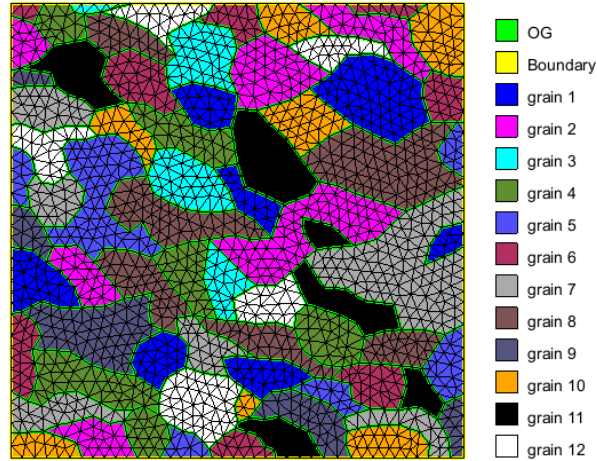


Figure 63 *POROFIS* FEM model with inter-granular joints only (8mm \times 8mm). In the legend, grain numbers refer to grain orientations (12 orientations considered in total), and OG is the color used for joint elements.

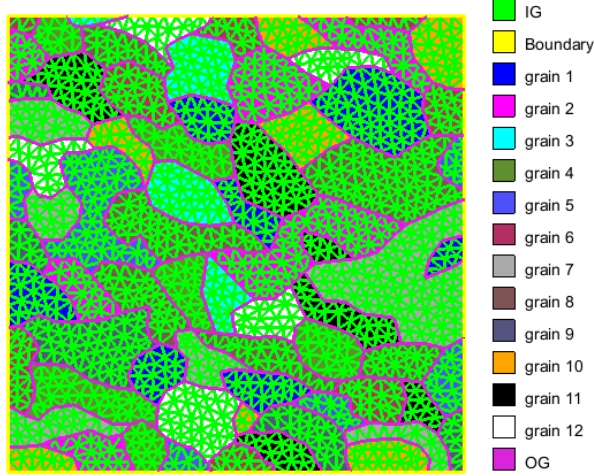


Figure 64 *POROFIS* FEM model with inter-granular and intra-granular joints (8mm \times 8mm). In the legend, grain numbers refer to grain orientations (12 orientations considered in total), OG is the color used for inter-granular joint elements, and IG is the color used for intra-granular joint elements.

5.2.5 Model Calibration

The *POROFIS* model requires the calibration of: (a) the elastic properties and viscous parameters of the grain Finite Elements; (b) the stiffness and damage parameters of the joint elements. For the elastic properties of single-crystals (grain FEs), we take a Young's modulus of 43 GPa (in reference to experimental data published in (Simmons and Wang, 1971)) and a Poisson's ratio of 0.3 (in reference to experimental data published in (Fuenkajorn and Phueakphum, 2010)). Note that the stiffness of a single-crystal is greater than that of halite polycrystal (typically, 23 GPa according to (Fuenkajorn and Phueakphum, 2010)). This statement is true in other materials such as Ottawa sand: the Young's modulus of a single sand particle is 105 GPa (Dutta and Penumadu, 2007), whereas the Young's modulus of Ottawa sandstone is only 1 GPa (Dittes and Labuz, 2002). In order to be consistent with the inclusion-matrix model, we perform the calibration in plane strain conditions, according to the three following steps:

1. We determine the stiffness of the inter-granular joint elements by matching the global Young's modulus of the *POROFIS* model with that of a reference specimen tested experimentally;
2. With the calibrated inter-granular joint stiffness, we calibrate the viscous parameters of the grain FEs so as to match the steady-state strain rate observed during secondary creep in the reference experiments;
3. We determine the inter-granular joint strength by matching the time of tertiary creep initiation predicted with *POROFIS* with that measured experimentally.

Table 12 summarizes the joint-enriched Finite Element parameters calibrated for the *POROFIS* model, and the calibration procedure is detailed below.

Table 12 Parameters calibrated for the *POROFIS* model with inter-granular joints only.

Grain			
E (GPa)	ν (-)	γ_0 (day^{-1})	n (-)
4.3×10^4	0.3	2.0×10^{-5}	4.0
Inter-granular Joint			
k_t (MPa/mm)	k_n (MPa/mm)	k_{tn} (MPa/mm)	σ_R (MPa)
1.0×10^4	1.0×10^5	0	6.13
C (MPa)	η (degrees)	β (-)	
6.13	30	1.0	

Stiffness of inter-granular joints. In order to obtain the global stress-strain curve of the *POROFIS* model (as opposed to the stress-strain curve of individual FEs or joint elements), we calculate the average values of stresses and strains over the entire set of integration points. The reference Young's modulus of the polycrystal (23 GPa) is measured experimentally during a uniaxial compression test (Fuenkajorn and Phueakphum, 2010). As shown in Fig. 65 and 66, in a log scale, the global Young's modulus calculated numerically increases almost linearly with the joint stiffness. For

very high values of the joint stiffness, the numerical specimen behaves like a solid made of grains that are perfectly glued together, and the global Young's modulus calculated numerically tends towards the Young's modulus of the grain element (43 GPa). We study five ratios k_t/k_n (k_t is the joint tangential stiffness, k_n is the joint normal stiffness). The green dashed lines in Fig. 65 and 66, for $k_t = 2 \times 10^3$ MPa/mm and $k_n = 2 \times 10^3$ MPa/mm respectively, show that the global Young's modulus is more impacted by changes of normal stiffness than by changes of tangential stiffness. Therefore we calibrate only the normal joint stiffness and assume a fixed ratio k_t/k_n . Because this study focuses on crack propagation induced by internal glide and inter-granular slip, we consider that the tangential joint stiffness is smaller than the normal joint stiffness: $k_t = 0.1k_n$. The red dashed lines in Fig. 65 and 66 represent the value of the Young's modulus of the reference specimen (23 GPa). In Fig. 66, the intersection between the red line and the curve that shows the variations of the global Young's modulus for $k_t = 0.1k_n$ provides the calibrated value of the normal joint stiffness. We obtain: $k_n = 1 \times 10^5$ MPa/mm and $k_t = 1 \times 10^4$ MPa/mm.

Viscous parameters of the grain FEs. We obtain the viscous parameters (γ_0 , n) of the grain elements by matching the steady strain rate predicted by *POROFIS* with the strain rate predicted by the inclusion-matrix model presented in Chapter 4 for a uniaxial creep tests simulated in the experimental conditions described in (Fuenkajorn and Phueakphum, 2010) (Fig. 67). The correlation established between the steady state creep rate and the creep loading stress made it possible to calibrate the two viscoplastic parameters. We obtained: $\gamma_0 = 2.0 \times 10^{-5} \text{ day}^{-1}$, $n = 4.0$. We simulated two other uniaxial creep tests, performed under 2 and 15 MPa (black triangles in Fig. 67), and verified that the calibrated values of (γ_0 , n) were satisfactory.

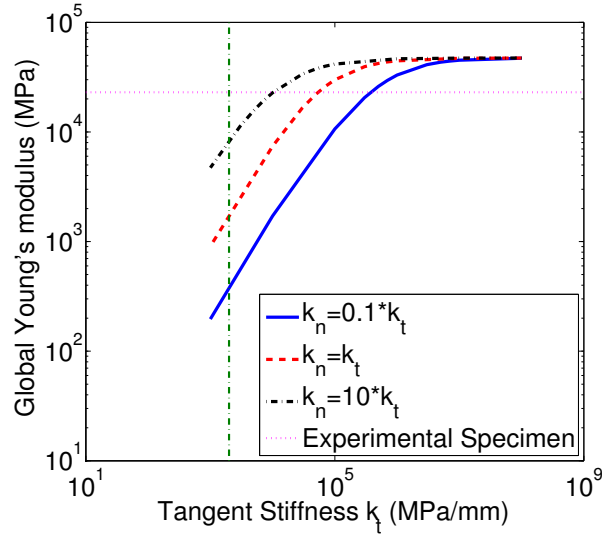


Figure 65 Evolution of the Young's modulus of the *POROFIS* model with intergranular joints only, for different values of joint tangential stiffness, and for three ratios of tangential vs. normal stiffness.

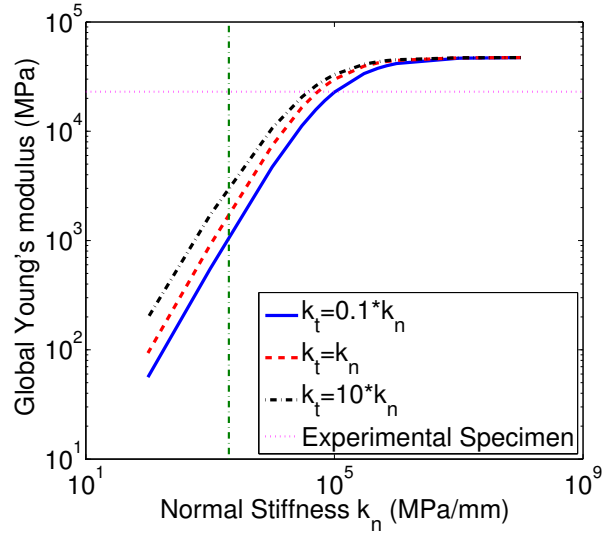


Figure 66 Evolution of the Young's modulus of the *POROFIS* model with intergranular joints only, for different values of joint normal stiffness, and for three ratios of tangential vs. normal stiffness.

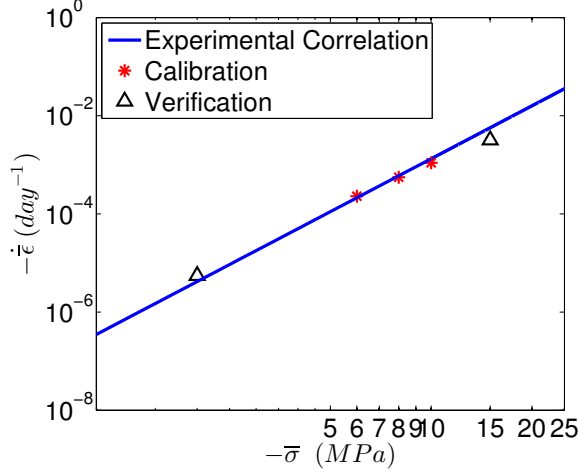


Figure 67 Correlation between macroscopic axial strain rate and macroscopic axial stress, obtained from the simulation of the uniaxial creep tests with *POROFIS*, in plane strain. The correlation line is obtained from a previous numerical study (Pouya et al., 2016) based on experimental results reported in (Fuenkajorn and Phueakphum, 2010). Red stars: numerical results used for calibration. Black triangles: numerical results used for verification.

Tensile strength of the inter-granular joint elements. As explained in Subsection 5.2.3, the joint strength criterion depends on the tensile strength parameter σ_R , the joint cohesion C , the joint friction angle η , and the ductility parameter β . At the transition between secondary and tertiary creep, the strain rate increases significantly. We expect that the initiation of tertiary creep will take more time when the joint strength, the joint cohesion, or the joint ductile parameter increases. In uniaxial creep tests performed under 30 MPa (Fuenkajorn and Phueakphum, 2010), the initiation of tertiary creep occurred after 0.22 days (i.e. 5.2 hours). A good match is found for $\sigma_R = C = 6.13$ MPa, $\eta = 30^\circ$, and $\beta = 1$ (along with the calibrated values for joint stiffness and grain viscous parameters). We verify that the tensile strength of the joint satisfies the criterion stated above (Eq. 91).

Fig. 68 confirms that lower strength values (5 MPa, 6 MPa) lead to an early triggering of tertiary creep, while higher strength values (7 MPa, 10 MPa) lead to

a later triggering of tertiary creep. It was expected that the tensile strength of the joints would be lower than that of the grains and higher than that of the polycrystal, because the joints represent defects that are naturally present in the polycrystal. We verified that the transition between secondary and tertiary creep was independent from the time increment size used in the simulations.

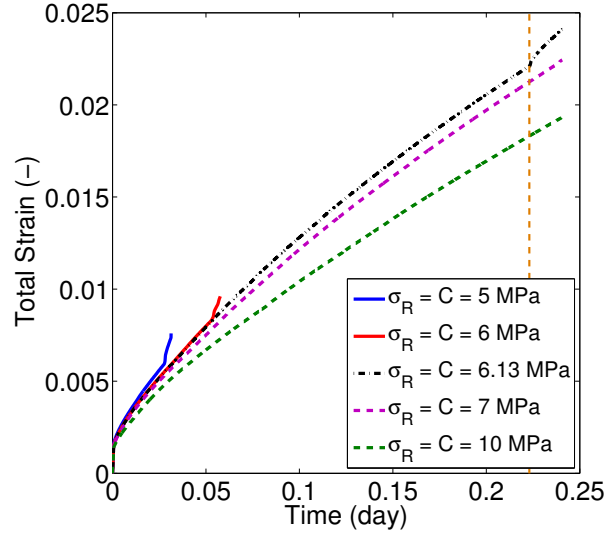


Figure 68 Calibration of the joint element strength parameters of the *POROFIS* model. For $\sigma_R = 5$ MPa, 6 MPa, and 6.13 MPa, the creep acceleration noted at the end of the simulation corresponds to the initiation of tertiary creep. The vertical dashed line (at $t=0.22$ days) indicates the initiation of tertiary creep noted during a uniaxial creep test performed under 30 MPa (Fuenkajorn and Phueakphum, 2010).

5.2.6 Comparison of the Inclusion-matrix Models with Joint-enriched FEM Models

We compare the effects of viscous damage and fatigue mechanisms that operate in halite polycrystals during uniaxial creep loading tests. We use the three following models:

1. *POROFIS* model (1): inter-granular crack propagation accounted for by damage evolution in one family of joint elements; 3,368 surface elements and 678

inter-granular joint elements; calibrated parameters presented in Subsection 5.2.5;

2. *POROFIS* model (2): inter-granular and intra-granular crack propagation accounted for by damage evolution in two families of joint elements; 3,368 surface elements, 678 inter-granular joint elements and 4,294 intra-granular joint elements; calibrated parameters presented in Subsection 5.2.5, with additional intra-granular joint parameters (see below);
3. Inclusion-matrix model programmed in MATLAB (in plane strain): polycrystal damage evolution accounted for by grain breakage; 200 possible grain orientations; calibrated parameters presented in Section 4.6.

We simulated a uniaxial creep test with the inter-granular crack propagation Finite Element model (1) and with the matrix-inclusion model of grain breakage (3). We used plane strain conditions in the *POROFIS* model (1), in order to be consistent with the formulation of the homogenization model (3). The axial stress was 35 MPa, which corresponds to the maximum stress amplitude that can be applied at the wall of a salt cavern by depressurization after sealing and abandonment (Bérest and Brouard, 2003). The time evolution of the axial stress applied during the simulations is shown in Fig. 69.

Contrary to the inclusion-matrix model (3), the joint-enriched Finite Element model (1) accounts for the geometric incompatibilities induced by shear deformation in the grains and by sliding relative displacements along grain boundaries. As expected, the macroscopic deformation of the polycrystal modeled with Finite Elements is higher than that of the polycrystal modeled with the self-consistent method (Fig. 70). For instance, the axial deformation predicted by model (1) at the end of the creep test is twice higher than that predicted with model (3). The strain-time history also indicates that the inclusion-matrix model predicts ultimate failure at the end of the test (after 0.012 days, which is about 17 minutes), whereas the joint-enriched

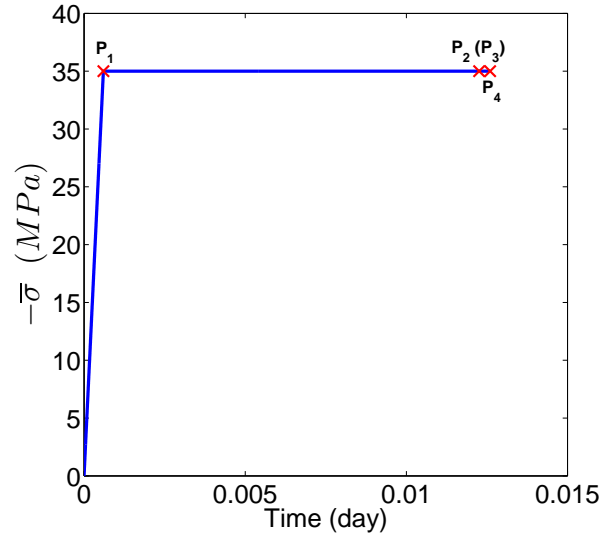


Figure 69 Stress-time input for the axial creep test simulated with models (1) and (3). P_1 indicates the time needed to apply the total loading stress, which is increased incrementally up to 35 MPa. P_2 (respectively P_3) marks the time just before (respectively after) the transition between secondary and tertiary creep. P_4 indicates the end of the creep test.

FEM model predicts that the polycrystal is still in steady state at the end of the creep test.

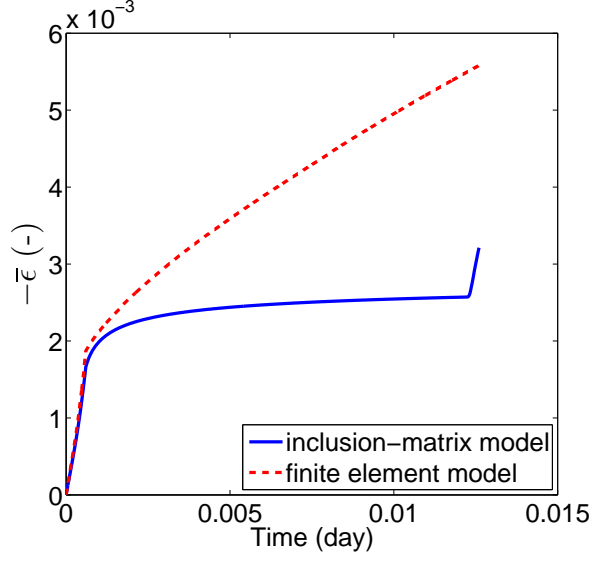


Figure 70 Time evolution of the macroscopic axial deformation of the polycrystal during the uniaxial creep test simulated with the joint-enriched FEM model of inter-granular crack propagation (1) and with the inclusion-matrix model of grain breakage (3).

In both models (1) and (3), the viscous grain parameters were calibrated so as to match secondary creep strain rates measured experimentally. In the inclusion-matrix model (3), the initiation of tertiary creep coincides with the first grain breakage that occurs in the polycrystal (Pouya et al., 2016; Zhu et al., 2015c). In the joint-enriched FEM model (1), joint strength was calibrated so as to capture the initiation of tertiary creep at the scale of the polycrystal. Therefore damage can propagate in the inter-granular joints before the initiation of tertiary creep, which corresponds to the coalescence of inter-granular cracks. In the present case, inter-granular cracks propagate during the incremental loading phase, before the creep stress loading is fully applied (see Fig. 74b). As a result, the stiffness of the polycrystal predicted with the FEM is less than the stiffness of the (intact) polycrystal modeled with the self-consistent method. This is the reason why the slope of the stress-strain curve during the initial loading phase is smaller for model (1) than for model (3), as can be

seen in Fig. 71.

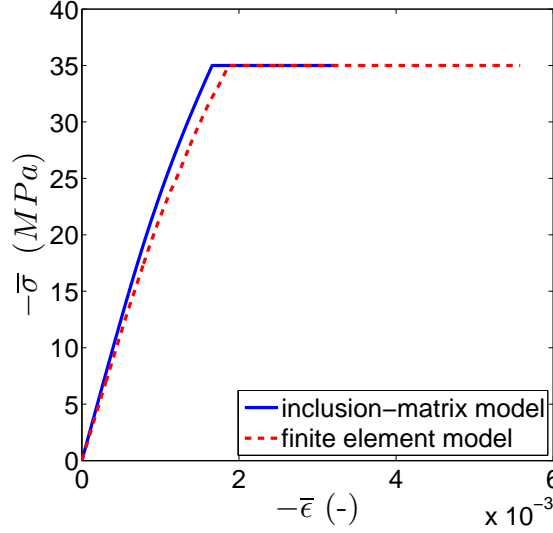


Figure 71 Macroscopic stress-strain curve of the polycrystal during the uniaxial creep test simulated with the joint-enriched FEM model of inter-granular crack propagation (1) and with the inclusion-matrix model of grain breakage (3).

The distributions of major and minor microscopic stresses in the inclusion-matrix model are shown in Fig. 72 and 73, respectively. Each point in the figure represents a principal stress value for one of the 200 grain orientations considered in the polycrystal. P_1 marks the state of the polycrystal after completion of the loading; P_2 (respectively P_3) marks the state of the polycrystal just before (respectively after) the transition between secondary and tertiary creep. At stage P_1 , the polycrystal is subjected to the total macroscopic stress load (35 MPa), but viscoplastic deformation in the grains has not started. At stage P_2 , viscous shear deformation in the grains induce stress concentrations within the polycrystal, which translates into higher microscopic stresses (more compression, and more tension). Microscopic slip mechanisms result in a redistribution of microscopic stresses. In particular, tensile microscopic stresses increase continuously in the lateral directions until the strength threshold is reached (Fig. 72). The maximum tensile micro-stress noted in the polycrystal is 7.495 MPa,

which corresponds to the grain tensile strength. At stage P_3 , the tensile stress in some grains exceeds the grain tensile strength, which results into local grain breakage (i.e., zero micro-stress in Fig. 73) and global stress redistribution. To restore the stress balance, non-broken grains become subjected to larger compressive stress in both axial and lateral directions (Fig. 72 and 73).

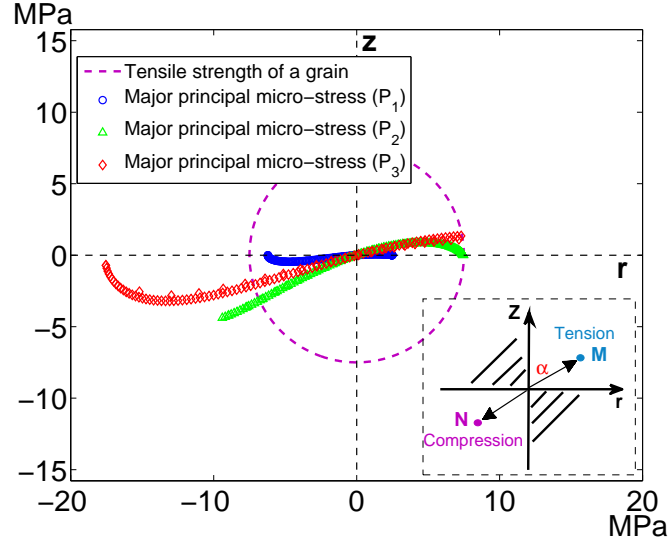


Figure 72 Distribution of the major principal micro-stresses of the polycrystal during the creep test simulated with the inclusion-matrix model.

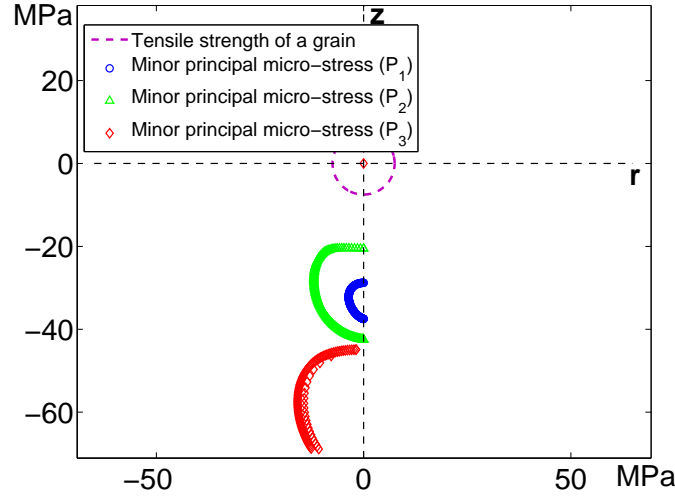


Figure 73 Distribution of the minor principal micro-stresses of the polycrystal during the creep test simulated with the inclusion-matrix model.

Post-processed Finite Element results explain the differences between the two models noted in Fig. 70 and 71. In model (1), concentrations of vertical stress are noted at the contact of angular grains even before the initiation of creep (Fig. 74a), which results in inter-granular slip and subsequent damage in some joints that are parallel to the loading axis (Fig. 74). At the end of the creep test, viscous shear deformation in the grains induces more geometric incompatibilities, which results in higher stress (Fig. 75a) and inter-granular crack coalescence (Fig. 75b). By contrast, in model (3), geometric incompatibilities are not accounted for, and ultimate failure occurs shortly after the first grain breakage. We conclude that the joint-enriched FEM model of inter-granular crack propagation provides a more realistic representation of the microstructure evolution and of the creep behavior of halite than the inclusion-matrix model. The main advantage of the inclusion-matrix model (3) is that it is less computation-intensive than a detailed Finite Element model like model (1).

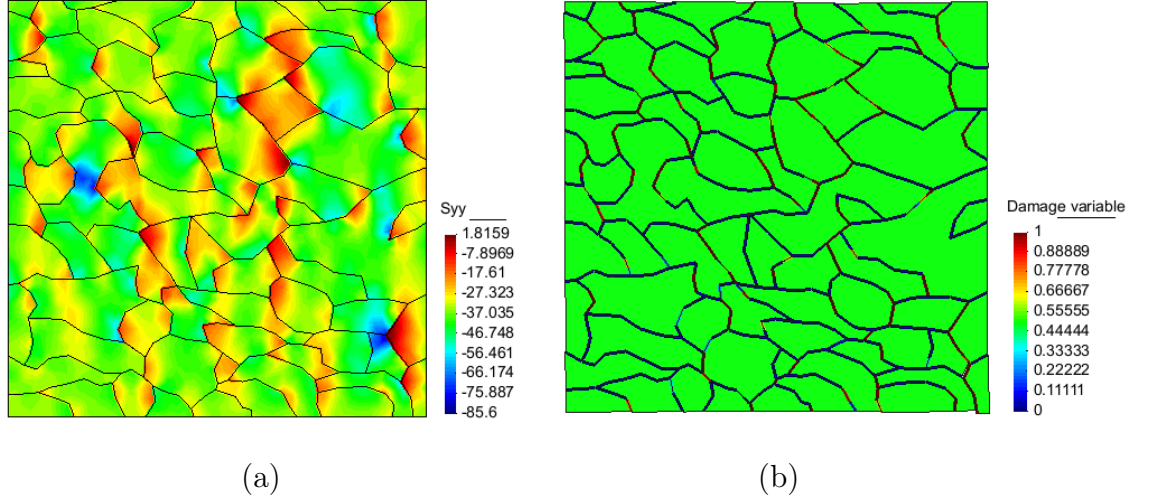


Figure 74 Results of the creep test obtained with the joint-enriched FEM inter-granular crack propagation model (1) after the initial loading phase (P_1): (a) vertical stress (in MPa); (b) damage in the joint elements - deformed mesh ($10\times$).

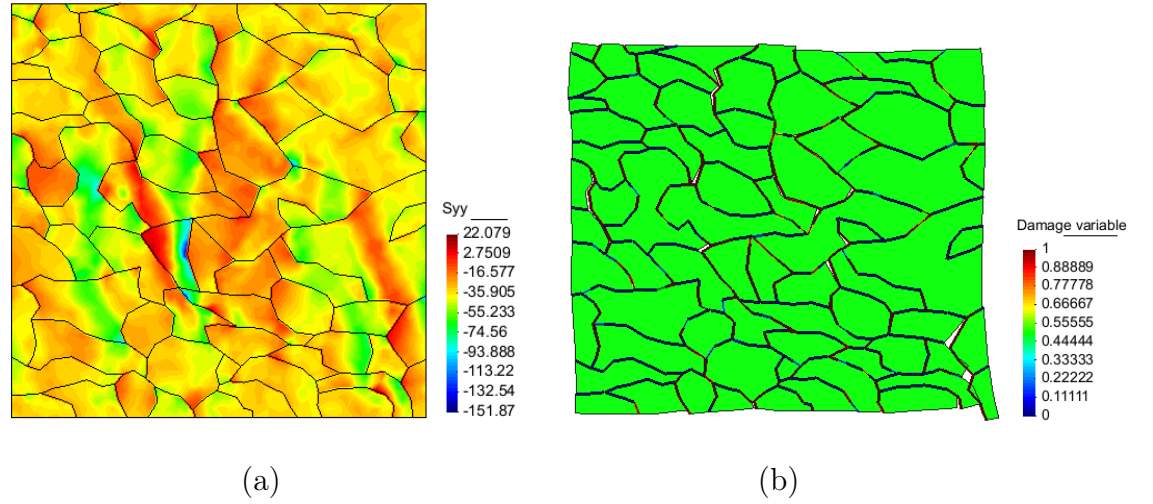


Figure 75 Results of the creep tests obtained with the joint-enriched FEM inter-granular crack propagation model (1) at the end of the creep test (P_4): (a) vertical stress (in MPa); (b) damage in the joint elements - deformed mesh ($10\times$).

To examine the influence of intra-granular crack propagation, we present a creep

test simulated in plane stress conditions under an axial loading stress of 9 MPa with the joint-enriched FEM model (2), which accounts for both intra- and inter- granular crack propagation. Model parameters are the same as for model (1) for the grain finite elements and for the inter-granular joint elements (see Subsection 5.2.5). We calibrate the intra-granular joint stiffness so as to maintain a global Young's modulus of 23 GPa for the polycrystal. In the absence of reference data on the tensile strength of a single crystal, we assume that the intra-granular joints have a higher strength than the inter-granular joints. For intra-granular joint elements, we choose $\sigma'_R = 7.495$ MPa, which is the same as the tensile strength of the grain in the inclusion-matrix model. Note that for inter-granular joint elements, we had $\sigma_R = 6.13$ MPa.

Fig. 76 shows the vertical (i.e. axial) stress distribution in the polycrystal at the end of the creep test. Most stress concentrations are located around joints where several angular grains are in contact. As a result, damage in the joints is mainly observed at the edges of the most angular grains (Fig. 77). Note that for the particular creep test simulated with model (2), damage propagates in intra-granular joints only (i.e. we observe no damage in inter-granular joints). It would be interesting to determine the tensile and shear strengths of the single crystal in order to understand in which loading conditions cracks initiate, propagate and coalesce within the grains as opposed to between the grains.

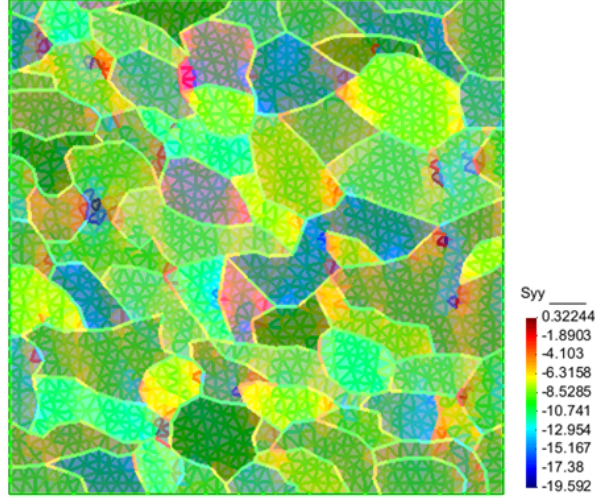


Figure 76 Vertical stress distribution (S_{yy} , MPa) at the end of the uniaxial creep test simulated with the joint-enriched FEM model that accounts for both intra- and inter-granular crack propagation. The test duration was 0.018 day, i.e. about 26 minutes.

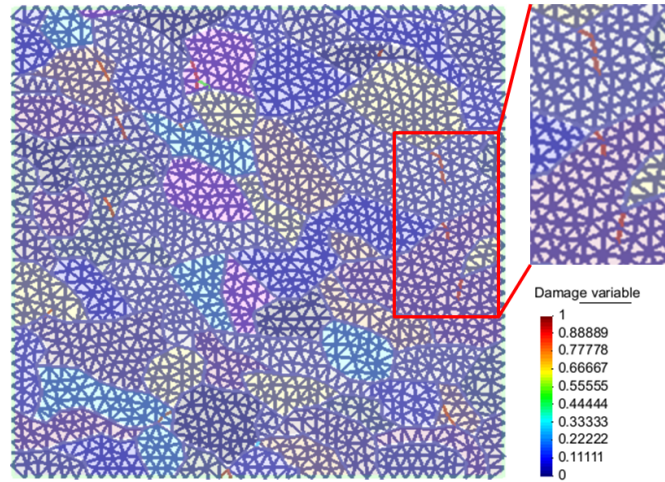


Figure 77 Distribution of damage in the joints at the end of the uniaxial creep test simulated with the joint-enriched FEM model that accounts for both intra- and inter-granular crack propagation. The test duration was 0.018 day, i.e. about 26 minutes.

5.2.7 Cyclic Loading Tests with the Joint-enriched FEM Model of Inter-granular Crack Propagation

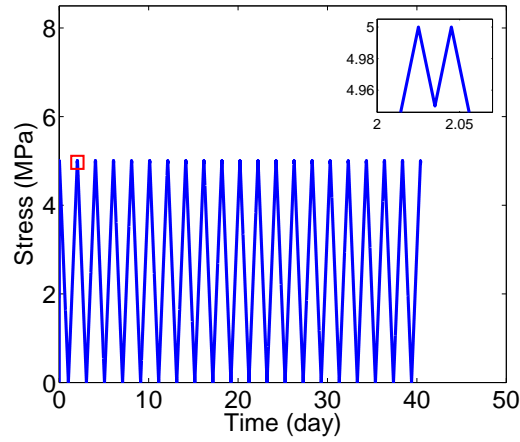
It is critical to understand the evolution of the mechanical properties of halite for the design of salt caverns used for natural gas storage or CAES. Typically, geological storage is done under pressures ranging between 5 MPa and 20 MPa, with loading frequencies up to one cycle per day (Bérest, 2011; Bullough et al., 2004; Raju and Khaitan, 2012). Cyclic loading tests at such low frequencies are experimentally challenging, because they are time consuming and require sophisticated power supply systems. We propose to address this issue by performing a series of virtual experiments with the joint-enriched FEM model of inter-granular crack propagation (1) presented in Subsection 5.2.6. Simulations explained in the following are done at the laboratory scale in plane stress conditions, which is in better agreement with the stress conditions applied in typical cyclic loading tests than plane strain conditions. Table 13 summarizes the five loading tests simulated with model (1). In order to track the gradual degradation of the stiffness of the polycrystal, we simulate rapid unloading and reloading after each loading cycle. We use the slope of the corresponding stress-strain curve to calculate the Young's modulus at the peak of each cycle (see Fig. 78a and 78b).

Table 13 Cyclic loading tests performed with the joint-enriched FEM model of inter-granular crack propagation (1 - axial direction; 3 - lateral direction).

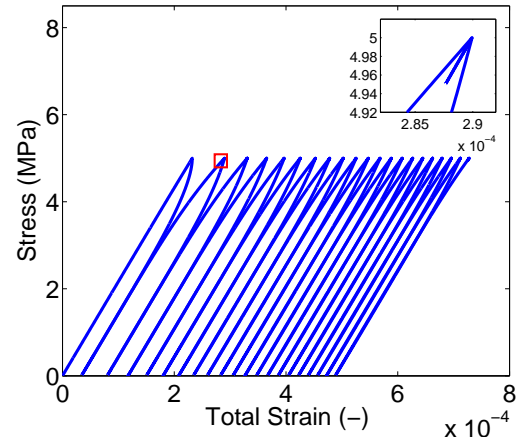
Test Number	Loading type	Applied stresses (MPa)	Period (day)
1	uniaxial ($\sigma_1 \geq \sigma_3 = 0$)	$\sigma_{1,max} = 5, \sigma_{1,min} = 0$	$T = 2$
2	uniaxial ($\sigma_1 \geq \sigma_3 = 0$)	$\sigma_{1,max} = 10, \sigma_{1,min} = 0$	$T = 2$
3	triaxial ($\sigma_1 \geq \sigma_3 > 0$)	$\sigma_{1,max} = 15, \sigma_{1,min} = 5, \sigma_3 = 5$	$T = 2$
4	triaxial ($\sigma_3 \geq \sigma_1 > 0$)	$\sigma_{3,max} = 15, \sigma_{3,min} = 5, \sigma_1 = 5$	$T = 2$
5	triaxial ($\sigma_3 \geq \sigma_1 > 0$)	$\sigma_{3,max} = 15, \sigma_{3,min} = 5, \sigma_1 = 5$	$T = 20$

Influence of the stress amplitude (tests 1-2). The comparison of tests 1 and 2 shows that: (a) When the stress amplitude increases, the number of cycles before failure decreases (Fig. 78a and Fig. 78c). For example, the polycrystal can undergo more than 20 loading cycles before failure for a loading stress of 5 MPa whereas it reaches failure after the 6th cycle for a loading stress of 10 MPa (Fig. 78b and 78d); (b) For the same number of cycles, strains and damage increase with stress amplitude (Fig. 78b, Fig. 78d and Fig. 79).

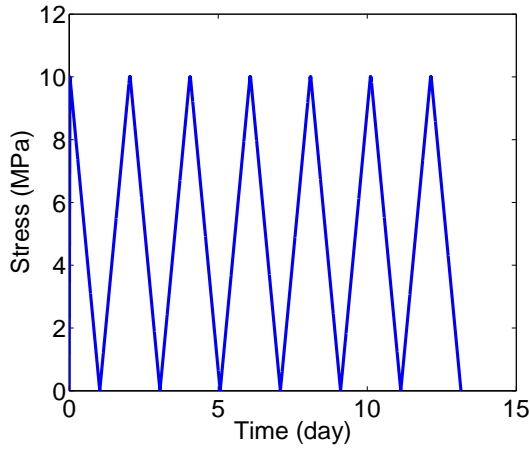
Influence of the confining stress (tests 1-2-3). The comparison of tests 2 and 3 shows that for the same axial stress amplitude, more confining stress delays failure (Fig. 78c and Fig. 78e) and reduces strains and damage (Fig. 78d, Fig. 78f and Fig. 79). The confining pressure effectively reduces the viscous-deformation that induces fatigue in the polycrystal, which increases the strength of the polycrystal and its ability to sustain more cycles. For the same deviatoric stress, a lower axial stress delays failure (Fig. 78a - Fig. 78e) and reduces strains and damage (Fig. 78b, Fig. 78f and Fig. 79). Note that in tests 1, 2 and 3, the stress-strain cycles tend to a limit behavior, in which the same constant strain increment adds up at each cycle. The inclusion-matrix model can predict that the Young's modulus decreases when the number of broken grains increases (Chapter 4), but it cannot predict properly the progressive degradation of the Young's modulus with the number of cycles, because failure occurs shortly after the first grain breakage. By contrast, in the proposed joint-enriched FEM model of inter-granular crack propagation, the Young's modulus decreases with the number of loading cycles according to an exponential relationship, which is in agreement with experimental observations made in salt (Fuenkajorn and Phueakphum, 2010; Ma et al., 2013), as well as in other geomaterials such as basalt (Heap et al., 2009).



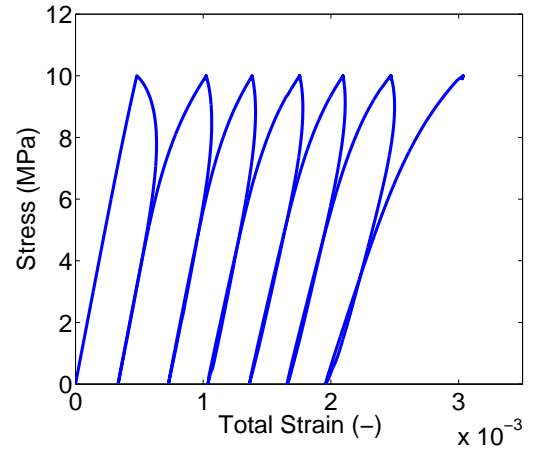
(a) Stress-time history for test 1



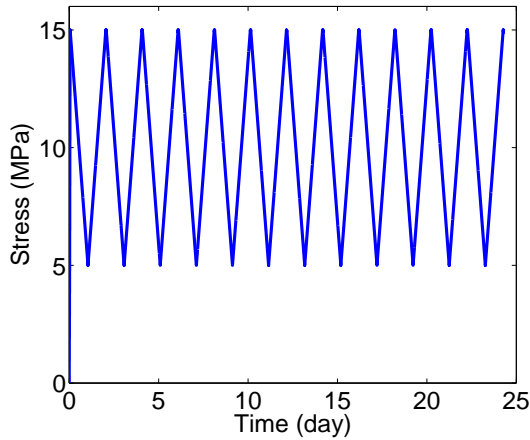
(b) Stress-strain for test 1



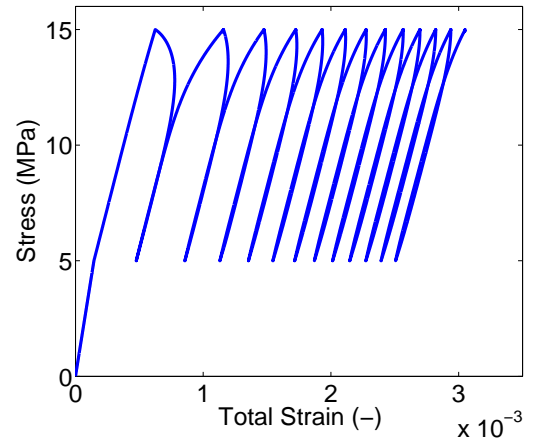
(c) Stress-time history for test 2



(d) Stress-strain for test 2



(e) Stress-time history for test 3



(f) Stress-strain for test 3

Figure 78 Cyclic loading tests 1-3 (vertical deviatoric stress), simulated with the joint-enriched FEM model of inter-granular crack propagation.

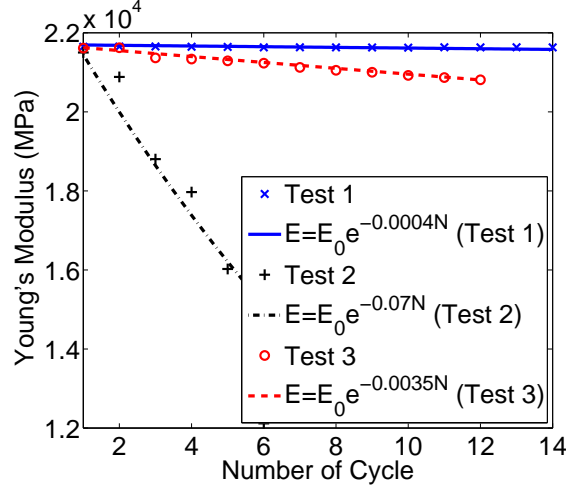
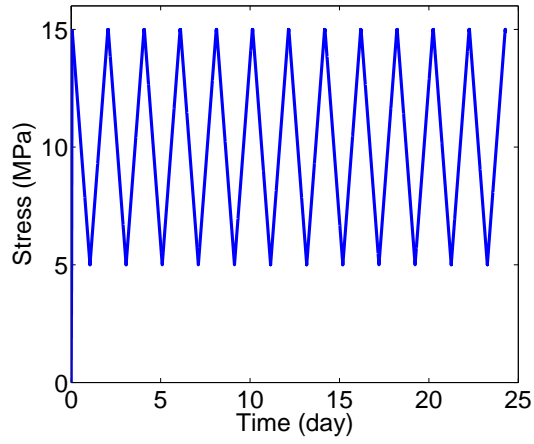


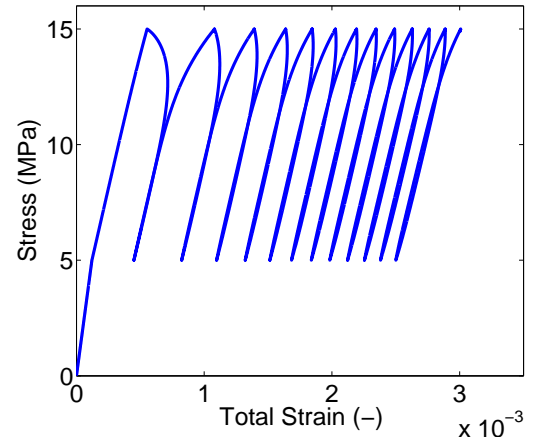
Figure 79 Variations of the polycrystal Young's modulus with the number of cycles in tests 1-3.

Influence of the loading direction vs. polycrystal anisotropy (tests 3-4). The only difference between tests 3 and 4 is the direction of the deviatoric stress: deviatoric compression is vertical in test 3, and horizontal in test 4. The stress-strain response is similar in both tests (Fig. 78e, 78f, 80a and 80b), which shows that the polycrystal model is relatively homogeneous (i.e. the orientations of grain FEs and joints elements approximatively follow a uniform distribution). Because the deviatoric stress is horizontal in test 4, damage after the first loading cycle mainly develops in horizontal joints (parallel to the differential compression axis - see Fig. 81).

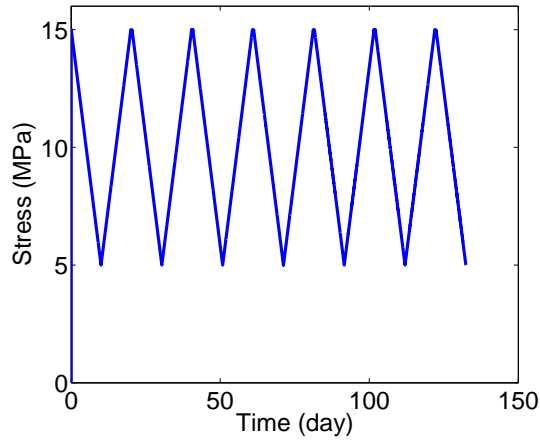
Influence of the loading frequency (tests 4-5). The period of the loading cycles in test 5 is 10 times longer than in test 4. Therefore in test 5, more viscoplastic deformation accumulates at each cycle, which results in earlier failure (Fig. 80a and Fig. 80c), higher strains (Fig. 80b and Fig. 80d) and higher damage (Fig. 82). Like in tests 1-3, the evolution of the Young's modulus with the number of cycles follows an exponential trend (note that in tests 1-3, the Young's modulus was calculated from the slope of the axial stress-strain curves, whereas in tests 4-5, the Young's modulus was calculated from the slope of the lateral stress-strain curves).



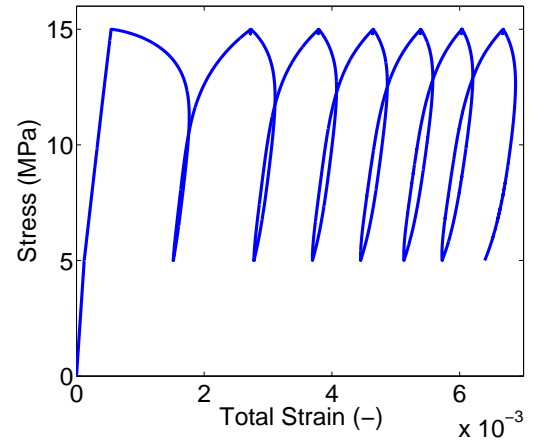
(a) Stress-time history for test 1



(b) Stress-strain for test 1



(c) Stress-time history for test 2



(d) Stress-strain for test 2

Figure 80 Cyclic loading tests 4-5 (horizontal deviatoric stress), simulated with the joint-enriched FEM model of inter-granular crack propagation.

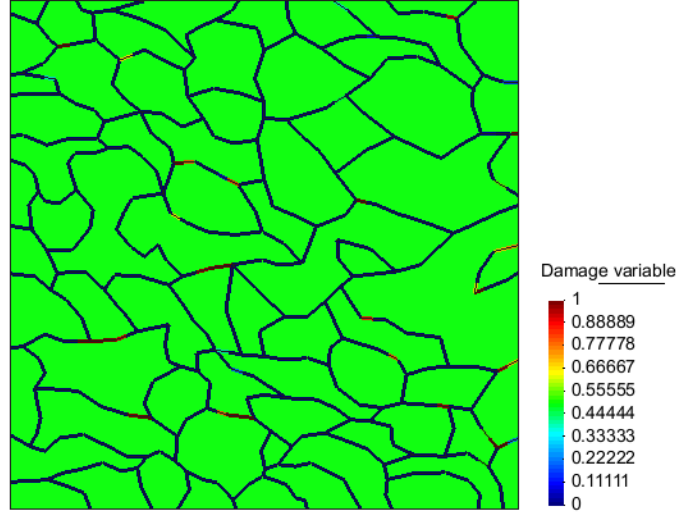


Figure 81 Damage in the joint elements at the end of the initial loading cycle in test 4 (mostly horizontal cracks).

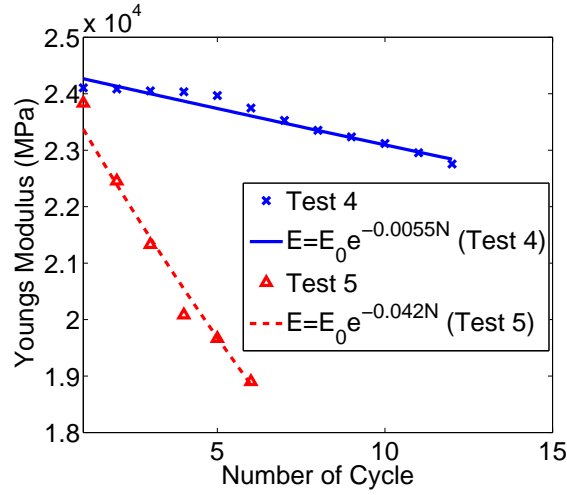


Figure 82 Variations of the polycrystal Young's modulus with the number of cycles in tests 4-5.

5.2.8 Comparison of different damage mechanisms

We used the joint-enriched FEM modeling approach presented above to understand the damage mechanisms that occur in salt polycrystals upon dry consolidation. Experiments were performed by our collaborators including Dr. F. Chester, Dr. J.

Chester, and Mr. J. Ding at Texas A&M University. Dry granular salt specimens were consolidated under different temperature and loading conditions. The average grain size was 1.7~2.0 mm. After consolidation, samples were first saturated with blue epoxy resin to enhance the grain and void interfaces, and then polished and cleaned with isopropyl alcohol. The typical thickness of a thin section was about 200 micrometers.

We selected a thin section micrograph that presented a relative homogeneity (Fig. 83). This specimen was consolidated at 473K under 52 MPa for about 10 minutes. The resulting porosity after consolidation was 6%. Intra-granular cracks can be observed in some grains as a result of the consolidation, which highlights the importance of accounting for intra-granular damage in the Finite Element model.

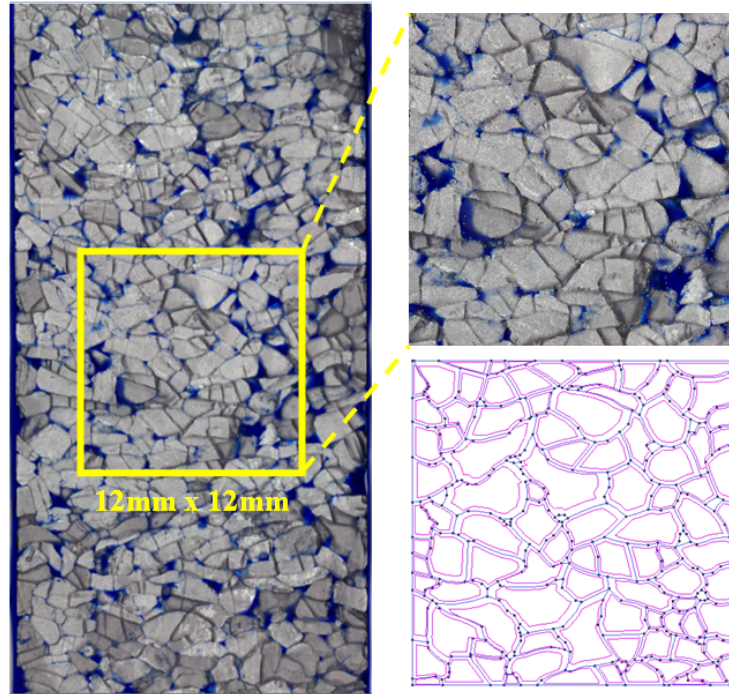


Figure 83 Thin section image of consolidated granular salt saturated with blue epoxy. Left: Grey regions represent granular salt particles while blue areas filled with epoxy indicates inter-granular pores. Right: The FEM mesh was generated with *Plot Digitizer* and *GiD*.

In order to minimize boundary effects, we constructed a 2D FEM polycrystal

model of the central region of the micrograph (bounded by a square in Fig. 83). Like in the previous sections, we used the software *Plot Digitizer* to extract grain and void boundaries from the microstructure image and export them into *GiD* FEM pre- and post-processor (GiD, 2002) for meshing.

Since the section selected was relatively homogeneous, we assumed that grain orientations in the mesh followed a uniform distribution. For simplicity, similar to the approach described in Subsection 5.2.4, we used 12 grain orientations, i.e., 12 cosine values of θ uniformly distributed in the interval $[\cos(\theta = 0) = 0, \cos(\theta = \frac{\pi}{2}) = 1]$. We assigned a grain orientation of the surface elements in such a way that the distribution of grain orientations be relatively isotropic and homogeneous (Fig. 84). Empty spaces (white color) represent the inter-granular voids. We also used joint elements along grain boundaries. Note that the microstructure topology, such as grain and void distributions, has a significant impact on numerical results. However, general damage and viscous phenomena should be independent from minor microstructure variations.

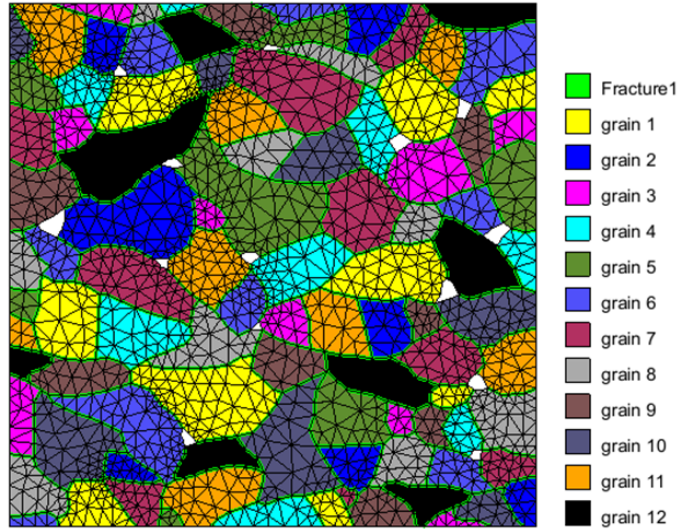


Figure 84 Joint-enriched FEM ($12mm \times 12mm$). In the legend, grain numbers refer to grain orientations. Fracture 1 is the inter-granular joint element.

We calibrated the joint-enriched FEM model according to the procedure explained

in Subsection 5.2.5. Table 2 summarizes the material parameters calibrated for the joint-enriched finite element model designed with *POROFIS*. Because joints are essentially contacts among grains and their physical properties are experimentally challenging to measure, the calibration process still requires further improvement in order to apply this model for more practical problems.

In the following simulations, the polycrystal is subjected to a rapid monotonic loading followed by a uniaxial creep load of 5 MPa applied for 0.3 days, which is a typical operation pressure at a CAES geological site (Raju and Khaitan, 2012). The creep loading is applied uniformly at both the upper and lower boundaries of the model (Fig. 84). Horizontal displacements are fixed ($U_x = 0$) for the central nodes of the upper and lower boundaries. Vertical displacement is fixed ($U_y = 0$) for the central node along the right boundary.

We compare the results obtained with the three models presented in Table 14 at two key stages of the consolidation experiment: (1) at the end of the monotonic loading phase ($t = 0.005\text{d}$, point A); (2) during the creep process ($t = 0.24\text{d}$, point B).

Table 14 Three finite element models based on different damage mechanisms.

Model Number	Inter-granular	Intra-granular
Model 1	Damageable joint elements	Visco-elastic surface elements
Model 2	Elastic joint elements	Visco-damageable surface elements
Model 3	Damageable joint elements	Visco-damageable surface elements

At point A, the stress and displacement fields are the same for the three models (Fig. 85). This is because both grains and joints remain intact at this initial stage ($D = D_g = 0$). Under the influence of uniaxial stress imposed at the top and bottom of the domain, grains expand laterally, which induces tensile stress at grain boundaries, mostly in the direction that is parallel to the loading axis (Fig. 86a).

Grains adjacent to voids undergo less deformation constraints. Compressive stress concentrations appear at the grain boundaries where grain shapes are highly irregular or where several angular grains are in contact. Because of the distribution of the crystal orientations, the displacement field within the grains is antisymmetric about the central axis of the polycrystal (Fig. 86b).

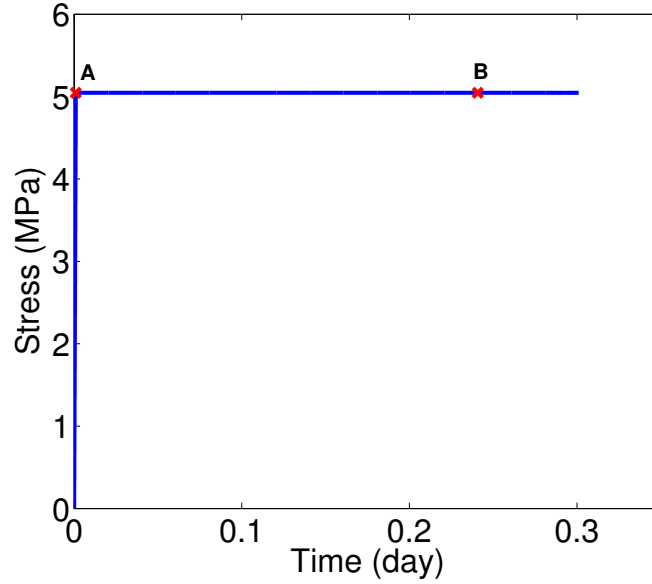


Figure 85 Stress time history imposed in the creep simulations. Point A marks the transition between the monotonic increasing stress loading and creep loading phases ($t = 0.005d$). Point B is during the creep process ($t = 0.24d$).

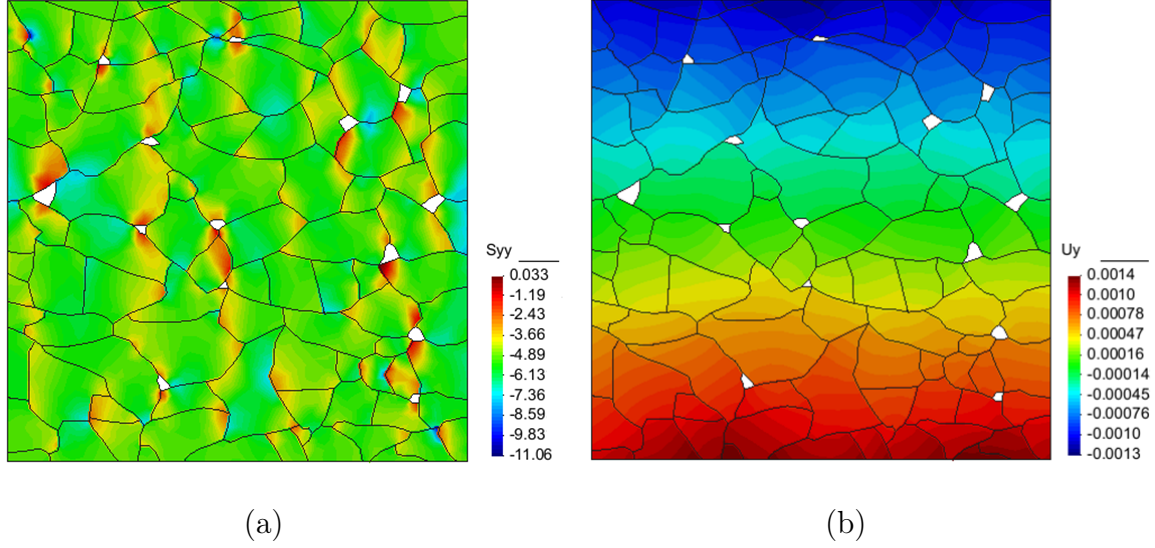
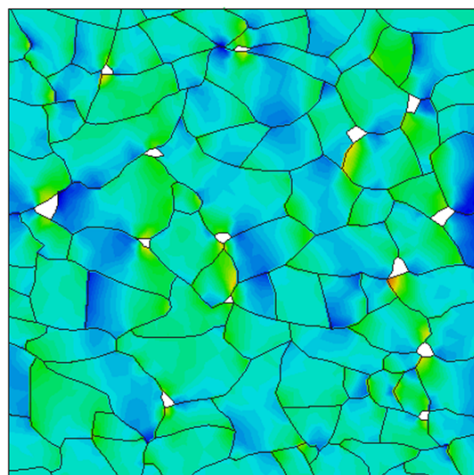
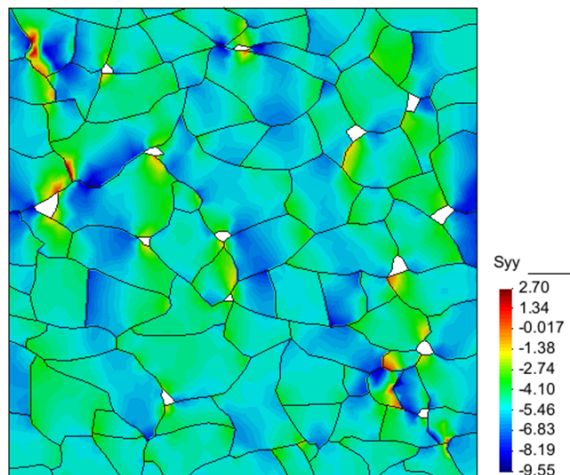


Figure 86 Results at the end of monotonic loading phase at $t = 0.005d$ - Point A (same for the three models): (a) vertical stress (MPa); (b) vertical displacement (mm). Note: compression is negative with *POROFIS*.

When the creep process starts, viscoplastic deformation in grains evolves. We continue to observe strong concentrations of vertical stresses at the contact of angular grains. This results in inter-granular slip and subsequent damage in joints and grains. Using the same stress scale in the legends of Fig. 87a, 87b, 88a, it can be seen that stress distributions and concentrations are similar in the three models. The highest tensile stress concentrations appear in model 2 at the locations where voids exist or several angular grains are in contact. This is due to the fact that unlike in models 1 and 3, energy cannot be dissipated by crack propagation in the joints. Energy accumulates until sudden dissipation occurs through grain breakage, leading to a brittle response. The contours of displacement fields are almost the same in the three models (Fig. 87c, 87d, 88b). Models 2 and 3 experience relatively higher deformation than model 1 since broken grains behave like voids, which allows neighboring grains to rearrange significantly.



(a)



(b)

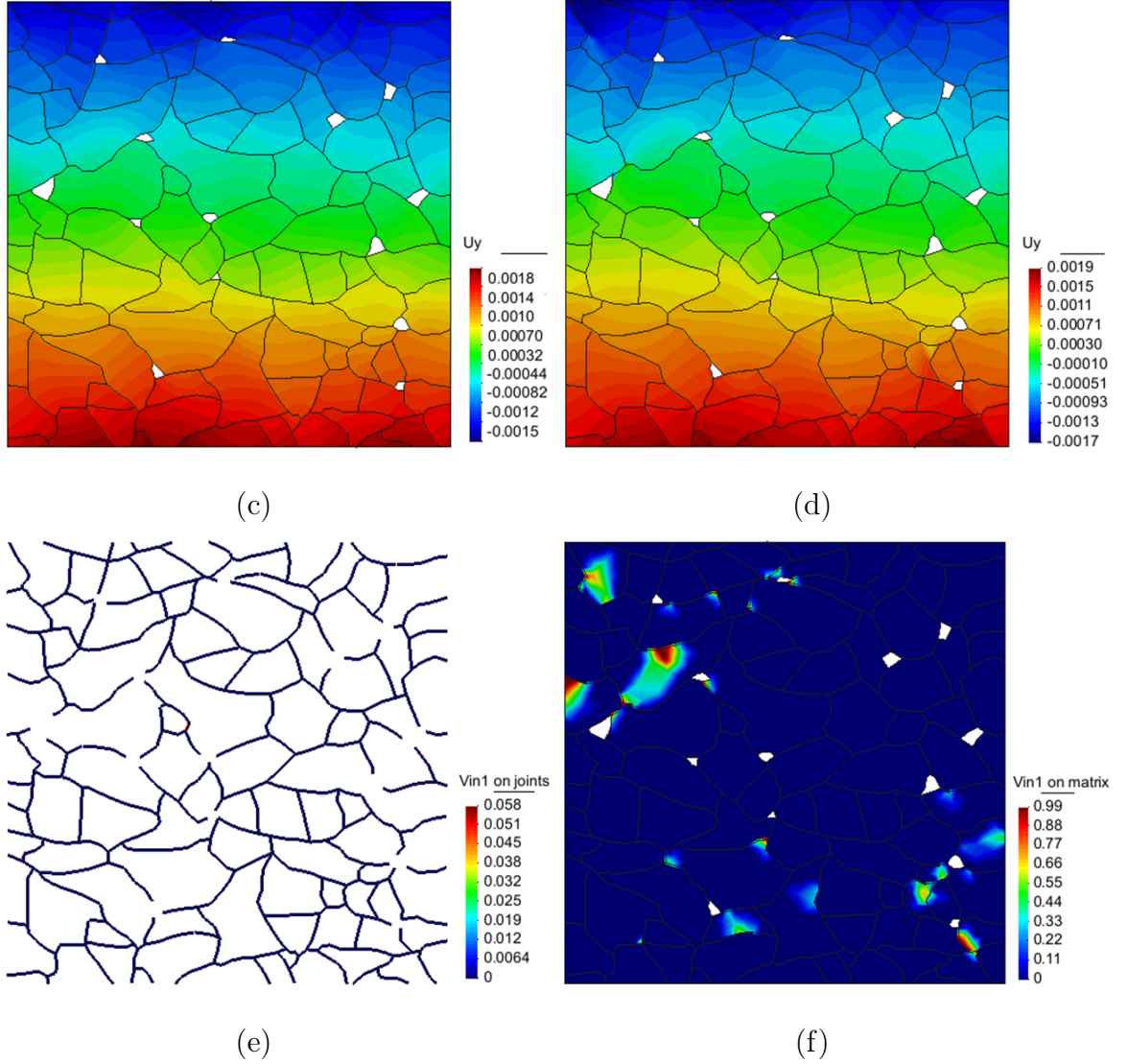


Figure 87 Simulation results during the creep process at $t = 0.24d$ - Point B: (a) vertical stress in model 1 (MPa); (b) vertical stress in model 2 (MPa); (c) vertical displacement in model 1 (mm); (d) vertical displacement in model 2 (mm); (e) damage in joint elements in model 1; (f) damage in grain elements in model 2.

The three models differ for the prediction of damage accumulation at point B ($t = 0.24d$), under the same loading magnitude and for the same loading period (Fig. 87e, 87f, 88c and 88d). In the absence of energy dissipation in the joints, model 2 is exposed to a considerable amount of damage in the grains. By contrast, as shown

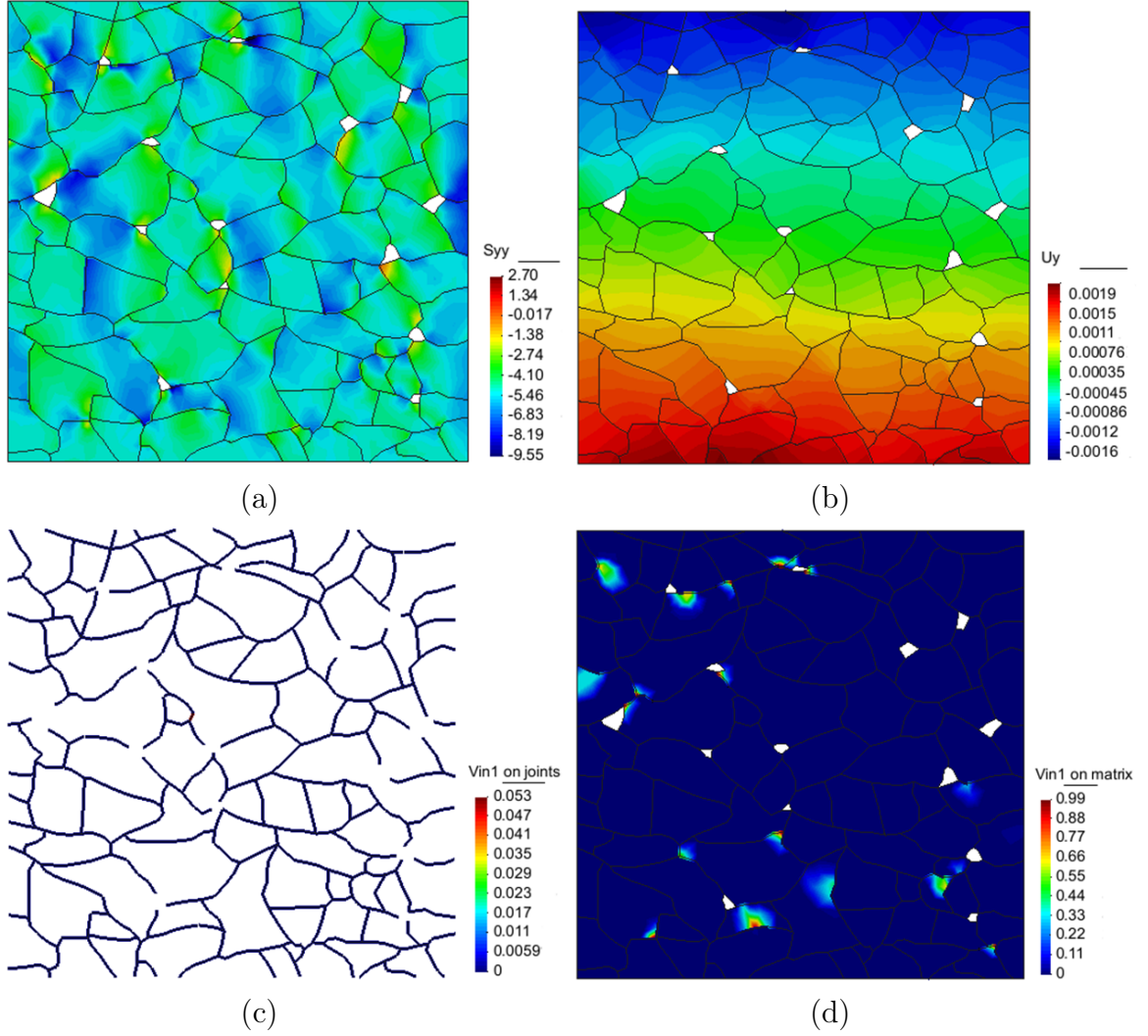


Figure 88 Simulation results during the creep process at $t = 0.24d$ - Point B: (a) vertical stress in model 3 (MPa); (b) vertical displacement in model 3 (mm); (c) inter-granular damage in joint elements in model 3; (d) intra-granular damage in grain elements in model 3.

in Fig. 88d, grains in model 3 undergo less damage since inter-granular joint breakage contributes to energy dissipation. In model 3, damage accumulates faster in grains than in joints and most joints remains undamaged at point B.

In order to obtain the creep curve of the polycrystal modeled with *POROFIS*, we calculated the average values of strains over the entire set of integration points. The plots of strain-time history for the three models during the creep phase are shown in Fig. 89. In model 1, the polycrystal remains in the steady state creep regime whereas tertiary creep is reached in models 2 and 3. With intra-granular damage mechanism only, model 2 presents the most brittle failure and reaches tertiary state at $t = 0.24d$, which shows a good agreement with the rapid damage accumulation in grain elements shown in Fig. 87f. Although the creep curve obtained from model 3 matches the general trend of the curve obtained with model 2, the transition between steady state and tertiary state is much smoother. This indicates the importance of accounting for inter-granular slip-induced damage in joints for salt polycrystals. However, the impact of intra-granular damage observed in the experiments cannot be ignored (Fig. 83). As shown in Fig. 89, results obtained with model 1 reveal a completely different behavior: the polycrystal is very ductile and remains almost undamaged (Fig. 87e). Future work will concentrate on the validation of these results, in particular the prediction of deformation at the macroscopic scale and fracture patterns at the microscopic scale.

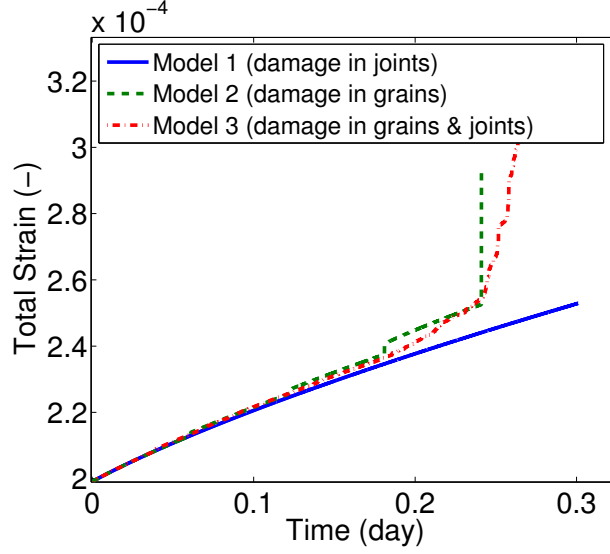


Figure 89 Creep curves obtained with the three models. Note that the strains from the initial monotonic loading phase are the same for the three models and not shown in this figure.

The rapid deformation observed during tertiary creep is the result of accelerated damage accumulation at the microscopic level. We continued the simulations until failure with the three models. We find that model 1 requires the longest time to reach failure (6.68 days, against 0.276 days with model 3 and 0.25 days with model 2). With model 1, most damaged joints are parallel to the creep loading direction. At failure, some damaged joints have coalesced with the pre-existing voids (Fig. 90). The ultimate damage distribution in model 2 exhibits only a few damage zones. The highest damage values are observed in the upper left region of the polycrystal, maybe because of the local heterogeneities (Fig. 91). Similar damage distributions in the grains are obtained with model 3 (Fig. 92b). In model 3, high stress concentrations not only lead to grain stiffness weakening, but also inter-granular damage (Fig. 92a). As a result of the coalescence of damaged joints and voids, the upper left portion tends to slip downward, along joint interfaces, which causes ultimate failure in model 3 (Fig. 92b).

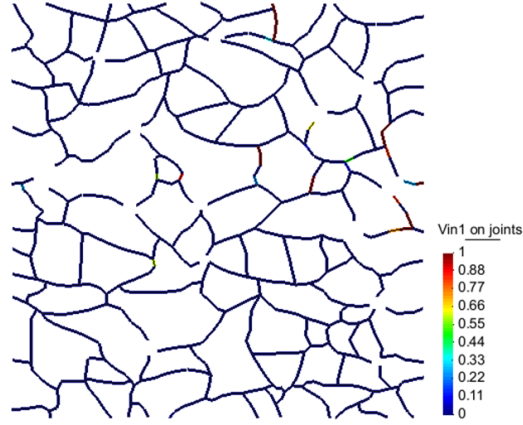


Figure 90 Damage in joints of model 1 at ultimate failure ($t = 6.68d$)

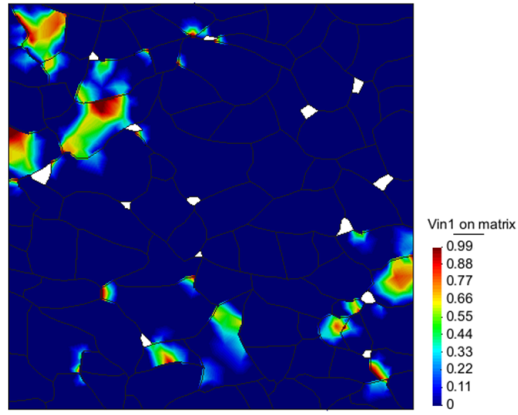


Figure 91 Damage in grains of model 2 at ultimate failure ($t = 0.25d$).

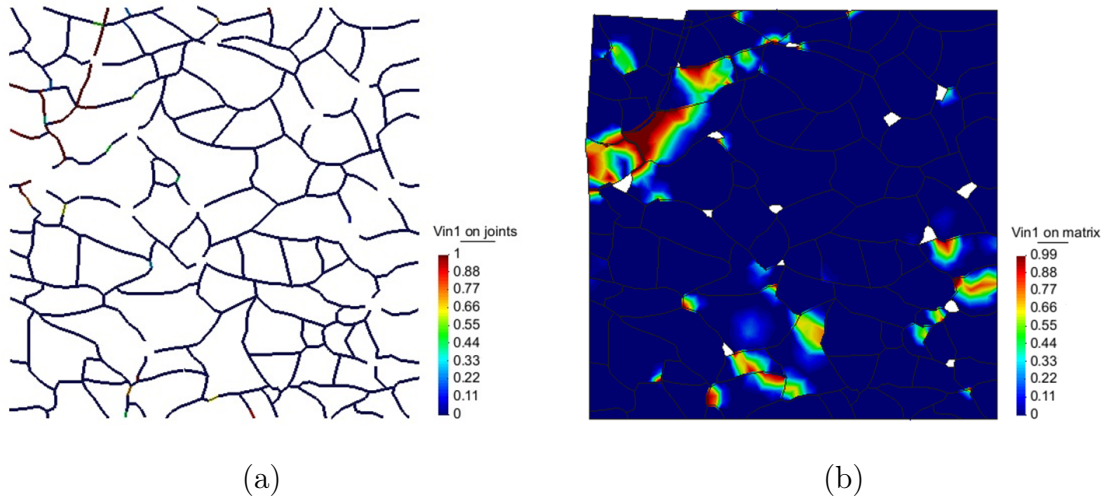


Figure 92 Results of model 3 at ultimate failure ($t = 0.276d$): (a) damage in joints; (b) grain damage in the deformed shape.

5.3 Viscous Damage in Salt Cavern

5.3.1 Phenomenological Modeling Framework

To study salt viscous damage at the field scale, we propose a phenomenological model of viscoplastic deformation that captures the transition between secondary and tertiary creep regimes (Zhu et al., 2015c). In the following, we calibrate this transition against the micro-macro model presented in Chapter 4. During the secondary creep regime, the viscoplastic deformation is the result of grain-scale sliding mechanisms. During tertiary creep, the strain rate increases with damage as the consequence of grain breakage. We use Norton-Hoff law for secondary creep (Carter and Hansen, 1983):

$$\dot{\epsilon}_{ss}^{vp} = \frac{3}{2} A_c \cdot \exp\left(-\frac{Q}{RT}\right) \left(\frac{\sigma_e}{\sigma_0}\right)^{n_1} \frac{1}{\sigma_e} \mathbf{s}, \quad (93)$$

in which A_c and n_1 are material constants, Q is the activation energy for the slip mechanism, R is the universal gas constant, T is the absolute temperature, \mathbf{s} is the deviatoric stress tensor, σ_0 is a reference stress, arbitrarily set equal to 1MPa, $\sigma_e = \sqrt{3J_2}$ is the equivalent von Mises stress, and $J_2 = \frac{s_{ij}s_{ij}}{2}$ is the second deviatoric stress invariant. Experiments conducted at various temperatures led to similar empirical power laws (Handin et al., 1986; Heard et al., 1972).

For the case of uniaxial creep, according to Eq. 93, we have

$$\dot{\epsilon}_a^{vp} = A_c \cdot \exp\left(-\frac{Q}{RT}\right) \left(\frac{\sigma_e}{\sigma_0}\right)^{n_1}, \quad (94)$$

in which σ_e is the uniaxial stress.

As shown in the previous sections, micro-stresses increase with macroscopic viscoplastic deformation, which may cause grain breakage if grain tensile strength is exceeded. The consequent redistribution of microstresses leads to higher local stress concentrations, which further accelerate viscoplastic deformation and damage propagation. This phenomenon is known as tertiary creep (Fig. 93).

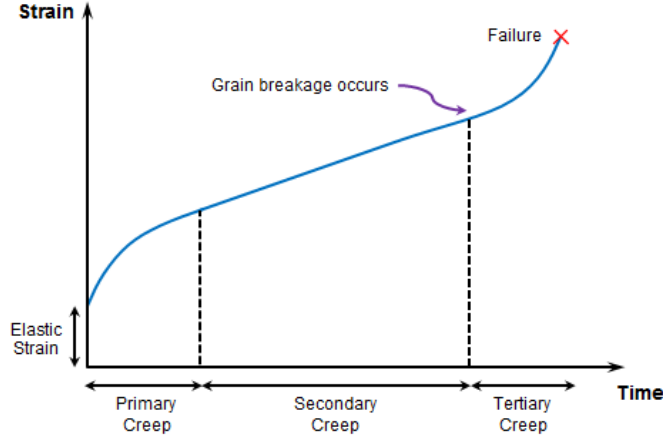


Figure 93 Complete creep curve. Tertiary creep phase initiates when first grain breakage occurs.

According to the micromechanical analysis presented in Chapter 4, the onset of the tertiary creep corresponds to the damage initiation. The consequent mechanical macroscopic damage (D_m) is obtained by scaling the elastic properties by the fraction of non-broken grains in the REV. In the following, we denote the damage variable in the phenomenological model as D_M to account for the change of viscoplastic strain rate induced by grain breakage (Ashby and Hallam, 1986; Hutchinson, 1983). The tertiary creep deformation law is similar to the secondary creep law (Leckie and Hayhurst, 1974):

$$\dot{\epsilon}_{ts}^{vp} = \frac{3}{2} B_c \cdot \exp\left(-\frac{Q}{RT}\right) \left[\frac{\sigma_e / (1 - D_M)}{\sigma_0} \right]^{n_2} \frac{1}{\sigma_e} \mathbf{s}, \quad (95)$$

in which B_c and n_2 are material constants. $\frac{\sigma_e}{1 - D_M}$ is the effective stress. The damage variable D_M contributes to the degradation of material stiffness, as follows:

$$\mathbf{C}_D = (1 - D_M) \mathbf{C}_0, \quad (96)$$

in which \mathbf{C}_D is the stiffness of the damaged material, \mathbf{C}_0 is the initial stiffness of the undamaged material. For uniaxial creep, Eq. 95 becomes:

$$\dot{\epsilon}_a^{vp} = B_c \cdot \exp\left(-\frac{Q}{RT}\right) \left[\frac{\sigma_e / (1 - D_M)}{\sigma_0} \right]^{n_2}, \quad (97)$$

in which σ_e takes the value of the uniaxial axial stress.

We compare two damage evolution laws. The first law (noted as damage evolution law 1), initially proposed for metallic materials (Hayhurst et al., 1984), depends on both the current damage and stress states as

$$\dot{D}_M = \frac{C_c \sigma_e^\xi}{(1 - D_M)^\varphi}, \quad (98)$$

in which C_c , ξ , and φ are material constants governing the damage accumulation during the tertiary creep phase. The second damage evolution law (denoted as damage evolution law 2), which depends on the current viscoplastic deformation state only, was successfully employed to model concrete (Mazars, 1984) and interfaces in cementitious materials (Jefferson, 1998). We assume that damage remains equal to zero up to a critical viscoplastic deformation ε_0^{vp} , and then increases exponentially with deformation as

$$D_M = 1 - e^{-\frac{\varepsilon^{vp} - \varepsilon_0^{vp}}{\varkappa \varepsilon_0^{vp}}}, \quad (99)$$

As a result, the rate of damage is expressed as:

$$\dot{D}_M = \frac{1}{\varkappa \varepsilon_0^{vp}} \|\dot{\varepsilon}^{vp}\| e^{-\frac{\varepsilon^{vp} - \varepsilon_0^{vp}}{\varkappa \varepsilon_0^{vp}}}, \quad (100)$$

in which ε_0^{vp} is the critical viscoplastic strain at the onset of tertiary creep state. \varkappa is a damage parameter which measures the ductility of the material: the larger the value of \varkappa , the more ductile the material. $\|\dot{\varepsilon}^{vp}\| = \sqrt{\frac{2}{3} \dot{\varepsilon}_{ij}^{vp} \dot{\varepsilon}_{ij}^{vp}}$ is the equivalent von Mises strain.

We used the micro-macro model presented in Chapter 4 to simulate creep tests under various axial stresses, and determined the critical viscoplastic strain as the accumulated viscoplastic strain reached at the first occurrence of grain breakage. In Fig. 94, the onset of tertiary creep (cross symbol) is indicated by the point where the viscoplastic deformation predicted in the absence of grain breakage (non-damage model) separates from the one predicted with the consideration of grain breakage (damage model).

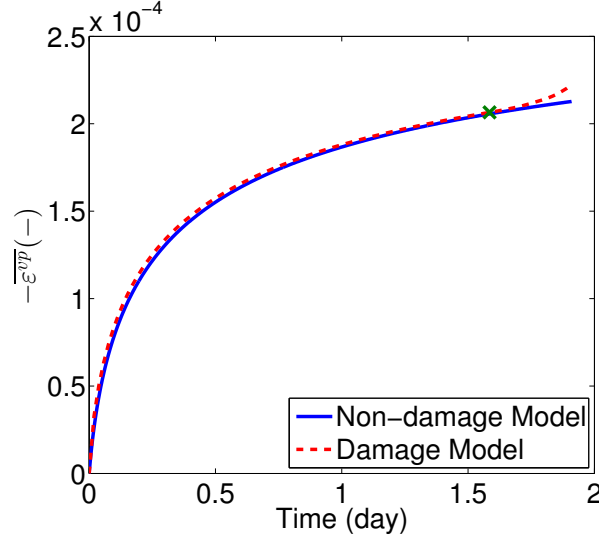


Figure 94 Evolution of macroscopic viscoplastic strain during the long-term creep test with 7 MPa creep load.

We determined the critical viscoplastic deformation for creep tests under various axial stresses, and established a relationship between critical viscoplastic strain ϵ_c^{vp} and creep load σ_c at a material point - for both short-term and long-term creep tests. Fig. 95 shows the resulting damage threshold, which is similar to a yield surface.

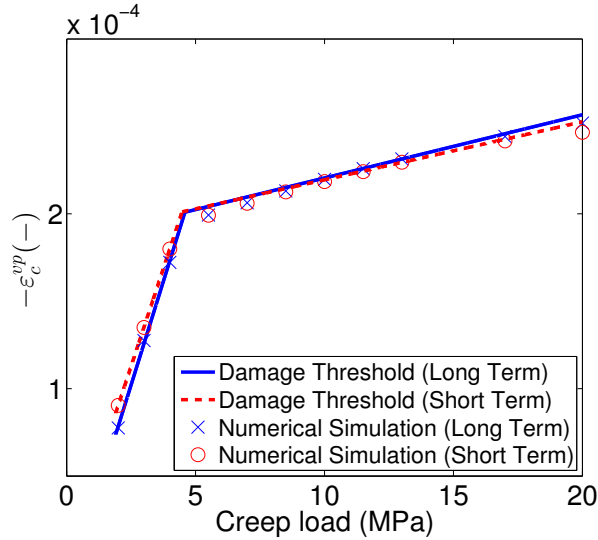


Figure 95 Damage criterion determined from micromechanical model (long term and short term).

Note that the damage criterion obtained with short-term creep parameters is similar to that obtained with long-term creep parameters, which confirms that the

occurrence of damage depends on the cumulated viscoplastic strain - as opposed to the viscoplastic strain rate. In addition, our modeling approach is in agreement with the work presented by Kranz and Scholz (1977), according to which the onset of tertiary creep should not depend on stress (but rather, on viscoplastic strain).

Since this study focuses on the long-term behavior of salt cavern subjected to creep load, we used the damage criterion based on long-term creep datasets for the following simulations. The damage threshold takes a bilinear form. Linear fitting provides:

$$\varepsilon_c^{vp} = 5 \times 10^{-5} \sigma_c - 2 \times 10^{-5} \quad (2 \leq \sigma_c \leq 4.78) \quad (101)$$

$$\varepsilon_c^{vp} = 4 \times 10^{-6} \sigma_c + 2 \times 10^{-4} \quad (\sigma_c > 4.78) \quad (102)$$

When σ_c is less than 2 MPa, we assume that microstress remains below 2 MPa in all grains, and therefore, that grain breakage does not occur (i.e., the material remains in the secondary creep regime at the macroscopic scale).

5.3.2 Model Calibration

We calibrated material constants A_c and n_1 against experimental results from steady state creep for both short-term and long-term tests. In the following, we calibrate tertiary creep constitutive parameters. For damage evolution law 1, these are B_c , n_2 , C_c , ξ , and φ ; For damage evolution law 2, these are B_c , n_2 , and \varkappa . At the transition between secondary and tertiary creep, when $D_M = 0$, we have:

$$A_c \cdot \exp\left(-\frac{Q}{RT}\right) \left(\frac{\sigma_e}{\sigma_0}\right)^{n_1} = B_c \cdot \exp\left(-\frac{Q}{RT}\right) \left(\frac{\sigma_e}{\sigma_0}\right)^{n_2}. \quad (103)$$

In addition, the creep deformation curve should fit experimental data. For consistency, we use the experimental data obtained from the same salt rock as in the calibration done in the secondary creep regime (Fuenkajorn and Phueakphum, 2010). Tests are carried out at room temperature ($T = 295K$). The activation energy Q for cross-slip in pure alkali halides is $1.538 \times 10^4 J \cdot mol^{-1}$ (Senseny et al., 1992). The universal gas constant R is $8.314 J \cdot mol^{-1} \cdot K^{-1}$.

For short term creep, we obtained $A_c = B_c$ and $n_1 = n_2$. After damage initiation, the viscoplastic strain rate kept its value of $6.89 \times 10^{-2} \text{ day}^{-1}$. We used the tertiary creep strain rate to fit the parameters involved in the damage evolution laws (Fig. 96). T_c and ε_c^{vp} represent the time and the critical viscoplastic strain at the onset of the tertiary phase, respectively.

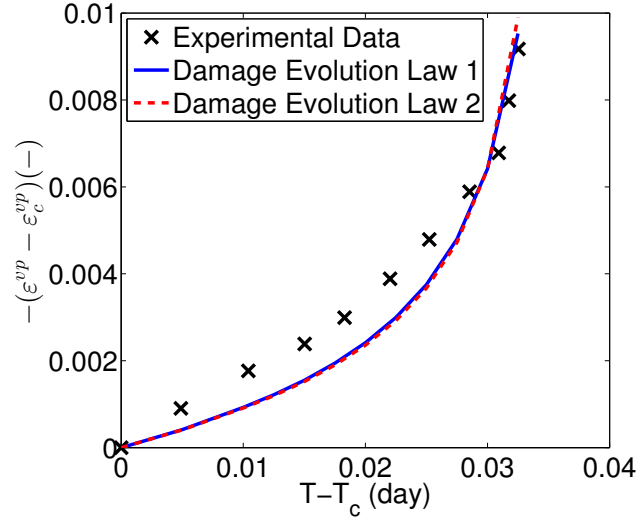


Figure 96 Calibration of short-term parameters for the tertiary creep phase. We obtain the experimental data from the short-term creep test with the creep load 30 MPa (Fuenkajorn and Phueakphum, 2010).

We also calibrated our model against long term creep datasets (Fuenkajorn and Phueakphum, 2010). The tertiary parameters B_c and n_2 were different from the secondary parameters A_c and n_1 (Fig. 97). The resulting strain rate for long term steady state creep is $5.61 \times 10^{-4} \text{ day}^{-1}$. Although some deviation exists between experimental data and theoretical model, the trend is well captured by both damage models.

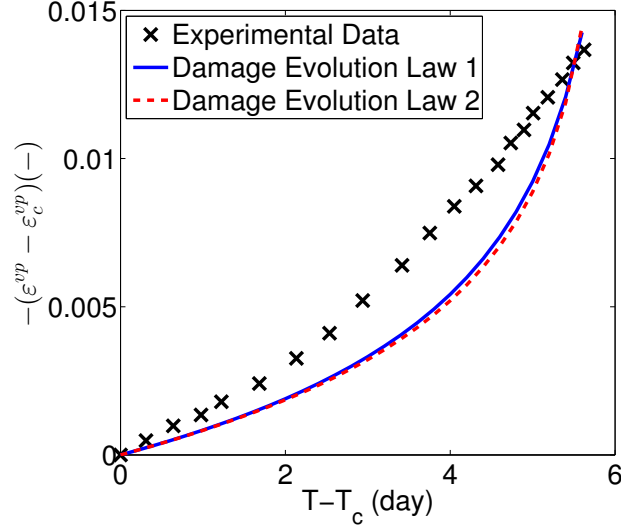


Figure 97 Calibration of long-term parameters for the tertiary creep phase. We obtain the experimental data from the short-term creep test with the creep load 12.6 MPa (Fuenkajorn and Phueakphum, 2010).

We verified our calibrated model against independent experimental datasets. For short term creep, we used the creep curve of another type of salt rock (Yang et al., 1999) (complete creep curve, including secondary and tertiary creep regimes). The steady state viscoplastic strain rate using calibrated parameters is $1.72 \times 10^{-2} \text{ day}^{-1}$, same as the reported experimental result. Damage evolution in salt rock depends on its microstructure and defects, which varies greatly among different types of salt rocks. So while keeping other parameters unchanged, we had to do an additional calibration of the two damage parameters. Using the experimental data reported in (Yang et al., 1999), we found $C_c = 0.18$ in model 1 and $\varkappa = 41$ in model 2.

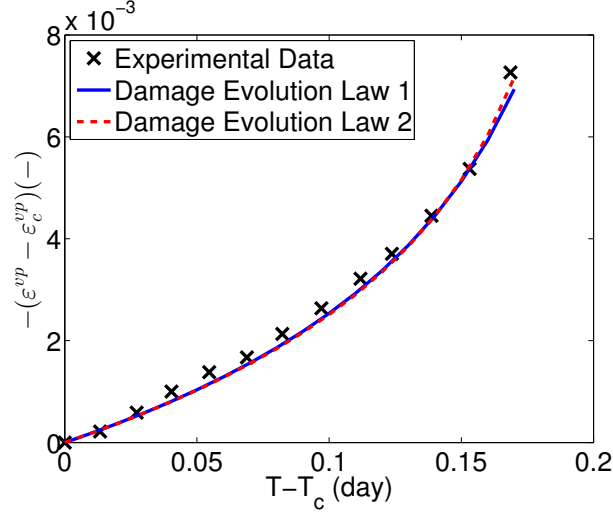


Figure 98 Verification of short-term parameters for the tertiary creep phase. We obtain the experimental data from the short-term creep test with the creep load 21.5 MPa (Yang et al., 1999).

Tables 15 and 16 summarize all calibrated parameters, for both damage evolution laws. As expected, the values of A_c and B_c for long-term creep are significantly smaller than those obtained for short term creep. The value of \varkappa is larger for long-term creep - as the material becomes more ductile. Note that the proposed model is able to capture the transition between secondary and tertiary creep with an input of 8 constitutive parameters.

Table 15 Model parameters calibrated for damage evolution law 1 based on the experimental data (Fuenkajorn and Phueakphum, 2010).

short term			
A_c (day^{-1})	n_1 (-)	B_c (day^{-1})	n_2 (-)
1.88×10^{-4}	3.58	1.88×10^{-4}	3.58
C_c (-)	ξ (-)	φ (-)	
0.915	0.7	2.05	
long term			
A_c (day^{-1})	n_1 (-)	B_c (day^{-1})	n_2 (-)
1.06×10^{-5}	4.04	1.00×10^{-8}	6.9
C_c (-)	ξ (-)	φ (-)	
0.0037	0.8	4.92	

Table 16 Model parameters calibrated for damage evolution law 2 based on the experimental data (Fuenkajorn and Phueakphum, 2010).

short term				
A_c (day^{-1})	n_1 (-)	B_c (day^{-1})	n_2	\varkappa (-)
1.88×10^{-4}	3.58	1.88×10^{-4}	3.58	23
long term				
A_c (day^{-1})	n_1 (-)	B_c (day^{-1})	n_2	\varkappa (-)
1.06×10^{-5}	4.04	1.00×10^{-8}	6.9	115

5.3.3 Pressurized Salt Cavern under Long-term Creep

We implemented the phenomenological models in *POROFIS*. The rock stiffness is updated at each time increment, which allows representing the accumulation of damage around the cavern and, in this way, we account for the damage effect on the stress field around the cavern.

We simulated the depressurization of an axisymmetric salt cavern of irregular shape (Fig. 99), which consists of both convex and concave regions and is similar to that of the Eminence salt dome site (Warren, 2006). The depth and height of the cavern were 850m, and 100m, respectively. The salt formation had a unit weight of $\gamma = 0.02 \text{ MN}/m^3$, a Young's modulus of 23 GPa and a Poisson's ratio of 0.3 (Fuenkajorn and Phueakphum, 2010). In the FEM analysis, to focus on the neighboring region, we extracted a 500m by 500m domain close to the salt cavern (Fig. 99). In order to account for the overburden, we applied a vertical stress of $P_V = \gamma z = 12$ MPa at the top boundary. To achieve a homogeneous stress field and apply an in-situ level storage pressure, we applied a 12 MPa lateral stress P_H and a 12 MPa initial storage pressure P_A in the cavern. The vertical displacement was fixed at the bottom of the domain and the radial displacement fixed at the left side of the domain (axis of symmetry). We carried out the FEM simulations with both damage evolution laws and simulated a depressurization process under typical CAES conditions, in three

stages:

- In stage 1 (steady state, time-independent), we applied the initial stresses.
- In stage 2 (transient state, time-dependent), within one time step, we reduced the cavern pressure from 12 MPa to 8 MPa - which is in the same order of magnitude as the stresses encountered in CAES (Ibrahim et al., 2008).
- In stage 3 (transient state, time-dependent), we maintained a stress of 8 MPa at the cavity wall for a long time (360 days), in order to reach a tertiary creep phase.

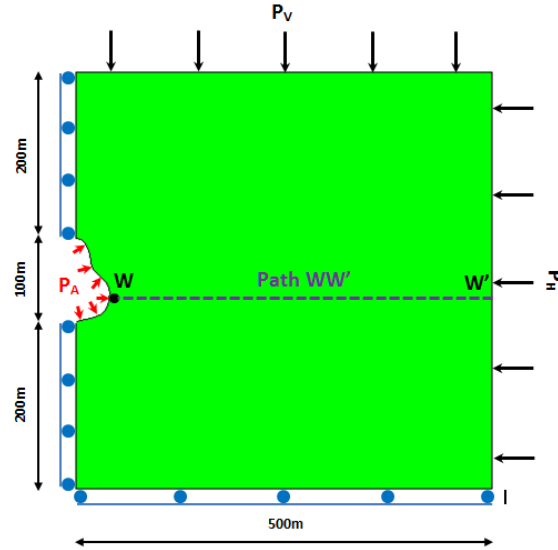


Figure 99 Geometry and boundary conditions of a typical salt cavern studied in *POROFIS*. Element W is the tracing element. Maximum width of the cavern is 40m at element W.

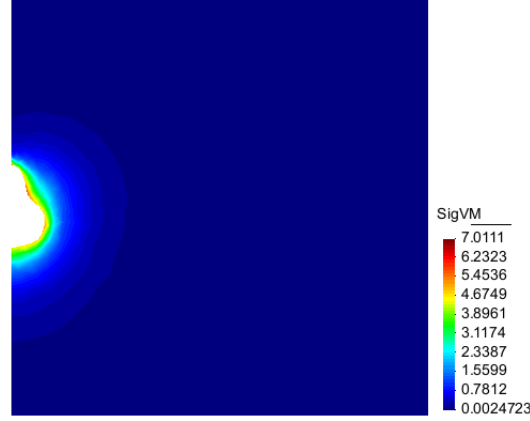


Figure 100 Equivalent stress distribution at the end of stage 2 using a $500m \times 500m$ domain.

We simulated the salt cavern depressurization by adopting a larger domain ($1100m$ height by $500m$ width for a $100m$ -high cavern) in order to check the boundary effect. At the end of stage 2, both the $500m \times 500m$ and the $1100m \times 500m$ models provide the same equivalent stress distributions, with less than 3% difference. The zones of stress concentration are also similar. Comparison of other results such as the distribution of various stress components further indicates that the discrepancy is within the acceptable range of 3%. Therefore, in the following analysis, to save computational time, we used the smaller domain shown in Fig. 99. Fig. 100 shows the equivalent stress distribution around the cavern for the small domain case. Note that results are reliable close to the cavern while relatively larger deviations exist at the far-field.

At the end of the first stage, the damage variable D_M is zero for all elements. The stress distribution is homogeneous. The resulting equivalent von Mises stress σ_e is close to zero all over the domain.

At the end of the second stage, after the depressurization in the cavern, we obtain extreme stresses around the cavern. The equivalent stress concentrates at the vicinity of the cavern, with the highest values appearing at specific locations including the roof, the most convex and concave parts (Fig. 100). This reveals the significant

influence of the irregular shape of the cavern on the stress distribution surrounding the cavern. Fig. 101a and 101b show the distribution of stress components S_{rr} and S_{zz} around the cavern after stage 2.

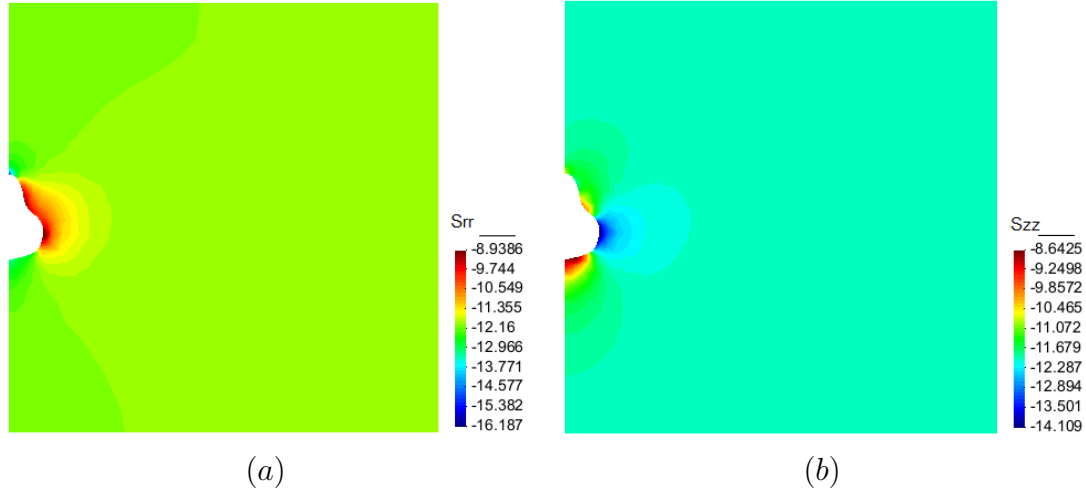


Figure 101 Stress distribution at the end of stage 2: (a) radial stress, (b) vertical stress.

Before the simulation reaches the end of the third stage, as a result of the stress dependence in the damage evolution law 1 (Eq. 98), damage increases rapidly in the element with the highest stress intensity (Fig. 102). Because the damage is so concentrated, it evolves very fast and does not propagate in the other elements. Therefore, damage evolution law 2 (Eq. 100) is more appropriate for the long-term creep test simulation. Using damage evolution law 2, we obtained the distribution of equivalent stress around the cavern after 360 days (Fig. 103).

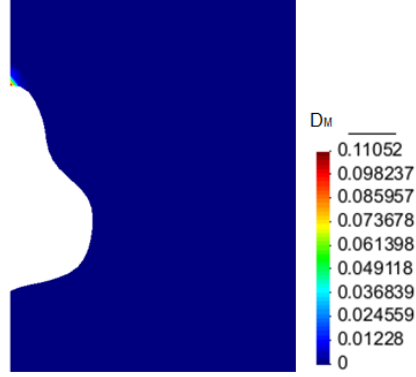


Figure 102 Damage distribution at the end of stage 3, using damage evolution law 1 (Eq. 98). Only roof elements are damaged in this magnified image.

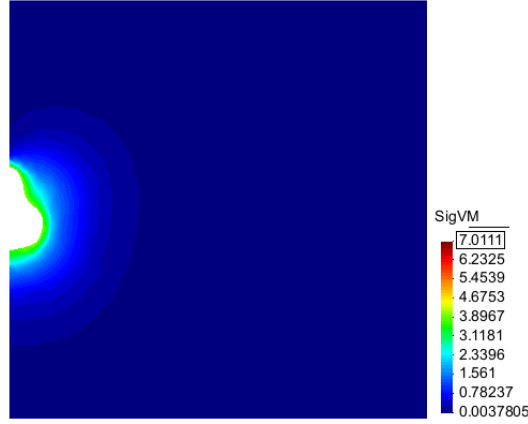


Figure 103 Equivalent stress distribution at the end of stage 3, using damage evolution law 2 (Eq. 100). We use the same scale of color bar as in Fig. 100.

As expected, damage predicted with damage evolution law 2 reaches its highest value at the roof. We can observe that in addition to the roof, damage tends to accumulate faster at the most convex and concave parts (Fig. 104). The damage evolution law 2 governed by Eq. 100 is more appropriate and allows the observation of the progressive damage accumulation in all elements surrounding the cavern. Therefore, the following results are all based on simulation with damage evolution law 2 (Eq. 100).

Overall, the cavern does not undergo severe damage for the particular geometry

and boundary conditions adopted in this problem. But as a result of viscoplastic deformation, salt caverns with complex geometries may be subjected to various types of failure such as rock fall (Djakeun, 2014). Irreversible strain evolves around the cavern because of the creep load induced by internal pressure (Fig. 105). The distribution of irreversible strain matches the distribution of damage.

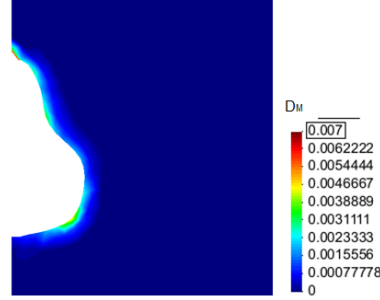


Figure 104 Damage distribution around the cavern wall at the end of stage 3, using damage evolution law 2 (Eq. 100).

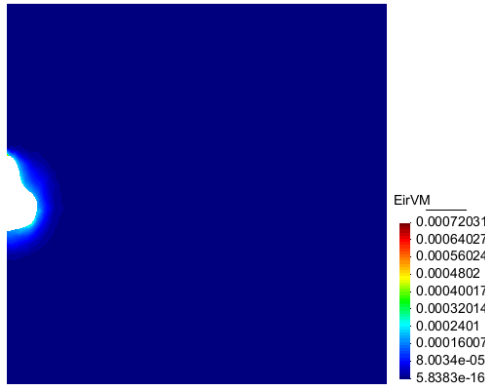


Figure 105 Irreversible equivalent strain at the end of stage 3, using damage evolution law 2 (Eq. 100).

Fig. 106 compares the stress distribution at the end of stage 2 and at the end of stage 3 along path WW' (refer to Fig. 99). Both radial and vertical stress components decrease during the creep process. This phenomenon corresponds to the stress relaxation that follows the initiation of damage. The distribution of equivalent stress along WW' confirms this phenomenon (Fig. 107). The equivalent stress drops at the cavern wall whereas it remains almost unchanged in the far field.

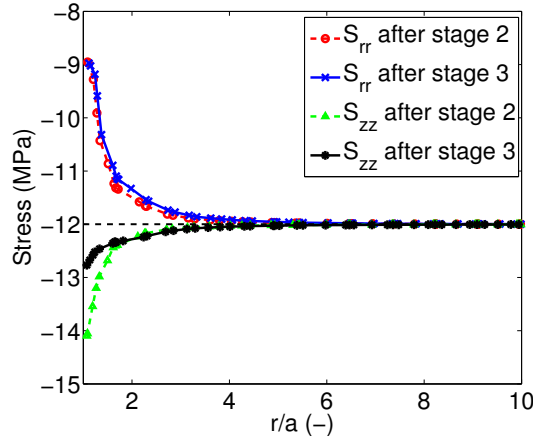


Figure 106 Radial/vertical stress distributions along path WW' after stages 2 and 3.

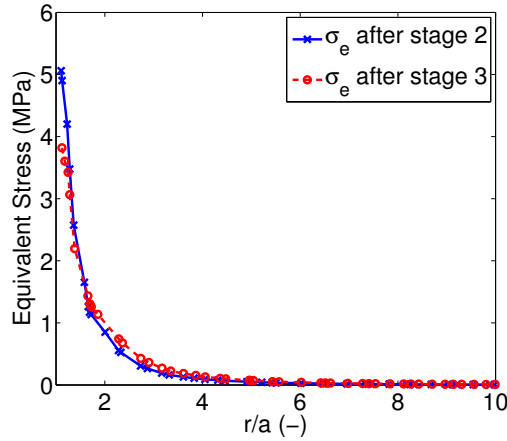


Figure 107 Equivalent stress distributions along path WW' after stages 2 and 3.

We tracked one element (element W in Fig. 99) at the cavern wall. We plotted the evolution of the equivalent stress in Fig. 108. Even though the pressure applied at the cavern wall is constant during stage 3, the equivalent stress decreases over time, as a result of stress relaxation induced by damage. Because of the bilinear relationship between critical viscoplastic strain and the equivalent stress, the evolution of the critical strain follows the evolution of the equivalent stress (Fig. 109). The evolution of damage in element W (Fig. 110) follows that of the viscoplastic equivalent strain, which can exceed the critical viscoplastic strain in this simulation.

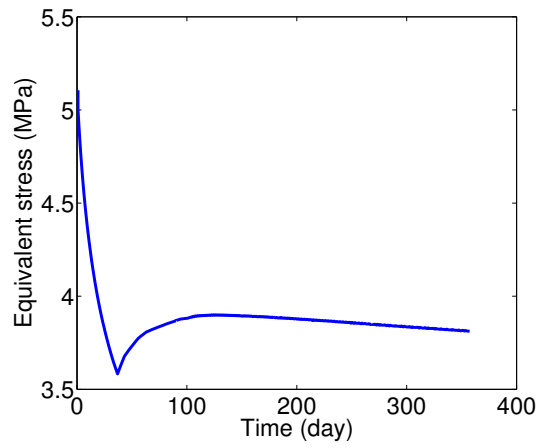


Figure 108 Evolution of equivalent stress of element W.

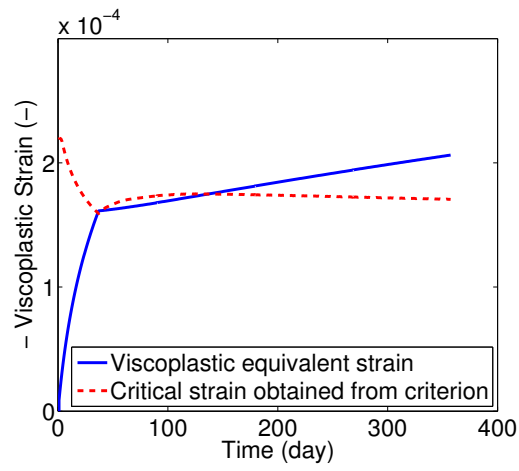


Figure 109 Evolution of equivalent viscoplastic strain of element W.

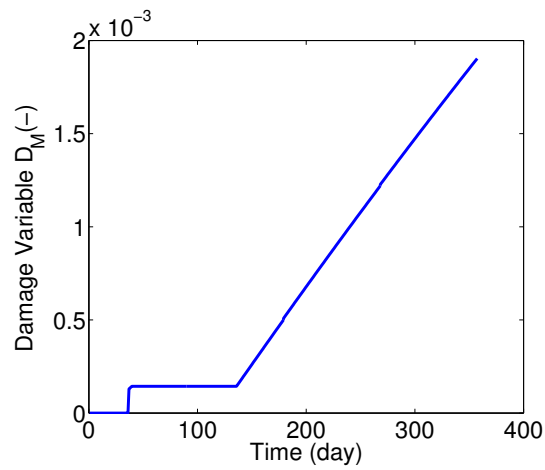


Figure 110 Evolution of damage variable of element W.

5.4 Conclusions

The FEM is used to investigate salt damage evolution at two different scales: fracture propagation in salt polycrystals and viscous damage in salt cavern. We implemented micromechanical and phenomenological models of viscoplasticity in *POROFIS* to perform the simulations.

For the study of the salt polycrystal, we first compared the performance of the self-consistent scheme in predicting grain breakage in a polycrystal subject to creep and cyclic loads to that of a joint-enriched FEM model. The self-consistent model is computationally economical and enables predicting important aspects of salt rock viscoplastic and damage behavior. By contrast, the FEM model is able to present the concentrations of vertical stresses at the contact of angular grains and the resulting geometric incompatibilities, which induces higher stress and inter-granular crack coalescence. The FEM model also captures the mechanical behavior of salt under cyclic loading: Higher stress amplitude, lower confining stress, and lower loading frequency increase the deformation and damage of the polycrystal; the Young's modulus of the polycrystal decreases exponentially with the number of cycles. We are currently working on the explicit representation of pores and cracks in FEM models, which is critical for analyzing intra- and inter-granular crack propagation and volumetric deformation during salt thermal consolidation.

For the study of the salt cavern, we used a tertiary creep law that is similar to the secondary creep law, except that the deformation rate is made dependent on a phenomenological damage variable. The transition between secondary and tertiary creep laws is governed by the bilinear damage threshold that was obtained from our self-consistent model. A salt cavern of irregular shape in axis-symmetric conditions was simulated. We compared two phenomenological damage evolution laws. Simulations of cavern depressurization with the stress-dependent damage evolution law provided concentrated damage at the crown, which led to numerical challenges. By

contrast, the strain-dependent damage evolution law allowed capturing the formation of a damaged zone that tends to appear at the most convex and concave parts of the cavity. Considering that salt caverns can undergo thermo-mechanical damage resulting in a decrease of its stiffness and strength, more work is needed to estimate the damage and potential failure in the near-field of underground salt cavities based on the stress and deformation fields. A more accurate estimation of the damage potential requires constitutive laws that account for both viscoplastic deformation and damage.

Through FEM analyses, we can understand better the viscous and damage behavior of a halite polycrystal at different scales. Capturing inter-granular and intra-granular damage allows us to explain the failure mechanism of the polycrystal. This is helpful for the study of polycrystals subjected to complex loading paths, and for the optimization of polycrystal mechanical properties for different engineering applications. FEM simulations at the reservoir scale enables the long-term assessment of geostorage facilities. Through the study of damage, stress, and deformation under long-term conditions, engineers could improve their design and operation plans for the cavern.

CHAPTER VI

CONCLUSIONS AND FUTURE STUDY

6.1 Summary

Continuum Damage Mechanics (CDM) models were initially formulated to predict the degradation of stiffness and strength properties of metals. With the increasing energy demand and the important environmental issues that arose from waste management, rocks became an interesting object of study for fracture mechanics and material scientists - and not only geologists. Compared to fracture mechanics, CDM was seen as a computationally efficient framework to predict the changes of stress and deformation at the bulk scale, which was well suited for engineering design. The first attempts to extend CDM to rock mechanics date back to the 1990's, with the works of French researchers like Dragon and Chaboche, who grounded their formulations on micromechanical analyses presented by Kachanov in the 1980's. Two damage mechanics schools emerged: the first puts emphasis on the thermodynamic consistency of phenomenological laws expressed for the continuum and the second focuses on fracture micromechanics and homogenization-based upscaling methods. In the late 1990's, models were improved to account for anisotropic unilateral effects induced by crack closure. In the early 2000's, researchers coupled CDM models to the Biot's theory to account for hydro-mechanical couplings, and later, to plasticity models. In the 2010's, the first theories of damage and healing mechanics were born, with the pioneering works of Ju and Voyiadjis in particular. However, these mathematical frameworks do not yet allow distinguishing crack closure and crack rebonding, and require using tensor variables that are unrelated to microstructure. As a result, evolution laws are expressed at the bulk scale and are disconnected from the

physical processes that drive crack healing and subsequent changes of stiffness and permeability.

In this thesis, we present the first attempt to couple Continuum Damage and Healing Mechanics to microstructure evolution, in order to understand why some rocks recover from mechanical damage, and some do not. Salt rock is an attractive host for deep waste disposals, due to favorable creep characteristics and low gas permeability. Salt cavities can also store high-pressure gas to activate turbines at peak hours. Halite is considered herein as a model material to characterize rock microstructure organization during brittle, ductile and viscoplastic deformation, and to study the microscopic processes leading to macroscopic mechanical recovery. Although polycrystalline halite (salt rock) is known for deformation by isochoric dislocation and diffusion processes, cracking is also an important grain-scale process at lower mean stress. The relationship between these micro-mechanisms and macroscopic strain evolution is still not well understood, especially in transient states. How and why do complex macroscopic phenomena (e.g., creep, damage, healing) emerge from elementary microscopic processes? We examined these fundamental scientific questions by performing a series of theoretical and numerical experiments.

In the first set of theoretical models, presented in Chapter 3, we adopt a “top-to-bottom” approach, in which the framework of CDM is enriched by internal variables defined as moments of probability of microstructure descriptors. The work involves: (i) image acquisition and processing during salt creep tests reported in the literature, performed by our collaborators at Texas A&M University, or conducted in our laboratory at Georgia Tech; (ii) statistical analysis of these images; (iii) theoretical derivations to relate probability density functions to field variables; (iv) formulation of a continuum mechanics framework; (v) numerical calibration and validation

with MATLAB. We successively improved a CDM model to: account for thermo-mechanical crack debonding, opening and closure; include mechanical recovery induced by Diffusive Mass Transfer in dry polycrystals; study mechanical anisotropy induced by healing; extend the concept of microstructure-enriched CDM to the prediction of permeability variations upon crack propagation and rebonding.

In the second theoretical modeling strategy, presented in Chapter 4, we use a "bottom-up" approach to upscale viscoplastic glide mechanisms that occur in salt mono-crystals to predict the transition between secondary and tertiary creep deformation regimes, and to gain fundamental understanding of fatigue in salt subject to cyclic loading. We propose a self-consistent scheme, which accounts for damage accommodation due to grain breakage. The model required: (i) defining an averaging method and kinetic laws at the micro-scale; (ii) formulating a continuum-based damage viscoplastic model based on the self-consistent method; (iii) explaining a computation algorithm to update iteratively microscopic and macroscopic variables and damage upon creep and cyclic loading paths; (iv) calibrating and validating the micro-macro model with MATLAB.

The third series of experiments presented in Chapter 5 is numerical and has two purposes: (i) we assessed the bottom-up model of creep damage and fatigue by comparing it with a joint-enriched Finite Element Method (FEM); (ii) we simulated the accumulation of damage around salt caverns subject to depressurization at the transition between secondary and tertiary creep. We used the FEM code *POROFIS*, developed by Dr. A. Pouya at Paris-Est University in France.

6.2 *Main Findings*

In Chapter 2, we explained why salt rock is a model material, relevant to the micro-macro modeling of coupled thermo-hydro-chemo-mechanical damage and healing processes. Salt is mono-mineralic, and heals within days at temperature, moisture and stress conditions that are achievable in the laboratory. Microscopic processes occurring in salt upon healing are also well documented, which makes it possible to benchmark different multi-scale mechanical models. We also reviewed the main strategies available to predict the effects of mechanical damage and healing, and discussed the capabilities of state-of-the-art numerical tools. The main challenge in rock mechanics is the linkage between continuum variables and microstructure descriptors.

In order to address this issue, in Chapter 3, a fabric-enriched Continuum Damage Mechanics (CDM) framework is proposed. The theoretical framework was built and improved step by step, in order to allow predicting damage and healing anisotropy induced by thermo-mechanical crack opening, closure and healing in rocks. In order to infer the form of fabric tensors from microstructure observation, creep tests were carried out on granular salt under constant stress and humidity conditions. Grain boundaries were viewed as analogs of cracks in salt rock. The rearrangement of salt particles and the rebonding of grain boundaries during creep were monitored by microscope and micro-CT scan imaging. Statistical analyses focused on three microstructure descriptors: the void area and the lengths of grain boundaries, which were used in the definition of the mechanical damage and healing variables, and the crack spacing, which was included in the expression of permeability. Crack closure was considered by adopting the concept of unilateral effect on rock stiffness. Crack rebonding was assumed to result from Diffusive Mass Transfer (DMT) processes. Net damage evolution obeys a diffusion equation in which the characteristic time scales with the typical size of a grain of salt. Healing parameters were calibrated by comparing crack cusp migration distance with published experimental results. Constitutive

models were programmed at the integration point in MATLAB to simulate thermo-mechanical loading and unloading cycles in axis-symmetric conditions. Macroscopic and microscopic model predictions are in agreement with the assumptions made in the constitutive framework, in particular: (i) under anisotropic mechanical boundary conditions, cracks can be produced during heating; (ii) the efficiency of healing increases with temperature, time, and the presence of moisture; (iii) permeability changes are predominantly controlled by changes in crack connectivity rather than the porosity change.

In Chapter 4, we used a self-consistent homogenization scheme to upscale the viscoplastic and damage behavior of salt polycrystals from mono-crystal viscous glide and breakage mechanisms. The micromechanical modeling approach enabled predicting important aspects of salt rock viscoplastic and damage behavior. Strain hardening during creep was evidenced by the increase of macroscopic viscoplastic strains at a decreasing rate, and by the progressive increase of microscopic stresses over time, until an asymptotic value. In creep tests in which a high compressive stress was applied before a lower compressive stress, tensile macroscopic strains were accompanied by a reorientation of microscopic stresses towards an isotropic distribution: simulations provided a microscopic interpretation to the phenomenon known as “creep recovery”, which is a memory effect. Grain breakage occurred for creep tests under high stress, and for cyclic loading tests simulated at lower frequencies, higher maximum stress, and/or higher loading amplitude. As expected, the Young’s modulus decreased with the increase of damage. Grain breakage provided a micromechanical explanation to the phenomenon known as “accelerated creep” (also called “tertiary creep”). The dependence of viscoplastic strains to cyclic loading frequency was well captured by the model: higher the frequency, smaller the macroscopic viscoplastic strain, and smaller the microscopic stresses. The increment of macroscopic viscoplastic deformation decreased over the cycles, which is in agreement with the phenomenon of plastic

adaptation or “shakedown” observed in elasto-plastic media.

In Chapter 5, we first compared the performance of the self-consistent scheme in predicting grain breakage in a polycrystal subject to creep and cyclic loads to that of a joint-enriched Finite Element Method (FEM) model. In the latter, different viscoplastic Finite Elements are used for grains of different orientations, and joint elements are introduced to predict crack propagation. The mesh is generated from an automated Electron BackScatter Diffraction (EBSD) map of salt microstructure. During creep tests, concentrations of vertical stress are noted at the contact of angular grains even before the initiation of creep, which results in inter-granular slip and subsequent damage in some joints. At the end of the creep test, viscous shear deformation in the grains induces more geometric incompatibilities, which results in higher stress and inter-granular crack coalescence. The joint-enriched FEM model captures the mechanical behavior of salt under cyclic loading: Higher stress amplitude, lower confining stress, and lower loading frequency increase the deformation and damage of the polycrystal; the Young’s modulus of the polycrystal decreases exponentially with the number of cycles. Second, we used the self-consistent model to calibrate the transition between secondary and tertiary creep against the critical viscoplastic strain at which grain breakage is initiated. We used phenomenological models of secondary and tertiary creep in order to simulate the accumulation of viscous damage around a salt cavern subject to depressurization with the FEM. The tertiary creep law is similar to the secondary creep law, except that the deformation rate depends on a phenomenological damage variable. We compared two phenomenological damage evolution laws. Simulations of cavern depressurization with the stress-dependent damage evolution law provided concentrated damage at the crown, which led to numerical challenges. By contrast, the strain-dependent damage evolution law allowed capturing the formation of a damaged zone that tends to appear at the most convex and concave parts of the cavity.

6.3 Plans for Future Study

Several unknowns and challenges still arouse our scientific curiosity. Below are a few suggestions for future studies:

- A more complete set of independent fabric descriptors is needed to better capture the evolution of mechanical and transport properties of rocks during damage and healing processes.
- The reconstruction of the pore network based on 3D image processing is required to estimate fluid flow anisotropy within the crack network.
- More work is needed to account for non-elastic inclusion-matrix interactions (known as “viscous accommodation”), which results from geometric incompatibilities between grains. The bottom-up damage model could also be improved in order to account for the residual stiffness of grains, which requires introducing elastic anisotropy for both the grains and the matrix.
- The explicit representation of pores and cracks in FEM models of polycrystals is still numerically challenging; research towards the improvement of joint-enriched FEM seems promising to address this issue. Such numerical scheme could be used to analyze intra- and inter-granular crack propagation during salt thermal consolidation for instance.
- The knowledge of the dominating halite crystal deformation mechanisms is critical to understand salt rock macroscopic creep rates observed around caverns and to predict the transition between secondary and tertiary creep. More work is needed to link grain breakage to the phenomenological damage variable used in CDM to predict the reduction of elastic moduli.
- Further studies on micro-macro damage mechanics are needed to understand the origin of the fatigue behavior of crystalline materials upon cyclic loading.

APPENDIX I

LITERATURE REVIEW

A.1 State of the Art: Experimental Assessment of Thermo-mechanical Damage in Rocks

Material	Experimental test	T (°C)	Peak stress σ_P (MPa)	Strain at peak stress ε_P	Stiffness (GPa) (high T - low T)	References
Limestone	UC without cooling	25 ~ 800	25 ~ 110	0.005 ~ 0.013	3.2 ~ 17.8 (E)	Mao et al. (2009)
	UC after cooling	20 ~ 250	43.2 ~ 46.4	0.0023 ~ 0.0029	23.7 ~ 25 (E)	Lion et al. (2005)
Salt rock	TC without cooling	23 ~ 200	15 ~ 65	0.02 ~ 0.35	29.6 ~ 36.5 (E)	Wawersik and Hannum (1980)
	UC without cooling	20 ~ 180	10 ~ 22	0.005 - 0.018	1.14 ~ 2.15 (E _t)	Liang et al. (2006)
Gabbro	UC after cooling	25 ~ 1000	35 ~ 230	0.0023 ~ 0.006	2.5 ~ 85 (E)	Keshavarz et al. (2010)
Breccia	UC after cooling	20 ~ 800	92.4 ~ 130.3	0.0034 ~ 0.0045 (high T - low T)	11.8 ~ 30.3 (E)	Zhu et al. (2006)
Granite	TC without cooling	20 ~ 700	600 ~ 1150	0.015 ~ 0.025	32 ~ 60 (E)	Wong (1982)
	UC without cooling	20 ~ 600	150 ~ 260	0.007 ~ 0.014	20 ~ 50 (E _t)	Homand- Etienne and Houpert (1989)
	UT without cooling	20 ~ 600	1 ~ 9	0.0002 ~ 0.0006	5 ~ 20 (E)	Homand- Etienne and Houpert (1989)
	UC and radial compression test under thermal hysteresis without restoring to room temperature	-160 ~ 100	σ_c heat: 155 ~ 195 cool: 180 ~ 220 σ_t heat: 8 ~ 9.5 cool: 8.5 ~ 14	heat: 0.00015 ~ 0.0008 cool: -0.0018 ~ -0.0001 (ε_τ)	heat: 46 ~ 54 cool: 40 ~ 50 (E _t)	Inada et al. (1997)
	UC after cooling	20 ~ 800	105.5 ~ 152.9	0.0026 ~ 0.0099	15.9 ~ 32.4 (E)	Zhu et al. (2006)

Material	Experimental test	T (°C)	Peak stress σ_P (MPa)	Strain at peak stress ε_P	Stiffness (GPa) (high T - low T)	References
Andesite	UC without cooling	23 ~ 200	100 ~ 117	0.0062 ~ 0.0093	16 ~ 21 (E)	Jeong et al. (2007)
Mudstone	UC without cooling	25 ~ 800	25 ~ 275	0.0045 ~ 0.013	6.6 ~ 24.7 (E)	Liu et al. (2014b)
Tuff	UC and radial compression test under thermal hysteresis without restoring to room temperature	-160 ~ 100	σ_c heat: 10 ~ 15 cool: 22 ~ 30 σ_t heat: 1.5 ~ 2.3 cool: 2 ~ 4	heat: 0.0001 ~ 0.0007 cool: -0.0016 ~ -0.0001 (ε_τ)	heat: 3.2 ~ 4 cool: 3.5 ~ 4.6 (E_t)	Inada et al. (1997)
	UC after cooling	20 ~ 800	101.6 ~ 147.7	0.0043 ~ 0.0069	19.9 ~ 30.7 (E)	Zhu et al. (2006)
Marble	UC after cooling	20 ~ 600	57 ~ 131	0.0087 ~ 0.0123	9.18 ~ 16.8 (E)	Shi et al. (2008)
<div> <div>Notations:</div> <div> E = elastic modulus σ_c = compressive strength T = temperature </div> <div> E_t = tangent modulus σ_t = tensile strength ε_τ = thermal strain </div> <div> UC = uniaxial compression TC = triaxial compression UT = uniaxial tension </div> </div>						

A.2 Review of Microstructure-enriched Permeability Model for Rocks

Rock type	Authors	Permeability Expression	Microstructure factors
sandstone	Koplik et al. (1984)	$k = g_m t, \quad t = < \frac{1}{A(P)} \sum_{b \cap P} L_b \cdot \hat{n} >$ $\sum_i N_i \frac{g_i - g_m}{g_i + (\frac{\pi}{2} - 1)g_m} = 0$	tortuosity, path length, throat size
sandstone and carbonate rocks	Katz and Thompson (1986)	$k = cl_c^2(\sigma/\sigma_0)$	characteristic length of pore space
cracked rocks	Gavrilenko and Gueguen (1989)	$K = \frac{4\pi}{15} N_f^0 < c^5 >$ $\int_0^{\alpha_M - \beta} \alpha^3 n_\alpha (\alpha + \beta) d\alpha F[x(\beta)]$	aspect ratio, fraction of cracks, crack number density, crack radius and aperture, crack roughness
naturally fractured rocks	Lee et al. (1995)	$K_{ij} = \frac{1}{12} (P_{kk} \delta_{ij} - P_{ij}) \quad P_{ij} = \sum_{k=1}^{N_f} P_{ij}^k$	effect of hydromechanical coupling, normal closure, and fracture geometry (aperture, size and orientation)
dolomite, siltstone, and sandstone	Ioannidis et al. (1996)	$lnk = a + b + ln(\phi) + cln(I_S)$ $I_S = \int_0^\infty R_z(u) du$	correlation length, lag vector measuring the separation of two points in space
salt	Peach and Spiers (1996)	$k = \frac{2}{15} \theta \alpha D < w >^2 [1 - 4((\frac{8A\alpha}{\pi D} - \frac{3}{4})^{1/2} - \frac{1}{2})^3 + 3((\frac{8A\alpha}{\pi D} - \frac{3}{4})^{1/2} - \frac{1}{2})^4]$	crack geometry and dilatancy
large-scale fractured outcrop	Brown and Bruhn (1998)	$K_{ij} = \lambda (P_{kk} \delta_{ij} - P_{ij})$ $\sigma^2 = -C \frac{\pi s^{\alpha-1} sec(\alpha\pi/2)}{2^{\alpha-1}[(\Gamma \frac{\alpha+1}{2})]^2}$	influence of crack closure, fracture surface roughness
salt	Chan et al. (2001)	$K = C_P (1-\gamma)^3 (1-D_f)^3 + C_{CK} [\frac{\gamma^3 (1-D_f)^3}{(1-\gamma+\gamma D_f)^2}]$	tortuosity parameter, specific pore surface area, geometric shape
granite	Oda et al. (2002)	$k_{ij} = \frac{\lambda}{12} (P_{kk} \delta_{ij} - P_{ij})$ $P_{ij} = \pi \rho \int_0^{r_m} \int_0^{t_m} \int_{\Omega/2} r^2 t^3 n_i n_j \times 2E(n, r, t) d\Omega dr dt n$	crack size, crack number
fractured rock masses	Min et al. (2004)	$k_x = k_{nx} + k_{dx} = \frac{f_x}{12} b_x^3 + \frac{f_{dx}}{12} d_x^3$ $k_y = k_{ny} + k_{dy} = \frac{f_y}{12} b_y^3 + \frac{f_{dy}}{12} d_y^3$	crack closure, shear dilation
brittle rocks	Shao et al. (2005)	$k = k^0 + k^c, \quad k^c = (\frac{N}{\Omega})(\frac{\lambda\pi}{12})\frac{1}{4\pi} \int_{S^2} R(n) e(n)^3 r(n)^2 (\delta - n \otimes n) dS$	crack orientation, radius, aperture, number of cracks
salt	Alkan (2009)	$k^{1/3} = m - n \ln \sigma_3$ $k = Ak_f [(1 - e^{-(\sigma_1/\sigma_{CD})}) - 0.63]^2$	aperture width, surface roughness, pore pressure
rocks	Arson and Pereira (2013)	$k = \frac{\gamma}{8\mu} \Phi \int_0^\infty \frac{1}{f(r)} dr \int_0^\infty f(r) r^2 dr$	pore radius, porosity, volumetric frequency
3D fractured porous media	Pouya and Vu (2012)	$\hat{k} = k\delta + \sum_m k_m^f$ $k_m^f = \rho_m \frac{16kc^m R^{m3}}{3c^m + \frac{16}{3}kR^m} (\delta - n^m \otimes n^m) \cdot A$	fracture radius, orientation, density, conductivity

A.3 Review of Experimental Studies of Salt Fatigue under Cyclic Loading

Salt studied	Loading conditions (σ_{\max} = maximum stress; σ_{\min} = minimum stress; N = Number of cycles; f = frequency; $\dot{\epsilon}$ = strain rate)	Key findings	Reference
78.84% NaCl, 18.92% water insoluble materials (quartz, clay, mud, and marl), 2.14-2.74% MgCl ₂ and CaSO ₄ (India)	σ_{\max} = 10, 20, 30, 40, 50, 60, 65, 70, 72, 75% of the compressive strength; $f = 3.5 \times 10^{-3}$ Hz; $N = 50-400$	Below a certain stress level, the compressive strength and the elastic modulus depend on intrinsic anisotropy (bedding plane) and on the number of cycles; above this stress level, the influence is negligible.	Dubey and Gairola (2000)
pure rock salt and less than 0.5% insoluble component (Russia)	$N = 2$: triaxial compression followed by uniaxial compression	Memory effects in stress were measured when the maximum in-situ stress exceeded the elastic limit.	Filimonov et al. (2001)
relatively pure halite with less than 1-2% anhydrite, clay minerals and ferrous oxide (Thailand)	$\sigma_{\max} = 15.9$ to 34.6 MPa; $\sigma_{\min} = 0.15$ MPa; $f = 0.001 - 0.3$ Hz; $N = 7-595$	Strength decreases for larger numbers of loading cycles; salt viscoplasticity decreases with increasing loading frequency.	Fuenkajorn and Phueakphum (2010)
two types of samples: salt rock with pure halite; salt rock dominated by thenardite (Na ₂ SO ₄) (China)	uniaxial compression; $\dot{\epsilon} = 2 \times 10^{-5}, 2 \times 10^{-4}, 2 \times 10^{-3} s^{-1}$; $\sigma_{\max} = 12.5-15.4$ MPa	Elastic moduli slightly increase with the strain rate; Poisson's ratio decreases with the strain rate; the failure stress is lower for lower strain rates.	Liang et al. (2011)
high purity (NaCl, Na ₂ SO ₄ , CaSO ₄) with less than 10% insolubles (glauberite, argillaceous, anhydrite) (China)	$\sigma_{\max} = 75-90\%$ of the compressive strength; $\sigma_{\min} = 37.5-45\%$ of the compressive strength; $f = 1$ Hz; $N = 1041-14789$	The maximum and mean stresses affect fatigue significantly; failure modes for uniaxial compression and cyclic loading are different.	Guo et al. (2012)
75-85% NaCl (halite), 0.72% Na ₂ SO ₄ (sodium sulfate), 1.2% CaSO ₄ (anhydrite), 7-10% insoluble components (China)	$\sigma_{\max} = 24.9-53.2$ MPa; $\sigma_{\min} = 16.9-28.2$ MPa; sinusoidal form; $f = 0.025, 0.05, 0.1$ Hz; confining pressure = 7, 14, 21 MPa; $N = 500-850$	Elastic moduli decrease exponentially for increasing number of cycles; modulus degradation is independent of stress level and confining pressure; higher loading frequencies cause less viscoplastic deformation; triaxial compressive strength and total strain increase with stress amplitude, loading frequency, and confining pressure.	Ma et al. (2013)
salt rock with salt content up to 84.76-93.76% (China)	$\sigma_{\max} = 20, 30, 40, 50, 60, 70, 85\%$ of the compressive strength (20 MPa); $\sigma_{\min} = 1$ MPa; sinusoidal form; $f = 1$ Hz; $N = 31$	The stress level leading to the initiation of fatigue damage under cyclic loading is 20% of the uniaxial compressive strength; damage accumulation accelerates beyond the point of volume expansion.	Liu et al. (2014a)

APPENDIX II

RELATION BETWEEN RESIDUAL STRESS AND PROBABILITY DENSITY FUNCTIONS OF FABRIC DESCRIPTORS

According to Table 6 in Section 3.3,

$$\sigma_R^{(i)} = N_v \frac{2\sqrt{2}}{\pi} \frac{\mu}{\kappa + 1} M_i \quad (104)$$

in which:

$$M_i = \frac{A_v}{R_j R_k} \quad (105)$$

M_i is a random variable, defined as the product of three independent random variables: A_v , $z_j = 1/R_j$ and $z_k = 1/R_k$. Therefore, the probability of M_i writes:

$$p(M_i) = p_A(A_v) \times p_{z_j}(z_j) \times p_{z_k}(z_k) \quad (106)$$

The components of the residual stress are updated with the means of M_1 , M_2 and M_3 , noted \overline{M}_1 , \overline{M}_2 and \overline{M}_3 respectively:

$$\sigma_R^{(i)} = N_v \frac{2\sqrt{2}}{\pi} \frac{\mu}{\kappa + 1} \overline{M}_i \quad (107)$$

$$\begin{aligned} \overline{M}_i &= \int_{A_{min}}^{A_{max}} \int_{1/(R_{max})^2}^{1/(R_{min})^2} A_v \times z_j \times z_k \\ &\times p_A(A_v) \times p_{z_j}(z_j) \times p_{z_k}(z_k) dz_k dz_j dA \end{aligned} \quad (108)$$

In the equation above, we have:

$$p_A(A_v) = a A_v^t \quad (109)$$

The probability $p_{zj}(z_j)$ is obtained by differentiating the cumulative density function

$$F_j^*(z_j) = p_{zj}(z \leq z_j):$$

$$p_{zj}(z_j) = \frac{dF_j^*(z_j)}{dz_j} \quad (110)$$

With:

$$F_j^*(z_j) = p_{zj}(R^{-1} \leq z_j) = p_j(R \geq z_j^{-1}) \quad (111)$$

$$F_j^*(z_j) = 1 - p_j(R \leq z_j^{-1}) = 1 - F_j(z_j^{-1}) \quad (112)$$

Therefore:

$$p_{zj}(z_j) = -\frac{dF_j(z_j^{-1})}{dz_j} = -\underbrace{\frac{dF_j(z_j^{-1})}{d(z_j^{-1})}}_{p_j(z_j^{-1})} \underbrace{\frac{dz_j^{-1}}{dz_j}}_{-z_j^{-2}} \quad (113)$$

As a result:

$$p_{zj}(z_j) = p_j(z_j^{-1}) \times (z_j)^{-2} \quad (114)$$

Using the expression of the probability density function of the crack length components:

$$p_{zj}(z_j) = \frac{z_j^{-1}}{\sqrt{2\pi} s_j} \exp \left[-\frac{(\ln(z_j^{-1}) - m_j)^2}{2s_j^2} \right] \quad (115)$$

By this means, the residual stress can be derived from the fabric descriptors, i.e. from the void area and the crack length components.

APPENDIX III

APPROXIMATED MACROSCOPIC VISCOPLASTIC LAW

For a homogeneous and isotropic elastic matrix, Kröner's model (Kröner, 1961), proposed initially for elasto-plastic materials, was extended by Weng for viscoplastic materials (Weng, 1982), in the following form:

$$\dot{\boldsymbol{\sigma}} - \dot{\bar{\boldsymbol{\sigma}}} = 2\mu(1 - \beta)(\dot{\bar{\boldsymbol{\epsilon}}}^{vp} - \dot{\boldsymbol{\epsilon}}^{vp}) \quad (116)$$

in which $\dot{\boldsymbol{\sigma}}$ is the rate of microscopic stress, and $\dot{\bar{\boldsymbol{\sigma}}}$ is the rate of macroscopic stress. $\dot{\bar{\boldsymbol{\epsilon}}}^{vp}$ and $\dot{\boldsymbol{\epsilon}}^{vp}$ denote the macroscopic and microscopic viscoplastic strain rates. β is given by:

$$\beta = \frac{2(4 - 5\nu)}{15(1 - \nu)} \quad (117)$$

In which ν is the Poisson's ratio of both the matrix and the grains (uniform elasticity). According to Eq. 50 in Section 4.2, the microscopic and macroscopic viscoplastic strains are purely deviatoric. Taking the deviatoric part of Eq. 116 yields:

$$\dot{\mathbf{s}} = \dot{\bar{\mathbf{s}}} + 2\mu(1 - \beta)(\dot{\bar{\boldsymbol{\epsilon}}}^{vp} - \dot{\boldsymbol{\epsilon}}^{vp}) \quad (118)$$

Where \mathbf{s} and $\bar{\mathbf{s}}$ are the micro- and macro- deviatoric stresses, respectively.

We derive a simple relationship between the macroscopic viscoplastic strain rate and the macroscopic stress imposed during the simulations. Let us recall the constitutive law adopted in the model:

$$\dot{\boldsymbol{\epsilon}}^{vp} = \sum_{l=1}^6 \dot{\gamma}^l \mathbf{a}^l, \quad \dot{\gamma}^l = \gamma_0 h^l \left| \frac{\tau^l}{\tau_0} \right|^n, \quad \tau^l = \boldsymbol{\sigma} : \mathbf{a}^l \quad (119)$$

And the homogenization scheme based on Weng's model (Eq. 118), for the axial loading (Eq. 71-72), provides:

$$\dot{\mathbf{s}} = \rho(\dot{t})\boldsymbol{\Psi} - 2\mu(1 - \beta)\dot{\boldsymbol{\epsilon}}^{vp} \quad (120)$$

Taking the average of Eq. 120:

$$\dot{\bar{\mathbf{s}}} = \dot{\rho}(t)\mathbf{\Psi} - 2\mu(1 - \beta)\langle \dot{\boldsymbol{\epsilon}}^{vp} \rangle \quad (121)$$

We propose to approximate the relation given in Eq. 120 by replacing the microscopic stress $\boldsymbol{\sigma}$ by the macroscopic stress $\bar{\boldsymbol{\sigma}} = q(t)\mathbf{r}$ in Eq. 119. Eq. 121 then becomes:

$$\dot{q}(t)\mathbf{\Psi} = \dot{\rho}(t)\mathbf{\Psi} - 2\mu(1 - \beta)\langle \sum_{l=1}^L \gamma_0 h^l \left| \frac{q(t)\mathbf{r} : \mathbf{a}^l}{\tau_0} \right|^n \mathbf{a}^l \rangle \quad (122)$$

Multiplying both sides of Eq. 122 by $\mathbf{\Psi}$:

$$\dot{q}(t)\mathbf{\Psi} : \mathbf{\Psi} = \dot{\rho}(t)\mathbf{\Psi} : \mathbf{\Psi} - 2\mu(1 - \beta)\langle \sum_{l=1}^L \gamma_0 h^l \left| \frac{q(t)\mathbf{r} : \mathbf{a}^l}{\tau_0} \right|^n \mathbf{a}^l : \mathbf{\Psi} \rangle \quad (123)$$

Then noticing that $Tr(\mathbf{a}^l) = 0$, Eq. 123 can be rewritten as:

$$\dot{q}(t)\mathbf{\Psi} : \mathbf{\Psi} = \dot{\rho}(t)\mathbf{\Psi} : \mathbf{\Psi} - 2\mu(1 - \beta)\langle \sum_{l=1}^L \gamma_0 h^l \left| \frac{q(t)\mathbf{r} : \mathbf{a}^l}{\tau_0} \right|^n \mathbf{r} : \mathbf{a}^l \rangle \quad (124)$$

Noticing that $h^l \cdot \mathbf{r} : \mathbf{a}^l$ has the same sign as $\tau^l \cdot \mathbf{r} : \mathbf{a}^l$, and since $q(t) \geq 0$, we have:

$$\tau^l \cdot \mathbf{r} : \mathbf{a}^l = (\bar{\boldsymbol{\sigma}} : \mathbf{a}^l) \cdot (\mathbf{r} : \mathbf{a}^l) = q(t) \cdot (\mathbf{r} : \mathbf{a}^l) \cdot (\mathbf{r} : \mathbf{a}^l) \geq 0 \quad (125)$$

Therefore:

$$h^l \cdot \mathbf{r} : \mathbf{a}^l = |\mathbf{r} : \mathbf{a}^l| \quad (126)$$

Eq. 124 can be rewritten as:

$$\dot{q}(t)\mathbf{\Psi} : \mathbf{\Psi} = \dot{\rho}(t)\mathbf{\Psi} : \mathbf{\Psi} - 2\mu(1 - \beta)\langle \sum_{l=1}^L \gamma_0 \left| \frac{q(t)}{\tau_0} \right|^n |\mathbf{r} : \mathbf{a}^l|^{n+1} \rangle \quad (127)$$

After dividing by $(\mathbf{\Psi} : \mathbf{\Psi})$:

$$\dot{q}(t) = \dot{\rho}(t) - q^n(t) \frac{1}{(\tau_0)^n} \frac{2\mu(1 - \beta)}{\mathbf{\Psi} : \mathbf{\Psi}} \langle \sum_{l=1}^L \gamma_0 |\mathbf{r} : \mathbf{a}^l|^{n+1} \rangle \quad (128)$$

Then recalling that $(\mathbf{\Psi} : \mathbf{\Psi}) = 2/3$, Eq. 128 can be simplified into:

$$\dot{q}(t) = \dot{\rho}(t) - \underbrace{\frac{q^n(t)}{(\tau_0)^n} 3\mu(1 - \beta) \langle \sum_{l=1}^L \gamma_0 |\mathbf{r} : \mathbf{a}^l|^{n+1} \rangle}_M \quad (129)$$

The expression of q as a function of time is obtained by solving the following non-linear differential equation:

$$\dot{q}(t) + M \frac{q^n(t)}{(\tau_0)^n} = \dot{\rho}(t) \quad (130)$$

Recalling that:

$$\dot{\rho}(t) = \dot{q}(t) + 3\mu(1 - \beta)\dot{p}(t) \quad (131)$$

The following equation is obtained:

$$\dot{p}(t) = \frac{M}{3\mu(1 - \beta)} \frac{q^n(t)}{(\tau_0)^n} \quad (132)$$

Eq. 132, based on an approximation, provides a direct relationship between the macroscopic viscoplastic strain rate $\dot{p}(t)$ and the macroscopic stress $q(t)$.

APPENDIX IV

2D PLANE STRAIN HILL'S TENSOR

As a result of an internal stress inside the inclusion (Fig. 60c in Section 5.2), the displacement u^1 and stress fields σ^1 are

$$u_r^1 = a_1 \frac{R^2}{r}, \quad u_\theta^1 = 0, \quad (133)$$

$$\sigma_{rr}^1 = -a_1 \frac{E}{1+\nu} \frac{R^2}{r^2}, \quad \sigma_{\theta\theta}^1 = a_1 \frac{E}{1+\nu} \frac{R^2}{r^2}, \quad (134)$$

in which R is the radius of the spherical inclusion, a is a stress-dependent coefficient, E is the Young's modulus, and ν is the Poisson's ratio.

For a pure shear displacement field homogeneous in r^{-3} , the displacement u^2 and stress fields σ^2 are

$$u_r^2 = a_2 \frac{R^4}{r^3} \cos 2\theta, \quad u_\theta^2 = a_2 \frac{R^4}{r^3} \sin 2\theta, \quad (135)$$

$$\sigma_{rr}^2 = -a_2 \frac{3E}{1+\nu} \frac{R^4}{r^4} \cos 2\theta, \quad \sigma_{\theta\theta}^2 = a_2 \frac{3E}{1+\nu} \frac{R^4}{r^4} \cos 2\theta, \quad \sigma_{r\theta}^2 = -a_2 \frac{3E}{1+\nu} \frac{R^4}{r^4} \sin 2\theta. \quad (136)$$

For an auxiliary homogeneous displacement field, the displacement u^3 and stress fields σ^3 are

$$u_r^3 = 2a_3(1-\nu) \frac{R^2}{r} \cos 2\theta, \quad u_\theta^3 = -a_3(1-2\nu) \frac{R^2}{r} \sin 2\theta, \quad (137)$$

$$\sigma_{rr}^3 = -a_3 \frac{2E}{1+\nu} \frac{R^2}{r^2} \cos 2\theta, \quad \sigma_{\theta\theta}^3 = 0, \quad \sigma_{r\theta}^3 = -a_3 \frac{E}{1+\nu} \frac{R^2}{r^2} \sin 2\theta. \quad (138)$$

The 2D Hill's tensor L^* , correlated by a stress tensor A and a strain tensor B , has to satisfy the condition that when $r = R$, we have

$$\sigma \cdot n = A \cdot n, \quad (139)$$

$$u = B \cdot x, \quad (140)$$

$$B = -M^* : A, \quad (141)$$

in which $M^* = L^{*-1}$ is the inverse of 2D Hill's tensor under plane strain condition.

For the transition from a Cartesian coordinate to a cylindrical coordinate, we know

$$\begin{bmatrix} \sigma_1 & 0 \\ 0 & \sigma_2 \end{bmatrix} \longleftrightarrow \begin{bmatrix} \sigma_1 \cos^2 \theta + \sigma_2 \sin^2 \theta & (\sigma_2 - \sigma_1) \sin \theta \cos \theta \\ (\sigma_2 - \sigma_1) \sin \theta \cos \theta & \sigma_1 \sin^2 \theta + \sigma_2 \cos^2 \theta \end{bmatrix}. \quad (142)$$

Therefore, in the cylindrical coordinate, the matrix J that represents the antisymmetric component of the strain can be writes as

$$J = \begin{bmatrix} 1 & 0 \\ 0 & -1 \end{bmatrix} \longrightarrow J = \begin{bmatrix} \cos 2\theta & -\sin 2\theta \\ -\sin 2\theta & -\cos 2\theta \end{bmatrix}. \quad (143)$$

We note the principal directions of A and choose them as the (x, y) axes:

$$A = \begin{bmatrix} \sigma_1 & 0 \\ 0 & \sigma_2 \end{bmatrix} = \frac{\sigma_1 + \sigma_2}{2} \delta + \frac{\sigma_1 - \sigma_2}{2} J, \quad (144)$$

in which δ represents the symmetric part and J represents the antisymmetric part.

On the cavity wall, we have

$$\sigma_{rr} = e_r \cdot \sigma \cdot e_r = \frac{\sigma_1 + \sigma_2}{2} + \frac{\sigma_1 - \sigma_2}{2} \cos 2\theta, \quad (145)$$

$$\sigma_{r\theta} = e_\theta \cdot \sigma \cdot e_r = -\frac{\sigma_1 - \sigma_2}{2} \sin 2\theta. \quad (146)$$

in which e_r and e_θ are the unit vectors along the radial and tangential directions, respectively.

The combination of the 3 fields $\sigma^1, \sigma^2, \sigma^3$ yields,

$$\sigma_{rr} = -\frac{E}{1 + \nu} [a_1 + (3a_2 + 2a_3) \cos 2\theta], \quad (147)$$

$$\sigma_{r\theta} = -\frac{E}{1 + \nu} (3a_2 + a_3) \sin 2\theta. \quad (148)$$

By comparing two sets of equations and ensuring that they satisfy all possible θ , we have

$$\begin{cases} a_1 = -\frac{1+\nu}{E} \frac{\sigma_1+\sigma_2}{2} \\ a_2 = \frac{1+\nu}{E} \frac{\sigma_1-\sigma_2}{2} \\ a_3 = -\frac{1+\nu}{E} (\sigma_1 - \sigma_2). \end{cases} \quad (149)$$

Similarly, the displacement field is $u = u^1 + u^2 + u^3$ on $r = R$:

$$u_r = a_1 R + a_2 R \cos 2\theta + 2a_3(1 - \nu) R \cos 2\theta, \quad (150)$$

$$u_\theta = a_2 R \sin 2\theta - a_3(1 - 2\nu) R \sin 2\theta. \quad (151)$$

If we write, on $r = R$, $x = R e_r$, then we have

$$B = b^0 \delta + b^1 J = b^0 \begin{bmatrix} 1 & 0 \\ 0 & -1 \end{bmatrix} + b^1 \begin{bmatrix} \cos 2\theta & -\sin 2\theta \\ -\sin 2\theta & -\cos 2\theta \end{bmatrix}, \quad (152)$$

$$u_r = (RB \cdot e_r)_r = Rb^0 + Rb^1 \cos 2\theta, \quad (153)$$

$$u_\theta = (RB \cdot e_r)_\theta = -Rb^1 \sin 2\theta. \quad (154)$$

Comparing the previous two sets of equations, we have

$$\begin{cases} b_0 = a_1 \\ b^1 = a_2 + 2a_3(1 - \nu) \\ b^1 = -a_2 + a_3(1 - 2\nu). \end{cases} \quad (155)$$

So we can obtain

$$\begin{cases} b_0 = a_1 = -\frac{1+\nu}{E} \frac{\sigma_1+\sigma_2}{2} = -\frac{1+\nu}{2E} \delta : A \\ b^1 = a_2 + 2a_3(1 - \nu) = \frac{1+\nu}{E} (4\nu - 3) \frac{\sigma_1-\sigma_2}{2}. \end{cases} \quad (156)$$

By substituting Eq. 156 into the expression for B (Eq. 141), we can deduce that,

$$M^* = L^{*-1} = \frac{1+\nu}{E} [(3 - 4\nu)I - (1 - 2\nu)\delta \otimes \delta], \quad (157)$$

in which $I_{ijkl} = \frac{1}{2}(\delta_{ik}\delta_{jl} + \delta_{il}\delta_{jk})$.

Bibliography

- Abràmoff MD, Magalhães PJ, Ram SJ (2004) Image processing with imagej. *Biophotonics international* 11(7):36–42
- Abu Al-Rub R, Voyiadjis G (2003) On the coupling of anisotropic damage and plasticity models for ductile materials. *Int J Solids Struct* 40(11):2611–2643
- Alkan H (2009) Percolation model for dilatancy-induced permeability of the excavation damaged zone in rock salt. *International Journal of Rock Mechanics and Mining Sciences* 46:716–724
- Anderson T (2005) *Fracture Mechanics: Fundamentals and Applications*, Third Edition. Taylor & Francis
- Arson C, Gatmiri B (2009) A mixed damage model for unsaturated porous media. *Comptes Rendus Mécanique* 337(2):68–74
- Arson C, Gatmiri B (2010) Numerical study of a thermo-hydro-mechanical damage model for unsaturated porous media. *Ann Solid Struct Mech* 1(2):59–78
- Arson C, Gatmiri B (2012) Thermo-hydro-mechanical modeling of damage in unsaturated porous media: Theoretical framework and numerical study of the edz. *International Journal for Numerical and Analytical Methods in Geomechanics* 36:272–306
- Arson C, Pereira JM (2013) Influence of damage on pore size distribution and permeability of rocks. *International Journal for Numerical and Analytical Methods in Geomechanics* 37:810–831
- Arson C, Xu H, Chester F (2012) On the definition of damage in time-dependent healing models for salt rock. *Géotechnique Lett* 2(April-June):67–71

- Ashby M, Hallam S (1986) The failure of brittle solids containing small cracks under compressive stress states. *Acta Metallurgica* 34(3):497 – 510
- Attewell P, Farmer I (1973) Fatigue behaviour of rock. *International Journal of Rock Mechanics and Mining Sciences & Geomechanics Abstracts* 10(1):1 – 9
- Bagde M, Petroš V (2005) Fatigue properties of intact sandstone samples subjected to dynamic uniaxial cyclical loading. *International Journal of Rock Mechanics and Mining Sciences* 42(2):237 – 250
- Barbe F, Decker L, Jeulin D, Cailletaud G (2001) Intergranular and intragranular behavior of polycrystalline aggregates. part 1: F.e. model. *International Journal of Plasticity* 17:513–536
- Barber Z, Leake J, Clyne T (2008) Lattice planes and miller indices. Tech. rep., University of Cambridge
- Bear J (1972) *Dynamics of Fluids in Porous Media*. American Elsevier, New York, NY, USA
- Beaudoin A, Dawson P, Mathur K, Kocks U (1995) A hybrid finite element formulation for polycrystal plasticity with consideration of macrostructural and microstructural linking. *International Journal of Plasticity* 11(5):501–521
- Becker R, Panchanadeeswaran S (1995) Effects of grain interactions on deformation and local texture in polycrystals. *Acta Metallurgica et Materialia* 43(7):2701–2719
- Bérest P (2011) Thermomechanical aspects of high frequency cycling in salt storage caverns. In: *International Gas Union Research Conference 2011*, Seoul, South Korea, Oct 2011
- Bérest P, Brouard B (2003) Safety of salt caverns used for underground storage. *Oil and Gas Science and Technology* 58(3):361–384

- Bérest P, Bergues J, Brouard B, Durup J, Guerber B (2001) A salt cavern abandonment test. *International Journal of Rock Mechanics and Mining Sciences* 38(3):357–368
- Berryman JG (1995) Mixture theories for rock properties. *Rock Physics & Phase Relations: A Handbook of Physical Constants* pp 205–228
- Bobet A, Einstein H (1998) Fracture coalescence in rock-type materials under uniaxial and biaxial compression. *International Journal of Rock Mechanics and Mining Sciences* 35(7):863–888
- Bornert M, Masson R, Castañeda PP, Zaoui A (2001) Second-order estimates for the effective behaviour of viscoplastic polycrystalline materials. *Journal of the Mechanics and Physics of Solids* 49(11):2737–2764
- de Borst R, Pamin J, Geers MG (1999) On coupled gradient-dependent plasticity and damage theories with a view to localization analysis. *Eur J Mech Solids* 18(6):939–962
- Brodsky N, Munson D (1994) Proc. first n. amer. rock mech. symp. In: Nelson P, Laubach S (eds) *Proc. First N. Amer. Rock Mech. Symp.*, pp 731–738
- Brown SR, Bruhn RL (1998) Fluid permeability of deformable fracture networks. *Journal of Geophysical Research* 103(B2):2489–2500
- Bullough C, Gatzen C, Jakiel C, Koller M, Nowi A, Zunft S (2004) Advanced adiabatic compressed air energy storage for the integration of wind energy. In: *Proceedings of the European Wind Energy Conference, EWEC 2004, London UK, 22-25 November*
- Burdine N (1963) Rock failure under dynamic loading conditions. *Society of Petroleum Engineers* 3(1):1–8
- Carter NL, Hansen FD (1983) Creep of rock salt. *Tectonophysics* 92(4):275–333

- Carter NL, Heard HC (1970) Temperature and rate dependent deformation of halite. American Journal of Science 269(3):193–249
- Cauvin A, Testa R (1999) Damage mechanics: basic variables in continuum theories. Int J Solids Struct 36(5):747–761
- Cervera M, Oliver J, Prato T (1999) Thermo-chemo-mechanical model for concrete. i: Hydration and aging. J Eng Mech 125(9):1018–1027
- Chaboche JL (1992a) Damage induced anisotropy: on the difficulties associated with the active/passive unilateral condition. Int J Damage Mech 1(2):148–171
- Chaboche JL (1992b) Damage induced anisotropy: on the difficulties associated with the active/passive unilateral condition. Int J Damage Mech 1(2):148–171
- Chan K, Bodner S, Fossum A, Munson D (1997) A damage mechanics treatment of creep failure in rock salt. International Journal of Damage Mechanics 6(2):121–152
- Chan K, Bodner S, Munson D (1998) Recovery and healing of damage in wipp salt. Int J Damage Mech 7(2):143–166
- Chan K, Bodner S, Munson D (2001) Permeability of WIPP salt during damage evolution and healing. Int J Damage Mech 10(4):347–375
- Chen Y, Zhou C, Jing L (2010) Numerical modeling of coupled thermo-mechanical response of a rock pillar. J Rock Mech Geotech Eng 2(3):262–273
- Clayton J, McDowell D (2004) Homogenized finite elastoplasticity and damage: theory and computations. Mechanics of Materials 36:799–824
- Cordebois J, Sidoroff F (1982) Endommagement anisotrope en élasticité et plasticité. J de Mécanique théorique et appliquée pp 45–60

- Cosenza P, Ghoreychi M, Bazargan-Sabet B, De Marsily G (1999) In situ rock salt permeability measurement for long term safety assessment of storage. *International Journal of Rock Mechanics and Mining Sciences* 36(4):509–526
- Cowin S (1985) The relationship between the elasticity tensor and the fabric tensor. *Mech Mater* 4(2):137–147
- Crotogino F, Mohmeyer K, Scharf R (2001) Huntorf caes: More than 20 years of successful operation. In: SMRI Spring Meeting 2001
- De Boer R (1977) On the thermodynamics of pressure solution; interactions between chemical and mechanical forces. *Geochimica et Cosmochimica Acta* 41(2):249–256
- De Gennes PG (1976) *The physics of liquid crystals*. Oxford University Press
- Delaire F, Raphanel J, Rey C (2000) Plastic heterogeneities of a copper multicrystal deformed in uniaxial tension: experimental study and finite element simulations. *Acta Materialia* 48(5):1075–1087
- Dienes JK (1982) Permeability, percolation and statistical crack mechanics. In: *The 23rd U.S Symposium on Rock Mechanics (USRMS)*, Berkeley, California
- Ding J, Chester F, Chester J, Zhu C, Arson C (2016) Mechanical behavior and microstructure development in consolidation of nominally dry granular salt. In: *50th US Rock Mechanics/Geomechanics Symposium of the American Rock Mechanics Association*
- Dittes M, Labuz JF (2002) Field and laboratory testing of st. peter sandstone. *Journal of Geotechnical and Geoenvironmental Engineering* 128(5):372–380
- Djakeun HD (2014) Stabilité mécanique d’une cavité saline soumise à des variations rapides de pression. PhD thesis, Ecole Polytechnique

- Dormieux L, Kondo D, Ulm FJ (2006) A micro mechanical analysis of damage propagation in fluid-saturated cracked media. *CR Mécanique* 334(7):440–446
- Dragon A, Halm D, Désoyer T (2000) Anisotropic damage in quasi-brittle solids: modelling, computational issues and applications. *Comput Methods Appl Mech Eng* 183(3):331–352
- Dubey R, Gairola V (2000) Influence of structural anisotropy on the uniaxial compressive strength of pre-fatigued rocksalt from himachal pradesh, india. *International Journal of Rock Mechanics and Mining Sciences* 37:993–999
- Dutta AK, Penumadu D (2007) Hardness and modulus of individual sand particles using nanoindentation. In: *Advances in Measurement and Modeling of Soil Behavior*, pp 1–10
- Eberl F, Forest S, Cailletaud GC, Wroblewski T, Lebrun JL (2002) Finite-element calculations of the lattice rotation field of a tensile-loaded nickel-based alloy multicrystal and comparison with topographical x-ray diffraction measurements. *Metallurgical and Materials Transactions A* 33(9):2825–2833
- Erieau P, Rey C (2004) Modeling of deformation and rotation bands and of deformation induced grain boundaries in if steel aggregate during large plane strain compression. *International Journal of Plasticity* 20:1763–1788
- Espinosa HD, Zavattieri PD (2003) A grain level model for the study of failure initiation and evolution in polycrystalline brittle materials. part i: Theory and numerical implementation. *Mechanics of Materials* 35:333–364
- Fam M, Santamarina J, Dusseault M (1998) Wave-based monitoring processes in granular salt. *Journal of Environmental and Engineering Geophysics* 3(1):15–26

- Filimonov YL, Lavrov A, Shafarenko Y, Shkuratnik V (2001) Memory effects in rock salt under triaxial stress state and their use for stress measurement in a rock mass. *Rock mechanics and rock engineering* 34(4):275–291
- Fuenkajorn K, Phueakphum D (2010) Effects of cyclic loading on mechanical properties of maha sarakham salt. *Engineering Geology* 112(1):43–52
- Fuenkajorn K, Phueakphum D (2011) Laboratory assessment of healing of fractures in rock salt. *Bulletin of Engineering Geology and the Environment* 70(4):665–672
- Gavrilenko P, Gueguen Y (1989) Pressure dependence of permeability: a model for cracked rocks. *Geophysical Journal International* 98(1):159–172
- Ghoreychi M (1996) Mechanical behavior of salt: 3rd conference, Ecole Polytechnique, Palaiseau, France, September 14-16, 1993, vol 20. *Trans Tech Pubn*
- GiD (2002) The personal pre and postprocessor. International Center for Numerical Methods in Engineering (CIMNE), www.gidhome.com
- Guéguen Y, Dienes JK (1989) Transport properties of rocks from statistics and percolation. *Mathematical Geology* 21(1):1–13
- Gui Y, Bui HH, Kodikara J (2015) An application of a cohesive fracture model combining compression, tension and shear in soft rocks. *Computers and Geotechnics* 66:142–157
- Guo Y, Yang C, Mao H (2012) Mechanical properties of jintan mine rock salt under complex stress paths. *International Journal of Rock Mechanics and Mining Sciences* 56:54–61
- Halm D, Dragon A (1998) An anisotropic model of damage and frictional sliding for brittle materials. *Eur J Mech Solids* 17(3):439–460

- Halm D, Dragon A (2002) Modélisation de l'endommagement par mésosfissuration du granite. *Revue Francaise de Génie Civil* 17:21–33
- Handin J, Russell JE, Carter NL (1986) Experimental deformation of rocksalt. *American Geophysical Union Geophysical Monograph Series*
- Havlicek F, Kratochvil J, Tokuda M, Lev V (1990) Finite element model of plastically deformed multicrystal. *International Journal of Plasticity* 6(3):281–291
- Hayhurst DR, Dimmer PR, Morrison CJ (1984) Development of continuum damage mechanics in the creep rupture of notched bars. *Philosophical Transactions of the Royal Society of London, Series A, Math Phys Sci* 311(1516):103–129
- Heap M, Vinciguerra S, Meredith P (2009) The evolution of elastic moduli with increasing crack damage during cyclic stressing of a basalt from mt. etna volcano. *Tectonophysics* 471:153–160
- Heard H, Borg I, Carter N, Raleigh C (eds) (1972) Steady-state flow in polycrystalline halite at pressure of 2 kilobars, vol 16, *American Geophysical Union*, pp 191–209
- Hill R (1965) Continuum micro-mechanics of elastoplastic polycrystals. *Journal of the Mechanics and Physics of Solids* 13(2):89–101
- Homand-Etienne F, Houpert R (1989) Thermally induced microcracking in granites: characterization and analysis. *Int J Rock Mech Min Sci Mech Abstr* 26(2):125–134
- Hou Z (2003) Mechanical and hydraulic behavior of rock salt in the excavation disturbed zone around underground facilities. *Int J Rock Mech Min Sci* 40(5):725–738
- Houben M, ten Hove A, Peach C, Spiers C (2013) Crack healing in rocksalt via diffusion in adsorbed aqueous films: Microphysical modelling versus experiments. *Physics and Chemistry of the Earth, Parts A/B/C* 64:95–104

- Hunsche U, Hampel A (1999) Rock salt — the mechanical properties of the host rock material rock salt - the mechanical properties of the host rock material for a radioactive waste repository. *Eng Geol* 52(3-4):271–291
- Hutchinson J (1983) Constitutive behavior and crack tip fields for materials undergoing creep-constrained grain boundary cavitation. *Acta Metallurgica* 31(7):1079 – 1088
- Ibrahim H, Ilinca A, Perron J (2008) Energy storage systems - characteristics and comparisons. *Renewable and Sustainable Energy Reviews* 12(5):1221–1250
- Inada Y, Kinoshita N, Ebisawa A, Gomi S (1997) Strength and deformation characteristics of rocks after undergoing thermal hysteresis of high and low temperatures. *Int J Rock Mech Min Sci* 34(3–4):140.e1 – 140.e14
- Ioannidis M, Kwiecien M, Chatzis I (1996) Statistical analysis of the porous microstructure as a method for estimating reservoir permeability. *Journal of Petroleum Science and Engineering* 16(4):251–261
- Ishizuka Y, Abe T, Kodama J (1990) Fatigue behavior of granite under cyclic loading. In: Brumer R (ed) *ISRM International Symposium - static and dynamic considerations in rock engineering*, pp 139–146
- Jafari M, Boulon M, Hosseini K (2004) Experimental study of mechanical behaviour of rock joints under cyclic loading. *Rock Mechanics and Rock Engineering* 37(1):3–23
- Jefferson AD (1998) Plastic-damage model for interfaces in cementitious materials. *J Eng Mech* 124(7):775–782
- Jeong Hs, Kang Ss, Obara Y (2007) Influence of surrounding environments and strain rates on the strength of rocks subjected to uniaxial compression. *Int J Rock Mech Min Sci* 44(3):321–331

- Kachanov M (1992) Effective elastic properties of cracked solids: critical review of some basic concepts. *Appl Mech Rev* 45(8):304–335
- Katz AJ, Thompson AH (1986) Quantitative prediction of permeability in porous rock. *Physics Review B* 34(11):8179–8181
- Keshavarz M, Pellet F, Loret B (2010) Damage and changes in mechanical properties of a gabbro thermally loaded up to 1,000 °C. *Pure and Applied Geophysics* 167(12):1511–1523
- Kessler M, White S (2001) Self-activated healing of delamination damage in woven composites. *Composites Part A: applied science and manufacturing* 32(5):683–699
- Kim HM, Rutqvist J, Ryu DW, Choi BH, Sunwoo C, Song WK (2012) Exploring the concept of compressed air energy storage (CAES) in lined rock caverns at shallow depth: a modeling study of air tightness and energy balance. *Applied Energy* 92:653–667
- Koplik J, Lin C, Vermette M (1984) Conductivity and permeability from microgeometry. *Journal of Applied Physics* 56(11):3127–3131
- Kranz RL, Scholz CH (1977) Critical dilatant volume of rocks at the onset of tertiary creep. *J Geophys Res* 82(30):4893–4898
- Kröner E (1961) Zur plastischen verformung des vielkristalls. *Acta metallurgica* 9(2):155–161
- Lacy TE, McDowell DL, Talreja R (1999) Gradient concepts for evolution of damage. *Mechanics of Materials* 31:831–860
- Ladani LJ, Dasgupta A (2009) A meso-scale damage evolution model for cyclic fatigue of viscoplastic materials. *International Journal of Fatigue* 31(4):703–711

- Lajtai E, Duncan E, Carter B (1991) The effect of strain rate on rock strength. *Rock Mechanics and Rock Engineering* 24(2):99–109
- Langer M (1981) The rheological behavior of rock salt. In: *Proc. First Conf. Mech. Behavior of Salt*, Trans Tech Publications, Germany, pp 201–240
- Lecampion B (2010) Stress-induced crystal preferred orientation in the poromechanics of in-pore crystallization. *J Mech Phys Solids* 58:1701–1715
- Leckie FA, Hayhurst DR (1974) Creep rupture of structures. *Royal Society Math Phys Eng Sci* 340(1622):323–347
- Lee CH, Deng BW, Chang JL (1995) A continuum approach for estimating permeability in naturally fractured rocks. *Engineering Geology* 1-2:71–85
- Lemaitre J, Desmorat R (2005) *Engineering Damage Mechanics. Ductile, creep, fatigue and brittle failure*. Springer - Verlag, Berlin Heidelberg
- Levasseur S, Collin F, Charlier R, Kondo D (2011) A two-scale anisotropic damage model accounting for initial stresses in microcracked materials. *Eng Fract Mech* 78:1945–1956
- Lewis A, Geltmacher A (2006) Image-based modeling of the response of experimental 3d microstructures to mechanical loading. *Scripta Materialia* 55(1):81–85
- Li G, Uppu N (2010) Shape memory polymer based self-healing syntactic foam: 3-d confined thermomechanical characterization. *Composites Science and Technology* 70(9):1419–1427
- Li L, Tang C, Wang S, Yu J (2013) A coupled thermo-hydrologic-mechanical damage model and associated application in a stability analysis on a rock pillar. *Tunnelling Underground Space Tech* 34:38–53

- Li N, Zhang P, YS C, G S (2003) Fatigue properties of cracked, saturated and frozen sandstone samples under cyclic loading. *International Journal of Rock Mechanics and Mining Sciences* 40:145–150
- Li S, Ghosh S (2004) Debonding in composite microstructures with morphological variations. *International Journal of Computational Methods* 1(1):121–149
- Liang W, Zhao Y, Xu S, Dusseault M (2011) Effect of strain rate on the mechanical properties of salt rock. *International Journal of Rock Mechanics and Mining Sciences* 48:161–167
- Liang WG, Xu SG, Zhao YS (2006) Experimental study of temperature effects on physical and mechanical characteristics of salt rock. *Rock Mechanics and Rock Engineering* 39(5):469–482
- Lion M, Skoczylas F, Ledesert B (2005) Effects of heating on the hydraulic and poroelastic properties of bourgogne limestone. *Int J Rock Mech Min Sci* 42(4):508–520
- Liu J, Xie H, Hou Z, Yang C, L C (2014a) Damage evolution of rock salt under cyclic loading in uniaxial tests. *Acta Geotechnica* 9:153–160
- Liu R, Mao X, Zhang L, Ma D (2014b) Thermal properties of mudstone at high temperature. *International Journal of Geomechanics* 14(5)
- Lu B, Torquato S (1992) Nearest-surface distribution functions for poly-dispersed particle systems. *Phys Rev A* 45:5530–5544
- Lubarda V, Krajcinovic D (1993) Damage tensors and the crack density distribution. *Int J Solids Struct* 30(20):2659–2677
- Luong MP (1990) Tensile and shear strengths of concrete and rock. *Eng Fract Mech* 35(1-3):127–135

- Lux K, Eberth S (2007) Fundamental and first application of a new healing model for rock salt. *Basic and Applied Salt Mechanics* pp 129–138
- Lux K, Düsterloh U, Hou Z (2000) Increasing the profitability of storage caverns by means of a new dimensioning concept (i). *Erdöl Erdgas Kohle* 118:294–300
- Ma J, XY L, MY W, Xu H, Hua R, PX F, SR J, GA W, Yi Q (2013) Experimental investigation of the mechanical properties of rock salt under triaxial cyclic loading. *International Journal of Rock Mechanics and Mining Sciences* 62:34–41
- Mahnken R, Kohlmeier M (2001) Finite element simulation for rock salt with dilatancy boundary coupled to fluid permeation. *Computer Methods in Applied Mechanics and Engineering* 190(32–33):4259 – 4278
- Maleki K (2004) Modélisation numérique du couplage entre l’endommagement et la perméabilité des roches. application à l’érude des ouvrages de stockage souterrain. PhD thesis, Ecole Nationale des Ponts et Chaussées
- Mao X, Zhang L, Li T, Liu H (2009) Properties of failure mode and thermal damage for properties of failure mode and thermal damage for limestone at high temperature. *Mining Science and Technology (China)* 19(3):0290–0294
- Mapother D, Crooks HN, Maurer R (1950) Self-diffusion of sodium in sodium chloride and sodium bromide. *The Journal of Chemical Physics* 18:1231
- Masson R, Zaoui A (1999) Self-consistent estimates for the rate-dependent elastoplastic behaviour of polycrystalline materials. *Journal of the Mechanics and Physics of Solids* 47(7):1543–1568
- Masson R, Bornert M, Suquet P, Zaoui A (2000) An affine formulation for the prediction of the effective properties of nonlinear composites and polycrystals. *Journal of the Mechanics and Physics of Solids* 48(6):1203–1227

- Mazars J (1984) Application of damage mechanics to non linear behavior and failure of concrete in structures (in french). Phd thesis, University Paris, Paris, France
- Meer S, Spiers C (1997) Uniaxial compaction creep of wet gypsum aggregates. *Journal of Geophysical Research Solid Earth* 102(B1):875–891
- de Meer S, Spiers CJ, Nakashima S (2005) Structure and diffusive properties of fluid-filled grain boundaries: an in-situ study using infrared (micro) spectroscopy. *Earth and Planetary Science Letters* 232(3-4):403–414
- Mercier S, Molinari A (2009) Homogenization of elastic–viscoplastic heterogeneous materials: Self-consistent and mori-tanaka schemes. *International Journal of Plasticity* 25(6):1024–1048
- Miao S, Wang M, Schreyer H (1995) Constitutive Models for healing of material with application to compaction of crushed rock-salt. *Journal of Engineering Mechanics* 121(10):1122–1129
- Min KB, Rutqvist J, Tsang CF, Jing L (2004) Stress-dependent permeability of fractured rock masses: a numerical study. *International Journal of Rock Mechanics and Mining Sciences* 41(7):1191–1210
- Munson D, Dawson P (1979) Constitutive model for the low temperature creep of salt (with application to wipp). Tech. rep., Sandia Labs., Albuquerque, NM (USA)
- Munson DE (1979) Preliminary deformation-mechanism map for salt (with application to wipp). Tech. rep., Sandia Labs., Albuquerque, NM (USA)
- Musienko A, Cailletaud G (2009) Simulation of inter- and transgranular crack propagation in polycrystalline aggregates due to stress corrosion cracking. *Acta Materialia* 57:3840–3855

- Musienko A, Tatschl A, Schmidegg K, Kolednik O, Pippan R, Cailletaud G (2007) Three-dimensional finite element simulation of a polycrystalline copper specimen. *Acta Materialia* 55:4121–4136
- Nagashima T, Suemasu H (2006) Stress analyses of composite laminate with delamination using xfm. *International Journal of Computational Methods* 3(4):521–543
- Nebozhyn MV, Gilormini P, Ponte Castañeda P (2001) Variational self-consistent estimates for cubic viscoplastic polycrystals: the effects of grain anisotropy and shape. *Journal of the Mechanics and Physics of Solids* 49(2):313–340
- Needleman A (1987) A continuum model for void nucleation by inclusion debonding. *Journal of Applied Mechanics* 54(3):525–531
- Nemat-Nasser S, Hori M (1993) *Micromechanics: overall properties of heterogeneous solids*. Applied Mathematics and Mechanics Elsevier, Amsterdam
- O’Connell RJ, Budiansky B (1974) Seismic velocities in dry and saturated cracked solids. *Journal of Geophysical Research* 79(35):5412–5426
- Oda M (1984) Similarity rules of crack geometry in statistically homogeneous rock masses. *Mech Mater* 3(2):119–129
- Oda M, Katsube T, Takemura T (2002) Microcrack evolution and brittle failure of inada granite in triaxial compression tests at 140 mpa. *Journal of Geophysical Research* B10:1–17
- Ortiz M (1985) A constitutive theory for the inelastic behavior of concrete. *Mechanics of materials* 4(1):67–93
- Ozarslan A (2012) Large-scale hydrogen energy storage in salt caverns. *International Journal of Hydrogen* 37:14,265–14,277

- Peach CJ, Spiers CJ (1996) Influence of crystal plastic deformation on dilatancy and permeability development in synthetic salt rock. *Tectonophysics* 1-4:101–128
- Pennock G, Drury M (2005) Low-angle subgrain misorientations in deformed nacl. *Journal of Microscopy* 217(2):130–137
- Pouya A (1991a) Comportement rheologique du sel gemme application a l’etude des excavations souterraines. PhD thesis, Ecole Nationale des Ponts et Chaussées, Paris
- Pouya A (1991b) Correlation between mechanical behaviour and petrological properties of rock salt. In: *The 32nd US Symposium on Rock Mechanics (USRMS)*, pp 385–392
- Pouya A (2000) Micro-macro approach for the rock salt behaviour. *Eur J Mech A/Solids* 19:1015–1028
- Pouya A (2015) A finite element method for modeling coupled flow and deformation in porous fractured media. *Int J Numer Anal Methods Geomech* 39(16):1836–1852
- Pouya A, Vu MN (2012) Fluid flow and effective permeability of an infinite matrix containing disc-shaped cracks. *Advances in Water Resources* 42:37–46
- Pouya A, Yazdi PB (2015) A damage-plasticity model for cohesive fractures. *International Journal of Rock Mechanics and Mining Sciences* 73:194–202
- Pouya A, Zhu C, Arson C (2016) Micro-macro approach of salt viscous fatigue under cyclic loading. *Mechanics of Materials* 93:13–31
- Prost G (1988) Jointing at rock contacts in cyclic loading. *International Journal of Rock Mechanics and Mining Sciences & Geomechanics Abstracts* 25(5):263 – 272
- Raj R (1982) Creep in polycrystalline aggregates by matter transport through a liquid phase. *Journal of Geophysical Research* 87:4731–4739

- Raju M, Khaitan SK (2012) Modeling and simulation of compressed air energy storage in caverns: A case study of the huntorf plant. *Applied Energy* 89:474–481
- Ray S, Sarkar M, TN S (1999) Effect of loading and strain rate on the mechanical behaviour of sandstone. *International Journal of Rock Mechanics and Mining Sciences* 36:543–549
- Rougier Y, Stolz C, Zaoui A (1994) Self-consistent modelling of elastic-viscoplastic polycrystals. *CR Acad Sci Paris, série II* 318:145–151
- Rutter E (1976) The kinetics of rock deformation by pressure solution [and discussion]. *Philosophical Transactions of the Royal Society of London* 283:203–219
- Schleder Z, Urai JL (2007) Deformation and recrystallization mechanisms in mylonitic shear zones in naturally deformed extrusive eoceneoligocene rocksalt from eyvanekey plateau and garmsar hills (central iran). *Journal of Structural Geology* 29(2):241 – 255
- Schulze O (2007) Investigations on damage and healing of rock salt. *Mechanical Behavior of Salt-Understanding of THMC Processes in Salt* pp 33–43
- Senseny P, Hansen F, Russell J, Carter N, Handin J (1992) Mechanical behaviour of rock salt: phenomenology and micromechanisms. *International journal of rock mechanics and mining sciences & geomechanics abstracts* 29(4):363–378
- Sethuraman R, Reddy C (2008) Pseudo-elastic analysis of elastic-plastic crack tip fields using element-free galerkin method. *International Journal of Computational Methods* 5(1):91–117
- Shao J, Zhou H, Chau K (2005) Coupling between anisotropic damage and permeability variation in brittle rocks. *Int J Numer Anal Methods Geomech* 29(12):1231–1247

- Shao JF, Rudnicki J (2000) A microcrack-based continuous damage model for brittle geomaterials. *Mechanics of Materials* 32(10):607–619
- Shi Y, Zhu Zd, Li Zj (2008) Deformation characteristics of deep-buried caverns considering thermal effect. *Adv in Sci Technol Water Resour (China)* 28(3):33–36
- Silberberg M (2012) *Principles of General Chemistry*. McGraw-Hill Higher Education
- Simmons G, Wang H (1971) Single crystal elastic constants and calculated aggregate properties: a handbook. M.I.T. Press
- Singh S (1989) Fatigue and strain hardening behaviour of graywacke from the flagstaff formation, new south wales. *Engineering Geology* 26(2):171 – 179
- Smith D, Evans B (1984) Diffusional crack healing in quartz. *Journal of Geophysical Research* 89:4125–4135
- Spiers CJ, Schutjens PMTM, Brzesowsky RH, Peach CJ, Liezenberg JL, Zwart HJ (1990) Experimental determination of constitutive parameters governing creep of rocksalt by pressure solution. Geological Society, London, Special Publications 54:215–227
- Stabler J, Baker G (2000) On the form of free energy and specific heat in coupled thermo-elasticity with isotropic damage. *Int J Solids Struct* 37(34):4691–4713
- Staudtmeister K, Rokahr R (1997) Rock mechanical design of storage caverns for natural gas in rock salt mass. *International Journal of Rock Mechanics and Mining Sciences* 34(3):300–e1
- Stauffer D (1985) *Introduction to percolation theory*. Taylor and Francis, London
- Stokes R (1966) Mechanical properties of polycrystalline sodium chloride. *Brit Ceram Soc Proc* 6:187–207

- Sukumar N, Srolovitz DJ, Baker TJ, Prevost JH (2003) Brittle fracture in polycrystalline microstructures with the extended finite element method. *International Journal for Numerical Methods in Engineering* 56:2015–2037
- Sulem J, Ouffroukh H (2006) Shear banding in drained and undrained triaxial tests on a saturated sandstone: porosity and permeability evolution. *Int J Rock Mech Min Sci* 43(2):292–310
- Suzuki T (2012) Understanding of dynamic earthquake slip behavior using damage as a tensor variable: Microcrack distribution, orientation, and mode and secondary faulting. *Journal of Geophysical Research* 117:1–20
- Takahashi H, Fujiwara K, Nakagawa T (1998) Multiple-slip work-hardening model in crystals with application to torsion-tension behaviors of aluminium tubes. *International Journal of Plasticity* 14(6):489–509
- Tao Z, Mo H (1990) An experimental study and analysis of the behavior of rock under cyclic loading. *International Journal of Rock Mechanics and Mining Sciences* 27(1):51–56
- Taylor LM, Chen EP, Kuszmaul JS (1986) Microcrack-induced damage accumulation in brittle rock under dynamic loading. *Computer Methods in Applied Mechanics and Engineering* 55(3):301 – 320
- Tian H, Kempka T, Xu NX, Ziegler M (2012) Physical properties of sandstones after high temperature treatment. *Rock Mech Rock Eng* 45(6):1113–1117
- Valko P, Economides M (1994) Propagation of hydraulically induced fractures a continuum damage mechanics approach. *International Journal of Rock Mechanics and Mining Sciences and Geomechanics Abstracts* 31(3):221–229

- Vorobiev O (2008) Generic strength model for dry jointed rock masses. *Int J Plasticity* 24(12):2221–2247
- Voyiadjis GZ, Shojaei A, Li G (2011) A thermodynamic consistent damage and healing model for self healing materials. *International Journal of Plasticity* 27(7):1025–1044
- Wanten PH, Spiers CJ, Peach CJ (1996) Deformation of nacl single crystals at 0.27 t \sim m. *Series on Rock and Soil Mechanics* 20:117–128
- Warren J (2006) *Evaporites: Sediments, Resources and Hydrocarbons*. Springer
- Wawersik W, Hannum D (1980) Mechanical behavior of new mexico rock salt in triaxial compression up to 200 c. *J Geophys Res: Solid Earth* (1978–2012) 85(B2):891–900
- Weertman J (1955) Theory of steady-state creep based on dislocation climb. *Journal of Applied Physics* 26(10):1213–1217
- Weng G (1982) A unified self-consistent theory for the plastic-creep deformation of metals. *J Appl Mech* 49:728–734
- Wexler A, Hasegawa S (1954) Relative humidity-temperature relationships of some saturated salt solutions in the temperature range 0° to 50° c. *Journal of Research of the National Bureau of Standards* 53(1):19–26
- Wong TF (1982) Effects of temperature and pressure on failure and post-failure behavior of westerly granite. *Mech Mater* 1(1):3–17
- Wu W, Hou ZM, Yang CH (2005) Investigations on evaluating criteria of stabilities for energy (petroleum and natural gas) storage caverns in rock salt. *Chinese Journal of Rock Mechanics and Engineering* 24(14):2497–2505

- Xiao JQ, Ding DX, Jiang FL, Xu G (2010) Fatigue damage variable and evolution of rock subjected to cyclic loading. *International Journal of Rock Mechanics and Mining Sciences* 47(3):461–468
- Xu H, Arson C, Buseti S (2013) Modeling the anisotropic damaged zone around hydraulic fractures: Thermodynamic framework and simulation of mechanical tests. In: *Proc. 47th US Rock Mech Geomech Symp*, San Francisco, California, USA, pp Paper 13–375
- Yang C, Daemen J, Yin J (1999) Experimental investigation of creep behavior of salt rock. *Int J Rock Mech Min Sci* 36(2):233–242
- Zhou H, Hu D, Zhang F, Shao J (2011) A thermo-plastic/viscoplastic damage model for geomaterials. *Acta Mechanica Solida Sinica* 24(3):195 – 208
- Zhu C, Arson C (2014a) A model of damage and healing coupling halite thermo-mechanical behavior to microstructure evolution. *Geotechnical and Geological Engineering* 33(2):389–410
- Zhu C, Arson C (2014b) A thermo-mechanical damage model for rock stiffness during anisotropic crack opening and closure. *Acta Geotechnica* 9(5):847–867
- Zhu C, Arson C (2015) Fabric-enriched modeling of anisotropic healing induced by diffusion in granular salt. In: *49th US Rock Mechanics/Geomechanics Symposium of the American Rock Mechanics Association*
- Zhu C, Arson C, Pouya A (2015a) Theoretical and numerical matrix-inclusion models of damage accommodation in salt subject to viscous fatigue. In: *Mechanical Behavior of Salt VIII*, Rapid City, SD, USA
- Zhu C, Jeong J, Dutta M, Arson C (2015b) Image processing of fabric evolution in

- granular salt subject to diffusive mass transfer. In: Mechanical Behavior of Salt VIII, Rapid City, SD, USA
- Zhu C, Pouya A, Arson C (2015c) Micro-macro analysis and phenomenological modelling of salt viscous damage and application to salt caverns. *Rock Mechanics and Rock Engineering* 48(6):2567–2580
- Zhu H, Yan Z, Deng T, Yao J, Zeng L, Qiang J (2006) Testing study on mechanical properties of tuff, granite and breccia after high temperatures. *Chin J Rock Mech Eng* 25(10):1
- Zumdahl SS, Zumdahl SA (2006) *Chemistry*. Cengage Learning

VITA

Cheng Zhu was born on November 3, 1987, in Huai'an City, Jiangsu Province, China. He obtained his Bachelor of Engineering Degree (2009) and Master of Engineering Degree (2012) from Nanyang Technological University in Singapore. From August 2012, he started his Ph.D. study under the supervision of Dr. Chloé Arson at the Georgia Institute of Technology. He obtained his Master of Science Degree in 2014 and will receive his Ph.D. degree in August 2016 from the Georgia Institute of Technology.